Novel Imaging using a MEG Scanner, and MRI Homogeneity Improvement Techniques

Ingrid Vella, B.Eng.(Hons), M.Sc.

Thesis submitted to The University of Nottingham

for the degree of Doctor of Philosophy

September 2016

Abstract

The general aims of the work in this thesis are to locate and quantify magnetic dipoles using a Magnetoencephalography (MEG) system based on Superconducting Quantum Interferance Device (SQUID) sensors, and to generate various target magnetic fields using magnetic dipoles.

MEG provides direct, real-time measurements of magnetic fields at sub-millisecond temporal resolution and femtoTesla sensitivity. It is typically used to describe sources in terms of current dipoles, but here we adapt a different approach and use it to characterise magnetic dipoles. In the first part of this thesis, we describe initial experiments which were carried out in order to demonstrate the feasibility of using the high sensitivity of MEG SQUID sensors to detect extremely small magnetic field shifts due to magnetised samples, and to then locate and quantify the magnetic dipoles. We show that a standard MEG system can be used to measure magnetic field shifts due to susceptibility effects from samples exposed to an Ultra Low Field (ULF), as well as to detect and image the distribution of decaying longitudinal nuclear magnetisation from pre-polarised samples. During our experiments, we also identified a long-lived magnetisation in biological samples, whose magnetisation orientation is fixed by the sample orientation. This finding led us to carry out experiments on samples including human tissue (the hand, wrist, and foot) using MEG, and to characterise the magnetisation behaviour.

Even though ULF Magnetic Resonance Imaging (MRI) has several benefits, it is difficult for it to compete with Ultra High Field (UHF) MRI since the higher

the field is, the larger does the SNR tend to be. Yet, higher fields increase the effects of intrinsic magnetic susceptibility differences, which in turn leads to field inhomogeneities. Thus, in the second part of this thesis, we aim at improving the quality of high field MR images. We show how magnetic dipoles can be used to generate different target fields that can be used to shim different inhomogeneous magnetic fields at UHF. These magnetic dipoles can be realised using either an array of orthogonal coils or pieces of strongly diamagnetic material.

Acknowledgements

I am sincerely and heartily grateful to my supervisor, Prof. Richard Bowtell, for his patient guidance, staunch support and valuable advice throughout the last four years. It has been a great privilege for me to work under his supervision.

Furthermore, I am indebted to Prof. Matt Brookes and Dr Paul Glover, for their constructive comments and useful critique about my work.

I wish to acknowledge the work of Alan Dorkes in constructing various pieces of apparatus for my studies.

Thanks must also go to all those who either kindly volunteered for, or assisted in the procedure of any of my experiments. I must especially mention Mobeen, George, and Ben.

Danke schön to Dr Josef Granwehr, for being a truly inspirational lecturer, and for the many insightful talks about nuclear magnetic resonance - and movies, on late nights at SPMIC in my first year.

It would be impossible for me to not mention my family at Derby Hall. I must particularly mention the support, encouragement and mentorship of Dr Mark Wenman and the friendship of the other tutors from my three years in the Derby Army: Ally, Negar, Hannah, Hamny, Chayce, Kieran, Angeliki, Alex, Becky, Harriet, Chloe, Haich, Frank, Laura and Tobias. Your friendship over the years has been invaluable to me and I have so many fond memories of you all. Thanks also

to Lisa, for overfeeding all of us!

I would also like to thank everyone who has been working in the Sir Peter Mansfield Imaging Centre over the last four years, for their academic - and their not so academic inputs. Also, I am grateful for the coffee breaks together, as well as the memorable trips in Poland and Malta. In particular, I owe my loving thanks to Aleksandra, Glyn, and Matt.

In addition, I am grateful to my friends, who supported and encouraged me throughout my degree from near or afar. Thanks especially to Matt for his sincere friendship, Karl for spoiling me when visiting and for supplying me with all the Kinnie and Twistees I needed, and Mark for his shrewd advice on anything that is not science. I am especially grateful to my boyfriend, Anthony, for putting up with me over the past two years.

Special thanks to my parents, Tessie and Edward, who have been supporting me for longer than anyone else. Thank you for laughing with me through the good times, and carrying me through the bad times.

Finally, I offer my regards to all those who helped and supported me in any respect during the completion of the project. Grazzi!

Contents

Chapter 1

Introduction

Magnetoencephalography (MEG) is a non-invasive technology that measures magnetic fields using SQUIDs [1]. It has a good temporal resolution and can measure fields of femtoTesla magnitude. MEG is typically used to measure magnetic fields produced by current sources, but in this thesis MEG was used to measure the weak magnetic fields produced by magnetisation, rather than current flow. We used a MEG system based on SQUID detectors to measure magnetic field shifts produced by changes in magnetic susceptibility, and from nuclear magnetisation. During these experiments we discovered a magnetic signal in protein and chicken samples that takes a significantly long time to decay. This spurred us on to study remanent magnetisation in human tissue.

Magnetic Resonance Imaging (MRI) is a powerful and non-invasive technology, used for imaging biological structures. Since higher static magnetic field strengths produce a higher SNR [2], there is a push for high field MRI scanners [3]. However, higher fields increase the effects of intrinsic magnetic susceptibility differences, and lead to inhomogeneities. Shimming is typically used to mitigate this problem. In this thesis, we discuss a way of using an array of magnetic dipoles to create several target fields, including spherical harmonic shimming fields.

The work presented in this thesis focusses on using MEG detectors to measure the magnetic field from magnetic sources, which is then used to localise and quantify the magnetic dipole strengths, and on using magnetic dipoles to simulate the generation of different target magnetic fields, which can then be generated using small electromagnetic coils or pieces of material with anisotropic magnetic susceptibility.

1.1 Thesis Overview

In addition to Chapter 1, this thesis is made up of the following chapters:

Chapter 2 This chapter provides a basic introduction to MEG. It touches on the theory of superconductivity and how this phenomenon can be used by SQUIDs to convert magnetic flux into voltage. Following this, is an overview of the MEG forward and inverse problems. Whereas MEG is typically used to measure weak magnetic fields produced by current flow, we used it to measure weak magnetic fields produced by magnetisation. Simulations demonstrating the feasibility of localising magnetisation based on magnetic field measurements using a typical MEG gradiometer detector array are described.

Chapter 3 This chapter explores the use of MEG in the detection of magnetic field shifts. We measured the magnetic field due to the magnetisation which some samples exhibit when exposed to a weak polarising field inside the MEG scanner, and used it to reconstruct the strength and location of the magnetic source. In a second set of experiments, we pre-polarised samples and used SQUIDs to record the longitudinal nuclear magnetisation relaxation in the presence of a weak imaging field inside the MEG helmet.

Chapter 4 This chapter explores the source of a long-lived magnetisation signal that we came across in biological samples. Our method involved magnetising several samples, such as milk powder, protein powder, and chicken meat, and then using MEG to detect and map the magnetic field shifts. We also applied the inverse problem relating the measured magnetisation distribution to the magnetic fields produced at the array of MEG sensors, so as to generate images of the distribution of induced magnetisation. We then moved on to human tissue (the hand, wrist, and foot), and we measured and characterised the magnetic fields generated by remanent magnetisation using a MEG scanner.

Chapter 5 This chapter is different from the others in that it is associated with MRI, rather than MEG. It explains how field inhomogeneities scale with the field, and describes several shimming techniques. It then presents a way of using magnetic dipoles located on the surface of a cylinder to generate different target fields, including gradient fields, spherical harmonics, and the inverse of a brain field map, which can then be superimposed onto the field map to reduce the inhomogeneity of the field.

Chapter 6 This chapter draws general conclusions based upon the work carried out in this thesis.

Chapter 2

Measuring Magnetisation using a MEG System

2.1 Introduction

Magnetoencephalography, MEG, is a non-invasive technique that measures the magnetic fields generated by brain activity [1, 4]. The term *magnetoencephalography* is composed of the three words: *magneto-* relates to magnetism, *encephalo-* relates to the brain, and *-graphy* refers to a scientific field of study.

MEG measures very weak, fast changing magnetic fields produced by the human brain [1]. It has high temporal resolution of approximately 1 ms [5], and a spatial resolution on the order of 5 mm [6].

Typically, the magnetic detectors used in MEG are Superconducting QUantum Interference Devices (SQUIDs). SQUIDs are very sensitive and relatively frequency-independent [7], and they can measure fT (10^{-15} T) fields [8, 9, 10]. In this project, we have used a MEG system to measure weak magnetic fields produced by magnetisation rather than current flow.

2.2 Theory

The hypothesis behind this project was that we can simulate magnetic field measurements from a typical MEG gradiometer detector system, for magnetic dipoles of varying strengths, at different locations and orientations, and use them to localise magnetisation.

The basic idea of conventional MEG [1] is to measure small changes in magnetic fields induced by current flow in the brain, and then to use these magnetic fields to reconstruct a map of the underlying flow of neural current in the brain. This idea can be split into two main problems. The first is the detection of the magnetic fields. This poses a challenge because the fields that are produced are typically of the order fT, and are thus almost ten orders of magnitude smaller than Earth's magnetic field, which varies between 25 µT and 65 µT. The second problem is the reconstruction of the underlying current, since the inverse problem [11] is ill-posed [12].

Detection of weak magnetic fields requires the use of sensitive magnetic sensors [13], and the reduction of noise [14]. In MEG, weak magnetic fields are detected by SQUIDs, which are generally formed from low temperature superconductors [8]. Noise is reduced by magnetic shielding [15, 16, 17] and by the use of gradiometers [18]. The following sections explain how the magnetic signals are picked up, how the noise is reduced, and how images are created from the data collected.

2.2.1 Superconductivity

Superconductivity is a property of materials that exhibit an abrupt transition to a state of zero electrical resistance below a well-defined critical temperature, T_c. A theory of superconductivity was proposed in 1957 by Bardeen, Cooper and Schrieffer [19], in which they suggested that superconducting electrons are bound

together in pairs, which are called *Cooper pairs*.

This is counter-intuitive as Coulomb interaction is expected to push apart these superconducting electrons. However, in a superconductor, the two electrons are not isolated. They are in a lattice of positively charged atoms that make up the solid with which they interact. Also, the repulsive force is partially screened out by other electrons. Consequently, what happens is that as an electron passes between positive ions, it causes a spatial disturbance (Figure 2.1). Each ion will be attracted towards the electron. The large positive ions move slowly, and the first electron leaves behind it a slight ripple of positive charges towards its path, that attracts and binds the second electron [20] (Figure 2.2).

Electrons are fermions, and the Pauli exclusion principle states that no two electrons can exist in the same state. However, a Cooper pair, which is essentially composed of two fermions, forms one boson, and any number of bosons can exist in the same state at the same time. The binding energy of Cooper pairs is maximised when all pairs are in the same state.

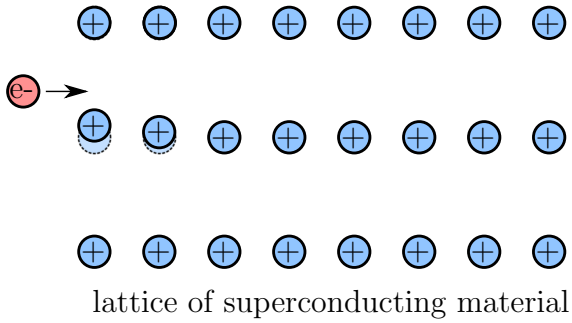

Figure 2.1: Schematic showing the effect of an electron passing through the lattice.

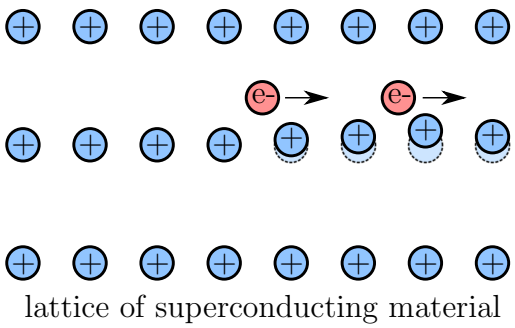

Figure 2.2: Schematic showing a Cooper pair formation.

Superconductivity is therefore a cooperative phenomenon, with a stronger binding energy for pairs acquiring the same wavefunction. The equivalent wavefunction of all of the Cooper pairs explains the superconductor's infinite conductivity. Since the pairs must exist in the same state, their centre of mass motion must be equivalent, so they will all travel in the same direction with equivalent momentum.

The resulting supercurrent is not affected by scattering because if one electron is affected, a second electron compensates. The supercurrent can only be affected by something that affects all pairs equally, such as an electric or magnetic field.

2.2.2 Josephson Junction

When two superconductors are separated by an insulating oxide layer, they are said to be weakly coupled, and a Josephson junction forms [21]. At a temperature below the critical temperature, Cooper pairs can tunnel across the Josephson junction even in the absence of an applied voltage [22].

Since all Cooper pairs have the same wavefunction, they can all be described by a single wavefunction. For two superconductors with wavefunctions $\psi_1 = |\psi_1|e^{i\theta_1}$ and $\psi_2 = |\psi_2|e^{i\theta_2}$, separated by a small gap, if there is no interaction across the gap, the phases θ_1 and θ_2 will be different. However, if the two samples are brought together, the phases of both regions will equalise and the Cooper pairs will be forced into the same state. If the interaction is weak, and a small tunnelling current flows or a voltage is applied, there will be a phase difference generated between the two regions (Figure 2.3).

Tunnelling across the gap happens as a result of the extension of the wavefunction for each superconductor into the gap. Within the gap, the wavefunctions add, and the current density across the junction will be

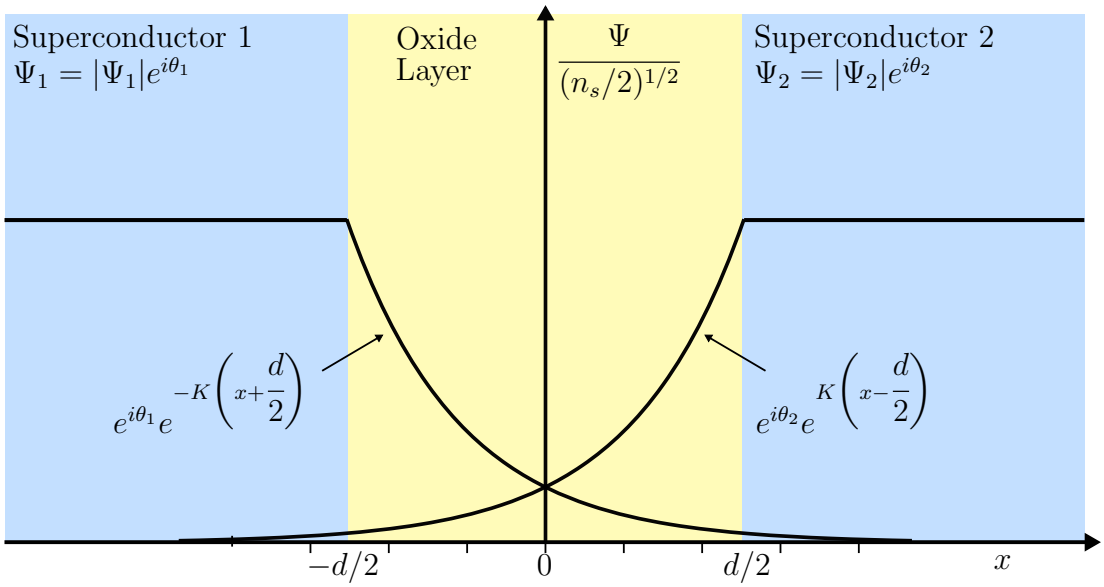

Figure 2.3: Diagram showing order parameters for two superconductors weakly coupled at Josephson junction, formed from an oxide layer of thickness, d.

$$j = j_0 \sin(\delta), \tag{2.1}$$

where

$$\delta = \theta_1 - \theta_2, \tag{2.2}$$

implying that the current across the gap depends on the two phases. The Cooper pair flow across the junction is known as the DC Josephson effect.

2.2.3 SQUIDs

SQUIDs are devices that convert magnetic flux into voltage [23]. MEG systems use SQUIDs, rather than induction coils because SQUIDs have a higher sensitivity and lower noise than induction coils [24]. SQUIDs are made up of a superconducting ring interrupted by two parallel Josephson junctions. In their operation, the following four superconducting phenomena [23] are necessary:

1. infinite conductivity; the complete loss of electric resistance at temperatures below the critical temperature,
2. the Meissner effect, which shows perfect diamagnetism with no magnetic flux inside the superconductor except for a thin penetration region near the surface,
3. the quantisation of magnetic flux in a superconducting ring, and
4. the DC Josephson effect.

Most MEG systems use Niobium (Nb) based SQUIDs that typically sit in a bath of liquid helium. Niobium has a superconductive transition temperature of 9.2 K, and when superconducting at 4.2 K, tunnelling of Cooper pairs can occur through the thin insulating layer separating the two superconductors. The Josephson junctions serve to limit the flow of supercurrent [1]. Nb-based SQUIDs are reliable against thermal cycling between 4.2 K and room temperature. Josephson junctions made of Niobium and Aluminium oxide (Nb/AlOx/Nb) show low leakage currents in the low frequency range [25].

Figure 2.4 is a schematic of the DC SQUID. When superconducting at a tem-

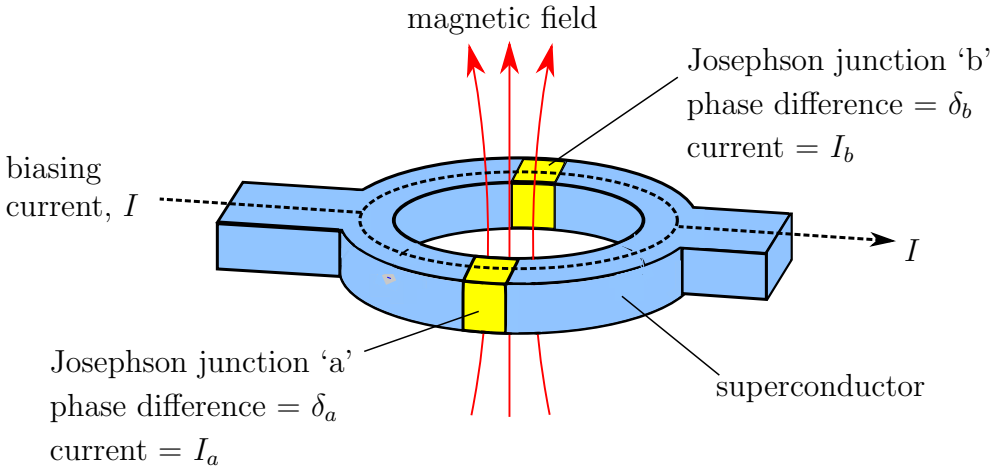

Figure 2.4: Schematic of the DC SQUID.

perature less than the critical temperature, a current flows across the Josephson junctions. The tunnelling of Cooper pairs allows a small current to pass through the SQUID. In the absence of external magnetic fields, the input current I, also referred to as the biasing current, splits equally into the two branches ($I_a = I_b$).

If a magnetic field impinges on the superconducting ring, it will induce a change in the magnitude of the current. A screening current, I_s, begins circulating around the loop, generating a magnetic field that cancels the applied external flux. This way, magnetic fields crossing the loop modulate the current.

The current, I, flowing through the two parallel Josephson junctions is given by

$$I = AJ_o[\sin(\delta_a) + sin(\delta_b)]. \tag{2.3}$$

Using trigonometric identities, this can be rearranged as

$$I = 2AJ_o \cos\left[\frac{\delta_a - \delta_b}{2}\right] \sin\left[\frac{\delta_a + \delta_b}{2}\right]. \tag{2.4}$$

$\delta_a - \delta_b$ depends on the magnetic flux through the ring, and

$$I = I_s \cos\left[\frac{e}{\hbar}\Phi\right], \tag{2.5}$$

where Φ is the magnetic flux threading the SQUID ring. Thus, the current, I, varies periodically with magnetic flux. This is known as *quantum interference*.

The induced current is in the same direction as the current in one of the branches in the superconducting loop, and opposite to the current in the other branch. Thus, in one branch the total current will be $\frac{I}{2} + I_s$, and in the other branch it

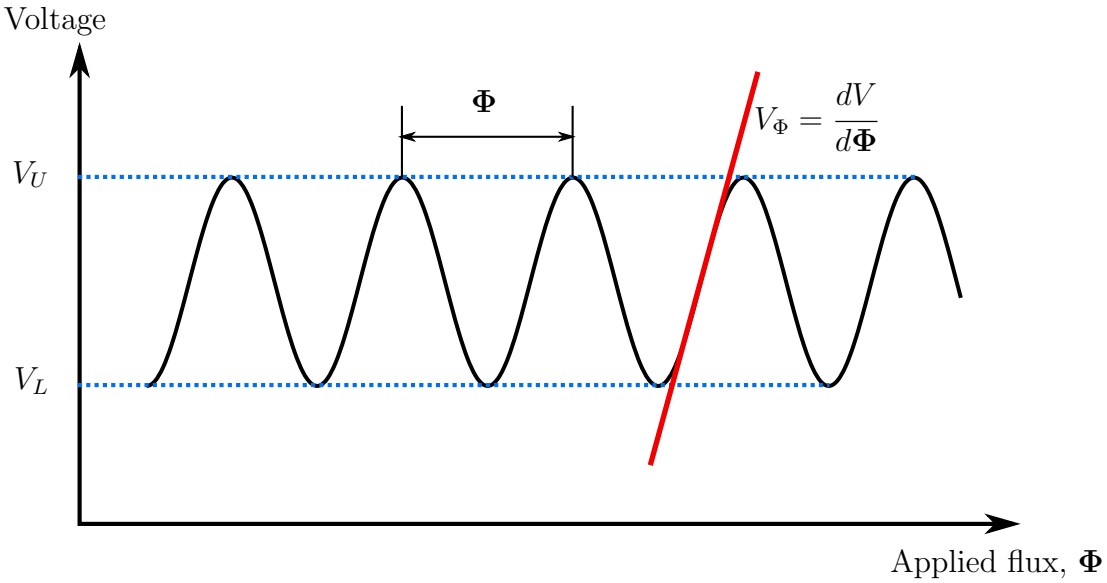

Figure 2.5: Diagram showing how voltage changes with applied flux.

will be $\frac{I}{2} - I_s$.

When the current in one of the branches exceeds the critical current, I_c, of the Josephson junction, a voltage appears across the junction. If the external flux is bigger than half the magnetic flux through the ring, $\frac{\Phi_0}{2}$, the SQUID increases the magnetic flux threading the ring so as to keep the external flux smaller than $\frac{\Phi_0}{2}$. The screening current will then flow in the opposite direction, changing direction whenever the flux increases by half integer multiples of Φ_0. Thus, the critical current oscillates as a function of the applied flux.

If the bias current is larger than the critical current, the junctions become resistive. In resistive mode, a change in the magnetic flux will not induce a change in the current, but will instead induce a change in voltage. The voltage drop across the SQUID is a multi-valued periodic function of the applied magnetic field (Figure 2.5). The SQUID is set to operate on the steepest part, i.e. where $\frac{dV}{d\Phi}$ is maximum. The relationship used to detect the small magnetic fields is

$$\Delta V = R\Delta I, \tag{2.6}$$

and

$$2I = 2\frac{\Delta\Phi}{L}, \tag{2.7}$$

where L is the self inductance of the superconducting ring. Using Equation 2.7 to substitute for I into Equation 2.6 yields

$$\Delta V = \frac{R}{L}\Delta\Phi. \tag{2.8}$$

A pickup coil that is much larger than the SQUID is used to pick up the applied magnetic field **B**. This is mutually coupled to a multi-turn signal coil integrated directly on the SQUID loop (Figure 2.6).

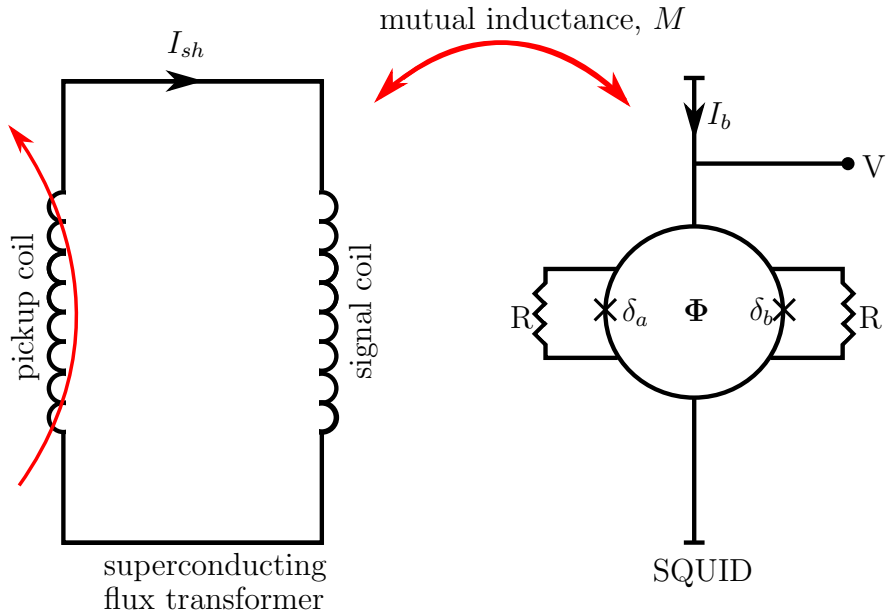

Figure 2.6: Schematic of the pickup coil and SQUID.

Changing magnetic fields cause current variation in the pickup coil, which in turn causes a current flow in the signal coil. The signal coil is coupled to the SQUID by mutual inductance. Thus, the current in the signal coil will alter the flux threading the SQUID. The SQUID responds with a measurable voltage change across the weak links. This is detected by the SQUID electronics that will apply a feedback current to the ring so as to counterbalance the induced current. This ensures that the operation of the SQUID is maintained within a single cycle of flux-voltage transfer. The output of the feedback is then measured as a voltage produced across a resistor in the feedback circuit. This will be the output in a magnetometer system.

The amplitude of the SQUID voltage output is small, and thus a low noise pre-amplifier is used to readout the SQUID output.

2.2.4 Pickup Coils and Gradiometers

Each SQUID detects magnetic fields via a superconducting circuit, known as a flux transformer. In order to increase the field detection of the SQUID, a flux transformer with a pickup coil that is much larger than the SQUID is used. Typically, the diameter of such a coil is 20 mm. As the SQUID inductance increases, so does the intrinsic flux noise [26]. Thus, it is favourable that the loop size is kept small. Yet, for effective coupling of magnetic flux with input coil, the SQUID loop size must have a practical minimum limit of about 100 µm, and the typical size of a SQUID is 10 mm^2.

There are three main types of pickup coils: magnetometers, axial gradiometers, and planar gradiometers. A magnetometer (Figure 2.7), first used in 1972 by Cohen [27], picks up the magnetic field through a loop, and converts it into flux through the input loop.

Gradiometers are coils that measure the magnetic field gradient, rather than the

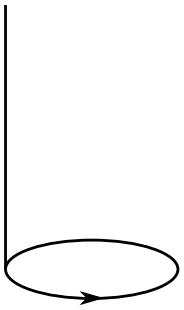

Figure 2.7: Schematic of magnetometer.

actual magnetic field. They are physically wound coils, whereby each detector is made of two loops of wire wound in opposition. The magnetic field passing through the detector induces voltages in the two loops, that partially cancel out. Thus, the net voltage measured represents the magnetic field gradient, G.

An axial gradiometer (Figure 2.8) comprises two coils arranged on top of one another, and connected in series. The magnetic field gradient measured by an axial gradiometer is given by

$$\mathbf{G}_{axial} = \mathbf{B}_1 - \mathbf{B}_2, \tag{2.9}$$

where $\mathbf{B}_1$ is the magnetic field at the lower loop, and $\mathbf{B}_2$ is the magnetic field at the upper loop.

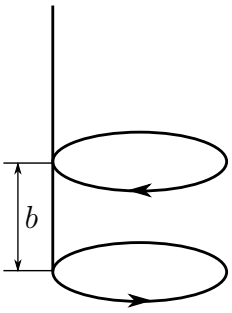

Figure 2.8: Schematic of axial gradiometer. b is the gradiometer baseline.

A planar gradiometer (Figure 2.9) is also comprised of two coils, but the two coils are aligned on the same horizontal plane. This gradiometer measures the field gradient in an orthogonal orientation to that measured by the axial gradiometer.

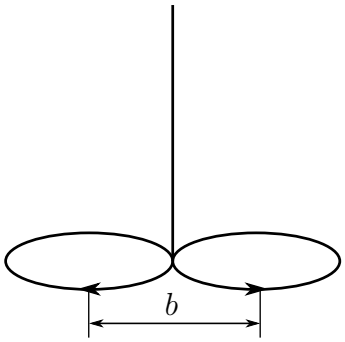

Figure 2.9: Schematic of planar gradiometer. b is the gradiometer baseline.

The effective magnetic field gradient measured by the planar gradiometer is given by

$$\mathbf{G}_{planar} = \mathbf{B}_1 - \mathbf{B}_2, \tag{2.10}$$

where $\mathbf{B}_1$ is the magnetic field at the left loop, and $\mathbf{B}_2$ is the magnetic field at the right loop.

Since the magnetic field strength from current sources falls off as $1/r^2$, gradiometers are more sensitive to superficial sources, than deeper sources. Figure 2.10

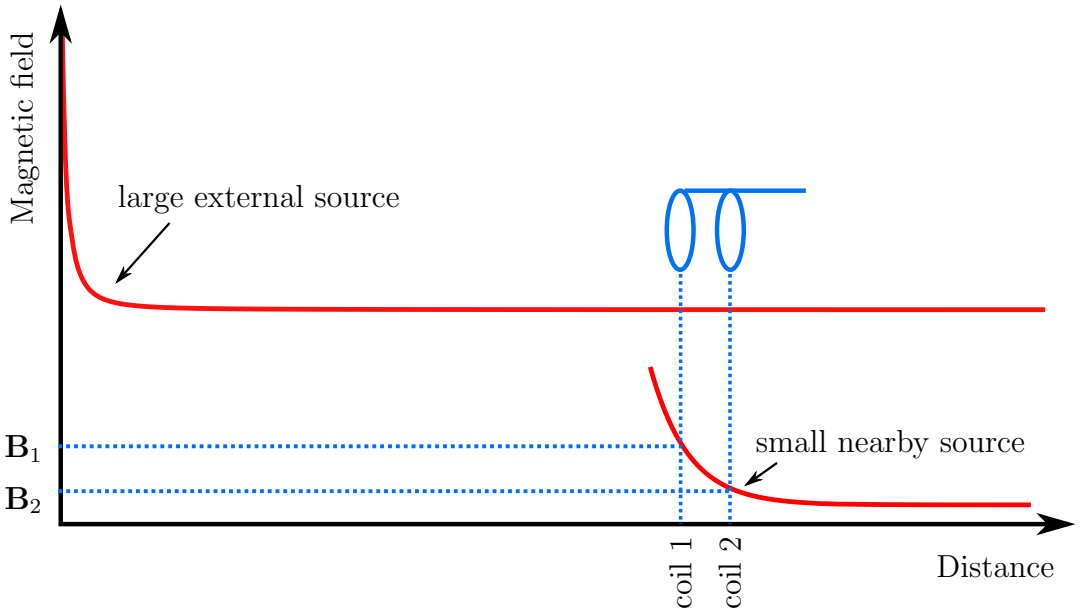

Figure 2.10: Diagram showing how the magnetic fields change with distance from source.

shows how the gradient field from a strong source located far from the gradiometers is generally negligible compared to the gradient field from smaller magnetic fields coming from nearby sources. The gradient becomes smaller with increasing distance away from source. Thus, interference from distant sources can be significantly reduced by measuring the field gradient.

Table 2.1 gives the flux density of distant sources whose effect is significantly reduced by the use of gradiometers.

Source	Flux Density (fT)
Earth's magnetic field	10^{10}
Laboratory noise	10^{9}
Urban noise	10^{8}
Geomagnetic noise	10^{7}

Table 2.1: Flux density from typical noise sources.

2.2.5 MEG Forward Problem

In MEG, the forward problem refers to computing the magnetic field at a set of sensor locations, given a well-defined source configuration. The relationship between the fields from the source distribution and the measured magnetic field at discrete sensor locations is linear [28]. The forward problem is a well-posed problem with a unique solution, that can be accurately determined using Maxwell's equations [29].

The electromotive force created in conducting tissue, gives rise to an impressed source current density, $\mathbf{J}_i$. If we assume that $\mathbf{J}_i$ lies in a conductor G, that has conductivity σ, and that $\mu = \mu_0$ everywhere, then the electric field, $\mathbf{E}$, and the magnetic induction, $\mathbf{B}$, that arise from the source $\mathbf{J}_i$, can be computed using the

quasi-static approximations of Maxwell's equations [30]:

$$\mathbf{E} = -\nabla V, \tag{2.11}$$

$$\nabla \times \mathbf{B} = \mu_0 \mathbf{J}, \tag{2.12}$$

$$\mathbf{J} = \mathbf{J}_i + \sigma \mathbf{E}, \tag{2.13}$$

$$\text{and } \nabla \cdot \mathbf{B} = 0 \tag{2.14}$$

where V is the electrical potential, $\mathbf{J}$ is the total current density, and $\sigma\mathbf{E}$ is the Ohmic current [30]. $\mathbf{B}$ is given by the Biot-Savart law [31] :

$$\mathbf{B}(\mathbf{r}) = \frac{\mu_0}{4\pi} \int_G \mathbf{J}(\mathbf{r}') \times \frac{\mathbf{r} - \mathbf{r}'}{|\mathbf{r} - \mathbf{r}'|^3} d\upsilon', \tag{2.15}$$

where $\mathbf{r}'$ is the coordinate of the current element and $\mathbf{r}$ is the point of detection. If we assume that σ is piecewise constant, Equation 2.13 can be re-written as

$$\mathbf{J} = \mathbf{J}_i - \sigma \nabla \mathbf{V}. \tag{2.16}$$

Since $\nabla.\mathbf{J} = 0$, then

$$\nabla \cdot (\mathbf{J}_i - \sigma \nabla \mathbf{V}) = 0$$

$$\nabla \cdot \mathbf{J}_i = \nabla \cdot (\sigma \nabla \mathbf{V}). \tag{2.17}$$

The potential, V, is obtained using Poisson's equation (Equation 2.18) with proper boundary conditions, and with the condition that $V(\mathbf{r}) \to 0$ as $|\mathbf{r}| \to \infty$. In a region of constant σ, this yields

$$\nabla^2 \mathbf{V} = \nabla \cdot \left(\frac{\mathbf{J}_i}{\sigma} \right). \tag{2.18}$$

Computing V is a heavy numerical procedure, that can be simplified for the cases of a homogeneous unbounded conductor, a horizontally layered conductor, and a spherically symmetric conductor [29]. Thus, in order to simplify the solution to the forward problem, we make the following two approximations.

1. Current-Dipole Approximation

   When viewed from a distance, the magnetic field resulting from a number of synchronised currents looks like the field from one current dipole. This approximation is reasonable if the volume where the sources are located is small. In these conditions,

   $$|Q| = lI, \tag{2.19}$$

   where l is the distance over which the current flows, assumed to be very small, and I is the magnitude of that current.

2. Spherically Symmetric Conductor Approximation

   The source volume is modelled as a conducting sphere with homogeneous conductivity. Using Stokes' Law, if the source volume is a perfect sphere, volume currents can be approximated to a surface current. This approximation implies that volume currents will not contribute to the radial part of the magnetic field.

Rewriting the Biot-Savart law, for a current dipole with a moment $\mathbf{Q}$ located at point $\mathbf{r}'$, the magnetic field generated at point $\mathbf{r}$, as shown in Figure 2.11, is given by

$$\mathbf{B} = \frac{\mu_0}{4\pi} \frac{\mathbf{Q} \times (\mathbf{r} - \mathbf{r}')}{|\mathbf{r} - \mathbf{r}'|^3}, \tag{2.20}$$

where $|\mathbf{r} - \mathbf{r}'|$ is the linear distance between the location of the dipole and the point of detection[32].

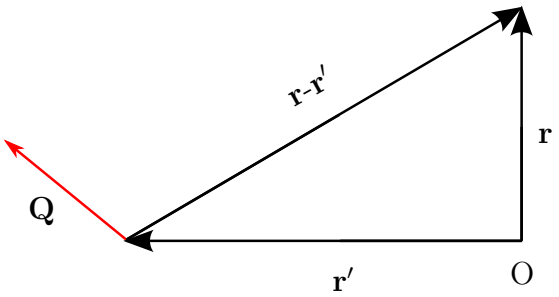

Figure 2.11: Diagram used to explain the Biot-Savart Law for a current dipole.

However, for a system of MEG detector coils that are oriented radially as shown in Figure 2.12, the magnetic field recorded at the detector is the radial field, given by

$$B_{detect} = \frac{\mu_0}{4\pi} \frac{\mathbf{Q} \times (\mathbf{r} - \mathbf{r}')}{|\mathbf{r} - \mathbf{r}'|^3} \cdot \hat{\mathbf{e}}_{\mathbf{r}}, \tag{2.21}$$

where $\hat{\mathbf{e}}_{\mathbf{r}}$ is a unit vector in the radial direction at $\mathbf{r}$ [32].

In a real MEG system, there will be more than one source and more than one

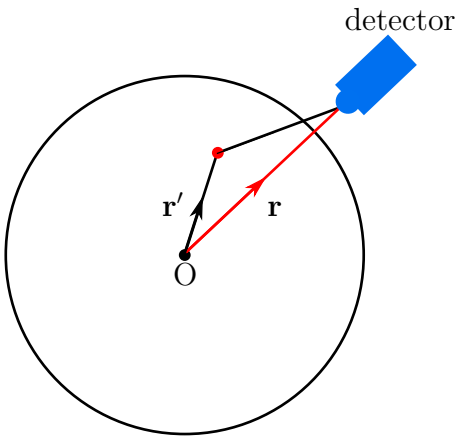

Figure 2.12: Diagram showing detector located at $\mathbf{r}$, oriented radially.

detector. The forward problem is then described by

$$\mathbf{d} = \mathbf{L}\mathbf{s}, \tag{2.22}$$

where $\mathbf{d}$ is a vector containing field strength at n sensor locations, $\mathbf{s}$ is a vector of length m, with the magnitudes of all the current sources with a given position and orientation, and $\mathbf{L}$ is a lead-field matrix.

The concept of a lead-field is widely used in source reconstruction. A *lead-field* is an n-dimensional column vector containing the magnetic fields that would be measured at each of the n MEG sensors, in response to a source of unit amplitude with some *a priori* determined location and orientation. The lead-field is also a forward field because it represents the solution to the forward problem for all sensor locations. The composite lead-field matrix is of size n channels by m voxels, and $L_{i,j}$ is the projection of current dipole j onto sensor i [33].

MEG measurements are a linear projection of dipole time-courses through the lead-fields, with additional noise. At a single time point, the magnetic field, B, at one sensor, from one dipole is

$$B = \mathbf{L}\mathbf{Q}. \tag{2.23}$$

For m dipoles, the magnetic field, B, at one sensor is

$$B_1 = L_{11}Q_1 + L_{12}Q_2 + \ldots + L_{1m}Q_m. \tag{2.24}$$

Extending this to n sensors and m sources,

$$\begin{bmatrix} B_1(t) \\ B_2(t) \\ \vdots \\ B_n(t) \end{bmatrix} = \begin{bmatrix} L_{11} & L_{12} & L_{13} & \dots & L_{1m} \\ L_{21} & L_{22} & L_{23} & \dots & L_{2m} \\ \vdots & \vdots & \vdots & \ddots & \vdots \\ L_{n1} & L_{n2} & L_{n3} & \dots & L_{nm} \end{bmatrix} \begin{bmatrix} Q_1(t) \\ Q_2(t) \\ \vdots \\ Q_m(t) \end{bmatrix} + \begin{bmatrix} e_1(t) \\ e_2(t) \\ \vdots \\ e_n(t) \end{bmatrix}, \tag{2.25}$$

where n is of the order 300, m is typically thousands, and $e_n(t)$ represents the noise at the n^{th} sensor at time t. In matrix form,

$$\mathbf{B}(t) = \mathbf{LQ}(t) + \mathbf{e}(t), \tag{2.26}$$

where $\mathbf{B}$ is a vector of length n, $\mathbf{L}$ is a non-square and singular $n \times m$ matrix, $\mathbf{Q}$ is a vector of length m and $\mathbf{e}$ is a noise vector of length n.

2.2.6 MEG Inverse Problem

The inverse problem attempts to reconstruct the underlying current distribution that generates the measured magnetic field distribution at the MEG sensors. Measured magnetic fields are a superposition of fields generated by all the dipoles, and magnetic interference. Magnetic field cancellation implies that a single field distribution can result from an infinite number of current distributions. Thus, this problem is ill-posed, and the MEG inverse problem is solved using optimisation approaches [34].

The Generative Model

We begin with the assumption that our region of interest is a spherical conductor of volume V (Figure 2.13).

The radial component of the magnetic field, $b(\mathbf{r}, t)$, measured by the detector,

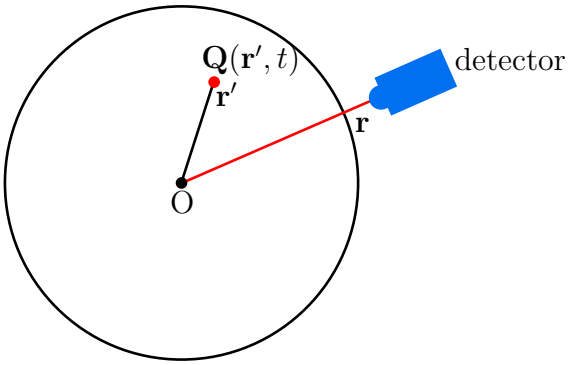

Figure 2.13: Diagram showing dipole source in spherical conductor.

can be modelled as an integral over volume of all sources:

$$b(\mathbf{r}, t) = \int_V L(\mathbf{r}, \mathbf{r}')Q(\mathbf{r}', t)dV + e(\mathbf{r}, t), \tag{2.27}$$

where $L(\mathbf{r}, \mathbf{r}')$ is the lead-field describing the magnetic field that would be induced at $\mathbf{r}$ by a current dipole of unit amplitude located at $\mathbf{r}'$, and $\mathbf{Q}(\mathbf{r}', t)$ is the current dipole strength at position $\mathbf{r}'$ and time t. The assumed orientation of the source is known *a priori*, and $e(\mathbf{r}, t)$ is the error on the sensor measurement that results from magnetic interference and noise on the sensor.

We then split the conductor volume into cubic voxels, such that

$$b(\mathbf{r}, t) = \sum_{m=1}^{M} L(\mathbf{r}, \mathbf{r}')Q(\mathbf{r}', t)dV + e(\mathbf{r}, t), \tag{2.28}$$

where m is the voxel number, and M is the total number of voxels.

Spatial Filter Formation

The time-course of electrical current $\hat{\mathbf{q}}(\mathbf{r}', t)$ is reconstructed at each voxel location, $\mathbf{r}'$ (Figure 2.14).

$\hat{\mathbf{q}}(\mathbf{r}', t)$ is formed from a linearly weighted sum of sensor measurements, and is

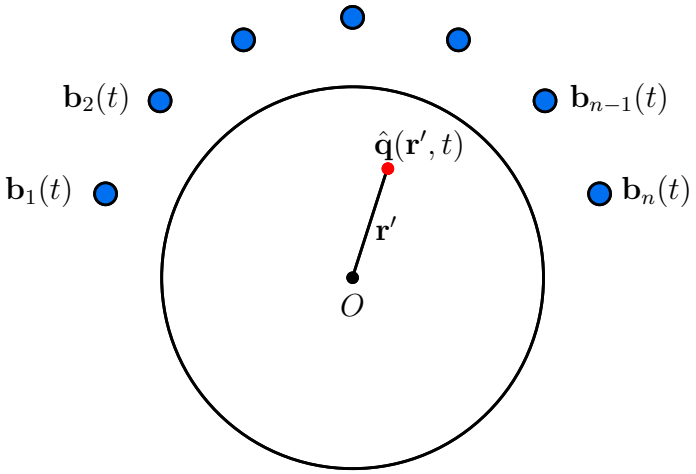

Figure 2.14: Diagram showing spatial filter formation.

given by

$$\hat{\mathbf{q}}(\mathbf{r}', t) = w_1(\mathbf{r}')b_1(t) + w_2(\mathbf{r}')b_2(t) + \ldots + w_n(\mathbf{r}')b_n(t)$$
$$\hat{\mathbf{q}}(\mathbf{r}', t) = \mathbf{w}(\mathbf{r}')\mathbf{b}(t) \tag{2.29}$$

where

$$\mathbf{w}(\mathbf{r}')^\top = [w_1 w_2 \ldots w_n]. \tag{2.30}$$

Beamforming

In beamforming [35], we attempt to find $\hat{\mathbf{q}}(\mathbf{r}', t)$ using the equation

$$\hat{\mathbf{q}}(\mathbf{r}', t) = \mathbf{W}_{BF}^\top(\mathbf{r}')\mathbf{b}(t). \tag{2.31}$$

The beamformer weights, $\mathbf{W}_{BF}$, are derived based on power minimisation, and thus $\hat{\mathbf{q}}(\mathbf{r}', t)$ is minimised with the linear constraint that the power originating from the location of interest remains. Mathematically, this can be formulated as

$$\min_{\mathbf{W}_{BF}} \left[\mathbb{E}\left[\hat{\mathbf{q}}(\mathbf{r}', t)^2 \right] \right] \qquad \text{s.t.} \qquad \mathbf{W}_{BF}(\mathbf{r}')\mathbf{I}(\mathbf{r}') = 1, \tag{2.32}$$

where $\mathbb{E}\left[\hat{\mathbf{q}}(\mathbf{r}', t)^2\right]$ is the expectation value of the reconstructed source power, and $\mathbf{W}_{BF}(\mathbf{r}')\mathbf{I}(\mathbf{r}') = 1$ comes from the definition of the lead-field. This minimisation ensures that any signal variance that does not originate at the location of interest is minimised. Mathematically,

$$\begin{aligned} \mathbb{E}\left[\hat{\mathbf{q}}(\mathbf{r}', t)^2 \right] &= \mathbb{E}\left[(\mathbf{W}_{BF}^{\top}(\mathbf{r}')\mathbf{b}(t))(\mathbf{W}_{BF}^{\top}(\mathbf{r}')\mathbf{b}(t)) \right] \\ &= \mathbb{E}\left[\mathbf{W}_{BF}^{\top}(\mathbf{r}')\mathbf{b}(t)\mathbf{b}(t)\mathbf{W}_{BF}(\mathbf{r}') \right] \\ &= \mathbf{W}_{BF}^{\top}(\mathbf{r}')\mathbf{C}\mathbf{W}_{BF}(\mathbf{r}'), \end{aligned} \tag{2.33}$$

where $\mathbf{C}$ is an $n \times n$ data covariance matrix, and $\mathbf{C}_{i,j}$ is the covariance between channels i and j.

The linear weights for the beamformer spatial filter are given by

$$\mathbf{W}_{BF}^{\top}(\mathbf{r}') = \frac{\mathbf{I}^{\top}(\mathbf{r}')\mathbf{C}^{-1}}{\mathbf{I}^{\top}(\mathbf{r}')\mathbf{C}^{-1}\mathbf{I}(\mathbf{r}')}. \tag{2.34}$$

The beamformer performs the inverse solution at every location in source space. It generates a weighted sum of sensor outputs to give a virtual electrode response. It assumes the data is generated by discrete dipolar sources, and makes no *a priori* assumption about the number of sources.

Minimum Norm Estimate

The Minimum Norm Estimate (MNE) [36] minimises the summed square of the difference between a measured field distribution and a model of the distribution based on the lead-fields. This can be mathematically formulated as

$$\min_{\hat{\mathbf{q}}(t)} ||\mathbf{b}(t) - \mathbf{L}\hat{\mathbf{q}}(t)||^2, \tag{2.35}$$

where $\hat{\mathbf{q}}(t)$ is the best estimate of the true dipole strengths $\mathbf{q}(t)$, and $||\mathbf{A}||$ is the norm of $\mathbf{A}$.

Using the generalised Moore-Penrose pseudo-inverse [37] gives

$$\hat{\mathbf{q}}(t) = \mathbf{L}^\top[\mathbf{L}\mathbf{L}^\top]^{-1}\mathbf{b}(t), \tag{2.36}$$

where $\mathbf{L}\mathbf{L}^\top$ is the *Gram matrix*, which is generally denoted as $\mathbf{G}$. The Gram matrix represents the linear dependence of the lead-fields of every voxel on each other, in source space. It only depends on the geometry of the source space, and the MEG sensor arrangement. $\mathbf{G}$ has dimensions $N \times N$ where N is the number of MEG channels in the system. Substituting for $\mathbf{G}$ in Equation 2.36,

$$\hat{\mathbf{q}}(t) = \mathbf{L}^\top\mathbf{G}^{-1}\mathbf{b}(t). \tag{2.37}$$

The Gram matrix is likely to be singular, and so the solution to Equation 2.37 is unstable. Tikhonov regularisation can be used to stabilise the inversion [38]. Effectively, this adds a constant to all the elements on the leading diagonal of the matrix that is to be inverted. So, instead of $\mathbf{G}^{-1}$, we would find $(\mathbf{G} + \epsilon\mathbf{I})^{-1}$, where ϵ is a positive constant, referred to as *the regularisation parameter*. Thus, Equation 2.37 becomes

$$\hat{\mathbf{q}}(t) = \mathbf{L}^{\top}(\mathbf{G} + \epsilon\mathbf{I})^{-1}\mathbf{b}(t). \tag{2.38}$$

The effect of this regularisation corresponds to minimising the cost function, such that

$$\min_{\hat{\mathbf{q}}(t)} \left[||\mathbf{b}(t) - \mathbf{L}\hat{\mathbf{q}}(t)||^2 + \epsilon||\hat{\mathbf{q}}(t)||^2 \right]. \tag{2.39}$$

Minimising $||\mathbf{b}(t) - \mathbf{L}\hat{\mathbf{q}}(t)||^2$ minimises the difference between the model and the measured data, and minimising $\epsilon||\hat{\mathbf{q}}(t)||^2$ minimises the norm of the solution itself. The regularisation parameter adjusts the trade-off between these two terms. Adjusting ϵ will affect the condition number of the Gram matrix. The condition number measures the sensitivity of the output of the function to the input and noise. We desire a condition number of the order of 10 to 1000.

$\mathbf{G}$ is used to calculate the Minimum Norm weighting matrix:

$$\mathbf{W}_{\theta}^{\top} = \mathbf{L}_{\theta}^{\top}\mathbf{G}^{-1}, \tag{2.40}$$

where $\mathbf{W}_{\theta}$ is the minimum norm weighting for a single voxel, and $\mathbf{L}_{\theta}$ is one column of the lead-field matrix. The minimum norm solution with Tikhonov regularisation, with one element representing one voxel in source space, is given by

$$\hat{\mathbf{s}}_{\theta}(t) = \mathbf{W}_{\theta}^{\top}\mathbf{b}(t). \tag{2.41}$$

Depth Scaling

A consequence of minimising the solution norm is that the filter is sensitive to activity in close proximity to the sensors, but struggles with deeper sources. It tends to mislocalise such sources, pulling them towards the surface.

To correct this, the inverse solution can be modified to include associated depth scaling. One way of doing this is to use the Dynamic Statistical Parametric Mapping (dSPM) [39] approach, whereby the weightings are normalised by their own norm, in order to ensure a uniform noise distribution across all sensor space. Thus,

$$\begin{aligned} \mathbf{W}_{\theta,dSPM}^{\top} &= \frac{\mathbf{L}_{\theta}^{\top}\mathbf{G}^{-1}}{||\mathbf{L}_{\theta}^{\top}\mathbf{G}^{-1}||} \\ &= \frac{\mathbf{L}_{\theta}^{\top}\mathbf{G}^{-1}}{\sqrt{\mathbf{L}_{\theta}^{\top}\mathbf{G}^{-2}\mathbf{L}_{\theta}}}. \end{aligned} \tag{2.42}$$

dSPM is implemented on a voxel-by-voxel basis.

In this project, we used MNE with dSPM because in scanning multiple samples, the time-courses are expected to be mutually correlated, and would otherwise be suppressed by beamforming.

2.2.7 Magnetic Dipoles

In this project, we aim to measure the magnetic fields created by magnetic dipoles, rather than current dipoles. The same theory as for measuring and mapping current dipoles applies for magnetic dipoles, but the expression for the field due to a magnetic dipole located at point $\mathbf{r}'$ is used, rather than the Biot-Savart law. This takes the form

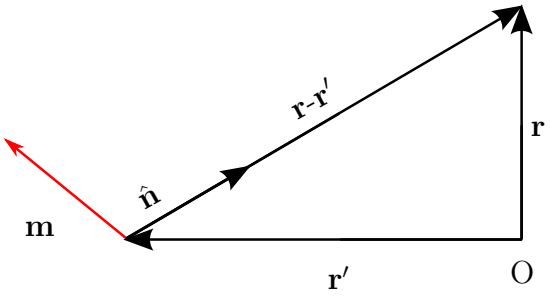

Figure 2.15: Diagram used to explain Biot-Savart Law for a magnetic dipole.

$$\mathbf{B} = \frac{\mu_0}{4\pi} \frac{3\hat{\mathbf{n}}(\hat{\mathbf{n}}.\mathbf{m}) - \mathbf{m}}{|\mathbf{r} - \mathbf{r}'|^3}, \tag{2.43}$$

where $\mathbf{m}$ is the magnetic moment of the dipole, $|\mathbf{r} - \mathbf{r}'|$ is the linear distance between the location of the dipole and the detection point, and $\hat{\mathbf{n}}$ is the unit vector in the direction of $|\mathbf{r} - \mathbf{r}'|$, as shown in Figure 2.15.

For a system with MEG detector coils that are oriented radially as shown in Figure 2.12, the magnetic field measured at the detector is given by

$$B_{detect} = \frac{\mu_0}{4\pi} \frac{3\hat{\mathbf{n}}(\hat{\mathbf{n}}.\mathbf{m}) - \mathbf{m}}{|\mathbf{r} - \mathbf{r}_Q|^3} \cdot \hat{\mathbf{e}}_\mathbf{r}, \tag{2.44}$$

where $\hat{\mathbf{e}}_\mathbf{r}$ is a unit vector in the radial direction at $\mathbf{r}$. This expression yields the lead-fields for use in solving the inverse problem to derive the distribution of magnetisation from measurements of the magnetic field.

2.3 Method

2.3.1 The MEG System

In this chapter, we simulated the magnetic field measurements made by 275 axial gradiometers with 5 cm baselines, fitted around a helmet. Figure 2.16 shows the

distribution of the MEG sensors. Inner coils are shown in red, outer coils in black, and the reference array in blue.

2.3.2 Forward Problem

To evaluate the feasibility of detecting magnetisation using a MEG system, we used `MATLAB` to model the forward problem for magnetic dipoles using the exact sensor arrangement of the MEG system in our laboratory, shown in Figure 2.16. We calculated the radial magnetic field at each sensor location, using Equation 2.44 by finding the dot product of the magnetic field vector and the vector normal to the sensor coil.

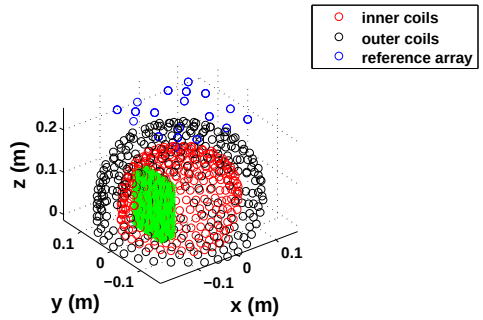

(a) Plot showing MEG sensor distribution, with target volume.

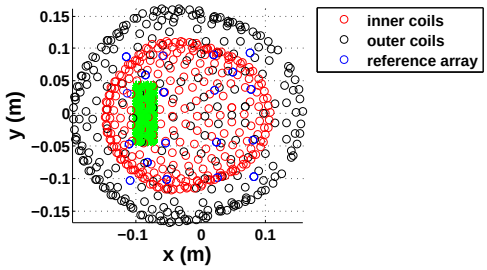

(b) Plot showing z-projection of MEG sensor distribution, with target volume.

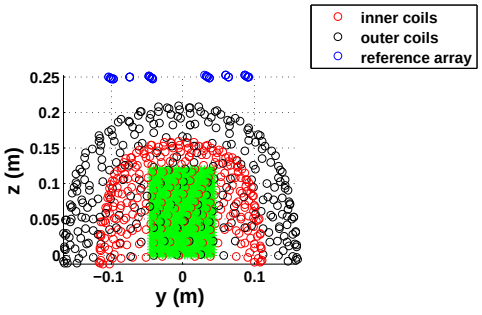

(c) Plot showing x-projection of MEG sensor distribution, with target volume.

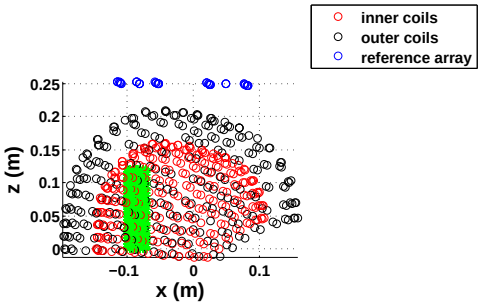

(d) Plot showing y-projection of MEG sensor distribution, with target volume.

Figure 2.16: Plots showing MEG sensor distribution, with target volume.

We subtracted the field detected by the outer coils from the field detected by the inner coils, to find the magnetic field gradient, and plotted this gradient field at the location of the inner sensors. We used the `MATLAB` in-built function, `scatteredInterpolant` [40], with nearest-neighbour interpolation [41] to create a continuous magnetic field distribution.

Whilst simulating a white noise of 10 fT, we looked at the forward solution for dipoles of different magnitudes, having magnetisation vector moments oriented at different angles in three orthogonal planes, and located in different locations within a pre-specified target space, selected with prior knowledge of the location of samples that we scanned in later stages of the project, and in the knowledge that the distance between the inner sensors and the inside of the helmet is approximately 3 cm.

2.3.3 Inverse Problem

In order to create simulation data for the inverse problem, we used Equation 2.44 and added 10 fT white noise to simulate the SQUID noise, to obtain the magnetic field that one magnetic dipole source would produce at each sensor. This yielded a vector of 270 measurements. Likewise, we simulated the magnetic field sensed at the corresponding outer sensors. The difference of the magnetic field recorded by the inner sensors, and that recorded by the outer sensors, gave the simulated gradiometer output data, a vector of 270 measurements.

We then ran sample reconstruction on the data, using the lead-field normalised, minimum norm spatial filter for varying SNR, and a range of dipole positions and orientations. The flowchart in Figure 2.17 shows how the Minimum Norm solution was computed.

The lead-fields were calculated at 4 mm resolution inside the target volume. The regularisation parameter, ϵ, introduced in Equation 2.38, was set to be 0.1 %

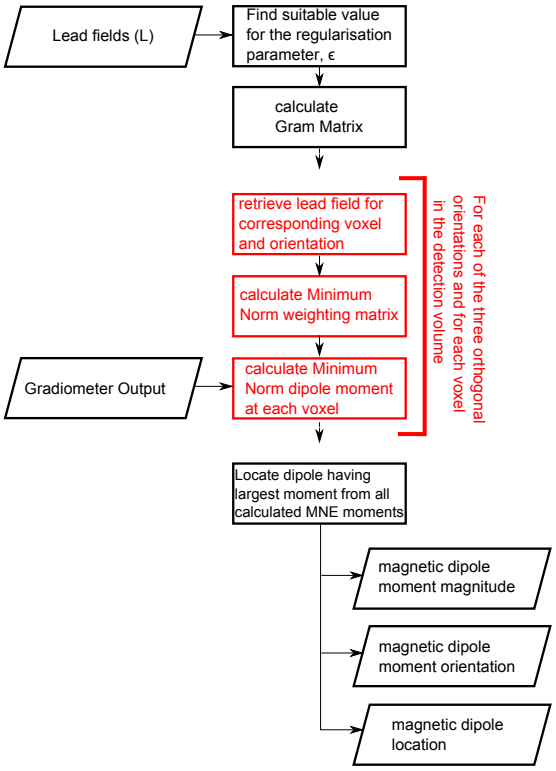

Figure 2.17: Flowchart showing how the Minimum Norm solution was computed.

of the maximum value in the singular value decomposition of $\mathbf{L}\mathbf{L}^\top$, in order to obtain a Gram matrix condition number of 1000.

Considering the sensor configuration, and the intended sample location for later applications, the target volume was limited to a box with x-coordinates varying from $-0.1\,\mathrm{m}$ to $-0.07\,\mathrm{m}$, y-coordinates from $-0.045\,\mathrm{m}$ to $0.045\,\mathrm{m}$, and z-coordinates from $0\,\mathrm{m}$ to $0.12\,\mathrm{m}$, as shown in Figure 2.16.

In checking how the MNE reconstruction accuracy changes for changes in different parameters, we ran the algorithm for multiple configurations. For each parameter that we tested, we kept all other settings at their default values. The default dipole was located at position (-0.085, 0, 0.06)m, with a magnetic moment of magnitude $10\,\mathrm{nA\,m^2}$, oriented in a direction parallel to the positive z-axis. The noise level was set to $10\,\mathrm{fT}$, which is of the order of the noise measured in experiments.

We checked how the MNE reconstruction accuracy changes with

- SNR, by changing the magnetic dipole moment magnitude from $1\,\mathrm{pA\,m^2}$ to $0.1\,\mathrm{A\,m^2}$ in 50 logarithmically spaced steps,
- dipole x-location, by varying the x-coordinate of the dipole from $-0.1\,\mathrm{m}$ to $-0.07\,\mathrm{m}$ in 10 equidistant spatial intervals,
- dipole y-location, by varying the y-coordinate of the dipole from $-0.045\,\mathrm{m}$ to $0.045\,\mathrm{m}$ in increments of $4\,\mathrm{mm}$,
- dipole z-location, by varying the z-coordinate of the dipole from $0\,\mathrm{m}$ to $0.12\,\mathrm{m}$ in 10 equidistant spatial intervals,
- dipole orientation in the x-y plane, by varying the dipole orientation from a direction parallel to the x-axis in increments of $\pi/8$,
- dipole orientation in the y-z plane, by varying the dipole orientation from a direction parallel to the y-axis in increments of $\pi/8$, and
- dipole orientation in the x-z plane, by varying the dipole orientation from a direction parallel to the x-axis in increments of $\pi/8$

The flowchart in Figure 2.18 shows how we tested the solution to the inverse problem.

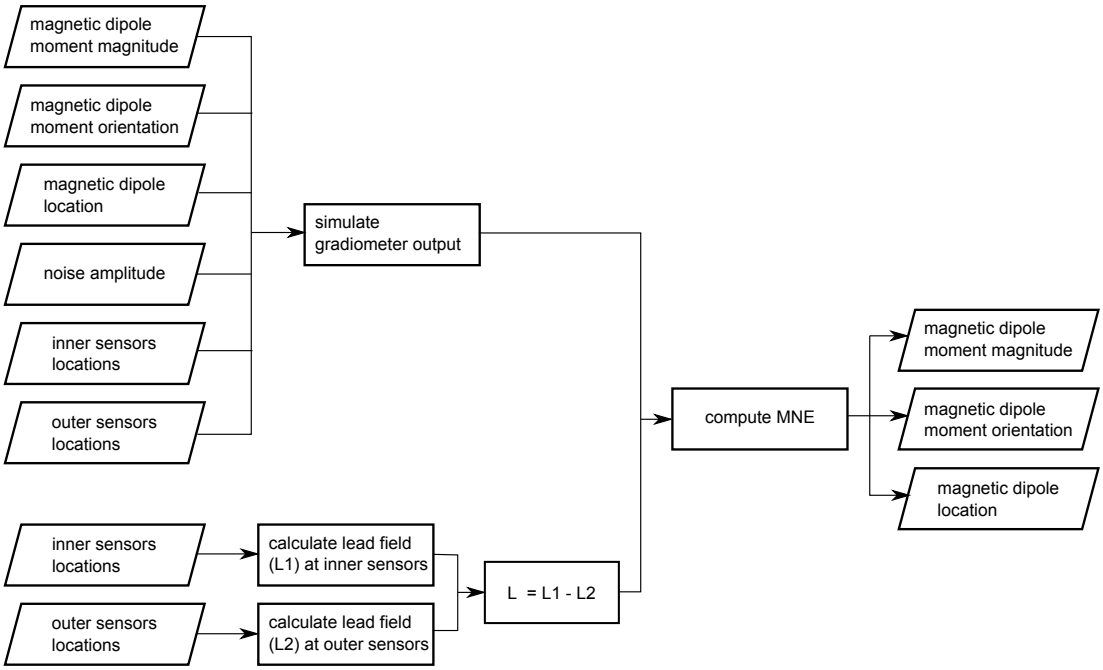

Figure 2.18: Flowchart showing how the solution to the inverse problem was tested.

2.4 Results

2.4.1 Forward Problem

We simulated the gradiometer output that would be measured at the sensors' locations following the actual MEG sensor configuration, for magnetic dipoles located within the target volume, shown in Figure 2.16. We plotted the signals at the locations of the inner sensors.

Figure 2.19 shows three orthogonal projections of the gradiometer output measured by the MEG sensors for a dipole whose magnetic moment has magnitude $10\,\mathrm{nA\,m^2}$, oriented in a direction parallel to the positive z-axis ($\hat{\mathbf{\Phi}} = (0, 0, 1)$), and which is located at position $(-0.085, 0, 0.06)$m.

Figure 2.20 shows three orthogonal projections of the gradiometer output measured by the MEG sensors after the dipole in Figure 2.19 is moved 1.5 cm in the positive x-direction, such that its location is now $(-0.07, 0, 0.06)$m.

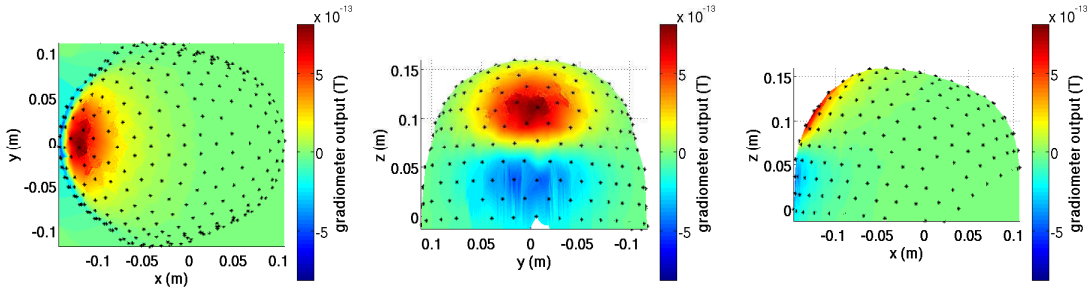

Figure 2.19: Plots showing the projections in the x-y plane (left), y-z plane (centre) and x-z plane (right) of the gradiometer output measured by sensors for a dipole located at $(-0.085, 0, 0.06)$m, with a magnetic moment of magnitude $10\,\mathrm{nA\,m^2}$, oriented in a direction parallel to the positive z-axis.

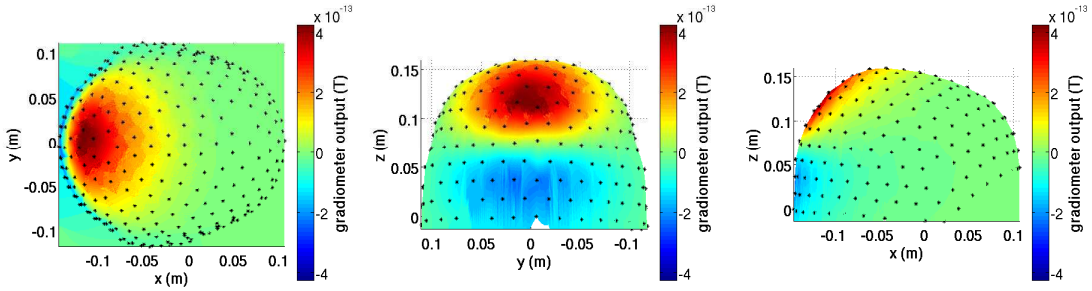

Figure 2.20: Plots showing the projections in the x-y plane (left), y-z plane (centre) and x-z plane (right) of the gradiometer output measured by sensors for a dipole located at $(-0.07, 0, 0.06)$m, with a magnetic moment of magnitude $10\,\mathrm{nA\,m^2}$, oriented in a direction parallel to the positive z-axis.

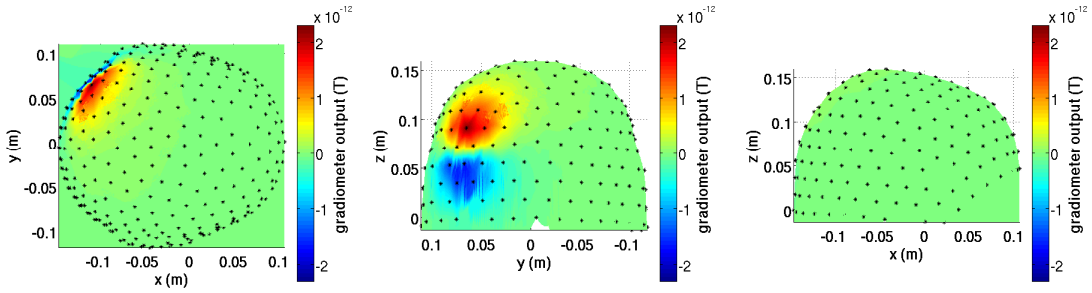

Figure 2.21: Plots showing the projections in the x-y plane (left), y-z plane (centre) and x-z plane (right) of the gradiometer output measured by sensors for a dipole located at (-0.085, 0.045, 0.06)m, with a magnetic moment of magnitude $10\,\mathrm{nA\,m^2}$, oriented in a direction parallel to the positive z-axis.

Figure 2.21 shows three orthogonal projections of the gradiometer output measured by the MEG sensors after the dipole in Figure 2.19 is now moved 4.5 cm in the negative y-direction, such that its location is now $(-0.085, -0.045, 0.06)$m. The gradiometer output recorded by the detectors can be seen shifted in the

negative y-direction.

After the dipole in Figure 2.19 is moved by 6 cm in the negative z-direction, such that its location is now $(-0.085, 0, 0)$, the three orthogonal projections of the gradiometer output measured by the MEG sensors become as shown in Figure 2.22, in which the detected peak gradiometer output is shifted in the negative z-direction.

Figures 2.23, 2.24 and 2.25 show the gradiometer output simulated for three magnetic dipoles of the same magnitude, located at the exact same location, but whose magnetisation vector is respectively oriented parallel to the x, y, and z axes, respectively.

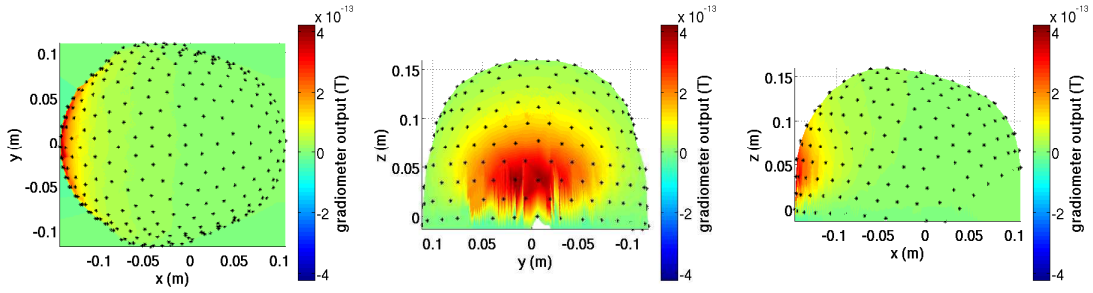

Figure 2.22: Plots showing the projections in the x-y plane (left), y-z plane (centre) and x-z plane (right) of the gradiometer output measured by sensors for a dipole located at (-0.085, 0, 0), with a magnetic moment of magnitude 10 nA m^2, oriented in a direction parallel to the positive z-axis.

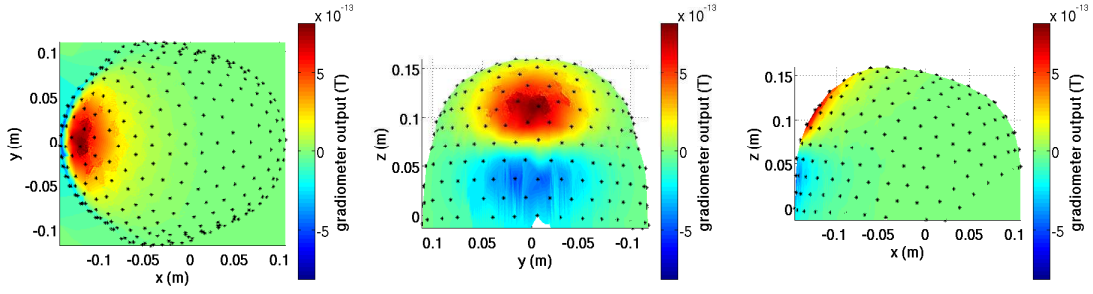

Figure 2.23: Plots showing the projections in the x-y plane (left), y-z plane (centre) and x-z plane (right) of the gradiometer output measured by sensors for a dipole located at (-0.085, 0, 0.06)m, with a magnetic moment of magnitude 10 nA m^2, oriented in a direction parallel to the positive z-axis.

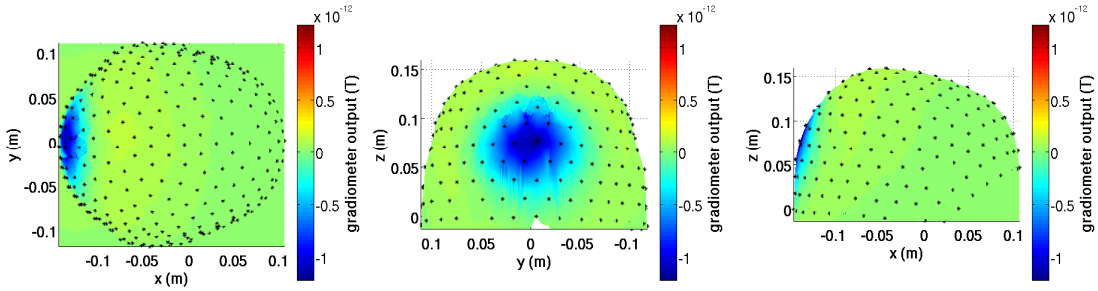

Figure 2.24: Plots showing the projections in the x-y plane (left), y-z plane (centre) and x-z plane (right) of the gradiometer output measured by sensors for a dipole located at (-0.085, 0, 0.06)m, with a magnetic moment of magnitude 10 nA m^2, oriented in a direction parallel to the positive x-axis.

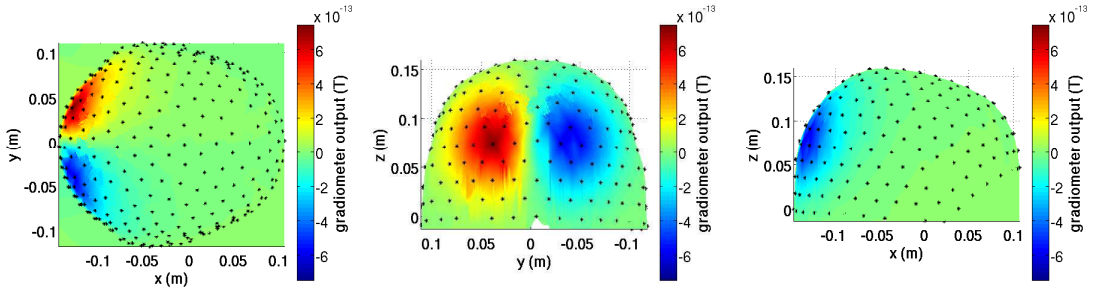

Figure 2.25: Plots showing the projections in the x-y plane (left), y-z plane (centre) and x-z plane (right) of the gradiometer output measured by sensors for a dipole located at (-0.085, 0, 0.06)m, with a magnetic moment of magnitude 10 nA m^2, oriented in a direction parallel to the positive y-axis.

2.4.2 Inverse Problem

We first simulated the magnetic field recorded by each sensor for a magnetic dipole positioned at position (-0.085, 0, 0.06)m, having a magnetic moment of 10 nA m^2, and oriented in a direction parallel to the positive z-axis. We added 10 fT white noise at each sensor in order to simulate the SQUID noise.

We then attempted to reconstruct the generating source using MNE. In computing the following results, we assumed a target volume box with x-coordinates varying from -0.1 m to -0.07 m, y-coordinates from -0.045 m to 0.045 m, and z-coordinates from 0 m to 0.12 m, as shown in Figure 2.16. We used an MNE voxel resolution of 4 mm.

We calculated the moment magnitude as

$$K = \left\| \frac{\mathbf{L}^\top \mathbf{d}}{\sum_{n=1}^{N} \mathbf{L}_{m,\theta}} \right\|, \tag{2.45}$$

where K is the dipole moment magnitude, $\mathbf{L}$ is the lead-field matrix, $\mathbf{d}$ is the field strength at N sensor locations, and $\mathbf{L}_\theta$ represents the columns of the lead-field matrix.

Figure 2.26 shows the reconstructed magnetic dipole source, $\mathbf{s}$, in the x-y plane at $z = 0.06\,\text{m}$, y-z plane at $x = -0.084\,\text{m}$, and x-z plane at $y = -0.001\,\text{m}$. A white circle represents the location of the test dipole, and a white cross represents the location of the MNE-reconstructed dipole, i.e. the voxel with the largest MNE-reconstructed dipole strength. The z, x, and y locations of the planes at which the reconstructed magnetic dipole sources are shown were selected to be the same as the z, x, and y coordinates at which the MNE algorithm located the magnetic dipole source.

We generated 100 simulations of the magnetic field recorded by the sensors for the same magnetic dipole, each time subject to a randomly generated 10 fT white

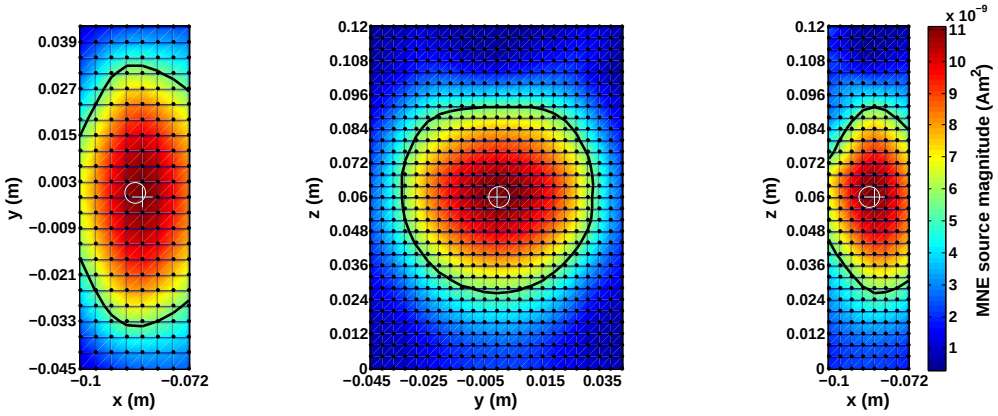

Figure 2.26: Plots showing the MNE-reconstructed magnetic dipole source in the x-y plane at $z = 0.06\,\text{m}$ (left), y-z plane at $x = -0.084\,\text{m}$ (centre) and x-z plane at $y = -0.001\,\text{m}$ (right) for a magnetic dipole with moment magnitude $10\,\text{nA}\,\text{m}^2$ located at (-0.085, 0, 0.06)m and oriented parallel to the positive z-axis.

noise. We then ran MNE on all simulations. The total computational time was 72 hours. Table 2.2 lists the mean values and standard deviation of the MNE-reconstructed dipole location, magnetic moment magnitude, and orientation.

	Test Dipole	MNE Dipole
x-location	$-0.085\,\mathrm{m}$	-0.084 ± 0.001 m
y-location	$0\,\mathrm{m}$	0.001 ± 0.001 m
z-location	$0.06\,\mathrm{m}$	0.063 ± 0.001 m
moment magnitude	$10\,\mathrm{nA\,m^2}$	9.00 ± 0.96 $\mathrm{nAm^2}$
moment orientation $(\theta_x, \theta_y, \theta_z)$	$(0, 0, 1)$	(-0.106 ± 0.029, -0.011 ± 0.009, 0.999 ± 0.002)

Table 2.2: MNE-reconstructed magnetic dipole source values.

We also looked at the accuracy and precision of the localisation. Figure 2.27 shows the Full Width at Half Maximum (FWHM) for the mean reconstructed magnetic dipole source taken over 100 iterations. The black contour shows the locations where the dipole moment falls to half the peak value.

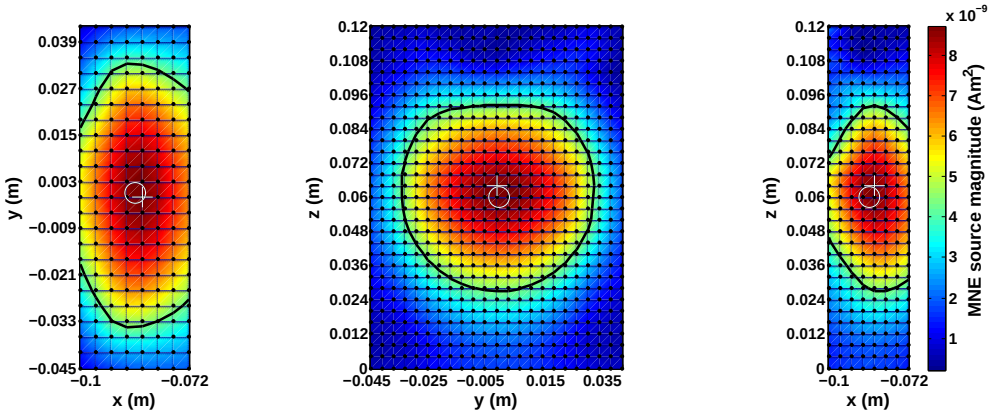

Figure 2.27: Plots showing the mean MNE-reconstructed FWHM magnetic dipole source localisation in the x-y plane at $z = 0.06\,\mathrm{m}$ (left), y-z plane at $x = -0.084\,\mathrm{m}$ (centre) and x-z plane at $y = -0.001\,\mathrm{m}$ (right) for 100 iterations of a magnetic dipole with moment magnitude $10\,\mathrm{nA\,m^2}$ located at (-0.085, 0, 0.06)m and oriented parallel to the positive z-axis.

In the following sections, we tested how the MNE reconstruction accuracy changes for different SNRs, and for dipole moments of different magnitudes, orientations and at different locations. We also looked at the accuracy and precision of the localisation.

MNE Reconstruction Accuracy with SNR

Figures 2.28 - 2.30 show the MNE-reconstructed FWHM magnetic dipole source localisation for magnetic dipoles of magnetic moment magnitudes $1\,\mathrm{pA\,m^2}$, $10\,\mathrm{nA\,m^2}$, and $0.1\,\mathrm{A\,m^2}$ respectively, located at (-0.085, 0, 0.06)m and oriented parallel to the positive z-axis.

As can be seen in Figure 2.28, the magnetic dipole with moment magnitude $1\,\mathrm{pA\,m^2}$ could not be accurately located by our MNE algorithm. On the other hand, the MNE-reconstructed dipole source for a magnetic dipole with moment magnitude $10\,\mathrm{nA\,m^2}$, can be located as can be seen in Figure 2.29, and the MNE-reconstruction does not appear to considerably improve for the magnetic dipole with moment magnitude $0.1\,\mathrm{A\,m^2}$ seen in Figure 2.30.

Figures 2.31 - 2.34 show how the precision of MNE-reconstructed magnetic dipole location, magnitude, and orientation for dipoles located at coordinates $(-0.085, 0, 0.06)$m, oriented at $(0, 0, 1)$, in a system of $10\,\mathrm{fT}$ noise, varies for dipole magnitudes that vary from $1\,\mathrm{pA\,m^2}$ to $0.1\,\mathrm{A\,m^2}$.

It can be seen in Figure 2.31, that the MNE-reconstructed dipole location is less than $5\,\mathrm{mm}$ displaced from the true dipole location for dipoles with magnetic moment magnitudes of $0.1\,\mathrm{nA\,m^2}$ or larger.

The difference between the MNE-reconstructed and the true magnetic moment magnitude is less than $25\,\%$ of the true magnitude for dipoles whose true magnetic moment magnitude is $7\,\mathrm{nA\,m^2}$ or higher. However, for the scope of our project, we are more interested in identification of accurate dipole locations, rather than accurate dipole magnitudes.

MNE-reconstructed dipole orientation is within 15° in x,y,z orientation of the orientation of the true dipole for dipoles with magnetic moments of $300\,\mathrm{pA\,m^2}$ or higher.

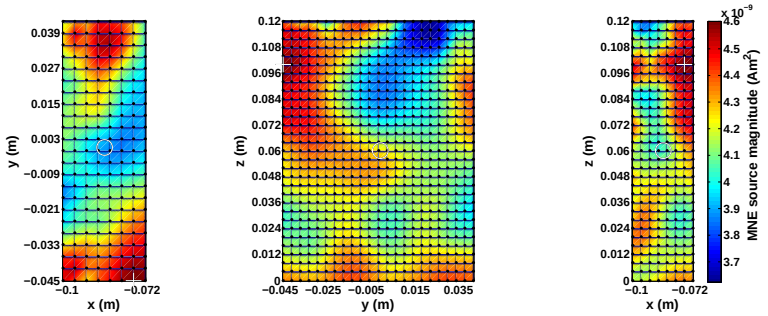

Figure 2.28: Plots showing MNE-reconstructed FWHM magnetic dipole source localisation in the x-y plane at $z = 0.072\,\mathrm{m}$ (left), y-z plane at $x = -0.096\,\mathrm{m}$ (centre) and x-z plane at $y = 0.039\,\mathrm{m}$ (right) for a magnetic dipole with moment magnitude $1\,\mathrm{pA\,m^2}$ located at (-0.085, 0, 0.06)m and oriented parallel to the positive z-axis.

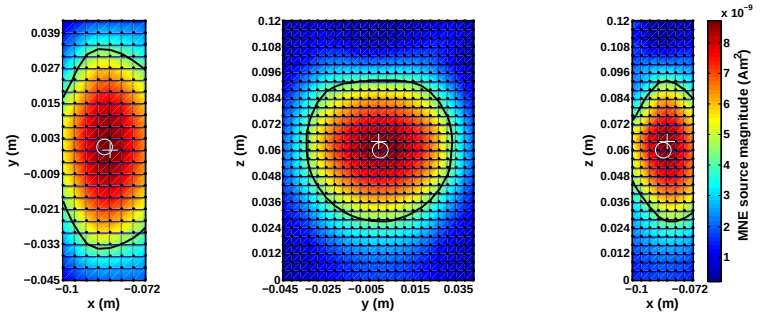

Figure 2.29: Plots showing MNE-reconstructed FWHM magnetic dipole source localisation in the x-y plane at $z = 0.064\,\mathrm{m}$ (left), y-z plane at $x = -0.084\,\mathrm{m}$ (centre) and x-z plane at $y = -0.001\,\mathrm{m}$ (right) for a magnetic dipole with moment magnitude $10\,\mathrm{nA\,m^2}$ located at (-0.085, 0, 0.06)m and oriented parallel to the positive z-axis.

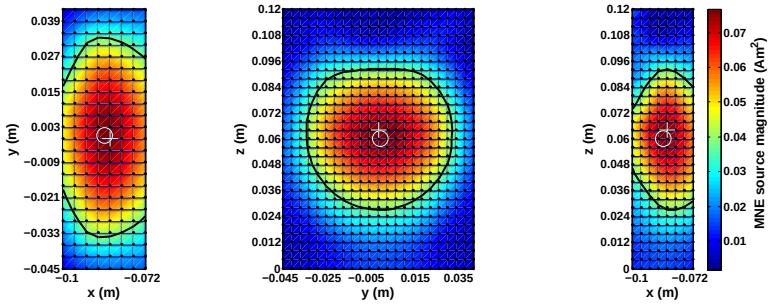

Figure 2.30: Plots showing MNE-reconstructed FWHM magnetic dipole source localisation in the x-y plane at $z = 0.064\,\mathrm{m}$ (left), y-z plane at $x = -0.084\,\mathrm{m}$ (centre) and x-z plane at $y = -0.001\,\mathrm{m}$ (right) for a magnetic dipole with moment magnitude $0.1\,\mathrm{A\,m^2}$ located at (-0.085, 0, 0.06)m and oriented parallel to the positive z-axis.

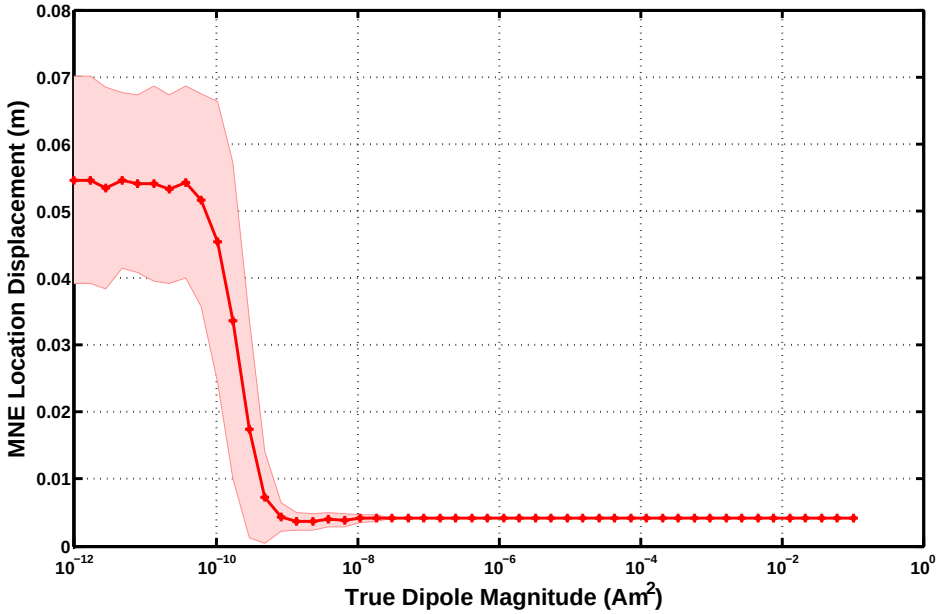

Figure 2.31: Plot showing displacement of MNE calculated location from dipole true location for dipoles of magnitudes varying from $1\,\mathrm{pA\,m^2}$ to $0.1\,\mathrm{A\,m^2}$. The pink region indicates the standard deviation of the results.

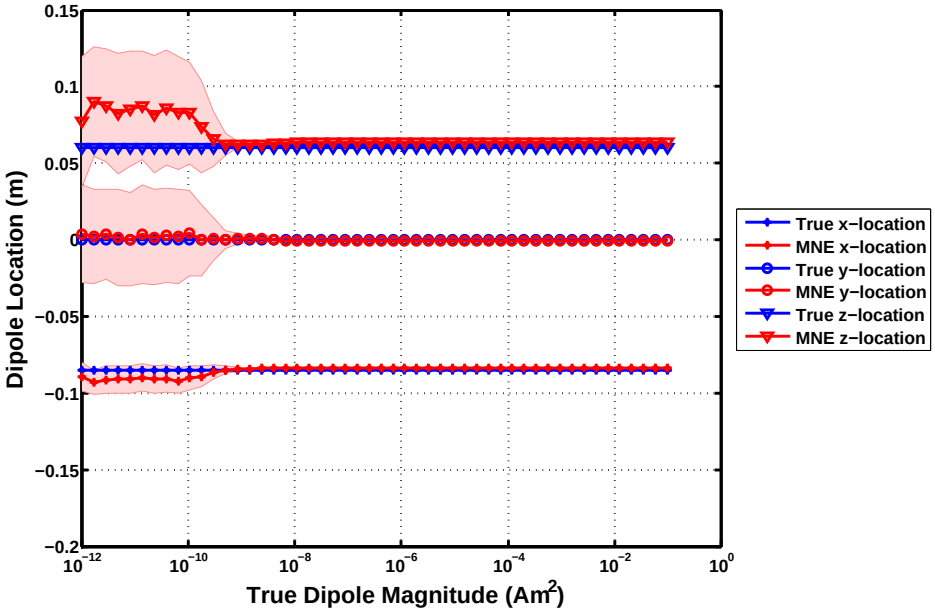

Figure 2.32: Plot showing MNE calculated (x, y, z) location coordinates for dipoles of magnitudes varying from $1\,\mathrm{pA\,m^2}$ to $0.1\,\mathrm{A\,m^2}$. The pink regions indicate the standard deviation of the results.

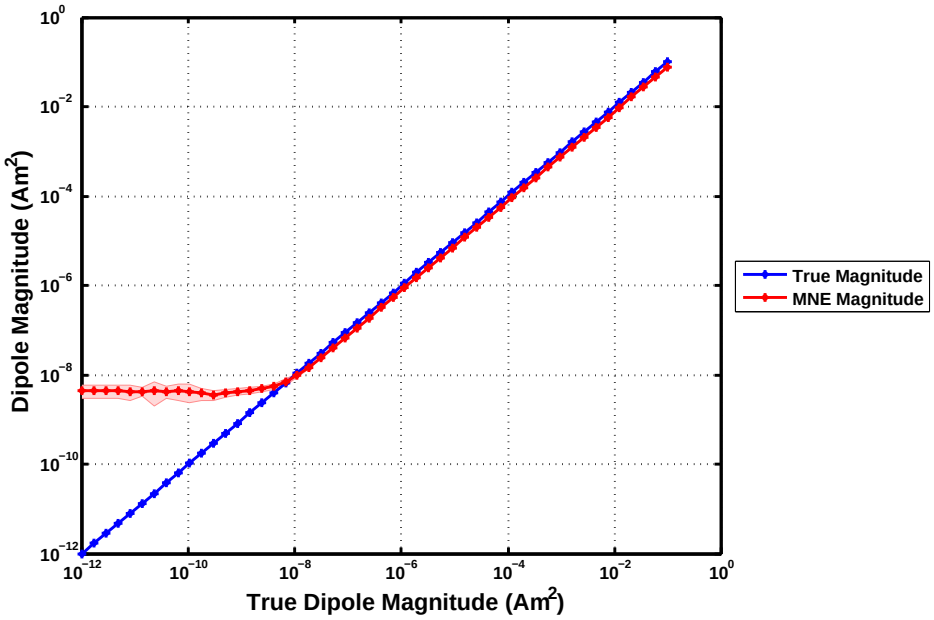

Figure 2.33: Plot showing MNE calculated dipole magnitude for dipoles of magnitudes varying from $1\,\mathrm{pA\,m^2}$ to $0.1\,\mathrm{A\,m^2}$. The pink region indicates the standard deviation of the results.

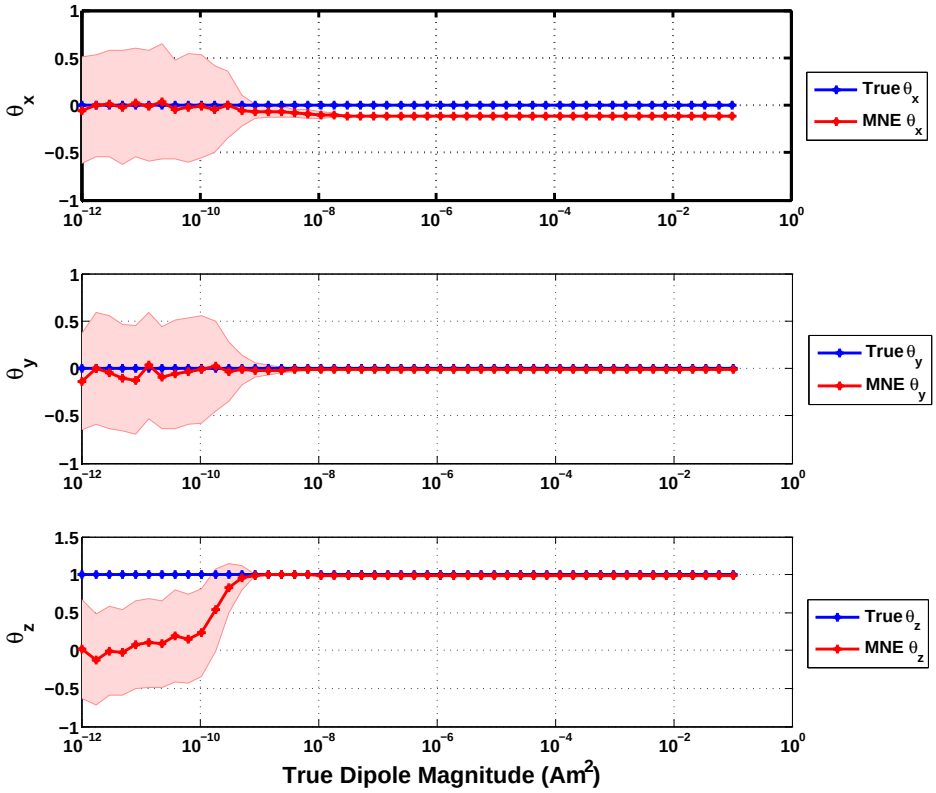

Figure 2.34: Plot showing MNE calculated dipole orientation $\hat{\mathbf{\Theta}} = (\theta_x, \theta_y, \theta_z)$ for dipoles of magnitudes varying from $1\,\mathrm{pA\,m^2}$ to $0.1\,\mathrm{A\,m^2}$. The pink regions indicate the standard deviation of the results.

MNE Reconstruction Accuracy for Dipoles at Different X-Locations

Figures 2.35 - 2.37 show the MNE-reconstructed FWHM magnetic dipole source localisation for magnetic dipoles located at x-locations $-0.1\,\mathrm{m}$, $-0.085\,\mathrm{m}$, and $-0.07\,\mathrm{m}$ respectively, with y-location $0\,\mathrm{m}$, z-location $0.06\,\mathrm{m}$, and orientation parallel to the positive z-axis.

As can be seen in Figures 2.35 and 2.37, for magnetic dipoles located at either end of the MNE target volume space, the MNE-reconstructed dipoles are more displaced than for a magnetic dipole located towards the centre of the MNE target volume space.

Figures 2.38 - 2.41 show how the precision of MNE-reconstructed magnetic dipole location, magnitude, and orientation varies for dipoles of magnitude $10\,\mathrm{nA\,m^2}$, located at a y-coordinate of 0, a z-coordinate of 0.06, oriented at $(0, 0, 1)$, in the presence of $10\,\mathrm{fT}$ noise, and in x-locations that vary from $-0.1\,\mathrm{m}$ to $-0.07\,\mathrm{m}$. The x-values of the MNE target space also varied from $-0.1\,\mathrm{m}$ to $-0.07\,\mathrm{m}$.

It can be seen in Figure 2.38, that the MNE-reconstructed dipole location is less than $5\,\mathrm{mm}$ displaced from the true dipole location for dipoles located at an x-location that falls between $-0.09\,\mathrm{m}$ and $-0.083\,\mathrm{m}$.

The difference between the MNE-reconstructed and the true magnetic moment magnitude is less than $25\,\%$ of the true magnitude for dipoles located at x-locations that lie between $-0.093\,\mathrm{m}$ and $-0.07\,\mathrm{m}$.

MNE-reconstructed dipole orientation is within 15° in x,y,z orientation of the orientation of the true dipole for all the tested dipoles, with the exception of the dipole located at $-0.1\,\mathrm{m}$, the most negative x-location in the MNE target volume space. At this location, the difference between the true moment orientation and the MNE orientation is 15.2° in the x-direction, 0.6° in the y-direction, and 2.1° in the z-direction.

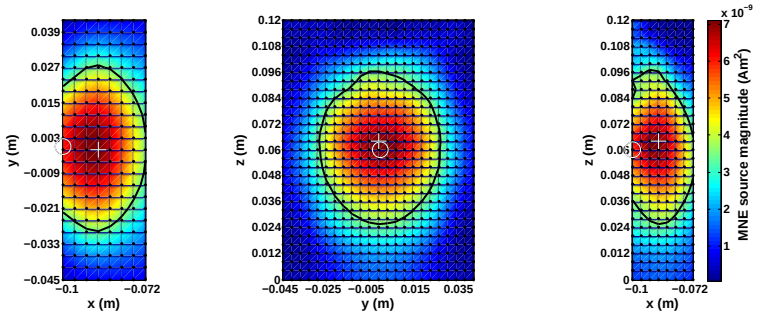

Figure 2.35: Plots showing MNE-reconstructed FWHM magnetic dipole source localisation in the x-y plane at $z = 0.064\,\mathrm{m}$ (left), y-z plane at $x = -0.088\,\mathrm{m}$ (centre) and x-z plane at $y = -0.001\,\mathrm{m}$ (right) for a magnetic dipole with moment magnitude $10\,\mathrm{nA\,m^2}$ located at (-0.1, 0, 0.06)m and oriented parallel to the positive z-axis.

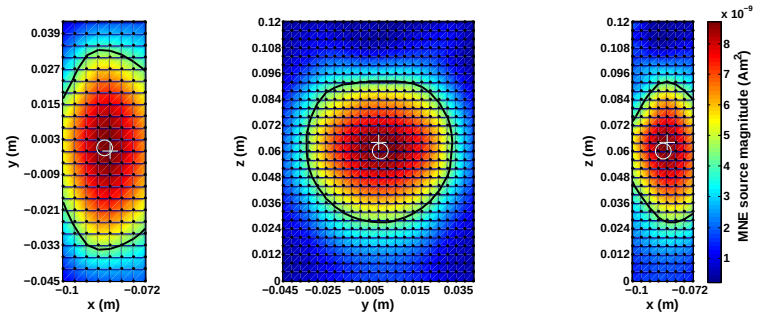

Figure 2.36: Plots showing MNE-reconstructed FWHM magnetic dipole source localisation in the x-y plane at $z = 0.064\,\mathrm{m}$ (left), y-z plane at $x = -0.084\,\mathrm{m}$ (centre) and x-z plane at $y = -0.001\,\mathrm{m}$ (right) for a magnetic dipole with moment magnitude $10\,\mathrm{nA\,m^2}$ located at (-0.085, 0, 0.06)m and oriented parallel to the positive z-axis.

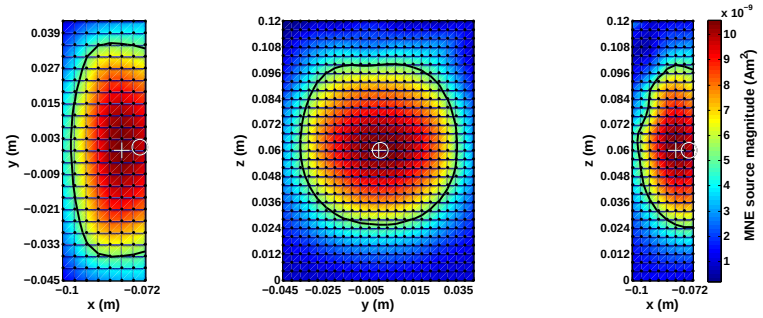

Figure 2.37: Plots showing MNE-reconstructed FWHM magnetic dipole source localisation in the x-y plane at $z = 0.060\,\mathrm{m}$ (left), y-z plane at $x = -0.080\,\mathrm{m}$ (centre) and x-z plane at $y = -0.001\,\mathrm{m}$ (right) for a magnetic dipole with moment magnitude $10\,\mathrm{nA\,m^2}$ located at (-0.07, 0, 0.06)m and oriented parallel to the positive z-axis.

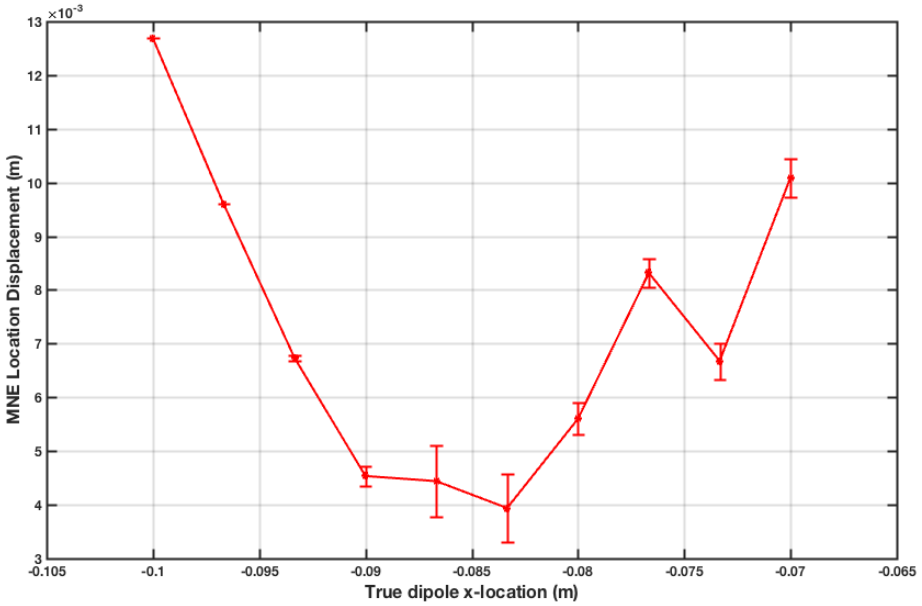

Figure 2.38: Plot showing displacement of MNE calculated location from dipole true location for dipoles whose x-location varies from $-0.1\,\mathrm{m}$ to $-0.07\,\mathrm{m}$. The error bars indicate the standard deviation of the results.

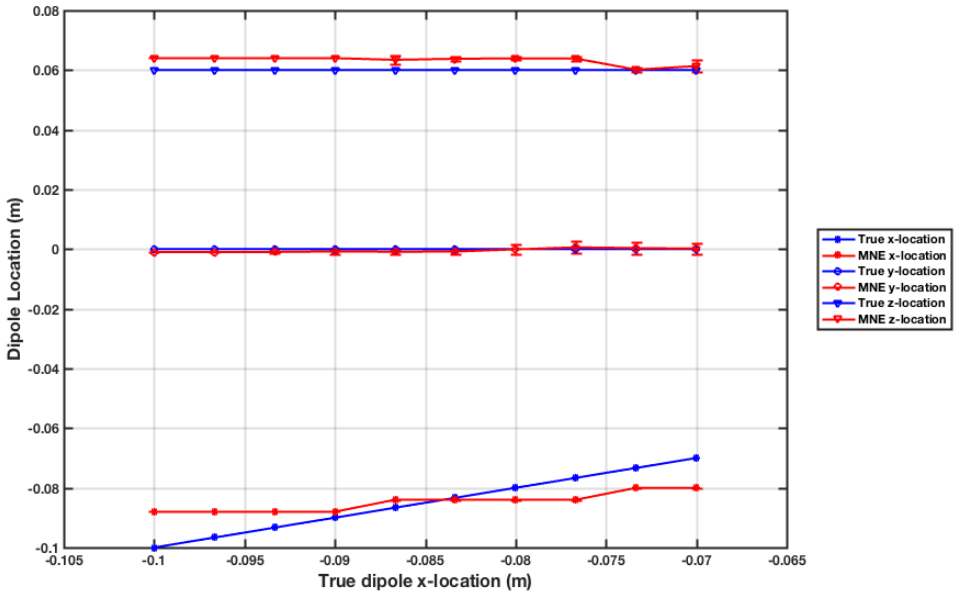

Figure 2.39: Plot showing MNE calculated (x, y, z) location coordinates for dipoles whose x-location varies from $-0.1\,\mathrm{m}$ to $-0.07\,\mathrm{m}$. The error bars indicate the standard deviation of the results.

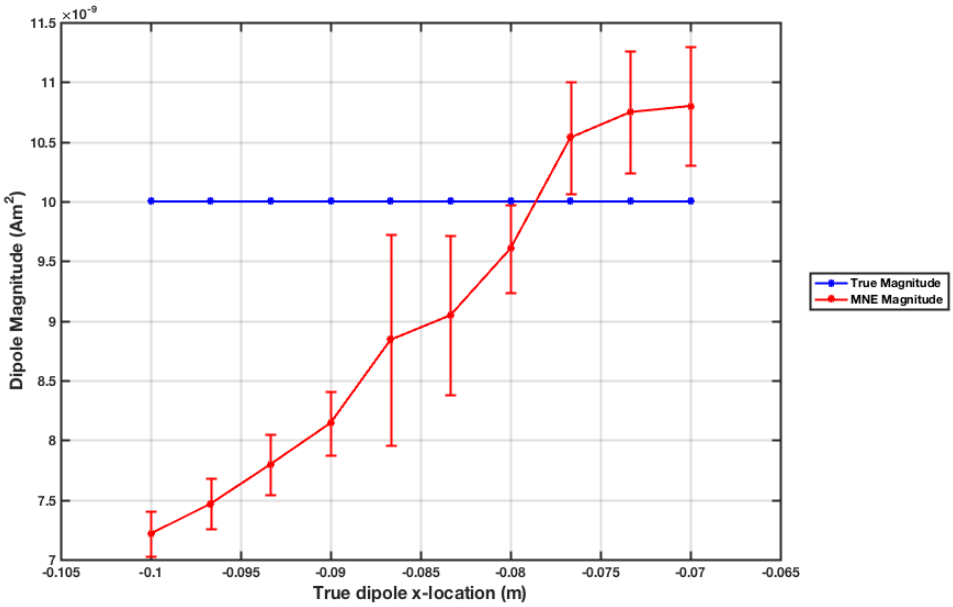

Figure 2.40: Plot showing MNE calculated dipole magnitude for dipoles whose x-location varies from $-0.1\,\mathrm{m}$ to $-0.07\,\mathrm{m}$. The error bars indicate the standard deviation of the results.

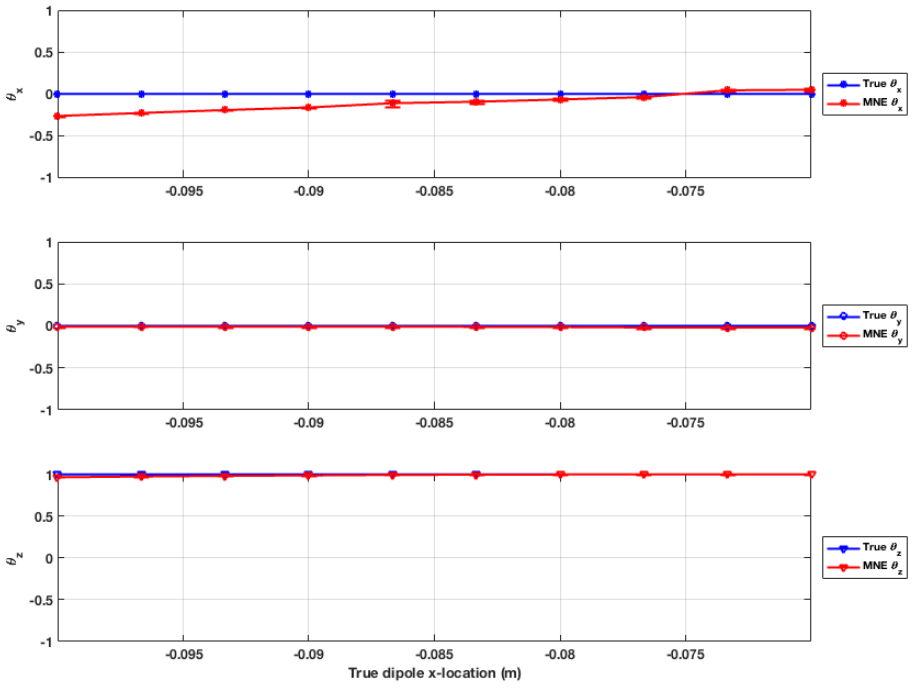

Figure 2.41: Plot showing MNE calculated dipole orientation $\hat{\mathbf{\Theta}} = (\theta_x, \theta_y, \theta_z)$ for dipoles whose x-location varies from $-0.1\,\mathrm{m}$ to $-0.07\,\mathrm{m}$. The error bars indicate the standard deviation of the results.

MNE Reconstruction Accuracy for Dipoles at Different Y-Locations

Figures 2.42 - 2.44 show the MNE-reconstructed FWHM magnetic dipole source localisation for magnetic dipoles located at y-locations $-0.045\,\mathrm{m}$, $0\,\mathrm{m}$, and $0.045\,\mathrm{m}$ respectively, with x-location $-0.085\,\mathrm{m}$, z-location $0.06\,\mathrm{m}$, and orientation parallel to the positive z-axis.

As can be seen in Figures 2.42 and 2.44, for magnetic dipoles located at either end of the MNE target volume space, the MNE-reconstructed dipoles are more displaced than for a magnetic dipole located towards the centre of the MNE target volume space.

Figures 2.45 - 2.48 show how the precision of MNE-reconstructed magnetic dipole location, magnitude, and orientation varies for dipoles of magnitude $10\,\mathrm{nA\,m^2}$, located at an x-coordinate of -0.085, a z-coordinate of 0.06, oriented at $(0, 0, 1)$, in the presence of $10\,\mathrm{fT}$ noise, and in y-locations that vary from $-0.045\,\mathrm{m}$ to $0.045\,\mathrm{m}$. The y-values of the MNE target space also varied from $-0.045\,\mathrm{m}$ to $0.045\,\mathrm{m}$.

It can be seen in Figure 2.45, that the MNE-reconstructed dipole location is less than $5\,\mathrm{mm}$ displaced from the true dipole location for dipoles located at a y-location that falls between $-0.017\,\mathrm{m}$ and $0.019\,\mathrm{m}$.

The difference between the MNE-reconstructed and the real magnetic moment magnitude is less than $25\,\%$ of the real moment magnitude for all dipoles.

MNE-reconstructed dipole orientation is within 15° in x,y,z orientation of the orientation of the true dipole for all the tested dipoles.

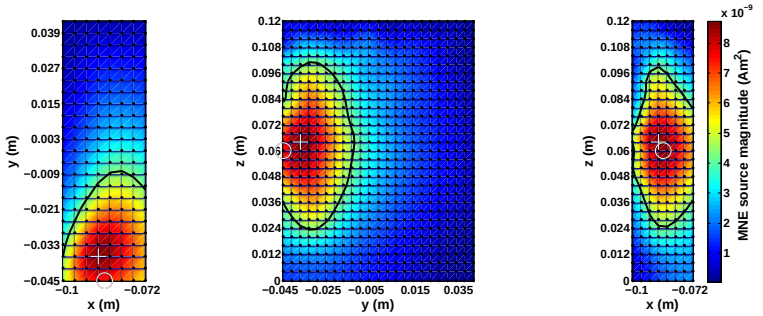

Figure 2.42: Plots showing MNE-reconstructed FWHM magnetic dipole source localisation in the x-y plane at $z = 0.064\,\mathrm{m}$ (left), y-z plane at $x = -0.088\,\mathrm{m}$ (centre) and x-z plane at $y = -0.037\,\mathrm{m}$ (right) for a magnetic dipole with moment magnitude $10\,\mathrm{nA\,m^2}$ located at (-0.085, -0.045, 0.06)m and oriented parallel to the positive z-axis.

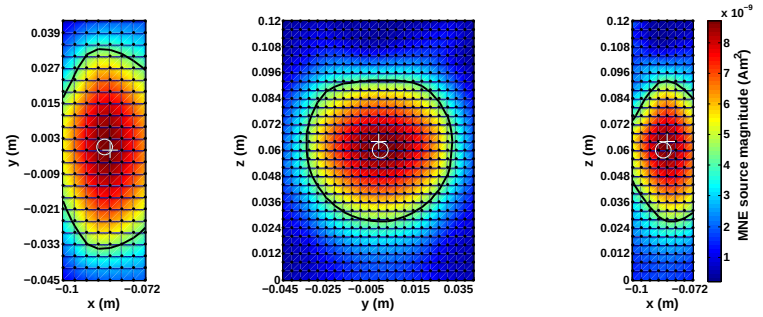

Figure 2.43: Plots showing MNE-reconstructed FWHM magnetic dipole source localisation in the x-y plane at $z = 0.064\,\mathrm{m}$ (left), y-z plane at $x = -0.084\,\mathrm{m}$ (centre) and x-z plane at $y = -0.001\,\mathrm{m}$ (right) for a magnetic dipole with moment magnitude $10\,\mathrm{nA\,m^2}$ located at (-0.085, 0, 0.06)m and oriented parallel to the positive z-axis.

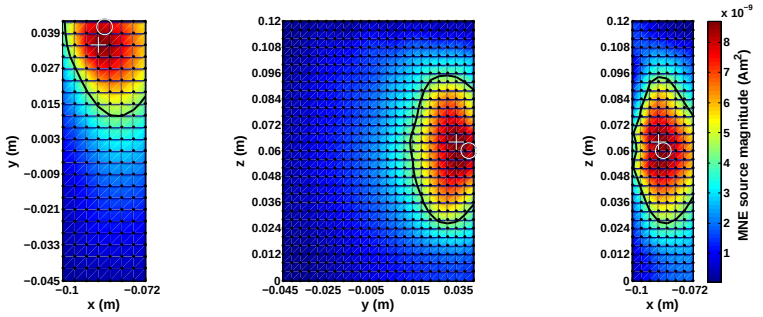

Figure 2.44: Plots showing MNE-reconstructed FWHM magnetic dipole source localisation in the x-y plane at $z = 0.064\,\mathrm{m}$ (left), y-z plane at $x = -0.088\,\mathrm{m}$ (centre) and x-z plane at $y = 0.035\,\mathrm{m}$ (right) for a magnetic dipole with moment magnitude $10\,\mathrm{nA\,m^2}$ located at (-0.085, 0.045, 0.06)m and oriented parallel to the positive z-axis.

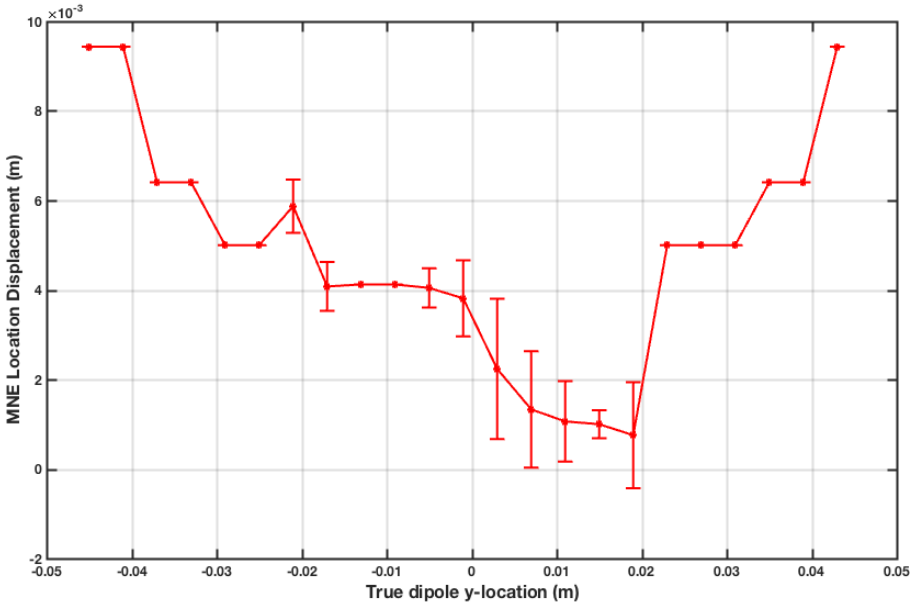

Figure 2.45: Plot showing displacement of MNE calculated location from dipole true location for dipoles whose y-location varies from $-0.045\,\mathrm{m}$ to $0.045\,\mathrm{m}$. The error bars indicate the standard deviation of the results.

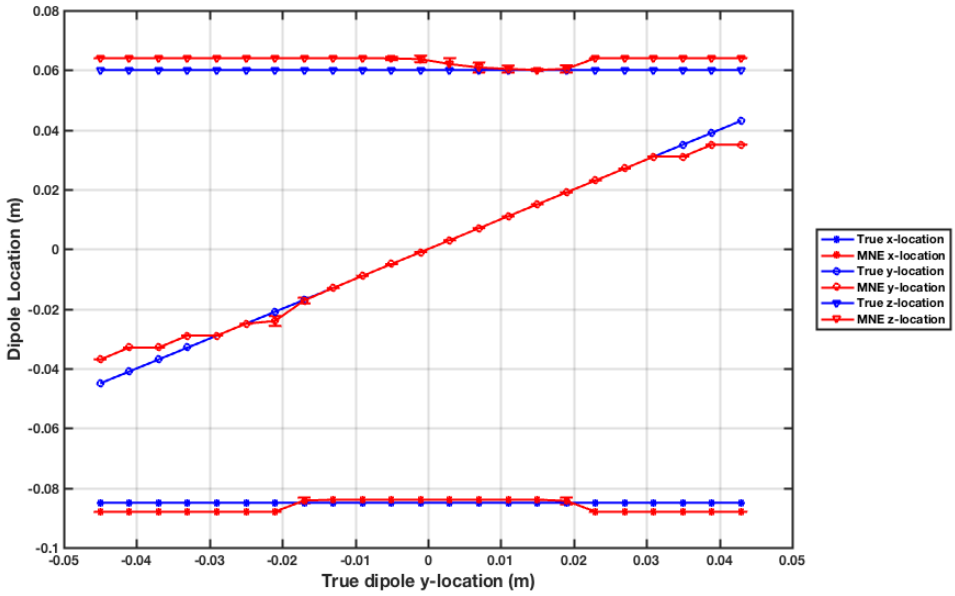

Figure 2.46: Plot showing MNE calculated (x, y, z) location coordinates for dipoles whose y-location varies from $-0.045\,\mathrm{m}$ to $0.045\,\mathrm{m}$. The error bars indicate the standard deviation of the results.

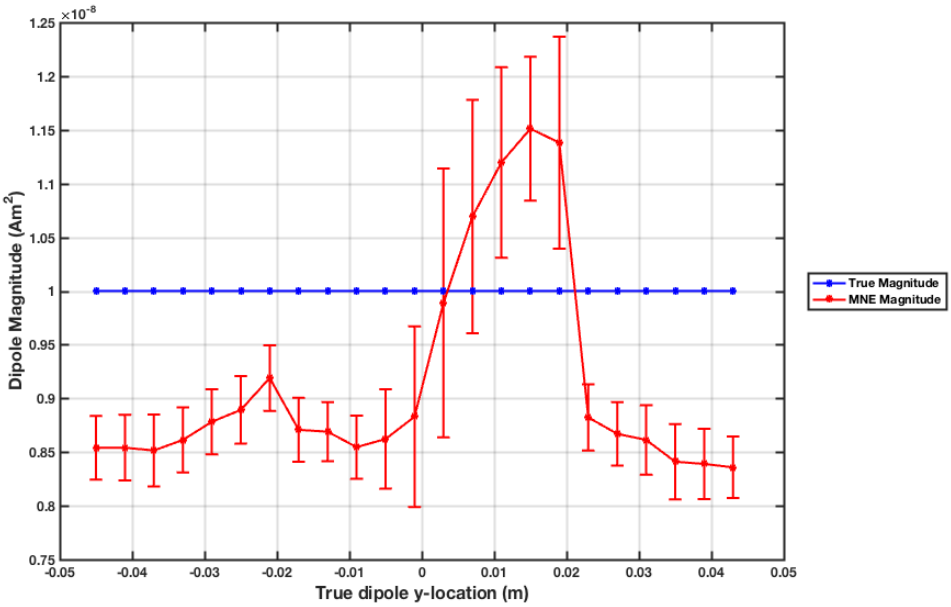

Figure 2.47: Plot showing MNE calculated dipole magnitude for dipoles whose y-location varies from -0.045 m to 0.045 m. The error bars indicate the standard deviation of the results.

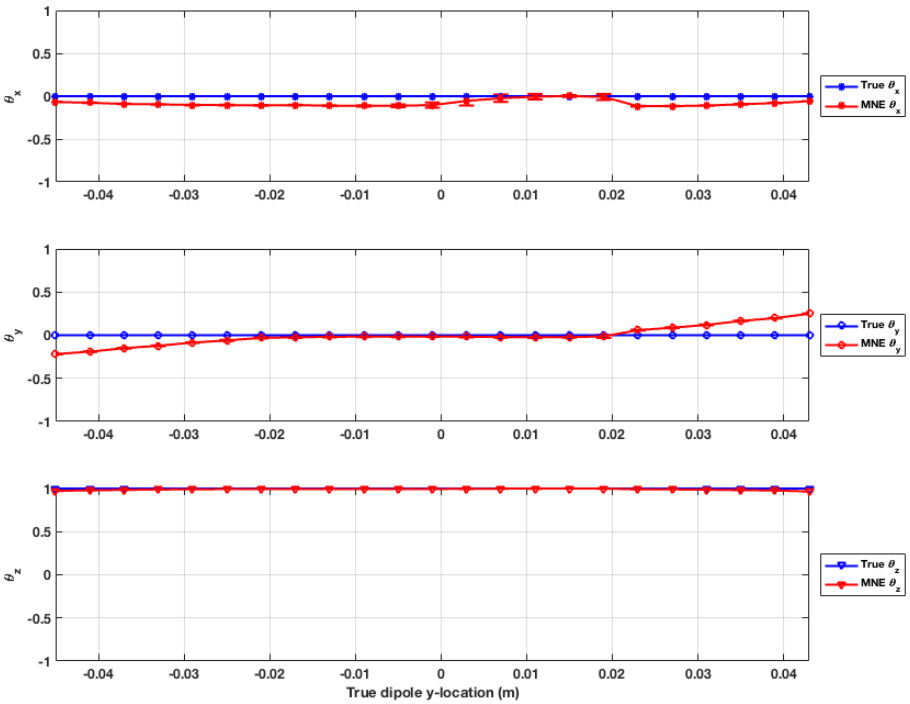

Figure 2.48: Plot showing MNE calculated dipole orientation $\hat{\mathbf{\Theta}} = (\theta_x, \theta_y, \theta_z)$ for dipoles whose y-location varies from -0.045 m to 0.045 m. The error bars indicate the standard deviation of the results.

MNE Reconstruction Accuracy for Dipoles at Different Z-Locations

Figures 2.49 - 2.51 show the MNE-reconstructed FWHM magnetic dipole source localisation for magnetic dipoles located at z-locations 0 m, 0.06 m, and 0.12 m respectively, with x-location -0.085 m, y-location 0 m, and orientation parallel to the positive z-axis.

As can be seen in Figures 2.49 and 2.51, for magnetic dipoles located at either end of the MNE target volume space, the MNE-reconstructed dipoles are more displaced than for a magnetic dipole located towards the centre of the MNE target volume space.

Figures 2.52 - 2.55 show how the precision of MNE-reconstructed magnetic dipole location, magnitude, and orientation varies for dipoles of magnitude 10 nA m^2, located at an x-coordinate of -0.085, a y-coordinate of 0, oriented at $(0, 0, 1)$, in the presence of 10 fT noise, and in z-locations that vary from 0 m to 0.12 m. The z-values of the MNE target space also varied from 0 m to 0.12 m, with less coils positioned towards the topmost part of the helmet because of the helmet's hemispherical shape.

It can be seen in Figure 2.52, that the MNE-reconstructed dipole location is less than 5 mm displaced from the true dipole location for dipoles located at a z-location that falls between 0.04 m and 0.067 m.

The difference between the MNE-reconstructed and the real magnetic moment magnitude is less than 25 % of the real magnitude for all dipoles, excluding those whose z-location lies between 0.013 m and 0.04 m.

MNE-reconstructed dipole orientation is within 15° in x,y,z orientation of the orientation of the true dipole for all dipoles except for a dipole located at a z-location of 0.12 m, which lies at the highest end of the MNE target volume.

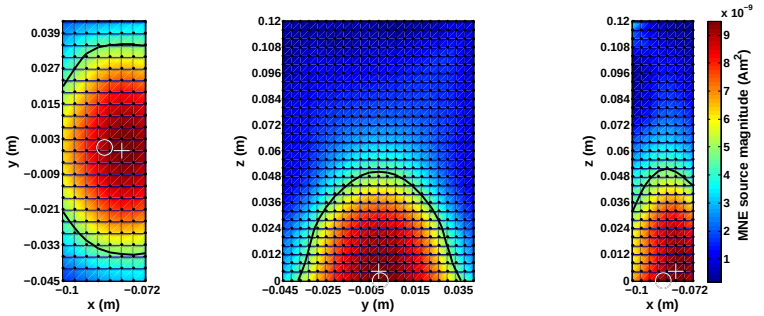

Figure 2.49: Plots showing MNE-reconstructed FWHM magnetic dipole source localisation in the x-y plane at $z = 0.004\,\mathrm{m}$ (left), y-z plane at $x = -0.080\,\mathrm{m}$ (centre) and x-z plane at $y = -0.001\,\mathrm{m}$ (right) for a magnetic dipole with moment magnitude $10\,\mathrm{nA\,m^2}$ located at (-0.085, 0, 0)m and oriented parallel to the positive z-axis.

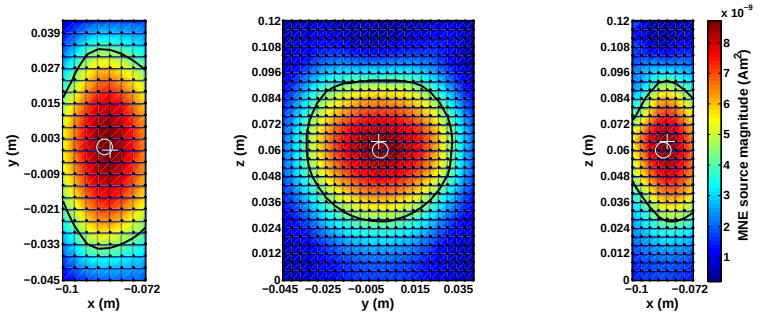

Figure 2.50: Plots showing MNE-reconstructed FWHM magnetic dipole source localisation in the x-y plane at $z = 0.064\,\mathrm{m}$ (left), y-z plane at $x = -0.084\,\mathrm{m}$ (centre) and x-z plane at $y = -0.001\,\mathrm{m}$ (right) for a magnetic dipole with moment magnitude $10\,\mathrm{nA\,m^2}$ located at (-0.085, 0, 0.06)m and oriented parallel to the positive z-axis.

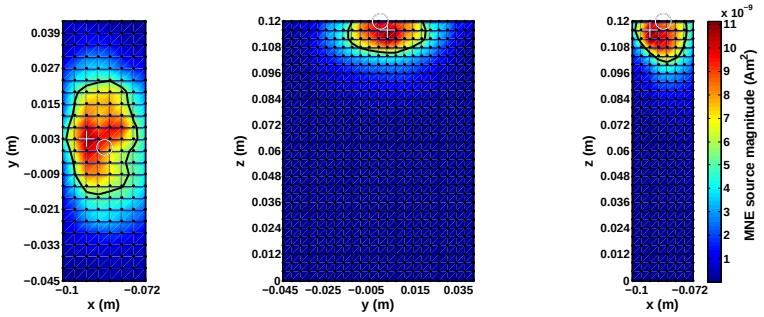

Figure 2.51: Plots showing MNE-reconstructed FWHM magnetic dipole source localisation in the x-y plane at $z = 0.064\,\mathrm{m}$ (left), y-z plane at $x = -0.088\,\mathrm{m}$ (centre) and x-z plane at $y = 0.035\,\mathrm{m}$ (right) for a magnetic dipole with moment magnitude $10\,\mathrm{nA\,m^2}$ located at (-0.085, 0, 0.12)m and oriented parallel to the positive z-axis.

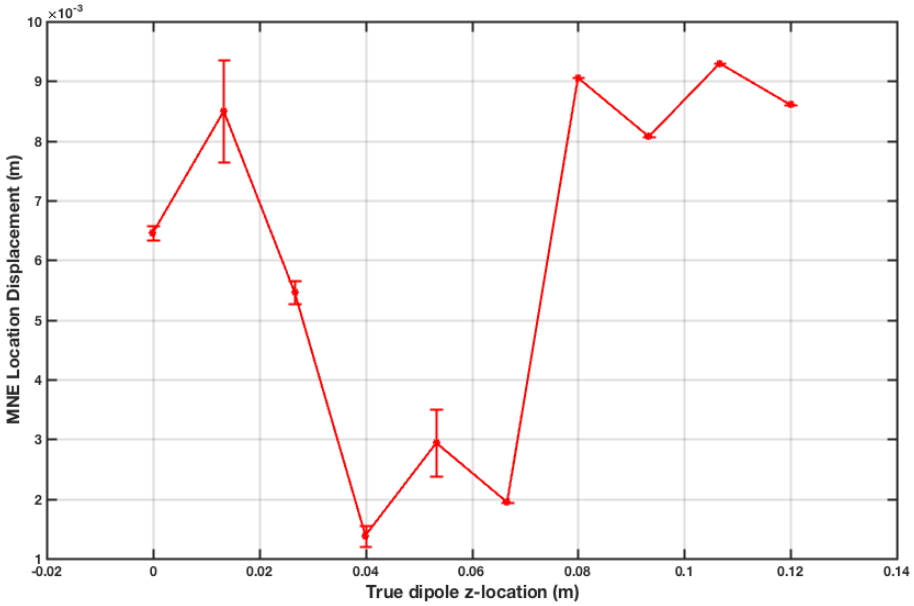

Figure 2.52: Plot showing displacement of MNE calculated location from dipole true location for dipoles whose z-location varies from 0 m to 0.12 m. The error bars indicate the standard deviation of the results.

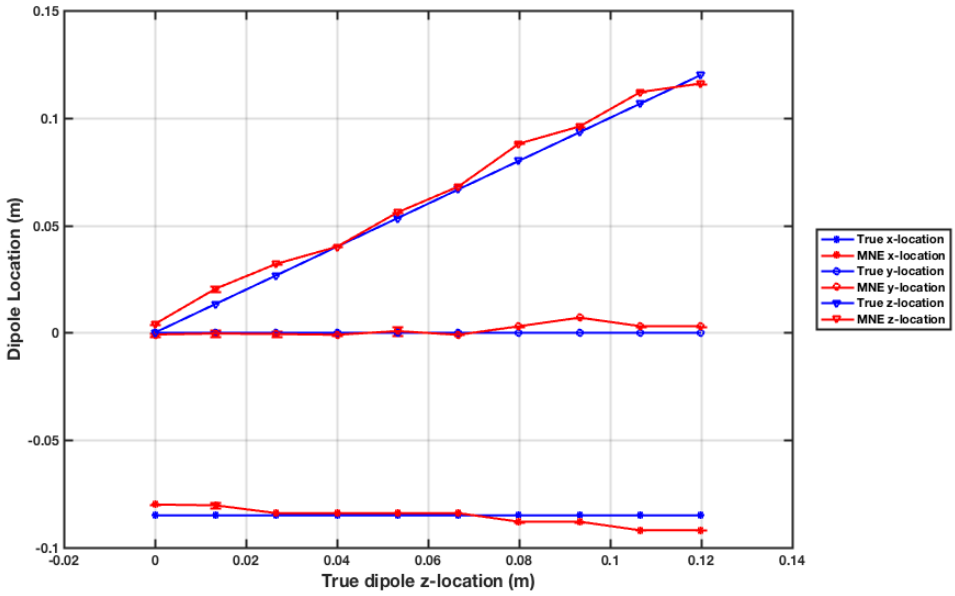

Figure 2.53: Plot showing MNE calculated (x, y, z) location coordinates for dipoles whose z-location varies from 0 m to 0.12 m. The error bars indicate the standard deviation of the results.

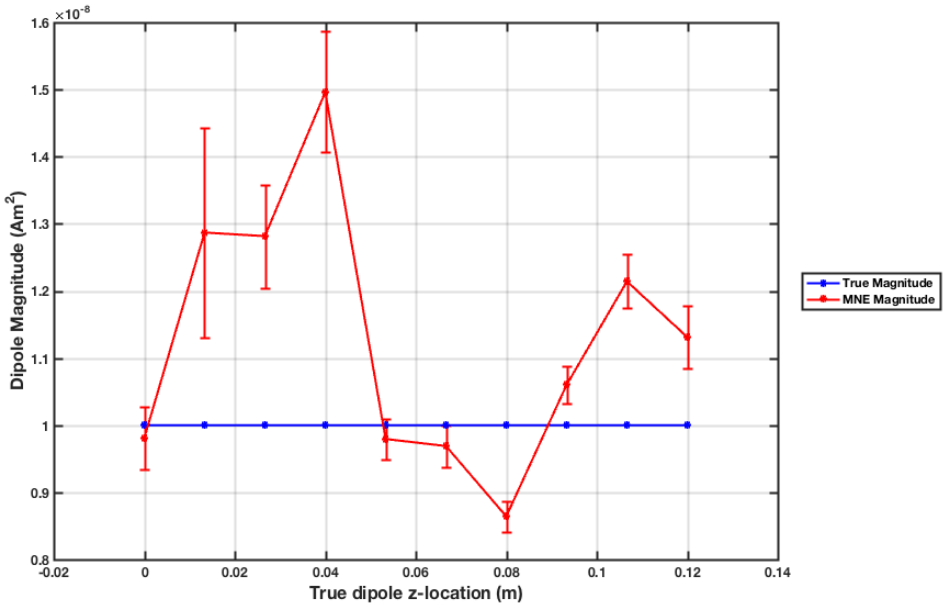

Figure 2.54: Plot showing MNE calculated dipole magnitude for dipoles whose z-location varies from 0 m to 0.12 m. The error bars indicate the standard deviation of the results.

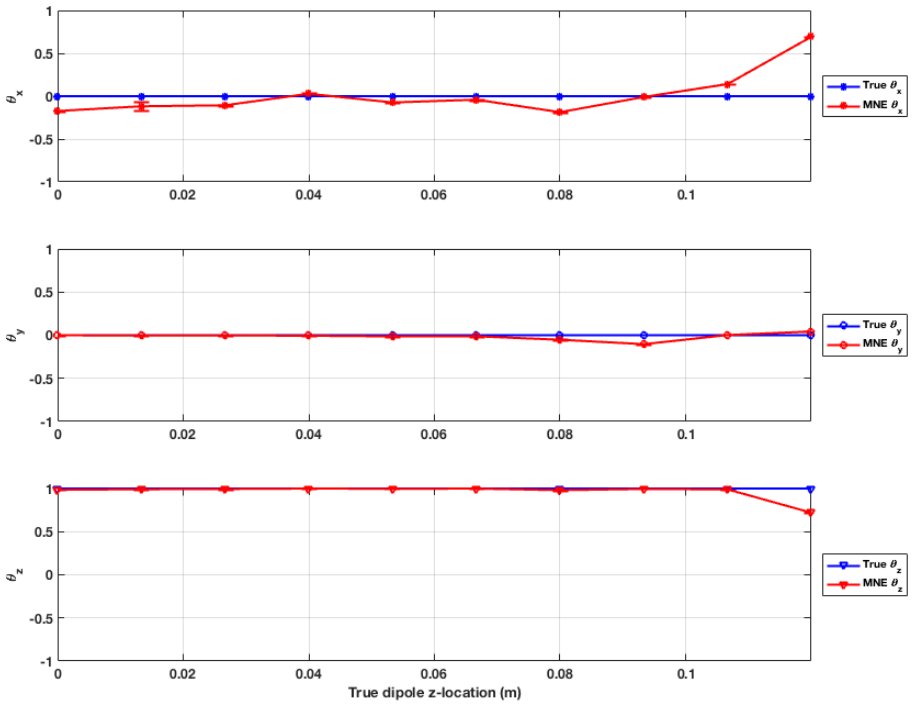

Figure 2.55: Plot showing MNE calculated dipole orientation $\hat{\mathbf{\Theta}} = (\theta_x, \theta_y, \theta_z)$ for dipoles whose z-location varies from 0 m to 0.12 m. The error bars indicate the standard deviation of the results.

MNE Reconstruction Accuracy for Dipole Magnetisation Vectors pointing at Different Orientations in the X-Y Plane

Figures 2.56 - 2.63 show the MNE-reconstructed FWHM magnetic dipole source localisation for magnetic dipoles located at (-0.085, 0, 0.06)m and oriented at varying angles in the x-y plane. These figures show that the MNE-reconstruction accuracy is not sensitive to the orientation of the test dipole.

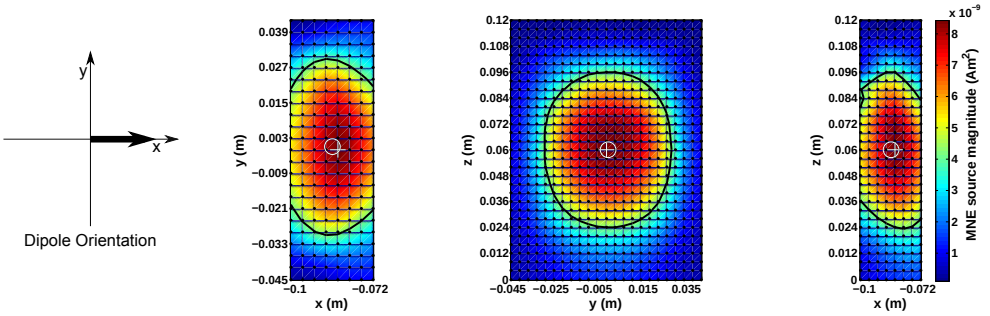

Figure 2.56: Plots showing MNE-reconstructed FWHM magnetic dipole source localisation in the x-y plane at $z = 0.06\,\mathrm{m}$ (left), y-z plane at $x = -0.084\,\mathrm{m}$ (centre) and x-z plane at $y = -0.001\,\mathrm{m}$ (right) for a magnetic dipole with moment magnitude $10\,\mathrm{nA\,m^2}$ located at (-0.085, 0, 0.06)m and oriented at (1,0,0).

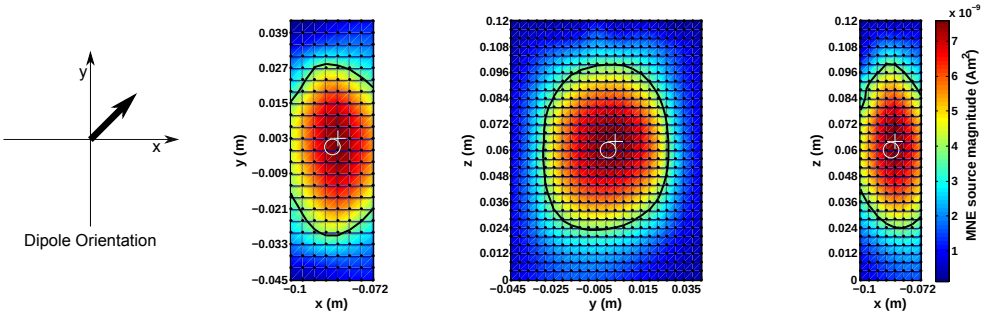

Figure 2.57: Plots showing MNE-reconstructed FWHM magnetic dipole source localisation in the x-y plane at $z = 0.064\,\mathrm{m}$ (left), y-z plane at $x = -0.084\,\mathrm{m}$ (centre) and x-z plane at $y = 0.003\,\mathrm{m}$ (right) for a magnetic dipole with moment magnitude $10\,\mathrm{nA\,m^2}$ located at (-0.085, 0, 0.06)m and oriented at (1,1,0).

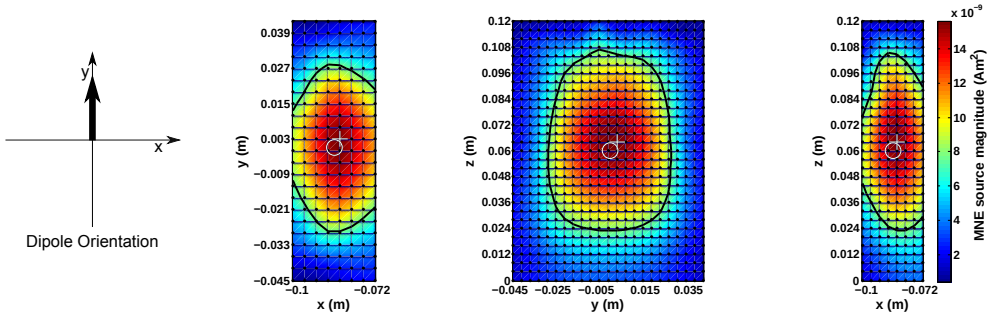

Figure 2.58: Plots showing MNE-reconstructed FWHM magnetic dipole source localisation in the x-y plane at $z = 0.064\,\mathrm{m}$ (left), y-z plane at $x = -0.084\,\mathrm{m}$ (centre) and x-z plane at $y = 0.003\,\mathrm{m}$ (right) for a magnetic dipole with moment magnitude $10\,\mathrm{nA\,m^2}$ located at (-0.085, 0, 0.06)m and oriented at (0,1,0).

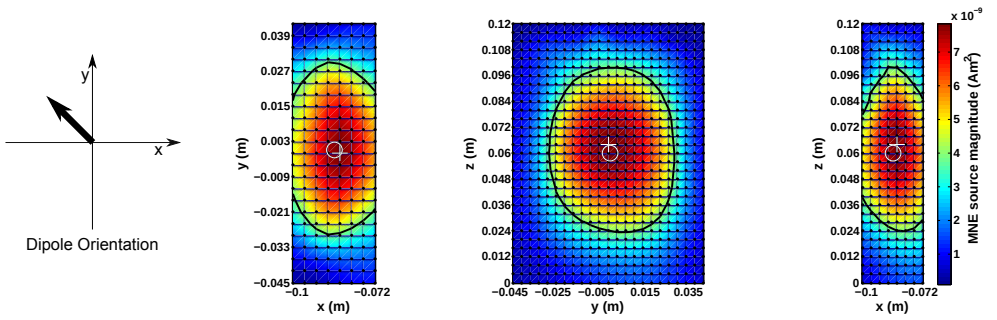

Figure 2.59: Plots showing MNE-reconstructed FWHM magnetic dipole source localisation in the x-y plane at $z = 0.064\,\mathrm{m}$ (left), y-z plane at $x = -0.084\,\mathrm{m}$ (centre) and x-z plane at $y = -0.001\,\mathrm{m}$ (right) for a magnetic dipole with moment magnitude $10\,\mathrm{nA\,m^2}$ located at (-0.085, 0, 0.06)m and oriented at (-1,1,0).

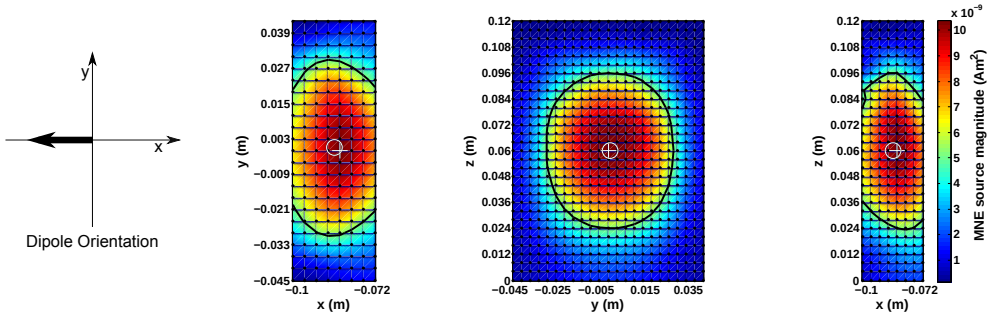

Figure 2.60: Plots showing MNE-reconstructed FWHM magnetic dipole source localisation in the x-y plane at $z = 0.06\,\mathrm{m}$ (left), y-z plane at $x = -0.084\,\mathrm{m}$ (centre) and x-z plane at $y = -0.001\,\mathrm{m}$ (right) for a magnetic dipole with moment magnitude $10\,\mathrm{nA\,m^2}$ located at (-0.085, 0, 0.06)m and oriented at (-1,0,0).

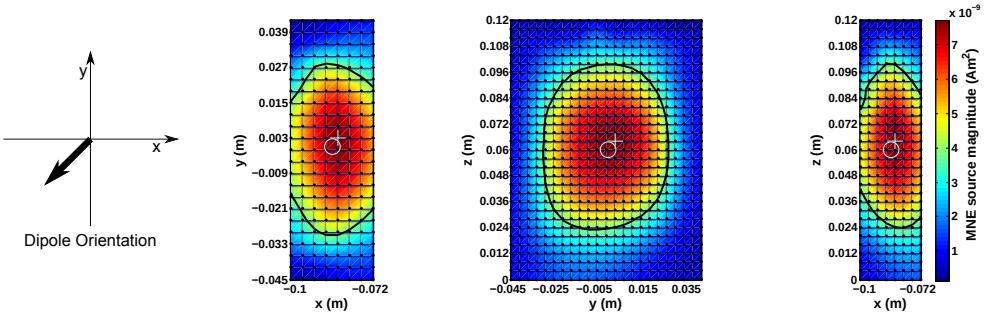

Figure 2.61: Plots showing MNE-reconstructed FWHM magnetic dipole source localisation in the x-y plane at $z = 0.064\,\mathrm{m}$ (left), y-z plane at $x = -0.084\,\mathrm{m}$ (centre) and x-z plane at $y = 0.003\,\mathrm{m}$ (right) for a magnetic dipole with moment magnitude $10\,\mathrm{nA\,m^2}$ located at (-0.085, 0, 0.06)m and oriented at (-1,-1,0).

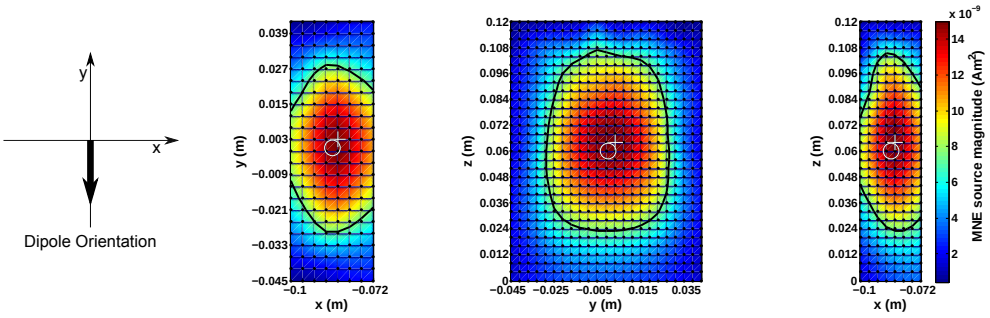

Figure 2.62: Plots showing MNE-reconstructed FWHM magnetic dipole source localisation in the x-y plane at $z = 0.064\,\mathrm{m}$ (left), y-z plane at $x = -0.084\,\mathrm{m}$ (centre) and x-z plane at $y = 0.003\,\mathrm{m}$ (right) for a magnetic dipole with moment magnitude $10\,\mathrm{nA\,m^2}$ located at (-0.085, 0, 0.06)m and oriented at (0,-1,0).

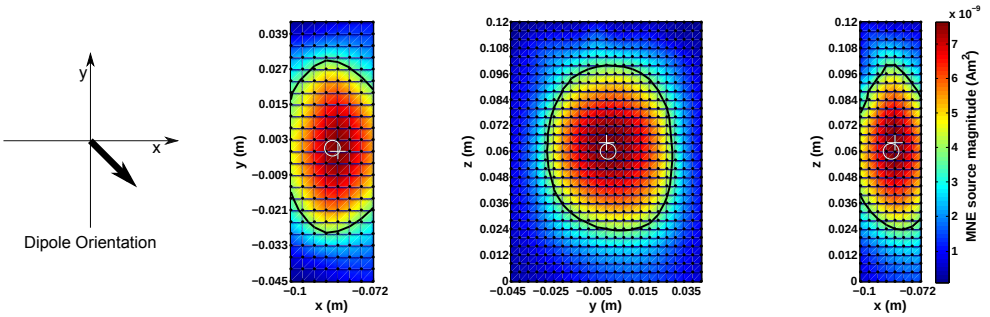

Figure 2.63: Plots showing MNE-reconstructed FWHM magnetic dipole source localisation in the x-y plane at $z = 0.064\,\mathrm{m}$ (left), y-z plane at $x = -0.084\,\mathrm{m}$ (centre) and x-z plane at $y = -0.001\,\mathrm{m}$ (right) for a magnetic dipole with moment magnitude $10\,\mathrm{nA\,m^2}$ located at (-0.085, 0, 0.06)m and oriented at (1,-1,0).

Figures 2.64 - 2.67 show how the precision of MNE-reconstructed magnetic dipole location, magnitude, and orientation for dipoles of magnitude 10 nA m^2, varies for dipoles located at (-0.085, 0, 0.06)m, in the presence of 10 fT noise, with varying orientations in the x-y plane.

It can be seen in Figure 2.64, that the MNE-reconstructed dipole location is less than 5.1 mm displaced from the true dipole location for all dipoles.

The difference between the MNE-reconstructed and the real magnetic moment magnitude is less than 25 % of the real magnitude for all tested dipoles with the exceptions of the ones oriented at 90° and 270° from the x-axis, in the x-y plane.

MNE-reconstructed dipole orientation is within 5° in x,y,z orientation of the orientation of the true dipole for all dipoles. It is closest to the true orientation, with less than a 2° difference, for dipoles whose magnetic moment is oriented at 67.5° and 247.5° from the z-axis in the x-y plane.

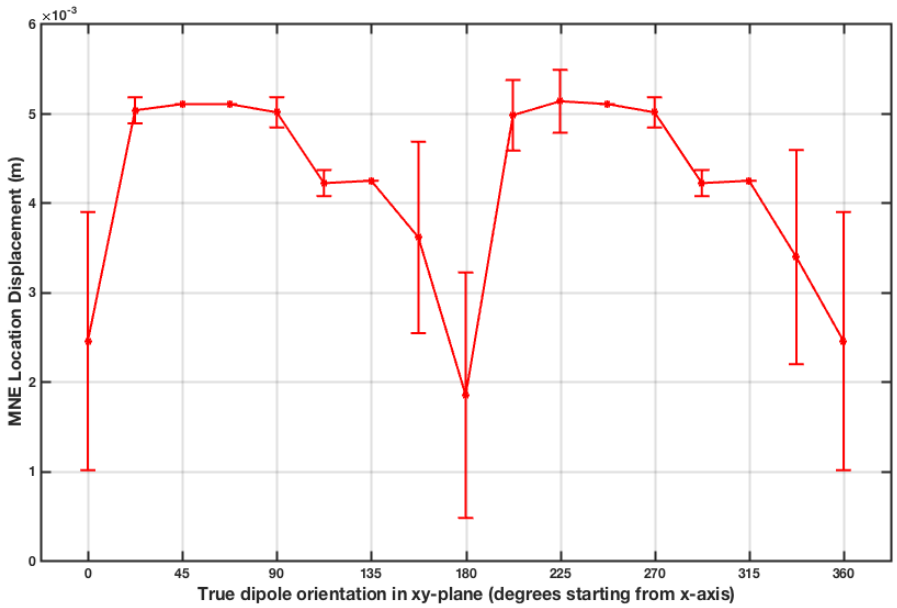

Figure 2.64: Plot showing displacement of MNE calculated location from dipole true location for dipoles with magnetisation vector orientation varying in the x-y plane. The error bars indicate the standard deviation of the results.

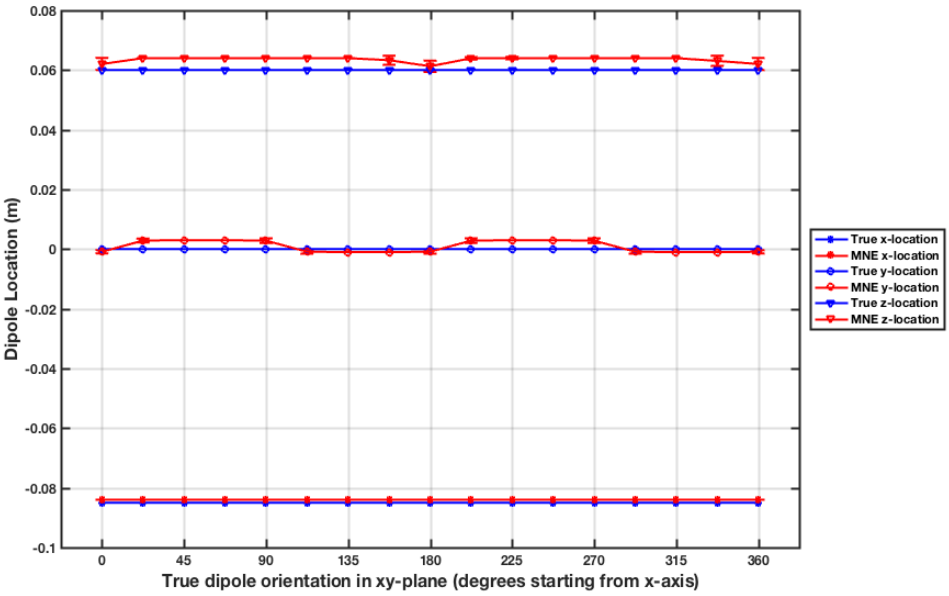

Figure 2.65: Plot showing MNE calculated (x, y, z) location coordinates for dipoles with magnetisation vector orientation varying in the x-y plane. The error bars indicate the standard deviation of the results.

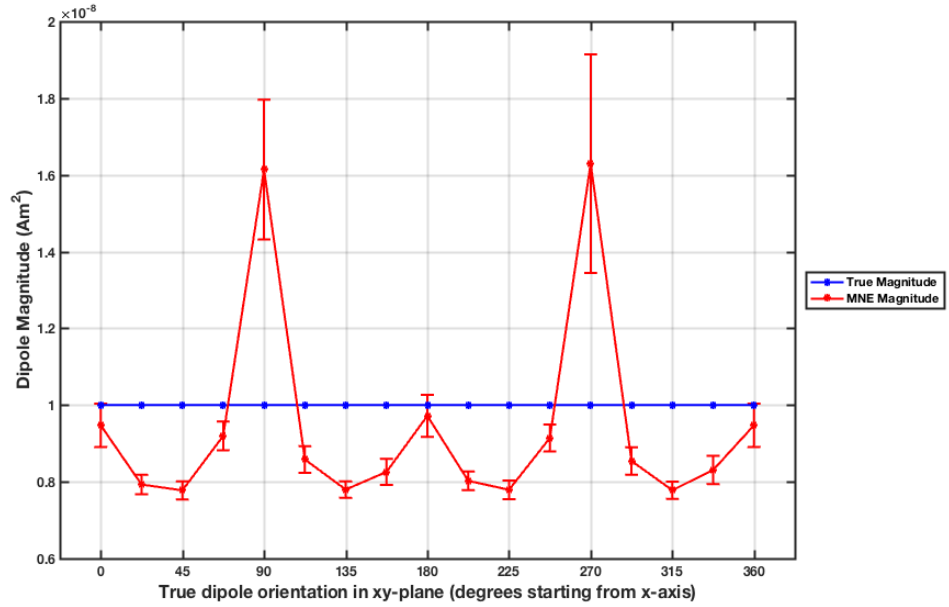

Figure 2.66: Plot showing MNE calculated dipole magnitude for dipoles with magnetisation vector orientation varying in the x-y plane. The error bars indicate the standard deviation of the results.

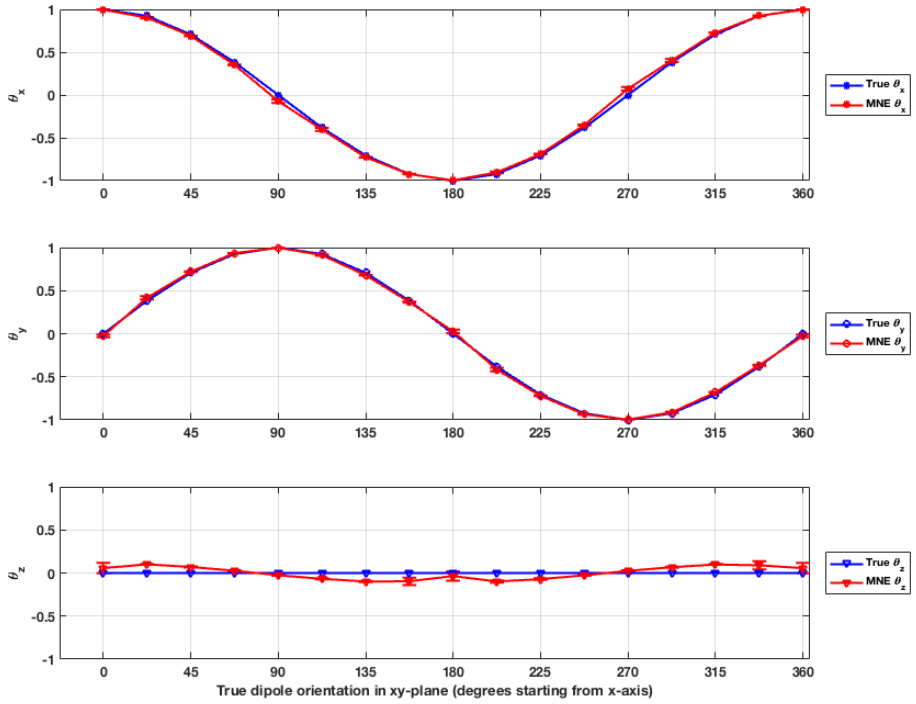

Figure 2.67: Plot showing MNE calculated dipole orientation $\hat{\mathbf{\Theta}} = (\theta_x, \theta_y, \theta_z)$ for dipoles with magnetisation vector orientation varying in the x-y plane. The error bars indicate the standard deviation of the results.

MNE Reconstruction Accuracy for Dipole Magnetisation Vectors pointing at Different Orientations in the Y-Z Plane

As in the previously described work, we found that the MNE-reconstruction accuracy did not depend on the true orientation of the test dipole (see Appendix A).

Figures 2.68 - 2.71 show how the precision of MNE-reconstructed magnetic dipole location, magnitude, and orientation varies for dipoles of magnitude 10 nA m^2, located at (-0.085, 0, 0.06)m, in the presence of 10 fT noise, with varying orientations in the y-z plane.

It can be seen in Figure 2.68, that the MNE-reconstructed dipole location is less than 5.1 mm displaced from the true dipole location for all tested dipoles.

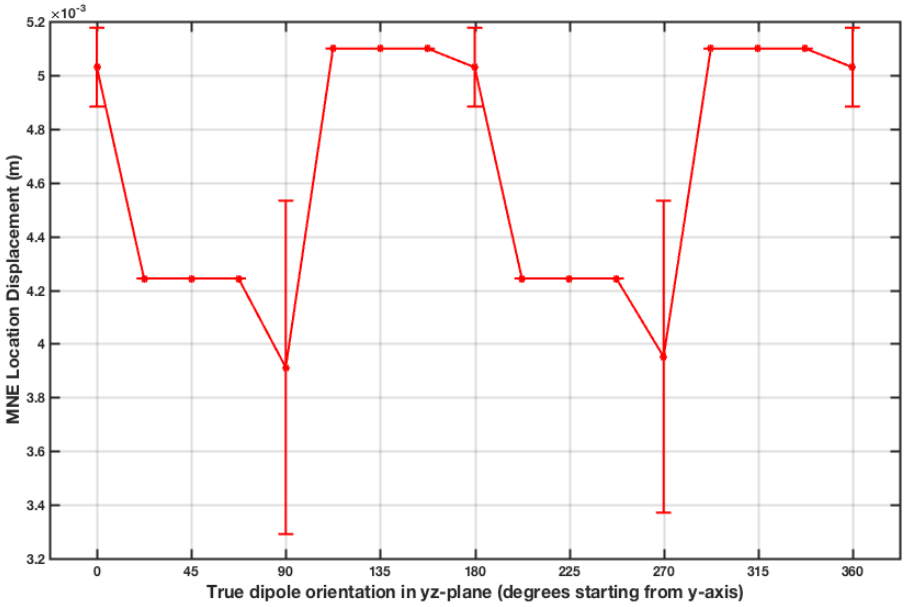

Figure 2.68: Plot showing displacement of MNE calculated location from dipole true location for dipoles with magnetisation vector orientation varying in the y-z plane. The error bars indicate the standard deviation of the results.

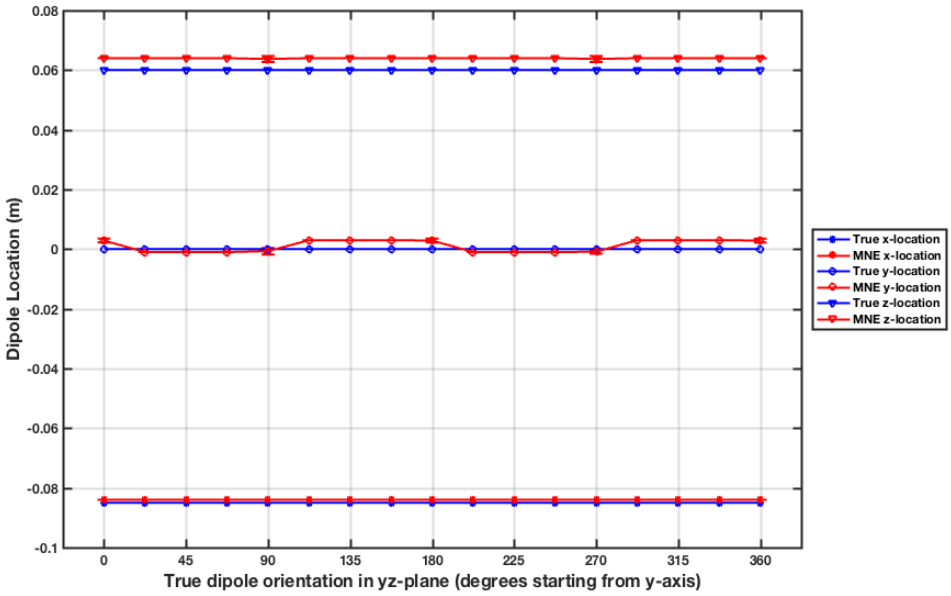

Figure 2.69: Plot showing MNE calculated (x, y, z) location coordinates for dipoles with magnetisation vector orientation varying in the y-z plane. The error bars indicate the standard deviation of the results.

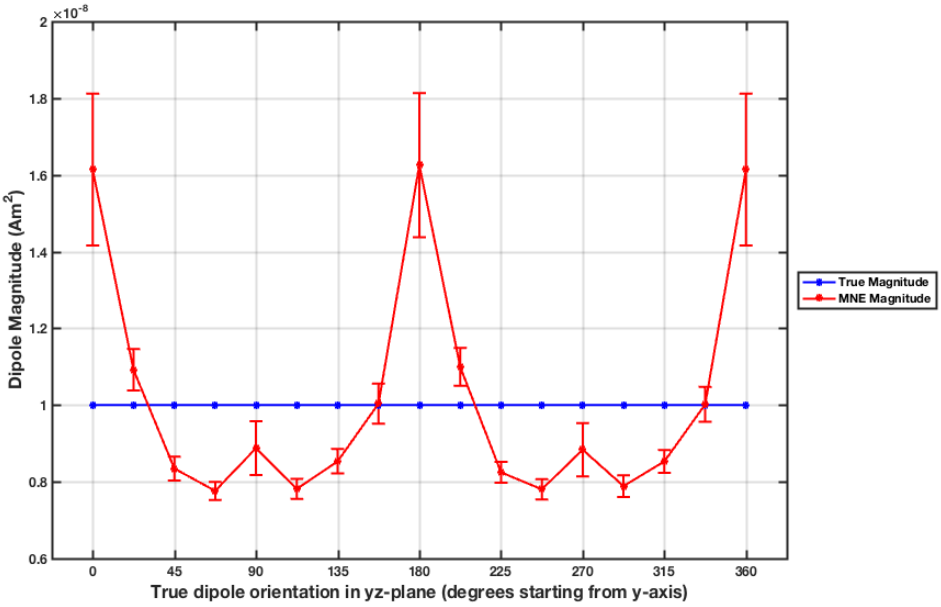

Figure 2.70: Plot showing MNE calculated dipole magnitude for dipoles with magnetisation vector orientation varying in the y-z plane. The error bars indicate the standard deviation of the results.

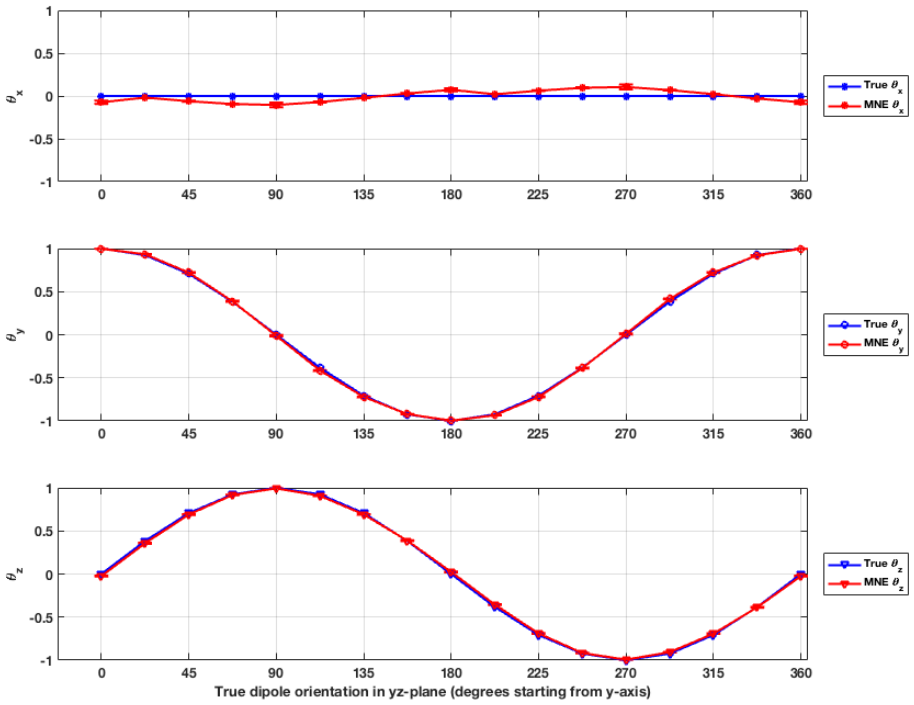

Figure 2.71: Plot showing MNE calculated dipole orientation, for dipoles with magnetisation vector orientation varying in the y-z plane. The error bars indicate the standard deviation of the results.

The difference between the MNE-reconstructed and real magnetic moment magnitude is less than 25 % of the real magnitude for all tested dipoles with the exceptions of those oriented at 0° and 180°.

MNE-reconstructed dipole orientation is within 5° in x,y,z orientation of the orientation of the true dipole for all dipoles. It is closest to the true orientation, with less than 2 degrees difference, for dipoles whose magnetic moment is oriented at 135° and 315° from the x-axis in the y-z plane.

MNE Reconstruction Accuracy for Dipole Magnetisation Vectors pointing at Different Orientations in the X-Z Plane

As described before, we found that the MNE-reconstruction accuracy did not depend on the true orientation of the test dipole (see Appendix A).

Figures 2.72 - 2.75 show how the precision of MNE-reconstructed magnetic dipole location, magnitude, and orientation varies for dipoles of magnitude 10 nA m^2, lo-

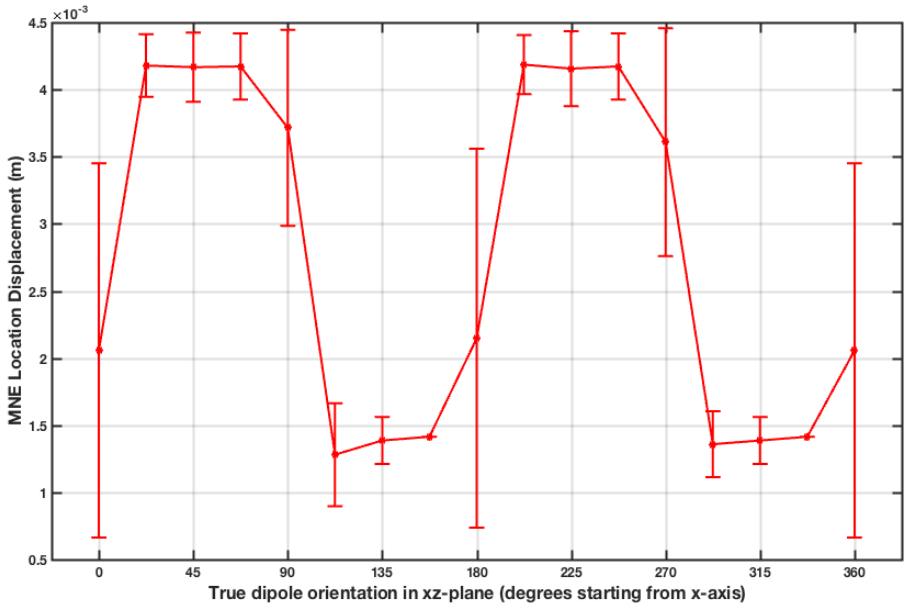

Figure 2.72: Plot showing displacement of MNE calculated location from dipole true location for dipoles with magnetisation vector orientation varying in the x-z plane. The error bars indicate the standard deviation of the results.

cated at (-0.085, 0, 0.06)m, in the presence of 10 fT noise, with varying orientations in the x-z plane.

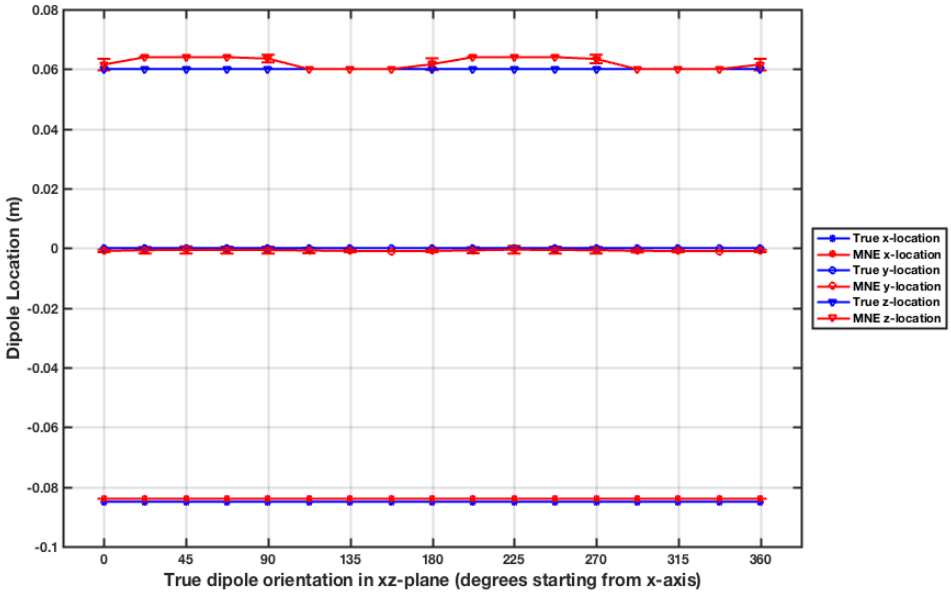

Figure 2.73: Plot showing MNE calculated (x, y, z) location coordinates for dipoles with magnetisation vector orientation varying in the x-z plane. The error bars indicate the standard deviation of the results.

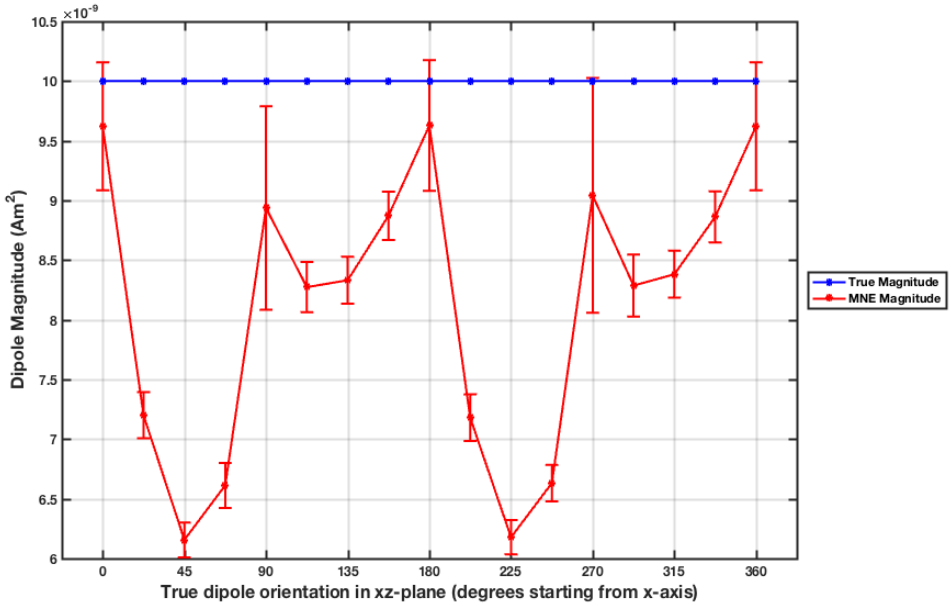

Figure 2.74: Plot showing MNE calculated dipole magnitude for dipoles with magnetisation vector orientation varying in the x-z plane.The error bars indicate the standard deviation of the results.

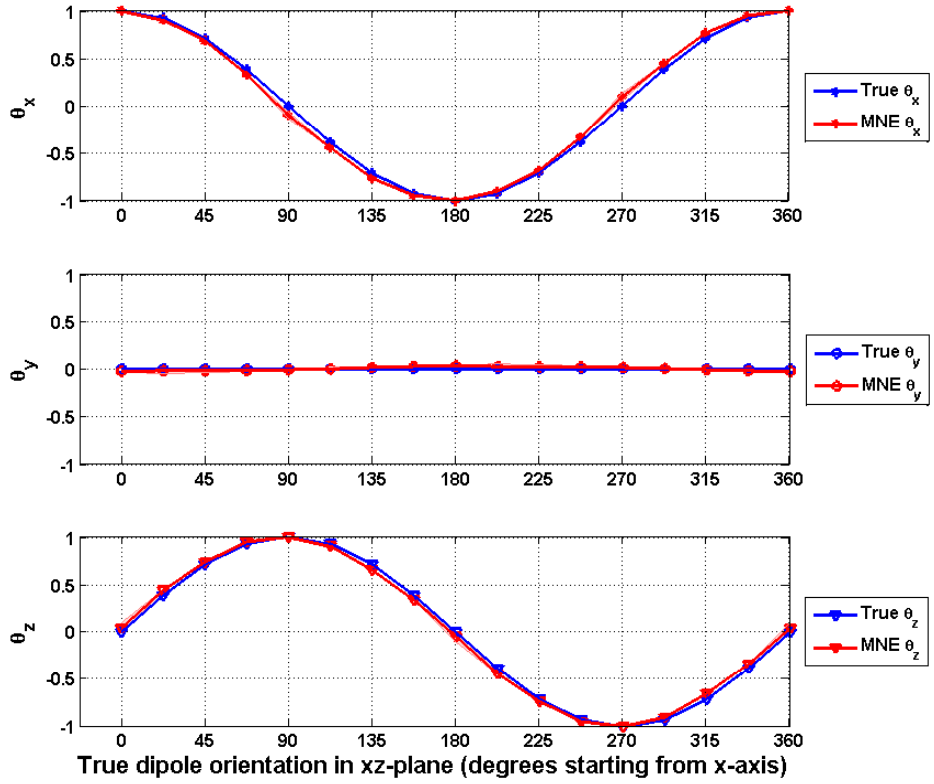

Figure 2.75: Plot showing MNE calculated dipole orientation $\hat{\mathbf{\Theta}} = (\theta_x, \theta_y, \theta_z)$ for dipoles with magnetisation vector orientation varying in the x-z plane. The error bars indicate the standard deviation of the results.

It can be seen in Figure 2.72, that the MNE-reconstructed dipole location is less than 5 mm displaced from the true dipole location for all dipoles.

The difference between the MNE-reconstructed and the real magnetic moment magnitude is less than 25 % of the real magnitude for all dipoles, with the exception of the dipoles oriented between 22.5° and 67.5°, and between 202.5° and 247.5° from the y-axis in the x-z plane.

MNE-reconstructed dipole orientation is within 5° in x,y,z orientation of the orientation of the true dipole for all dipoles.

2.5 Conclusions

The results indicate that the MNE inverse solution can locate dipoles best when a dipole located at (-0.085, 0, 0.06)m has a magnetic moment strength of at least $0.1\,\mathrm{nA\,m^2}$. This is equivalent to an SNR of around 20 at the detector that detects the biggest signal.

It is expected that the displacement of the MNE-reconstructed dipole location from the true location will decrease with higher SNR values. Most of our results in Figure 2.31 comply with this expectation, with the exception of dipoles whose moment magnitudes range between $3\,\mathrm{nA\,m^2}$ and $20\,\mathrm{nA\,m^2}$. This might be a result of the selected MNE voxel resolution (4 mm).

For dipoles located at different x, y, and z locations, the MNE algorithm produced the most accurate localisation when the dipole was located towards the middle of the target volume, and in the middle of the sensor range.

For dipoles oriented at different orientations, it was expected that the best localisation occurs when the dipoles are oriented normal to the local surface, since this yields the largest magnetic field in the coil. However, our simulations showed that for dipoles oriented at different orientations in the x-y plane, the MNE produced the most accurate localisation for dipoles whose orientation vector was close to being parallel with the x-axis. Dipoles oriented at different orientations in the y-z plane, had the most accurate localisation when the orientation vector was oriented in directions that were at 45° to the z-axis. Similarly, for dipoles oriented at different orientations in the x-z plane, the algorithm yielded the least displacement when the real dipole's magnetisation vector pointed at 45° to the z-axis.

In conclusion, the localisation accuracy is mostly affected by the SNR, which depends on the location of the dipole and the strength of its magnetic moment.

To keep the localisation error within 5 mm or less, magnetised samples should be positioned towards the middle of the sensor range.

In this chapter, we have demonstrated the feasibility of localising magnetisation based on magnetic field measurements using a typical MEG gradiometer detector array. In the next chapter, we carry out experiments to test this approach.

Chapter 3

Detecting Magnetic Field Shifts using MEG SQUIDs

3.1 Introduction

Recently, there has been a spate of interest in the development of Ultra Low Field (ULF) MRI systems that use sensitive magnetic field sensors for the detection of the NMR signals [42, 43, 44, 45]. Benefits of Ultra Low Field (ULF) MRI using SQUID-based detectors include low cost [45, 46, 47, 48], a strong contrast [47, 49], and the potential for carrying out MEG and MRI on the same system [46, 48].

The implementation of ULF NMR with a reasonable SNR generally requires:

1. Pre-polarisation of proton spins by a much larger magnetic field than the field used for subsequent imaging,

2. Detection of the NMR signal using SQUIDs. Unlike a Faraday detector, the SQUID has a frequency-independent response to magnetic flux. At low field, one can then obtain spectra of two nuclear species in a single acquisition, and directly detect J-coupling in heteronuclear spin systems [50].

Using an ULF MRI system that operates at 132 µT, a research group in Berkeley generated a 3D in-vivo image of an arm with an in-plane resolution of 2 mm [51]. Since field inhomogeneity due to high susceptibility materials is reduced at ULF, the group was able to produce an undistorted image even in the presence of a metal bar, which could for example be an orthopaedic screw.

It is also possible to carry out a simultaneous acquisition of a stimulated magnetic signal from the human brain, using MEG, and an ULF NMR signal from protons in the brain using a single SQUID [50]. The two systems can be combined by adding an appropriate set of coils to existing MEG systems. Using one system mitigates difficulties in co-registration of the two images produced with the two different systems.

There are several applications for simultaneous MEG and MRI. Prior to the surgical removal of brain tumors or vascular malformations, the motor, sensory and language centres in the brain need to be localised [52]. This is one main clinical application of Blood Oxygen Level-Dependent functional Magnetic Resonance Imaging (BOLD fMRI). BOLD fMRI does not directly measure the neuronal firing. It infers neural activation from small MR signal changes that are due to the decreased concentration of deoxyhaemoglobin that occurs in the more active areas of the brain [53].

Thus, even though BOLD fMRI has a high spatial resolution of about 1 mm, it lacks the temporal resolution required to characterise changes in neuronal activity from a haemodynamic response. The temporal resolution of BOLD fMRI is of the order of seconds, yet we require a much higher temporal resolution in order to track neuronal activity involved in cognitive functions [54, 55].

On the other hand, MEG is a non-invasive way of directly measuring, in real time, the neuronal activity of the brain in vivo. Its detectors translate very weak, changing magnetic fields into measurable signals. MEG signals have only little

attenuation because they are hardly affected by the tissues of the brain and the unevenness of the skull and scalp, in contrast to EEG. MEG can produce functional images of the brain, and has a high temporal resolution of approximately one millisecond. However, its spatial resolution is rather low, in the order of five millimetres. Thus, high spatial resolution MRI data are often used to more accurately model the high temporal resolution MEG results.

The combination of MEG and MRI data is thus an important approach, which potentially offers both high temporal and high spatial resolution in monitoring brain function. Since SQUIDs are sensitive to weak magnetic fields, they can also be used to detect NMR signals [56]. This is most easily done at very low magnetic fields, and there have consequently been several recent reports [23] of the development of systems for combined MEG and low-field MRI.

Yet, because of the sensitivity of the SQUID detectors to variations in the applied magnetic field, using non-inductive detection schemes with the time-varying magnetic fields that are required for imaging of the transverse magnetisation, is not straightforward. In this chapter, we describe initial experiments that use MEG to detect and image the distribution of decaying longitudinal Nuclear Magnetisation (NM) from polarised aqueous samples [57]. We then solve the inverse problem relating the measured magnetisation distribution to the magnetic fields produced at an array of sensors, explained in Chapter 2, to generate images.

The pre-polarisation required to enhance the magnetisation relative to the weak thermal polarisation available at ULF can be carried out at a distance away from the MEG scanner, and no gradient fields are required for this approach to imaging. We use a standard MEG system for detection, along with a small permanent magnet to polarise aqueous samples, and another permanent magnet to produce a weak field inside the MEG helmet, thus allowing detection and imaging of the decaying longitudinal nuclear magnetisation [58].

We also show how a MEG system can be used to map susceptibility-related magnetisation induced in samples at ULF.

3.2 Theory

The hypothesis behind this project was that if we first polarise a sample, we can then use highly sensitive magnetic sensors to detect the magnetic field shifts due to a change in magnetisation, and thus can record the relaxation of longitudinal nuclear magnetisation.

The rationale was that we first use a polarising magnet to magnetise the samples, and then in the presence of an imaging magnet, record the magnetic field using MEG SQUIDs. Figure 3.1 shows the setup of the experiment.

The polarising magnet was 0.2 T in strength, and the imaging magnet had a strength of 0.5 T. The SQUIDs lie approximately 5 cm away from the sample, and the imaging magnet was located at a distance of 2 m from the sample, inside the Magnetically Shielded Room (MSR) pictured in Figure 3.2.

At this distance, the magnetic field generated by the 0.5 T imaging magnet is similar to that generated from a magnetic dipole of magnetic moment 220 A m^2. Using the Biot-Savart law explained in Chapter 2, the magnetic field strength **B**,

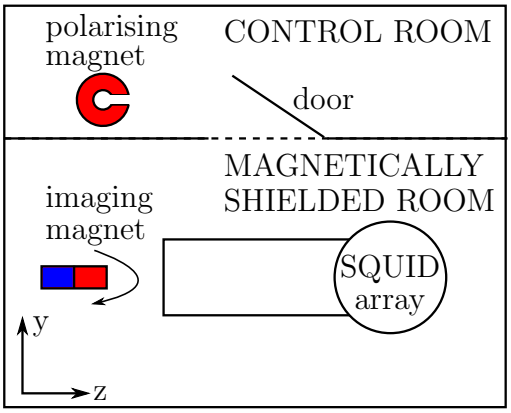

Figure 3.1: Schematic of experimental setup.

generated from a dipole of magnetic moment 220 A m^2, located 2 m away on-axis, is given by

$$\mathbf{B} = \frac{\mu_0}{4\pi} \frac{3\hat{\mathbf{n}}(\hat{\mathbf{n}}.\mathbf{m}) - \mathbf{m}}{|\mathbf{r} - \mathbf{r}'|^3}, \tag{3.1}$$

which yields a value of $|\mathbf{B}| = 5.5\,\mu$T.

For a 10 cm^3 water sample, polarised at 0.2 T, and located 5 cm away from the SQUIDs, the magnitude of the magnetic field that will be generated at the MEG detectors by nuclear magnetisation is of the order of 10 pT, which is large enough to be measured by SQUIDs.

In the following sections, we explain what happens to the sample throughout the experiment, starting with what happens to the sample when it is exposed to the polarising field.

Figure 3.2: Picture of MEG system used.

3.2.1 Boltzmann Statistics of Spin 1/2 System

In quantum mechanics, when a spin 1/2 system is exposed to a magnetic field, B_0, the number of spins in the lower energy level, N^+ (aligned with the field), slightly exceeds the number of spins in the upper energy level, N^- (oriented anti-parallel to the field). This ratio is given by the Boltzmann distribution in Equation 3.2 [59, 60],

$$\frac{N^-}{N^+} = e^{-\frac{\Delta E}{k_B T}} \tag{3.2}$$

and

$$\Delta E = \gamma \hbar B_0 \tag{3.3}$$

ΔE is the difference in energy of the two states, k_B is Boltzmann's constant, T is the absolute temperature in Kelvin, γ is the gyromagnetic ratio of the nuclei in the sample, and $\hbar$ is the reduced Planck's constant.

At room temperature, where $\Delta E << k_B T$, a magnetisation, M_0, given by Equation 3.4, is induced in the sample.

$$M_0 \sim \frac{N(\gamma\hbar)^2}{4k_B T} B_0 \tag{3.4}$$

where N is the number of spins per cubic metre.

For a water sample, having a density of $1000\,\mathrm{kg\,m^{-3}}$, a molar weight of $0.018\,\mathrm{kg\,mol^{-1}}$, and two spins per molecule,

$$N \sim \frac{2(6.02 \times 10^{23})(1000)}{0.018} = 6.67 \times 10^{28}\,\text{spins}\,\text{m}^{-3} \tag{3.5}$$

Substituting this value for N in Equation 3.4, the internal magnetisation of a water sample is

$$\begin{aligned} M_0 &\sim \frac{(6.67 \times 10^{28})(6.63 \times 10^{-34})^2(267.513 \times 10^6)^2}{16\pi^2(1.38 \times 10^{-23})(293)} B_0 \\ &\sim (3.25 \times 10^{-3}) B_0 \end{aligned} \tag{3.6}$$

Thus, for $10\,\text{cm}^3$ water, polarised at $0.2\,\text{T}$,

$$\begin{aligned} m &= Mv \\ &\sim (3.25 \times 10^{-3})(0.2)(10 \times 10^{-6}) \\ &\sim 6.5 \times 10^{-9}\,\text{A}\,\text{m}^2 \end{aligned} \tag{3.7}$$

3.2.2 Dipole Field

The magnetic field generated at point P, by a magnetic dipole located at point O with magnetic moment $\mathbf{m}$, as shown in Figure 2.11, is given by

$$\mathbf{B} = \frac{\mu_0}{4\pi} \frac{3\mathbf{n}(\mathbf{n}.\mathbf{m}) - \mathbf{m}}{|\mathbf{x}|^3} \tag{3.8}$$

where $\mathbf{m}$ is the magnetic moment of the dipole, $\mathbf{x}$ is the vector between the location of the dipole and the target point of interest, and $\mathbf{n}$ is the unit vector in the direction of $\mathbf{x}$.

The largest value of $\mathbf{B}$ occurs when $\mathbf{n}.\mathbf{m} = |\mathbf{n}||\mathbf{m}| \cos\theta$ takes its maximum value, which occurs when θ, the angle between vectors $\mathbf{n}$ and $\mathbf{m}$, is $0°$. Therefore, the largest value of $\mathbf{B}$ is found on the dipole axis, and is given by Equation 3.9.

$$\mathbf{B} = \frac{\mu_0}{2\pi} \frac{|\mathbf{m}|}{|\mathbf{x}|^3} \tag{3.9}$$

Therefore, the magnetic field, $\mathbf{B}$, from the dipole in Equation 3.7 at a distance of 5 cm is

$$\mathbf{B} = \frac{(4\pi \times 10^{-7})(6.5 \times 10^{-9})}{(2\pi)(0.05)^3} = 10.4\,\text{pT} \tag{3.10}$$

The SQUIDs in the MEG scanner are capable of measuring fields down to 1 fT, and thus, 10.4 pT can readily be measured in the MEG scanner.

3.2.3 Magnetisation Relaxation

When the polarising field is removed, $\mathbf{M}$ decays according to the characteristic longitudinal relaxation time, T_1, as shown in Equation 3.11 [61] and Figure 3.3.

$$M(t) = M_0 e^{-\frac{t}{T_1}} \tag{3.11}$$

The relaxation time for protons in water [62, 63] is given by

$$\frac{1}{T_1} = K\left[\frac{\tau_c}{1+\omega^2\tau_c^2} + \frac{2\tau_c}{1+4\omega^2\tau_c^2}\right], \tag{3.12}$$

where

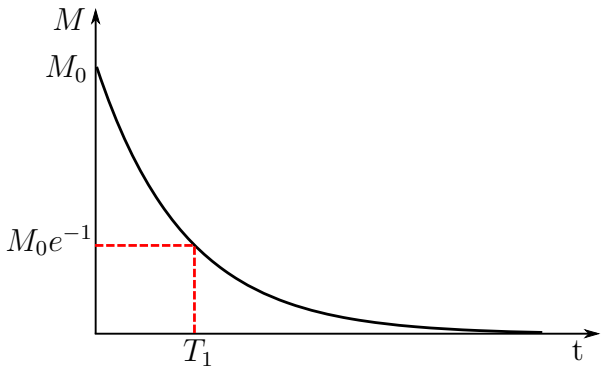

Figure 3.3: Diagram showing relaxation of longitudinal magnetisation.

$$K = \frac{3\mu_0}{160\pi^2}\frac{\hbar^2\gamma^4}{r^6}. \tag{3.13}$$

τ_c is the correlation time of the molecular tumbling motion, and r is the interproton distance in a water molecule. The variation of r with temperature is negligible, and a typical value of r is 2.95×10^{-10} m. K is a collective term for the factors that are independent of temperature and frequency.

For water, τ_c is 5×10^{-12} s, γ is 267.51×10^6 rad s^{-1} Hz^{-1} at 20 °C. Substituting these values into Equation 3.12 and 3.13, gives a T_1 value of 3.9 s for pure water at low field, where $\omega\tau_c \ll 1$.

We therefore expect to be able to detect decaying magnetic fields from pre-polarised magnetisation in a water sample placed in the MEG scanner, and to be able to measure T_1 values [64].

3.2.4 Magnetisation due to Susceptibility Effects

Magnetisation induced by exposing a material of non-zero magnetic susceptibility to a magnetic field can also be detected using a MEG system

Equation 3.14 describes the magnetic moment, m, produced by a sample of volume, v, and susceptibility, χ, exposed to a magnetic field, B_0.

$$m = Mv$$

$$m = \chi \frac{B_0}{\mu_0} v, \tag{3.14}$$

where M is the volume magnetisation. Assuming a magnetic field of 5 µT can be generated inside the MEG, then the magnetic moment induced due to the magnetic susceptibility of a $10\,\mathrm{cm}^3$ water sample of susceptibility -9.035 ppm is

$$\begin{aligned} m &= \chi \frac{B_0}{\mu_0} v \\ m_{water} &= -9.035 \times 10^{-6} \frac{5 \times 10^{-6}}{4\pi \times 10^{-7}} (10 \times 10^{-6}) \\ m_{water} &= -3.59 \times 10^{-10}\,\mathrm{A\,m}^2 \end{aligned} \tag{3.15}$$

Substituting this value into Equation 3.9 with $|\mathbf{x}| = 5\,\mathrm{cm}$,

$$\begin{aligned} B &= \frac{\mu_0}{2\pi} \frac{m}{x^3} \\ B_{water} &= \frac{4\pi \times 10^{-7}}{2\pi} \frac{-3.59 \times 10^{-10}}{(0.05)^3} \\ B_{water} &= 0.57\,\mathrm{pT}. \end{aligned} \tag{3.16}$$

This value can be increased by using a material that has a larger magnetic susceptibility than water. For example, manganese sulphate has a volume magnetic susceptibility of 3.4×10^{-3}. Substituting this into Equation 3.14, the magnetic moment of a $10\,\mathrm{cm}^3$ volume becomes

$$
\begin{aligned}
m &= \chi \frac{B_0}{\mu_0} v \\
m_{MnSO_4} &= 3.4 \times 10^{-3} \frac{5 \times 10^{-6}}{4\pi \times 10^{-7}} 10 \times 10^{-6} \\
&= 1.35 \times 10^{-7}\,\mathrm{A\,m^2}
\end{aligned} \tag{3.17}
$$

and thus, the magnetic field along the dipole axis, at a distance of 5 cm is

$$
\begin{aligned}
B &= \frac{\mu_0\, m}{2\pi\, x^3} \\
B_{MnSO_4} &= \frac{(4\pi \times 10^{-7})(1.35 \times 10^{-7})}{2\pi (0.05)^3} \\
B_{MnSO_4} &= 216\,\mathrm{pT}.
\end{aligned} \tag{3.18}
$$

The susceptibility effect from manganese sulphate is approximately 380 times larger than that from water. We can use this effect to test the feasibility of detecting weak fields due to the magnetic susceptibility of a sample placed in the MEG scanner in the presence of a small applied field, and we can also use it to measure the amplitude of the applied field.

3.3 Method

The experimental setup used for the experiments described in this chapter is detailed in Figure 3.1, and comprised of a SQUID array, a polarising magnet, an imaging magnet, and a sample holder placed inside the SQUID array.

The SQUID array used here is part of a 275-channel MEG system (MEG Inter-

national Services Limited (MISL), Coquitlam, BC, Canada). The system is fitted with axial gradiometers with 5 cm baselines, fitted around a helmet, and also comprises 29 sensors in a reference array, located distal to the head. Each sensor is incorporated into a superconducting circuit, which is magnetically coupled to a SQUID detector, yielding an average noise level of $10\,\mathrm{fT/Hz^{1/2}}$. The effect of external interference is greatly reduced by using the signals from the reference array to form synthetic third order gradiometers.

The SQUIDs are bathed in liquid helium, and the system is housed in a magnetically shielded room, pictured in Figure 3.2, made of layers of aluminium, and mu-metal. Pure aluminium shields high frequency noise by eddy current shielding. High permeability mu-metal shields low frequency magnetic fields from inside the room.

3.3.1 Sample Holder

For reproducibility, and in order to locate more accurately the sample, we securely fitted a moulded fibreglass sample holder with five cylindrical 40 mm diameter plastic inserts (Figures 3.4 and 3.5) inside the MEG helmet. This allowed reproducible placement of plastic bottles of diameter 40 mm, length 60 mm, and capacity 78 ml. For placement of smaller capsules, we used additional plastic inserts of capacity 14.0 ml.

In order to co-register images from MEG and MRI, we require a mapping of the same points in the two image datasets [65]. The MEG system records the location of the three fiducial coils inside the helmet, but the location of these coils relative to the MRI image is not initially known. Three fiducial coils (Figure 3.6) were fixed to the sample holder at predetermined positions, corresponding to the usual locations of the left and right preaurical points and the nasion (Figure 3.7), to allow the helmet's position to be measured relative to the detector array, for

Figure 3.4: Picture of the custom-built helmet showing the location of five sample holders.

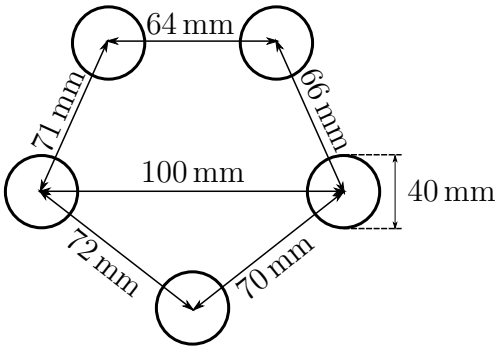

Figure 3.5: Schematic showing distance between plastic holder centres inside the helmet.

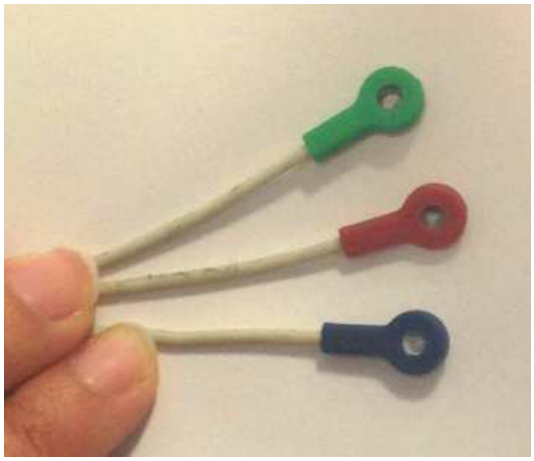

Figure 3.6: Picture of the localisation coils.

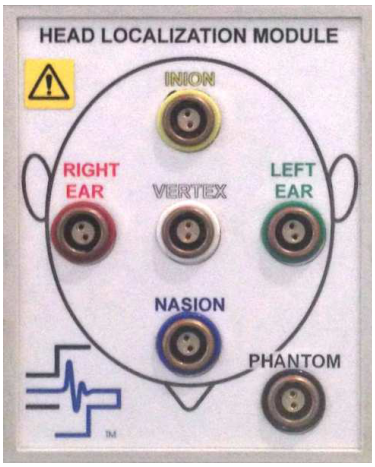

Figure 3.7: Picture of the localisation module indicating positioning of localisation coils.

subsequent co-registration of magnetisation images with MRI data [66]. These coils were periodically energised during data collection to allow determination of their Cartesian coordinates.

Before scanning the helmet in the MRI magnet, the fiducials were replaced by vitamin E capsules. Such capsules are often used as markers in MRI [67]. This allowed for the points at which the fiducials are positioned, to be located also

on the MR image, and thus the geometry of the MEG system and of the sample holder could be coregisted, allowing for the direct overlay of the images generated via the SQUID array with the MRI data.

3.3.2 Polarising Magnet

The polarising magnet used for pre-polarisation of aqueous samples was a 0.2 T C-shaped permanent magnet. This magnet, shown in Figure 3.8, had a 40 mm gap and 50 mm diameter pole pieces. We kept the polarising magnet outside the MSR housing the MEG system.

Figure 3.8: Picture of the polarising magnet.

3.3.3 Imaging Field

The imaging magnet, which was a 0.5 T cylindrical permanent magnet, of diameter 65 mm and height 70 mm, was located inside the MSR. We positioned this magnet on-axis to the scanner, at an axial distance of 2 m from the sample holder. At this distance, the magnetic field from the imaging magnet can be well approximated as that from a magnetic dipole of magnetic moment 215 A m^2. The magnetic fields have a magnitude between 2.58 ± 0.04 µT and 5.22 ± 0.07 µT, over the sample region when the magnet is aligned with the z-axis.

The magnet could be freely rotated through 360° in the y-z plane, so as to change the magnitude and orientation of the imaging field at the sample.

To check for the imaging magnet's strength, we used a gaussmeter to measure the spatial variation of the magnetic field produced by the imaging magnet. We measured the magnetic field at distances up to 10 cm away from the poles, at points that lie along orthogonal diameters parallel to the magnet's surface. We repeated the measurements with the orientation of the Hall probe rotated by 180°, and took half the difference with the original measurements to remove the effect of any zero offset.

Figure 3.9 and 3.10 show the mean magnetic field measured away from the positive pole of the imaging magnet, along two orthogonal directions. Similarly, Figures 3.11 and 3.12 show measurements for the negative pole of the magnet.

Figures 3.13 for the positive pole, and 3.14 for the negative pole, show the difference in the magnetic fields measured in the two orthogonal directions. Figures 3.15 and 3.16 show the difference in the magnetic fields measured between the two poles, along two orthogonal directions.

These measurements indicate that the magnetic field from the positive pole of the magnet is similar in magnitude to that from the negative pole of the magnet.

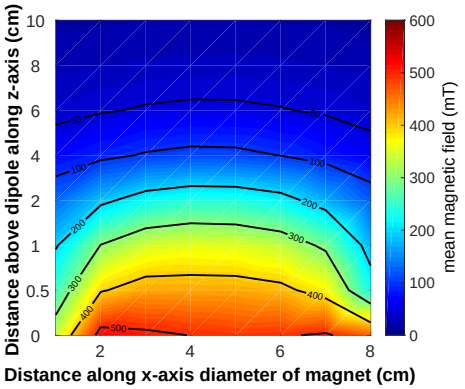

Figure 3.9: Mean magnetic field from +ve pole of imaging magnet, measured along x-axis.

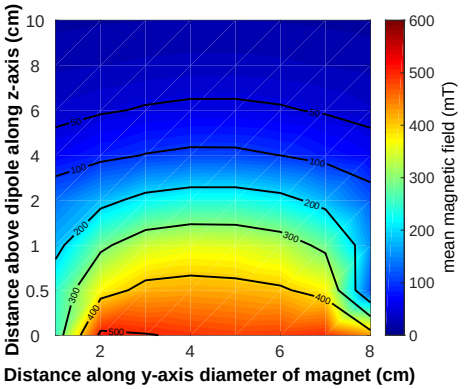

Figure 3.10: Mean magnetic field from +ve pole of imaging magnet, measured along y-axis.

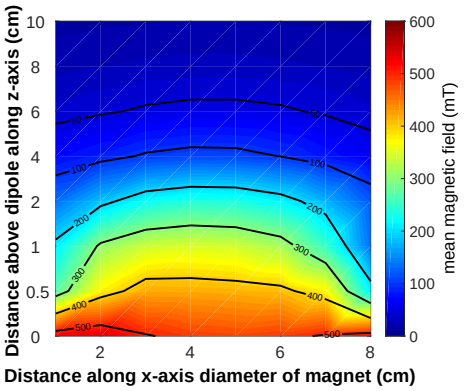

Figure 3.11: Mean magnetic field from -ve pole of imaging magnet, measured along x-axis.

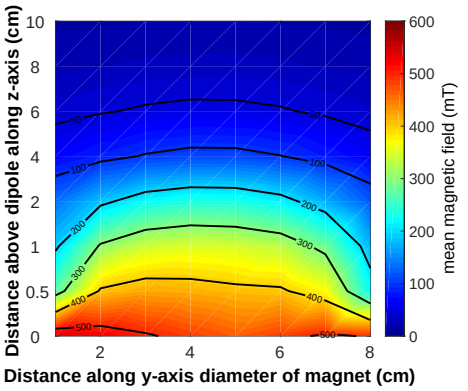

Figure 3.12: Mean magnetic field from -ve pole of imaging magnet, measured along y-axis.

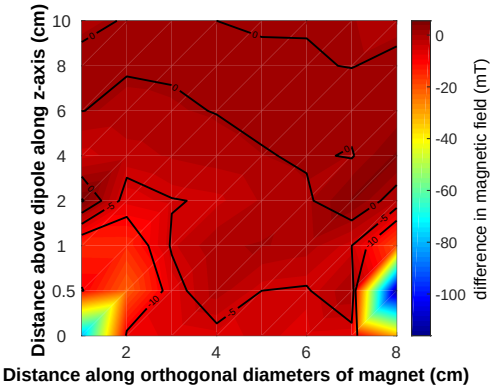

Figure 3.13: Difference in the magnetic fields measured in the two orthogonal directions, from +ve pole of imaging magnet.

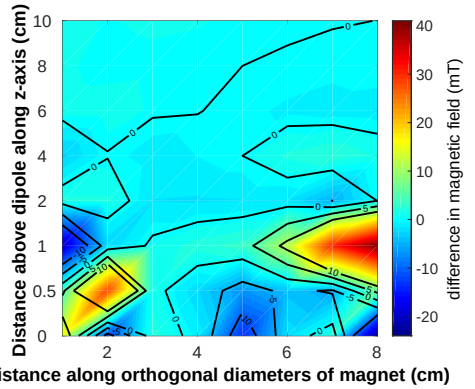

Figure 3.14: Difference in the magnetic fields measured in the two orthogonal directions, from -ve pole of imaging magnet.

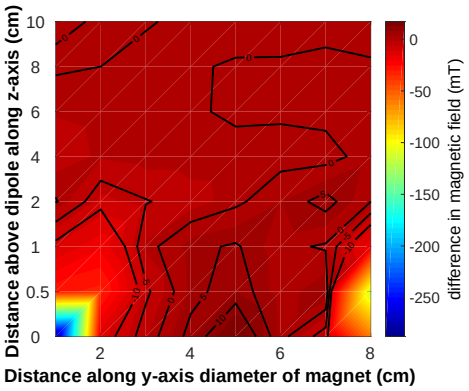

Figure 3.15: Difference in the magnetic fields measured for the two poles, along the y-axis diameter of the imaging magnet.

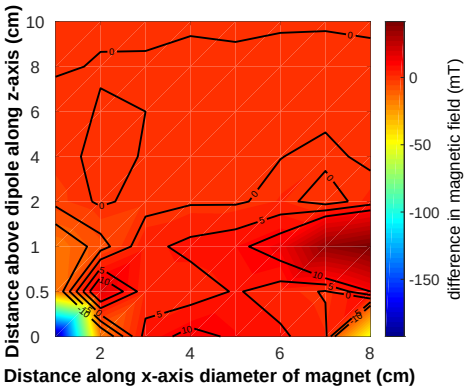

Figure 3.16: Difference in the magnetic fields measured for the two poles, along the x-axis diameter of the imaging magnet.

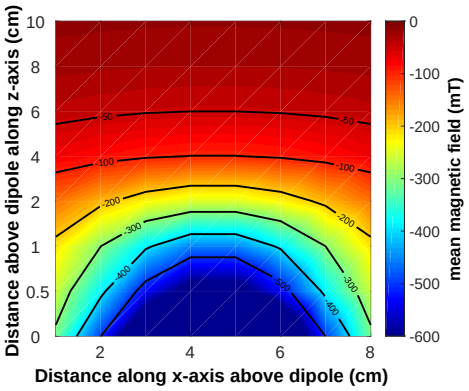

Figure 3.17: Simulation of the magnetic field from a magnetic dipole, along x-axis.

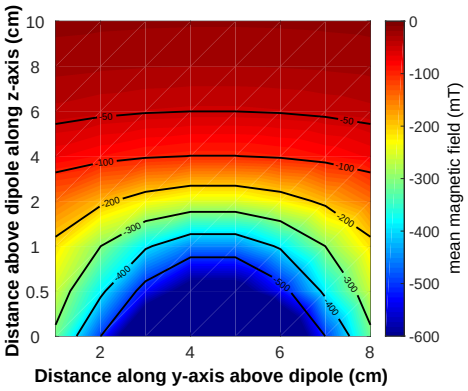

Figure 3.18: Simulation of the magnetic field from a magnetic dipole, along y-axis.

Moreover, the magnetic fields along the x-axes diameters of the magnet are also similar to the fields along the y-axes diameters.

Also, comparing Figures 3.9 and 3.10 to the magnetic field expected from the positive pole of the dipole along two orthogonal directions in Figures 3.17 and 3.18 respectively, indicates that the measured magnetic field is similar to that expected from a magnetic dipole at distances of a few centimetres from the magnet's surface.

3.3.4 Data Collection

The SQUID array used is part of a 275 channel MEG system (MEG International Services Limited (MISL), Coquitlam, BC, Canada). The system is fitted with axial gradiometers with a 5 cm baseline, fitted around a helmet, and also includes 29 sensors in a reference array, located distal to the head. Each axial gradiometer is incorporated into a superconducting circuit, which is magnetically coupled to a SQUID detector, yielding an average noise level of $10\,\mathrm{fT/Hz^{1/2}}$.

We ran these experiments with the MEG gantry in the supine position. The gantry was lowered at least twenty minutes prior to running the experiment, to allow enough time for the liquid helium to settle in position. Otherwise, the recorded signals might drift.

The sampling rate of the outputs of the field sensors was 600 Hz throughout data collection.

3.3.5 Data Filtering

Following data collection, we used the `Data Editor` program [68] provided on the *MISL* system to filter and display the data from all separate channels, preview the data to check for problems on any channels, and to plot field maps. Before analysing the recorded data, we applied the filters shown in the screenshot in Figure 3.19.

We used a 50 Hz notch filter of width 2 Hz to eliminate interference occuring at the mains frequency.

Since we ran these experiments with the door to the MSR open, the low fre-

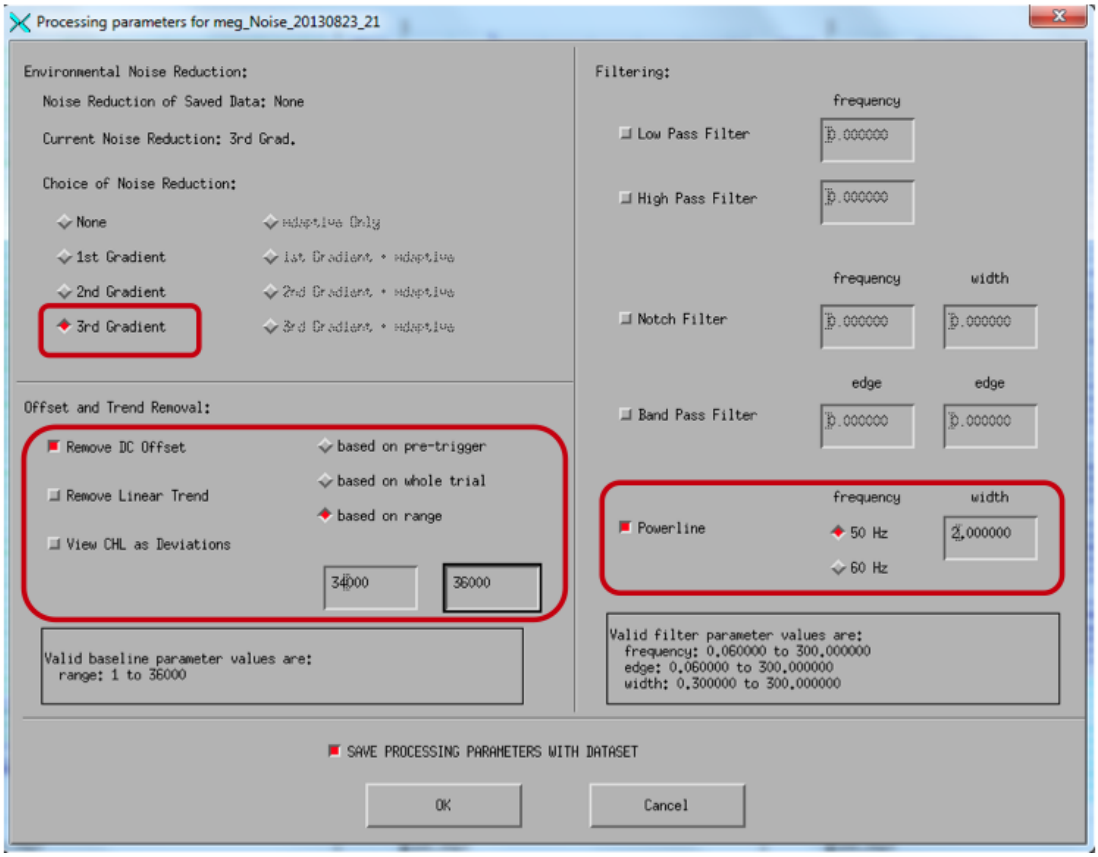

Figure 3.19: Screenshot showing the data filtering applied.

quency noise resulting from magnetic fields generated outside the sensor array, is comparable to the fields we expect to be able to measure from decaying nuclear magnetisation or susceptibility effects. In MEG, it is not the magnetic field that is generally measured, but rather, the magnetic field gradient between the reference sensors and the main sensors. Thus, we used the MEG system in the third order synthetic gradiometer configuration significantly to reduce the time-varying external magnetic interference [35].

We also used a DC offset based on the data acquired during the last 3 s of the recording. We did this to remove the susceptibility effect from the whole signal, to end up with the nuclear magnetisation decay. The susceptibility effect is present throughout the time that the sample is inside the MEG. We used the last few seconds, rather than the first few seconds as baseline because there is more instability during the first few seconds of the recording whilst the sample is being prepared to enter the MEG. Since we inserted the sample inside the MEG a few seconds after the start of the recording, then after using the last seconds of the recording as a baseline, the first seconds represent the opposite effect of the susceptibility, i.e. the negative of the field due to susceptibility effects.

After filtering, we transferred the data to `MATLAB` for data processing.

3.3.6 Measurement of Field Shifts due to Magnetic Susceptibility

The magnetisation recorded from a pre-polarised sample inserted in the MEG, is a combination of the susceptibility effect from exposure of the sample to the imaging field, and the nuclear magnetisation of the sample following its polarisation. Figure 3.20 illustrates this.

The susceptibility effect remains constant after the sample is introduced in the

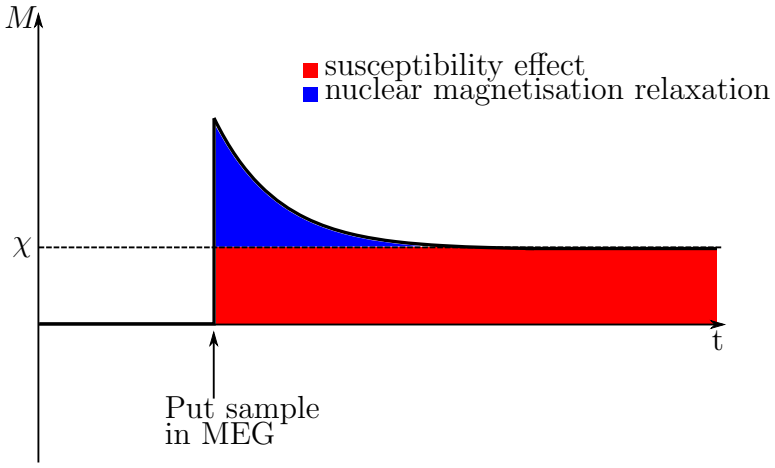

Figure 3.20: Diagram showing superposition of susceptibility effect and magnetisation relaxation.

sample holder. The nuclear magnetisation starts to decay as soon as the sample is removed from the polarising magnet. The recorded magnetisation is a superposition of these two effects. The expected graph would look similar to the one in Figure 3.21.

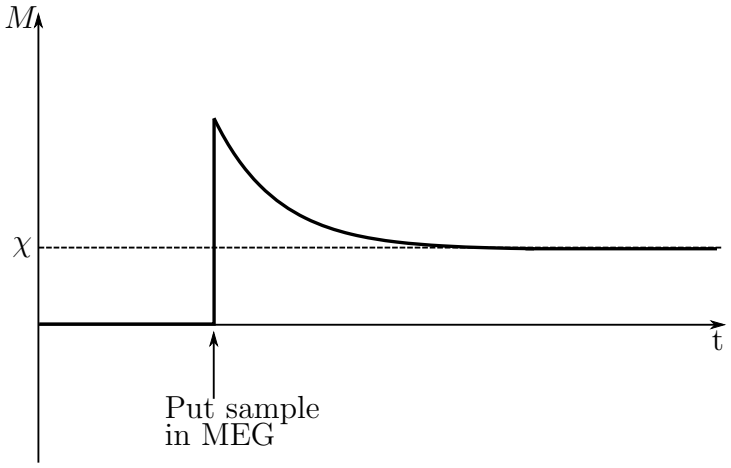

Figure 3.21: Diagram showing graph outline of superimposed positive susceptibility effect and magnetisation relaxation.

If the data from the last few seconds of the signal is taken as a baseline, then we expect to obtain the graph in Figure 3.22. However, the susceptibility, χ, can be negative. Figure 3.23 is a block diagram displaying the expected signal in this case. The signal shape will appear similar to the one in Figure 3.24.

When the last part of the signal is used as a baseline, a graph similar to the one in Figure 3.25 is expected.

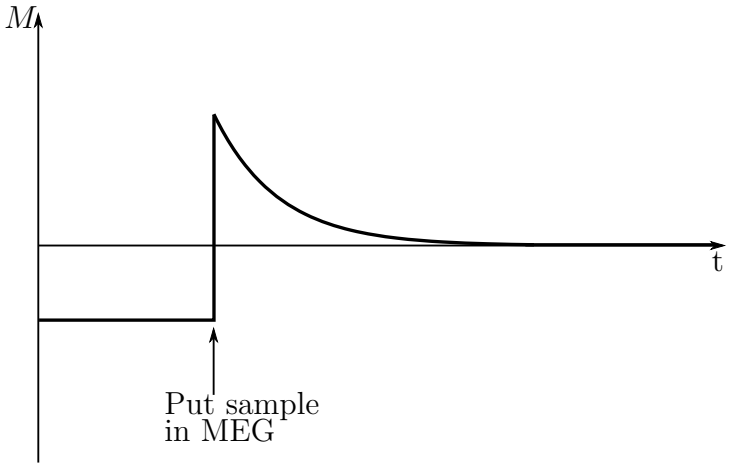

Figure 3.22: Diagram showing effects of positive susceptibility and nuclear magnetisation relaxation, using the last few seconds of the recorded data as a baseline.

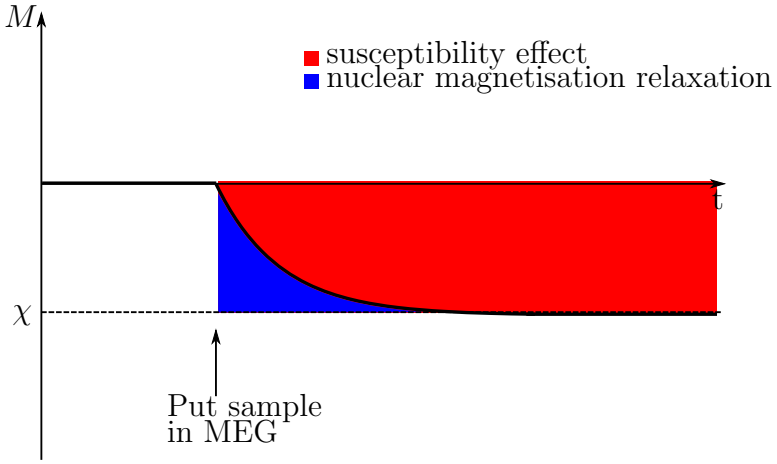

Figure 3.23: Diagram showing effects of negative susceptibility and nuclear magnetisation relaxation.

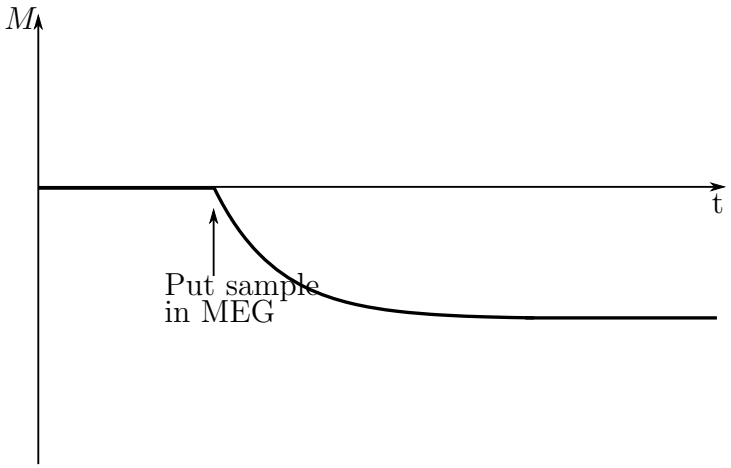

Figure 3.24: Diagram showing graph outline of superimposed negative susceptibility effect and nuclear magnetisation relaxation.

The closer the imaging magnet is positioned to the SQUID array, the larger is the signal that we would expect to record as a result of susceptibility effects.

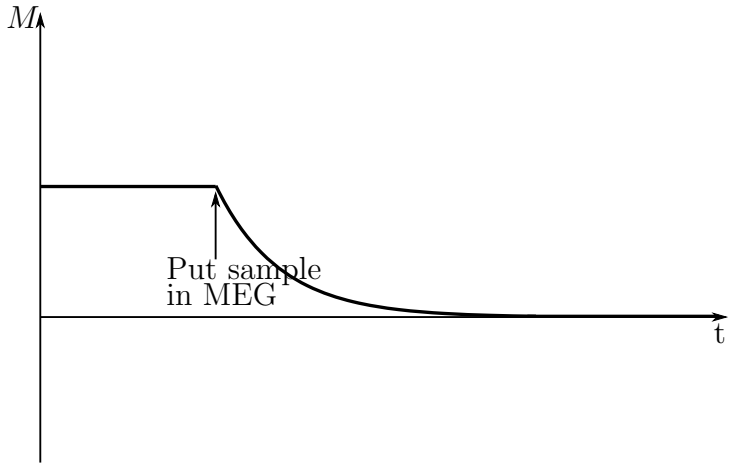

Figure 3.25: Diagram showing effects of negative susceptibility and nuclear magnetisation relaxation, using the last few seconds of the recorded data as a baseline.

However, there is a limit to how close the imaging magnet can be brought to the SQUID array. If the magnet is too close to the SQUID array, the SQUIDs can trap flux. On the other hand, the farther away that the imaging magnet is from the SQUIDs, the less dominant over the earth's magnetic field its effect will be.

In order to test that the imaging field was dominating the earth's magnetic field, we used a sample of Manganese (II) sulphate monohydrate ($MnSO_4.H_2O$) with a volume magnetic susceptibility of 3.414×10^{-3}. We inserted a small capsule containing 9.67 g of powdered Manganese (II) sulphate monohydrate in one of the five slots in the sample holder.

The MEG system was set to record field measurements over a time window $0\,\mathrm{s} < t < 60\,\mathrm{s}$. At $t \sim 20\,\mathrm{s}$, the scanner operator manually took the sample into the MSR, quickly inserted the sample into the sample holder, and immediately exited the MSR. The time lapse between useful measurements being obtained after the scanner operator had exited the MSR, was typically 5 s. We recorded the magnetic field for four different angles of the imaging magnet relative to the line joining the magnet and helmet (0°, 90°, 180° and 270°).

To estimate the field change due to the sample susceptibility, we subtracted the mean of the magnetic field strength measured in the last 2000 samples, $56.66\,\mathrm{s} <$

$t < 60\,\text{s}$, from the mean of the magnetic field strength measured in the first 2000 samples, $0\,\text{s} < t < 3.33\,\text{s}$, for each channel. We only used these sections of the data to avoid the transient field disturbances caused by the scanner operator entering and exiting the MSR.

We repeated this experiment, for samples located at different positions in the helmet, using the specially constructed sample holder.

We then applied the Minimum Norm Estimate (MNE) to the filtered data, and applied a mask that blocks out all the target volume except for the space occupied by the helmet. We ran sample reconstruction on the data, using the lead-field normalised, minimum norm spatial filter, described earlier in Figure 2.17, and an MR image of the sample holder with five bottles of water inside (Figure 3.27), for co-registration of the two images. We obtained the MR image with a Philips 3T Achieva MRI system, running a fast gradient echo sequence.

The flowchart in Figure 3.26 shows how the images were generated.

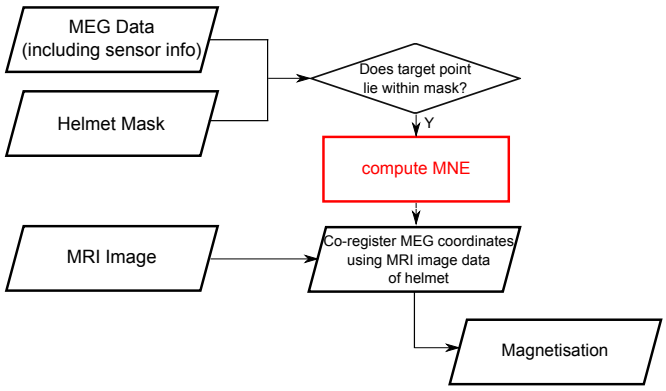

Figure 3.26: Flowchart showing how the MNE-reconstructed images were generated.

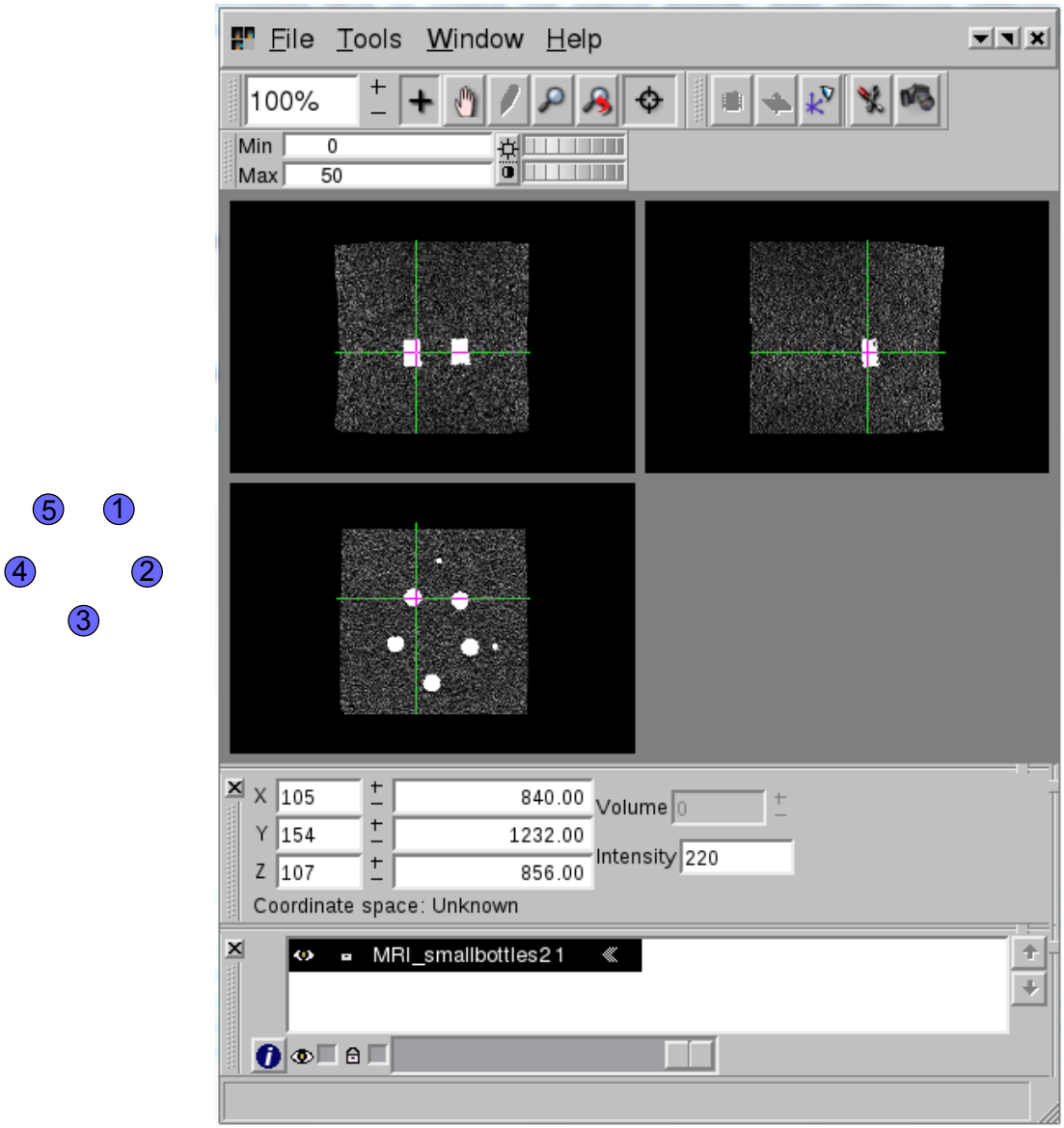

Figure 3.27: MR image showing the locations of the sample inserts.

3.3.7 Measurement of Field Shifts due to Nuclear Magnetisation Relaxation (NMR)

The scope of this experiment was to detect and image the decaying longitudinal nuclear magnetisation from pre-polarised samples of distilled water, in 78 ml plastic bottles. We filled the bottles to the brim so that the water did not move irregularly upon inserting the bottle in the sample holder. We polarised the samples by positioning them in between the poles of the polarising magnet for 180 s

at 0.2 T, and then immediately transferring the bottles to the sample holder in the MSR.

We recorded the magnetic field from 20 s prior to the insertion of the sample into the sample holder, and for a subsequent 40 s. The transit time during which we entered the MSR to position the sample, was typically 5 s, and this data segment was not considered in the data analysis.

We then subtracted the mean field measurement in the last 10 s of the recording, from each channel, and this provided us with a direct measurement of the decay of induced nuclear magnetisation.

Since the polarising field in the C-magnet is more than 10000 times larger than the imaging field at the sample, the decaying magnetisation at location $\mathbf{r}$ is described by

$$\mathbf{M}(\mathbf{r}, t_m) = \mathbf{M_0}(\mathbf{r}) e^{-t_m/T_1(\mathbf{r})}, \tag{3.19}$$

where t_m is the measurement time from when the polarisation field is removed, $\mathbf{M_0}(\mathbf{r})$ is the magnetisation at $t_m = 0$, and whose orientation depends on the direction of the imaging field at $\mathbf{r}$, and whose magnitude depends on the strength of the polarising field that was used, the number of hydrogen nuclei per unit volume at $\mathbf{r}$, and the amount of magnetisation decay occurring during the transit from the polarising magnet into the sample holder. T_1 is the longitudinal relaxation time constant.

$\mathbf{M_0}(\mathbf{r})$ depends on the polarising field strength, the spin density, the sample temperature, and the proton gyromagnetic ratio. T_1 depends on the imaging field strength, and on the chemical environment of the sample.

After filtering the data, we fitted exponential plots of the form

$$y = Ae^{-Bt} + C \tag{3.20}$$

to the relaxation curves, where A, B and C are unknown parameters to be found, and the inverse of B gives an estimation of T_1.

3.3.8 Measurement of T_1 Variation with Gadoteridol

The aim of this experiment was to measure variations in T_1 of different samples. To this end, we used 78 ml bottles filled with different concentrations (0 - 40 µmol) of Gadoteridol. Gadoteridol is a gadolinium-based contrast agent, typically used in MRI.

We placed the bottles, one at a time, between the poles of the polarising magnet for 180 s to polarise the hydrogen nuclei in the sample. After this, the scanner operator transferred the bottle from the polarising magnet straight into the sample holder, and immediately left the MSR.

Magnetic fields were recorded for 60 s, and the sample was inserted into the sample holder at $t \sim 20$ s. The time lapse between the sample being removed from the polarising magnet, and useful measurements being obtained after the scanner operator had exited the MSR, was typically 5 s.

The mean of the magnetic fields recorded during $56.66<t<60$ s was subtracted from the mean of the magnetic fields recorded during $0<t<3.33$ s to eliminate any fields due to the susceptibility of the sample and any other external sources of constant interference. This left us with the fields produced by the decaying nuclear magnetisation.

3.4 Results

3.4.1 Measurement of Field Shifts due to Magnetic Susceptibility

Figure 3.28 shows the results of measuring magnetic field shifts induced by a change in magnetic susceptibility at the sample holder, with the imaging magnet oriented at 0° in the z-direction. The separate rows show results from 9.67 g of powdered Manganese sulphate, inserted in each of the five locations of the sample holder.

The first column shows the location of the sample within the sample holder. The second column shows the reconstructed image superimposed on a greyscale image of a single slice MR image of the sample holder with all five sample locations filled.

The reconstructed images are thresholded at the maximum intensity returned from the MNE calculation, and the minimum threshold is 66% of this value, with the exception of the third figure, which was thresholded at a minimum of 50% of the maximum intensity. The third column shows the magnetic field gradient topography measured at the MEG sensors.

The mean strength of the MNE-reconstructed magnetic dipole source moment was $97 \pm 87\,\mathrm{nA\,m^2}$, with values ranging from $55\,\mathrm{nA\,m^2}$ to $164\,\mathrm{nA\,m^2}$. For all five trials, the source was well-located.

Using Equation 3.14, for a known susceptibility of 3.414×10^{-3} ppm, a sample volume of $3\,\mathrm{cm^3}$, and an imaging field of approximately $5\,\mu\mathrm{T}$ over the sample region when the magnet is aligned with the z-axis, the expected strength of the MNE-reconstructed magnetic dipole source is

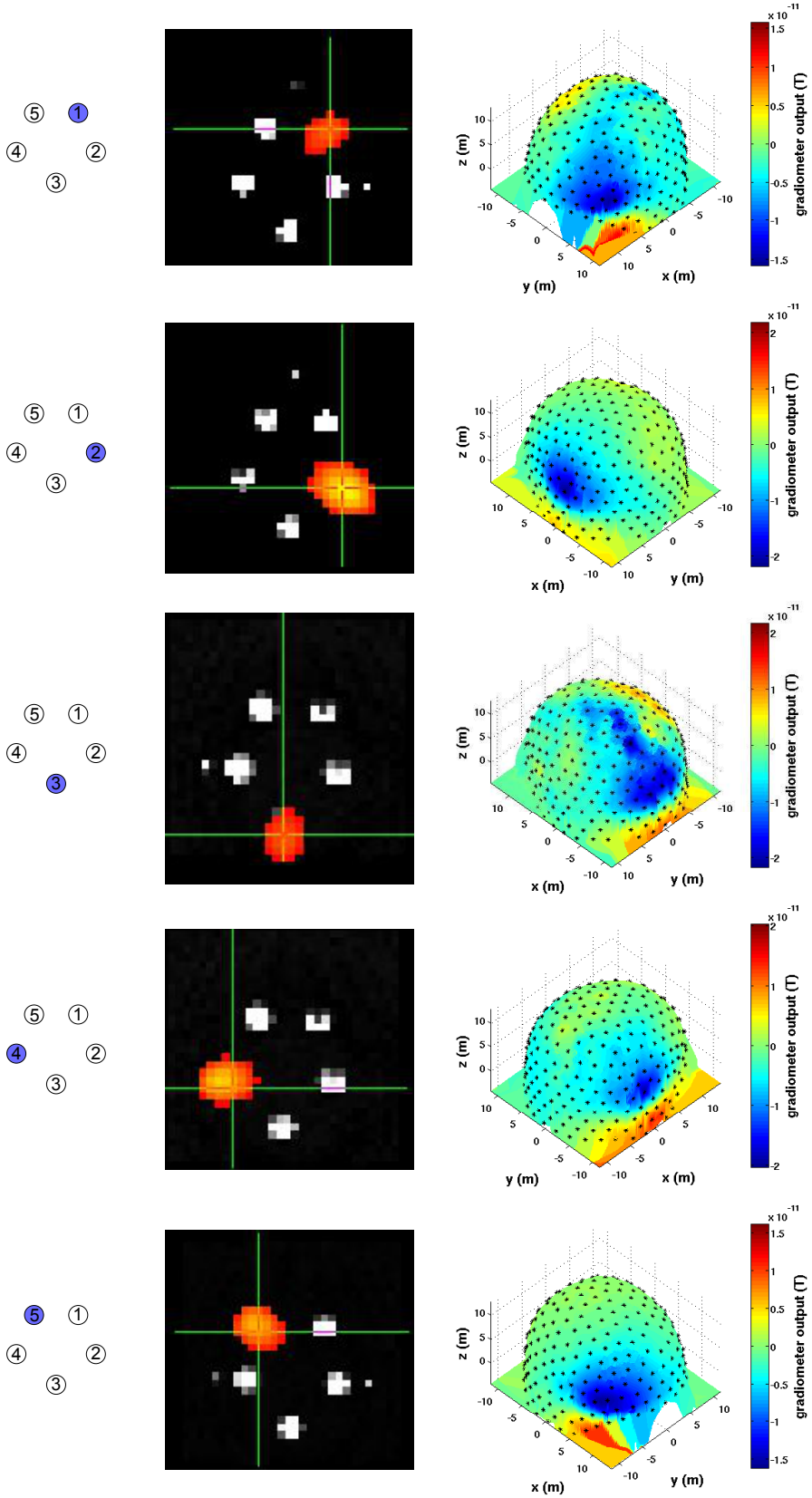

Figure 3.28: Plots showing the results of measurements on samples of manganese sulphate, with the imaging magnet oriented at 0° to the z-axis. The left column shows the location of the sample in the sample holder; the central column shows the magnetic inverse image overlaid onto the structural (MR) image, and the right column shows the measured field shift at the MEG sensors.

$$
\begin{aligned}
m &= \chi \frac{B_0}{\mu_0} v \\
m &\approx 3.414 \times 10^{-3} \frac{5 \times 10^{-6}}{4\pi \times 10^{-7}} (3 \times 10^{-6}) \\
m &\approx 40.8\,\mathrm{nA\,m^2}, \qquad (3.21)
\end{aligned}
$$

which is of a similar order of magnitude to the values found experimentally.

3.4.2 Measurement of Field Shifts due to Nuclear Magnetisation Relaxation (NMR)

Figure 3.29 shows images generated from measurements of the magnetic fields produced by decaying nuclear magnetisation in a 78 ml pre-polarised water sample. The sample was magnetised for 180 s, and immediately transferred to the sample holder inside the MEG. The scan time was 60 s and the sample was transferred from the polarising magnet, to the MEG, 20 s from the start of the recording. The transit time was typically 5 s.

In these plots, we show the signal decay occurring over 15 s starting 1.5 s after the sample was inserted in the sample holder. 1.5 s was chosen because after this time, the transit noise is negligible.

The first column shows the location of the sample within the sample holder. The second column shows the reconstructed image superimposed on a greyscale image of a single slice of the MR image of the sample holder, with all five sample locations filled. The third column shows the magnetic field gradient topography measured at the MEG sensors.

Results in each of the four rows correspond to the results obtained for when the

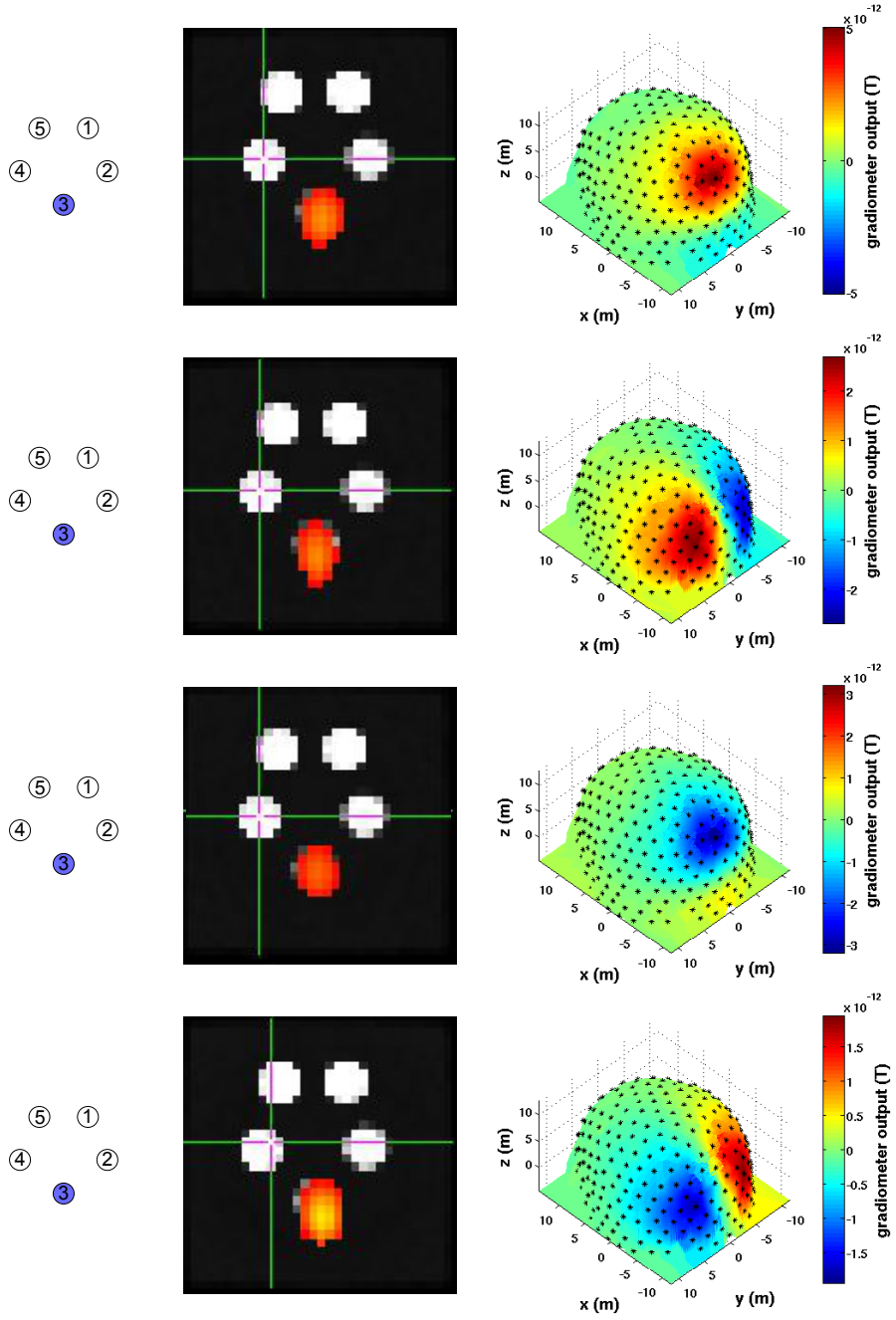

Figure 3.29: Plots showing the results obtained for samples of pre-polarised water samples, with the imaging magnet oriented at 0°, 90°, 180°, and 270°, to the z-axis. The left column shows the location of the sample in the sample holder; the central column shows the magnetic inverse image overlaid onto the structural (MR) image, and the right column shows the measured field shift at the MEG sensors.

imaging magnet was oriented at 0°, 90°, 180°, and 270° respectively, to the z-axis. In the plots of the measured field decay, shown in the third column, the measured field pattern is consistent with the orientation of the imaging magnet, i.e. along the z-axis at 0°, along the negative z-axis at 180°, and so on. The thresholded

magnetic inverse images indicate that the sample was properly located for all four tested imaging magnet orientations.

We repeated this experiment with the bottle placed in the four other helmet locations. The results are shown in Figure 3.30. The schematics in the first column indicate the location of the sample within the sample holder. The next four columns show the inverse images produced, with the imaging magnet oriented at 0°, 90°, 180° and 270° respectively.

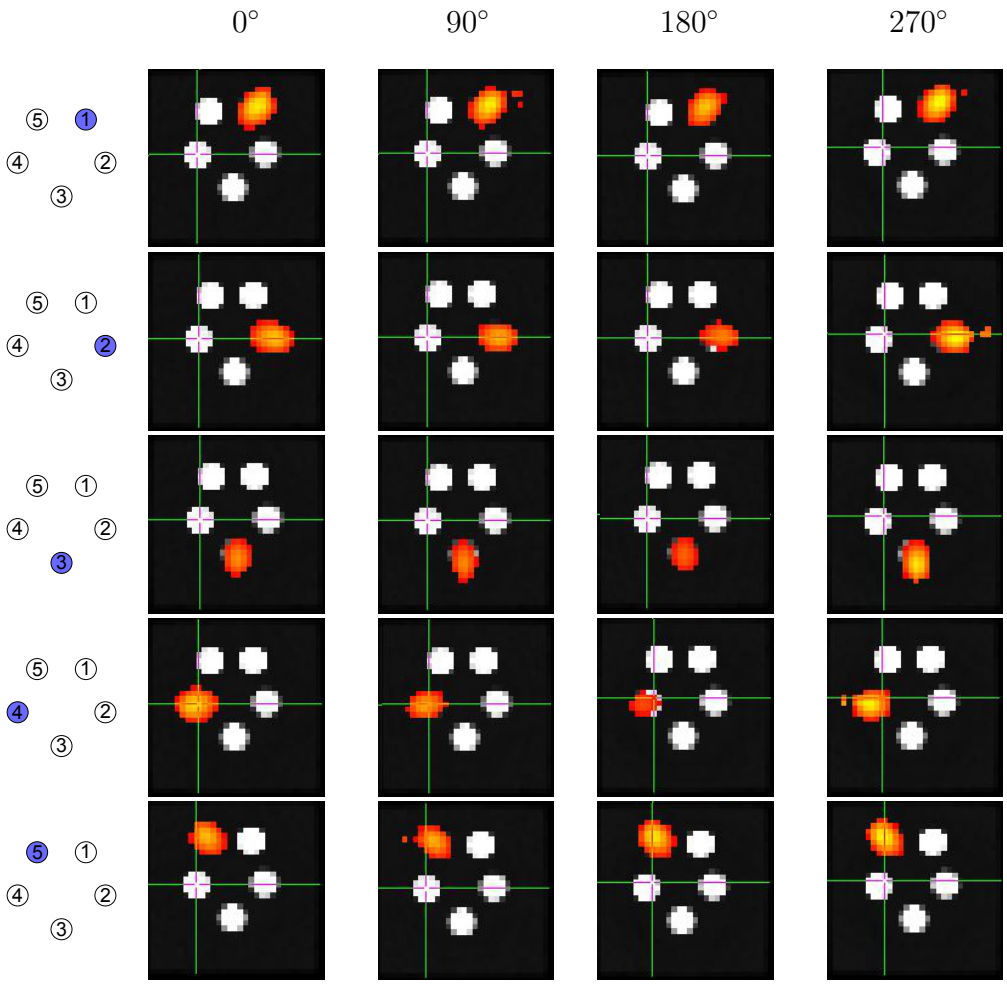

Figure 3.30: Plots showing the inverse images of nuclear magnetisation overlaid onto axial slices of the structural MR image. Each column of inverse images corresponds to a particular orientation of the imaging magnet (0°, 90°, 180° and 270° to the x-axis) in the x-y plane.

For the inverse image, the FSL threshold was set to between 50% and 100% of the maximum intensity of each image. As can be seen, all samples were located properly.

Figure 3.31 shows how the calculated MNE magnetic dipole moment strength varies for different orientations of the imaging magnet, and different sample locations. For all of the orientations of the imaging magnet, the largest MNE magnetic dipole strengths were calculated when the samples were located in the bottom insert.

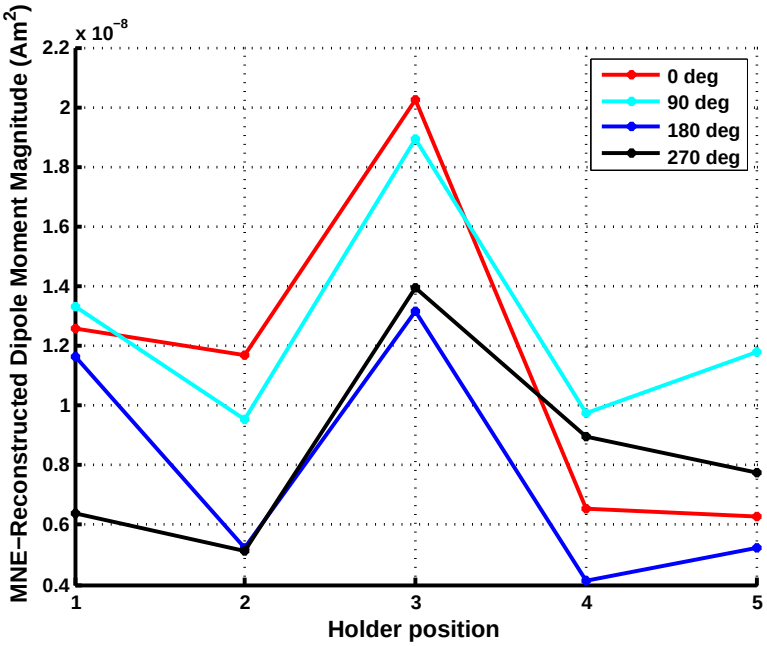

Figure 3.31: Plot showing the MNE calculated dipole moment magnitude for the inverse images of the pre-polarised water samples, located in each of the five helmet inserts, and for the imaging magnet oriented at 0°, 90°, 180° and 270° to the x-axis, in the x-y plane.

Theoretically, the expected MNE-reconstructed dipole moment magnitude can be calculated using Equations 3.4, 3.7, 3.11 and 3.8. Substituting values into Equation 3.9, the magnetisation from polarisation is

$$
\begin{aligned}
M_0 &\sim \frac{N(h\gamma)^2}{16\pi^2 k_B T} B_0 \\
&\sim \frac{(6.67\times10^{28})(6.63\times10^{-34})^2(267.513\times10^{6})^2}{16\pi^2(1.38\times10^{-23})(293)} \quad (0.2) \\
&\sim 6.57\times10^{-4}\,\mathrm{A\,m^{-1}}. \qquad (3.22)
\end{aligned}
$$

While the sample is being transferred, the magnetisation decays. Considering approximately 6.5 s of combined transit time and the time from when the sample is inserted in the sample holder until the transit noise is negligible, the magnetisation decay that occurs during 15 s from the start of the usable data is

$$
\begin{aligned}
M(t) &= M_0 e^{-\frac{t}{T_1}} \\
M &= 6.57\times10^{-4}\left[e^{-\frac{6.5}{2.42}}\right] \\
M &= 4.47\times10^{-5}\,\mathrm{Am^{-1}} \qquad (3.23)
\end{aligned}
$$

In the above equation, a T_1 value of 2.42 s was chosen after determining this value experimentally.

Substituting this magnetisation and volume of the sample into Equation 3.7 gives

$$
\begin{aligned}
m &= Mv \\
&\sim (4.47\times10^{-5})(78\times10^{-6}) \\
&\sim 3.53\times10^{-9}\,\mathrm{A\,m^2}, \qquad (3.24)
\end{aligned}
$$

and thus, using Equation 3.9, the magnetic field detected at the SQUIDS should be of the order

$$\begin{aligned}\mathbf{B} &= \frac{\mu_0}{2\pi}\frac{|\mathbf{m}|}{x^3} \\ &= \frac{(4\pi \times 10^{-7})(3.53 \times 10^{-9})}{(2\pi)(0.05)^3} \\ &= 5.65\,\mathrm{pT}. \end{aligned} \tag{3.25}$$

This is similar to the measured peak field shown in Figure 3.29.

The results in Figure 3.31 indicate that the orientation of the imaging field does not have a significant effect on the MNE reconstructed magnetic dipole strength, as would be expected.

Figure 3.32 shows the time evolution of the magnetic field over 15 s starting from $\sim$ 1.5 s after the sample was placed in the holder. The schematics in the first column of Figure 3.32 indicate the location of the sample within the sample holder. The next four columns show the timecourses of the magnetisation, with the imaging magnet oriented at 0°, 90°, 180° and 270° respectively. The dotted plots are the plots of the real data, and the red plots are curves fit to the data.

For the curve fits above, the mean value of T_1 is 2.42 ± 0.43 s. Using the equation given by Bloemberg, Purcell and Pound, described earlier in Section 3.2.3, the T_1 value is expected to be around 3.92 s. However, in the experimental section of the same paper [62], T_1 for water at 20 °C is 2.3 s, which is close to our calculated T_1 value, possibly due to the presence of some impurities.

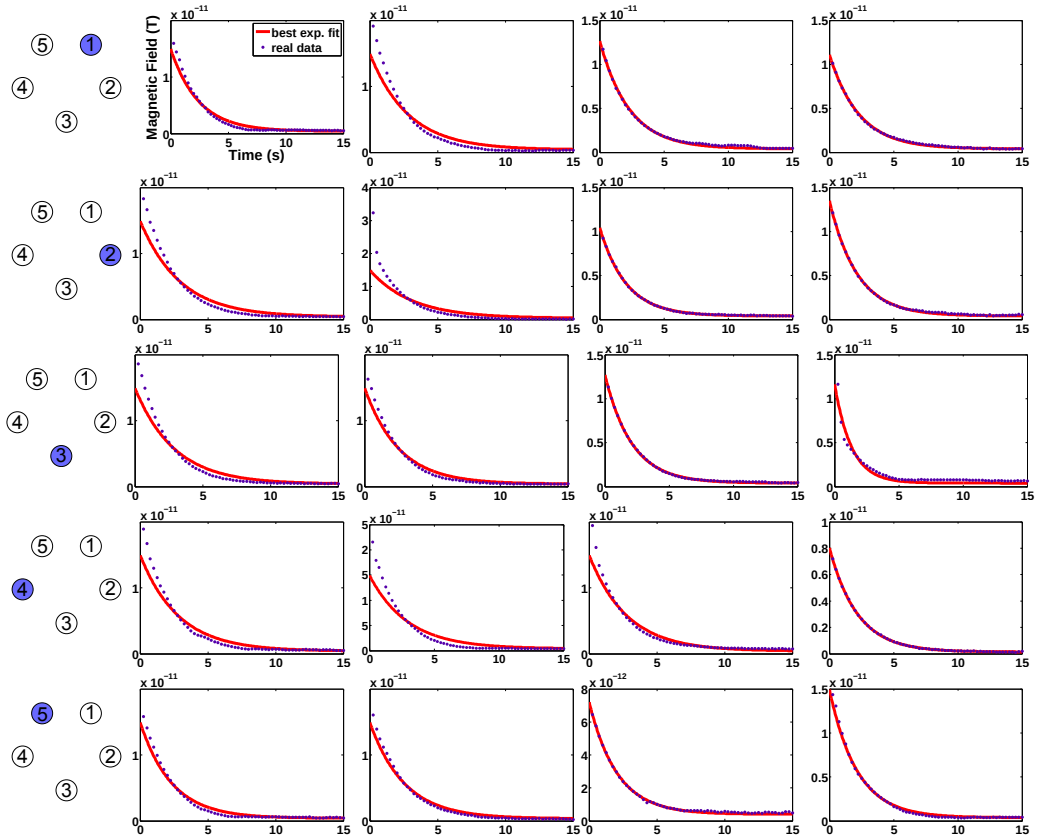

Figure 3.32: Plots showing the time evolution of the measured magnetisation decay. The first column indicates the location within the sample holder at which the sample is located. The following columns show the magnetic decay recorded for different orientations of the imaging magnet (0°, 90°, 180° and 270° to the x-axis) in the x-y plane. The dotted plots are the plots of the real data, and the red plots are exponential curves fit to the data.

3.4.3 Measurement of T_1 Variation with Gadoteridol

Figure 3.33 shows the magnetic field decay in pre-polarised aqueous samples of different Gadoteridol concentrations, varying from 0 µM of Gadoteridol (distilled water) to 20 µM of Gadoteridol.

It can be seen that higher concentrations of Gadoteridol result in a lower starting value of recorded magnetisation (Figure 3.33), and have faster decays (Figure 3.34). The former is attributed to a greater decay in the time spent transferring the sample from the polarising magnet into the sample array. Both observations are indicative of shorter relaxation times.

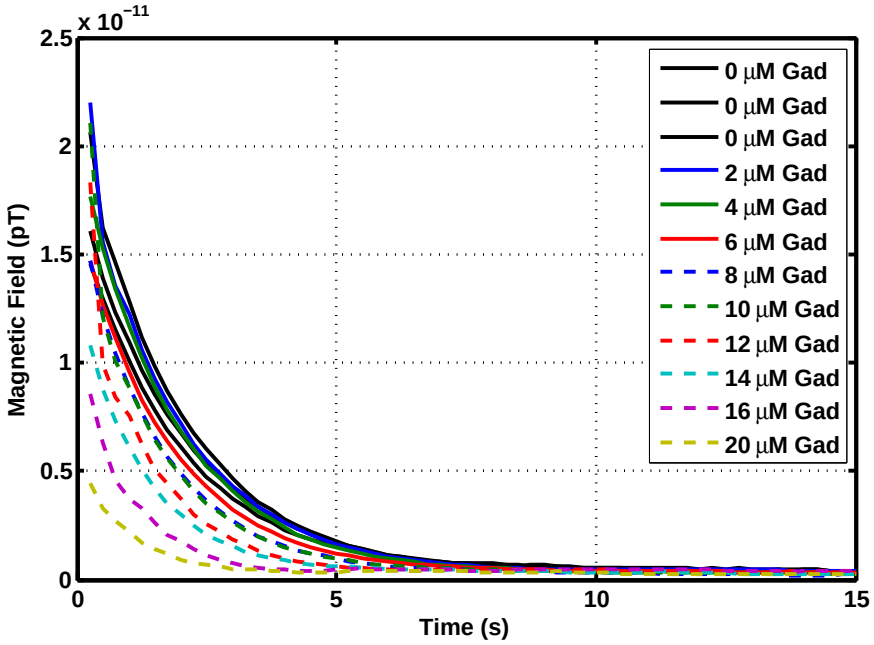

Figure 3.33: Plot of the time evolution of magnetisation relaxation in pre-polarised aqueous samples, doped with varying concentrations of Gadoteridol.

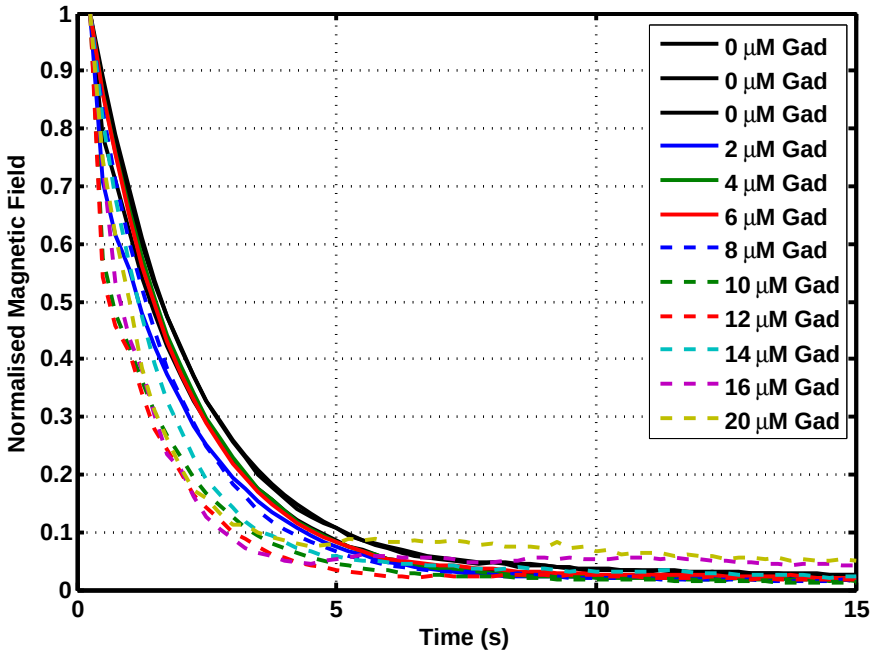

Figure 3.34: Plot of the time evolution of normalised magnetisation relaxation in pre-polarised aqueous samples, doped with varying concentrations of Gadoteridol.

Figure 3.35 shows the fitted T_1 values for the magnetic relaxations corresponding to the different concentrations of Gadoteridol. As can be seen, T_1 values become smaller for higher concentrations of Gadoteridol.

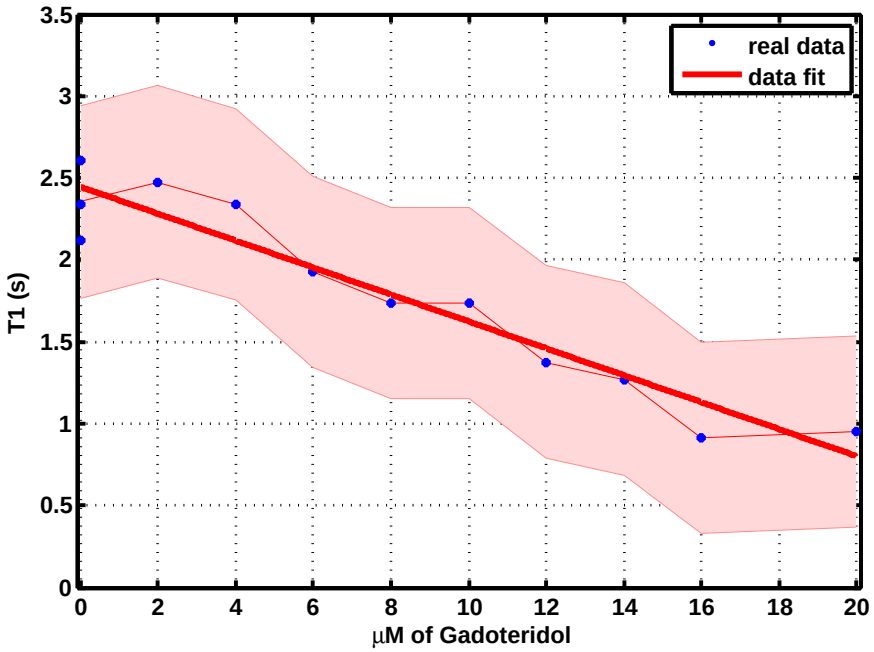

Figure 3.35: Plot of estimated T_1 values of pre-polarised aqueous samples, doped with varying concentrations of Gadoteridol. The pink region indicates the standard deviation of the results.

3.5 Conclusions

In this chapter, we showed that we can reconstruct the location of a magnetic source and its strength from measurements of the pattern of the magnetic field generated. We tested this approach by measuring the fields generated when a sample containing a known amount of manganese sulphate was placed inside the MEG system in the presence of a weak ($\sim 5\,\mu$T) imaging field. For this method, we allowed the reconstructed magnetic dipole to assume any orientation.

In a second set of experiments, we measured the fields generated by decaying nuclear magnetisation in a pre-polarised water sample. For this method, we constrained the MNE reconstructed source magnetisation to be oriented along the direction of the imaging field.

The strength of the magnetisation in the NMR experiment is smaller than the strength of the magnetisation in the magnetic susceptibility experiment. It should be noted that in the NMR experiment, some signal is lost due to T_1 relaxation

during transfer time. The order of magnitude of the MNE-reconstructed magnetic dipole moment in the NMR experiment is up to $20\,\mathrm{nA\,m^2}$, and in the magnetic susceptibility experiment is of the order $100\,\mathrm{nA\,m^2}$.

Applying a dSPM approach to magnetic field shifts originating from a change in magnetic susceptibility, due to the insertion of samples of manganese sulphate, and measured with a 275-channel MEG scanner, yielded reasonable quality images.

The dSPM approach yielded good quality images also for measured nuclear magnetisation decay. The images obtained from the nuclear magnetisation decay were of good quality, irrelevant of the orientation of the imaging magnet.

When looking at how the relaxation time, T_1, changes for varying concentrations of Gadoteridol, we saw that the T_1 values that we obtained were longer than those obtained by Michelak et al with a $0.6\,\mathrm{T}$ polarising field [49]. This is counterintuitive since T_1 values are expected to shorten with smaller polarising fields.

As expected, our results indicated that T_1 is shortened for higher concentrations of Gadoteridol. Since the T_1 in biological systems tends to be short, a dSPM approach is expected to be limited in imaging biological tissue, unless the transfer of the sample from the polarising magnet into the scanner is speeded up.

Chapter 4

Measurement and Imaging of Remanent Magnetisation in Human Tissue

4.1 Introduction

While looking at NMR signals in previous experiments, we came across a long-lived magnetisation signal in biological samples. We initially thought that this was an unusually long-lived nuclear magnetisation, but we ruled this out when we saw that the magnetisation orientation is fixed by the sample orientation with respect to the applied polarising field. We then deduced that this long-lived magnetisation must be coming from remanent ferrimagnetism and/or ferromagnetism of a tissue constituent that is most likely magnetite.

We have also found literature about Isothermal Remanent Magnetisation (IRM) in tissue linked to magnetite particles [69]. Humans and many organisms biochemically precipitate the paramagnetic mineral ferrihydrite, which is the mineral in the core of the ferritin molecule [69]. Some organisms also produce the ferrimag-

netic mineral magnetite, and there is evidence that small amounts of magnetite are present in the human body. Because it is ferrimagnetic, magnetite interacts more than a million times more strongly with external magnetic fields than any other biological material [69, 70].

Magnetite is the first material to be discovered as a biochemical precipitate in human tissues, and is the only one which is ferrimagnetic at room temperature - everything else in the human bones and soft tissue is diamagnetic or paramagnetic [71]. In other species, magnetite seems to be involved in tissues that are associated with magnetic field sensing, particularly geomagnetic field sensing [72], but it is also found in human and mouse tumors. This could suggest that magnetite could be a localised source of iron that activates iron-based enzymes. Moreover, high levels of magnetite in fast-growing tumors in mice suggests that it may have a role in cell division [69].

Magnetite is a black mineral form of iron oxide. It is composed of Iron (II) and Iron (III) oxide. Magnetite crystals are often organised into linear membrane-bound chains, that are a few micrometres long, with up to 80 crystals per chain. Individual crystals have their 111-axis aligned along the length of the chain [73]. Figure 4.1 shows a scan of magnetite crystals at a low magnification.

Magnetite has also been seen to form single-domain permanently magnetic crys-

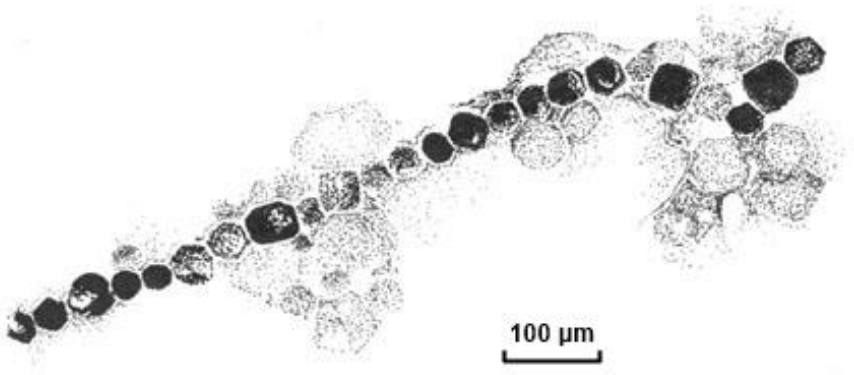

Figure 4.1: Magnetite crystals under low magnification. Image adapted from [73].

tals in lipid bilayer vacuoles called *magnetosomes*, strung together in linear chains. These act as biological bar magnets [69, 70, 74].

In this chapter, we apply a magnetic field to human tissue, and use MEG to detect and map the magnetic field shifts from the magnetised human tissue. We then apply the inverse problem relating the measured magnetisation distribution to the magnetic fields produced at an array of sensors, as described in Chapter 2, so as to generate images of the distribution of induced magnetisation. We also evaluate differences in the results across different subjects, as well as assessing magnetisation induced in different body parts, including the wrist, the hand, and the foot.

4.2 Theory

The hypothesis behind this project was that if we first magnetise different body parts (mainly the hand, wrist, and foot), we can then use the SQUIDs in a MEG scanner to measure the magnetic field shifts produced when the magnetised tissue is inserted into the MEG helmet, and could also follow the decay of the magnetisation using the resulting information, to generate images of the magnetised body part.

Isothermal remanent magnetisation results from the presence of magnetised particles in the tissue. The remanent magnetisation is not affected by diamagnetic tissue or paramagnetic materials in the tissue. Whereas paramagnets align with an applied magnetic field, their magnetisation is lost when the applied magnetic field is removed, because of the random effect of thermal fluctuations on the magnetisation vectors.

The magnetisation that remains in the tissue is the remanent magnetisation. As the magnetisation in more magnetic particles in the tissue aligns parallel to the

applied magnetic field, the magnetisation of the tissue increases until it saturates. When it saturates, all magnetic particles have their magnetisation aligned parallel to the applied field direction [72].

In magnetite particles, thermal energies are overcome by quantum mechanical coupling of electron spins, allowing them to retain their magnetisation even when the field is removed [72].

When tissue is subjected to a magnetic field, any ferrimagnetic or ferromagnetic particles in the human tissue will become magnetised in alignment with the magnetic field. When the magnetic field is removed, the magnetic particles in the tissue start to lose their magnetic alignment, and the net magnetisation decays.

The relaxation of a stable magnetic fluid can be described by two superimposed exponential decays related to Néel relaxation and Brownian relaxation [75]. The relaxation time of the magnetisation in magnetic particles is strongly dependent on the particle size, as is the dominant mode of relaxation [76].

4.2.1 Néel and Brownian Relaxations

Large magnetic particles often have no net magnetisation, even below the Curie temperature. This is because they are made up of domains, and each domain has a net magnetisation pointing in a random direction. However, if the size of the material is made small enough, the magnetostatic energy competes with the energy used for forming the domain walls, and a single domain state becomes more preferable [77].

The magnetisation vector of a single domain particle is given by

$$\mathbf{M} = VM_0\hat{\mathbf{n}}, \tag{4.1}$$

where $V = 4\pi r_c^3/3$ is the volume of a particle of radius r_c, M_0 is the saturation magnetisation, and $\hat{\mathbf{n}}$ is a unit vector in the direction of magnetisation [77]. In the case of uniaxial anisotropy (e.g. in z-direction), the magnetic energy is given by

$$E = VK\sin^2\theta, \tag{4.2}$$

where K is the effective magnetic anisotropy constant and θ is the angle between the z-axis and $\hat{\mathbf{n}}$. The minimum energy occurs at $\theta = 0$ and $\theta = \pi$, defining two equilibrium orientations, corresponding to magnetisations $+VM_0$ and $-VM_0$. If thermal fluctuations are strong enough, the magnetic moment of the particle is reversed by overcoming the energy barrier of height VK. This reversal is called Néel relaxation, and the characteristic time constant for Néel relaxation τ_N is given by

$$\tau_N = \tau_o e^{VK/k_BT}, \tag{4.3}$$

where τ_0 is related to the inverse of the attempt frequency of magnetic reversal. In summary, the Néel relaxation is due to the reorientation of the magnetisation vector inside the magnetic core against an energy barrier, as shown in Figure 4.2.

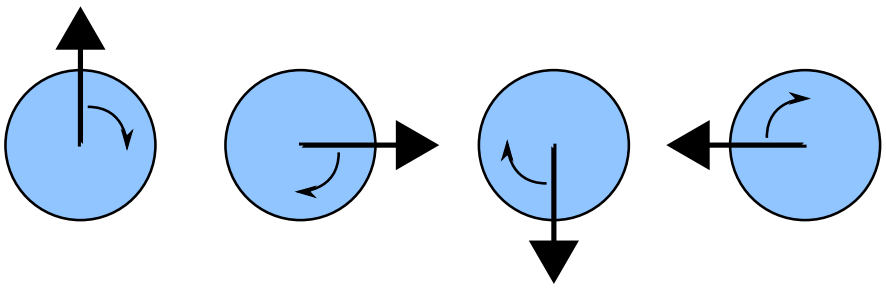

Figure 4.2: Schematic showing Néel relaxation due to reorientation of the magnetisation vector.

The second mechanism of relaxation, which occurs in liquids, is Brownian rotational motion, or Brownian relaxation. This happens because of the physical

rotation of the whole particle within the fluid, that occurs due to thermal fluctuations. The Brownian relaxation time is given by

$$\tau_B = \frac{4\pi\eta r_h^3}{k_B T}, \tag{4.4}$$

where η is the dynamic viscosity of carrier liquid and r_h is the hydrodynamic radius defined as the sum of the radius r_c of the particle and the thickness of any surfactant coating δ over it [78]. The schematic in Figure 4.3 shows the mechanism of Brownian relaxation.

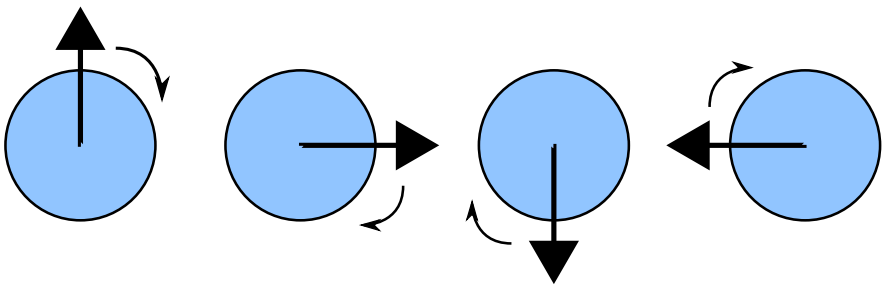

Figure 4.3: Schematic showing Brownian relaxation due to reorientation of the magnetic particle.

From Equations 4.3 and 4.4, it can be seen that the particle size influences both the Néel and Brownian relaxation times. τ_N increases exponentially, and τ_B grows linearly with the particle dimension. The effective relaxation time, τ_e, [79] is defined as

$$\frac{1}{\tau_e} = \frac{1}{\tau_N} + \frac{1}{\tau_B} \tag{4.5}$$

For small particles, $\tau_N \ll \tau_B$, and therefore $\tau_e \approx \tau_N$. In this case, most of the relaxation takes place by rotation of the magnetic moment inside the particle.

For large particles, $\tau_B \ll \tau_N$, and therefore $\tau_e \approx \tau_B$. In this case, The relaxation is due to a physical rotation of the particle in the suspension. Thus, the effective relaxation time is determined by the faster relaxation, and so depends strongly

on the particle size.

In the case of magnetic particles embedded in a solid matrix, Néel relaxation is the dominant relaxation mechanism, and $\tau_E = \tau_N$.

4.3 Method

The experimental setup used for the experiments described in this chapter is detailed in Figure 4.4, and comprises a polarising magnet, a SQUID array housed inside a Magnetically Shielded Room (MSR), and a fibreglass helmet placed inside the SQUID array.

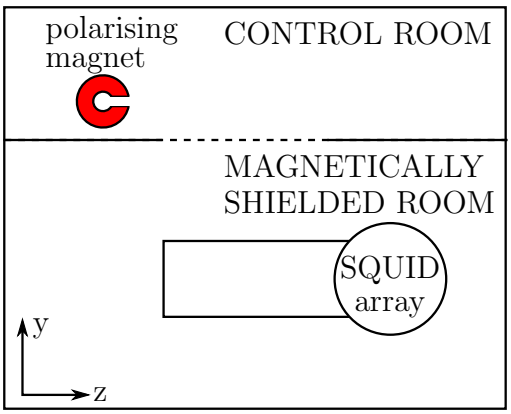

Figure 4.4: Schematic of experimental setup.

4.3.1 Polarising Magnet

The polarising magnet used for pre-polarisation of samples was an 0.5 T cylindrical permanent magnet, of diameter 6.5 cm and height 7 cm, previously described in Chapter 2. We kept this magnet outside the MSR housing the MEG system, such that the magnetic field from it was small at the SQUID array.

4.3.2 Helmet

For reproducibility, and for localisation improvement, we used a moulded fibre-glass helmet, custom-made to fit inside the MEG helmet. We marked the helmet at three points; the left auricle, right auricle, and the nasion, and we attached fiducial coils at these points, for localisation.

4.3.3 Data Collection

The SQUID array used is part of a 275 channel MEG system (MEG International Services Limited (MISL), Coquitlam, BC, Canada). The system is fitted with second order axial gradiometers with a 5 cm baseline, fitted around a helmet, and also includes 29 sensors in a reference array, located distal to the head. Each axial gradiometer is incorporated into a superconducting circuit, which is magnetically coupled to a SQUID detector, yielding an average noise level of around $10\,\mathrm{fT/Hz^{1/2}}$.

We ran these experiments with the MEG gantry in the supine position. The gantry was lowered at least twenty minutes prior to running the experiment, to allow enough time for the liquid Helium to settle in position.

The sampling rate of the outputs of the field sensors was 600 Hz throughout data collection.

4.3.4 Data Filtering

Following data collection, we used the `Data Editor` program provided on the *MISL* system to filter and display the data from all separate channels, preview the data to check for problems on any channels, and to plot field maps. Before analysing the recorded data, we applied the filters shown in the screenshot in

Figure 4.5. We used a 50 Hz notch filter of width 2 Hz to eliminate interference occurring at the mains frequency. Since we ran these experiments with the door to the MSR open, it was particularly important to use the MEG system in the third order synthetic gradiometer configuration to reduce the time-varying external magnetic interference.

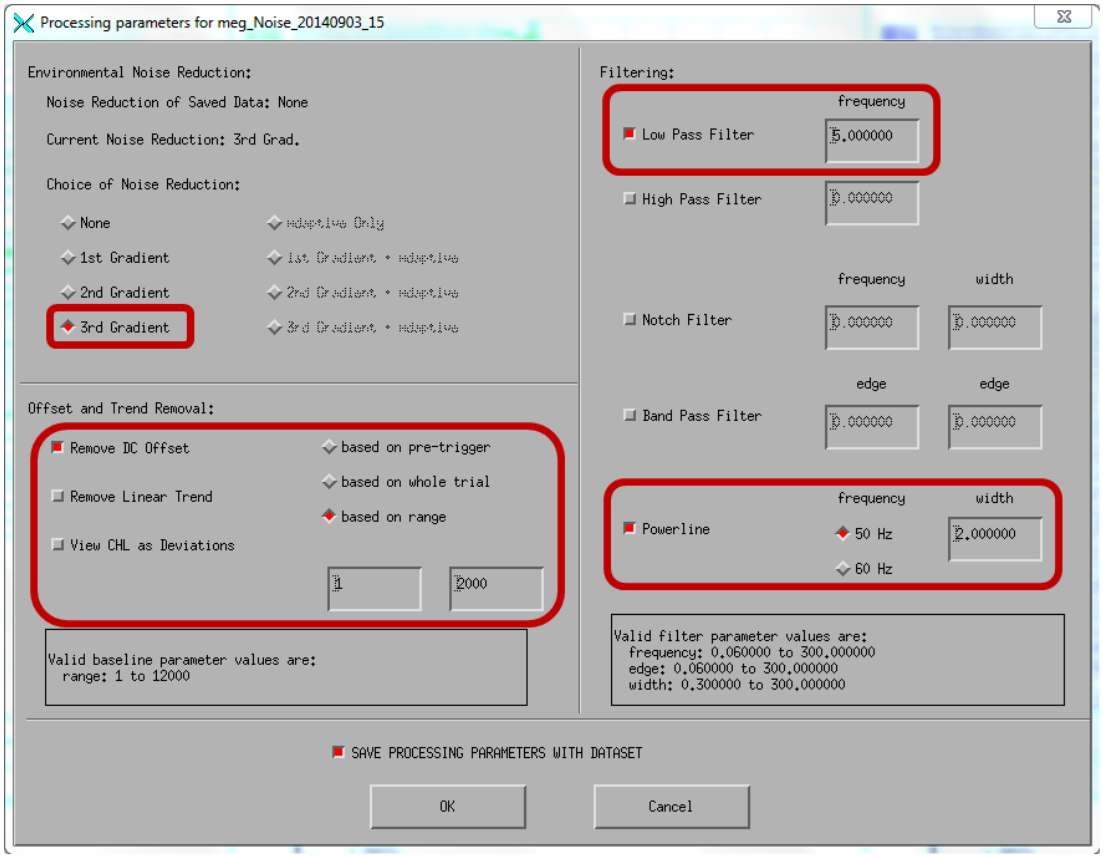

Figure 4.5: Screenshot showing the data filtering applied.

In experiments on inanimate samples, we also used a DC offset based on the data acquired during the last 3 s of the recording. In scanning human participants, we used as baseline the data acquired during the first few seconds, rather than the data acquired during the last few seconds, because small changes in the position of the body region, have a significant effect on the measured magnetic fields.

Moreover, since the induced magnetisation varies only on a time-scale of seconds, and there are higher frequency sources of noise, such as muscle artefacts [80], we applied a 0.5 Hz low pass filter to the data. After filtering, we transferred the data to `MATLAB` for data processing.

4.3.5 Magnetic Relaxometry in Inanimate Samples

Using the 0.5 T polarising magnet located outside the MSR, we magnetised the sample for 10 s, and then quickly transferred it into the MEG helmet. The transfer process took around 7 s. We recorded the magnetic field at specific time intervals. Samples included:

- a chicken wing wrapped in paper *,
- a chicken bone wrapped in paper *,
- chicken meat wrapped in paper *,
- powdered milk,
- powdered protein

Our initial assumption was that the measured signals arose from long-lived nuclear magnetisation, so some of these experiments denoted by an asterisk were carried out with an imaging magnet in the MSR. As it became clear that the fields measured from the samples were insensitive to the presence of the imaging magnet, we dispensed with its use.

We applied the Minimum Norm Estimate (MNE) to the filtered data and applied a mask that blocks out all of the target volume except for the space occupied by the helmet. We ran sample reconstruction on the data using the lead-field normalised, minimum norm spatial filter, described in Chapter 2. We also generated images of the magnetic fields produced by the magnetised material.

4.3.6 Magnetic Relaxometry in Human Tissue

We also ran experiments on the human wrist, hand, foot, and head. For these experiments, we required that the participants would not have been in the MRI scanner in the previous 3 days. Just before scanning, we asked the participants

to de-metal and to wear scrubs.

For experiments on the wrist and hand, we asked the participants to thoroughly wash their hands before we started the experiment.

We first ran three recordings of 20 s each, for which the relevant body region was not magnetised. The participants were asked to enter the MSR after 7 s from the start of the recording, and to place the wrist, hand or head into the MEG scanner, and then to remain still.

We then asked the subjects to position their wrist/hand/foot on top of the polarising magnet for 40 s, after which they were asked to immediately enter the MSR as fast as possible. This recording was 180 s long, and started 20 s before the participants were asked to enter the MSR.

Following this, we ran 20 s recordings, every 2 min or faster, for the first hour, and 3 repeats of 20 s recordings after 1 h and 2 h. The participants were told not to go close to any magnets throughout the 3 h, with the exception of the polarising magnet before the fourth recording. While scanning their fingers inside the MEG scanner, participants were asked to keep their fingers closed together, and to keep their thumb out of the helmet.

We ran the wrist experiment on 9 males, and we repeated the experiment on 4 of these participants.

We ran the hand experiments on 12 males, of whom, one was left-handed. We discarded the data from one participant because the scanner was faulty during the recording. We also ran the experiment three times on one of the subjects, with an 8 week interval between the first two experiments, and a 3 day interval between the second and third repetitions of the experiment.

We ran the experiment for the foot and for the head, on one participant.

For identifying the source of the measured magnetic fields, we applied the Minimum Norm Estimate (MNE) to the filtered data and applied a mask that blocked out all the target volume except for the space occupied by the helmet. We used the lead-field normalised, minimum norm spatial filter, described in Chapter 2. We thresholded the reconstructed images at the maximum intensity returned from the MNE calculation, and the minimum threshold at 15% of this value.

We generated images using the difference in the field measured before and immediately after inserting the magnetised body part into the MEG helmet, and also using the change in magnetic field from the magnetised tissue over the period of recording, which reflects any decay of the magnetisation.

4.4 Results

4.4.1 Magnetic Relaxometry in Inanimate Samples

After inserting the pre-polarised samples in the MEG scanner, we measured the magnetisation using the MEG SQUIDs. Figures 4.6 - 4.10 show (in blue) the variation with time of the magnetisation recorded from the channel that detected the highest magnetisation change. The red plots are curves of the best exponential curve fit to the data.

Figure 4.6 shows the magnetisation decay with time, after magnetising a chicken wing. The decay plot suggests that there is a long-lived signal with a time constant of about 33 s. We initially thought that this long-lived signal could be attributed to phosphorus in the bone, and so we ran the experiment on a chicken bone. However, as can be seen in Figure 4.7, there was no long-lived signal from the bone. Thus, we repeated the experiment on chicken meat. Figure 4.8 shows a long-lived signal, similar to when we scanned the chicken wing. The time constant in this decay was about 32 s, similar to the value found for the chicken wing. Note

that in this sample, the magnetic field was negative in the channel showing the largest absolute signal change. We also ran the experiment for powdered milk and protein powder. Figures 4.9 and 4.10 show that the magnetisation in prepolarised samples of powdered milk and protein decayed with approximate time constants of 23 s and 29 s, respectively. Table 4.1 summarises the relaxation time values measured from the different samples.

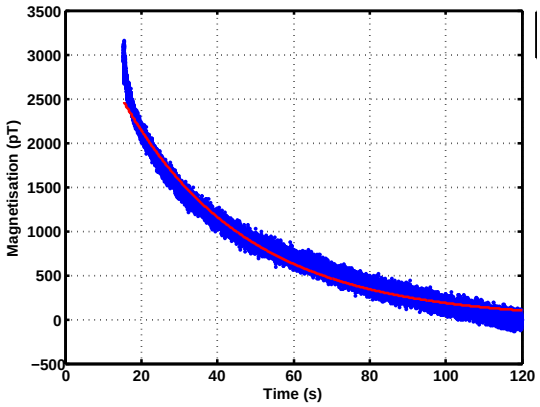

Figure 4.6: Plot (blue) and curve fit (red) showing the magnetisation decay recorded on the channel that detected the maximum change in magnetisation, after polarising a chicken wing.

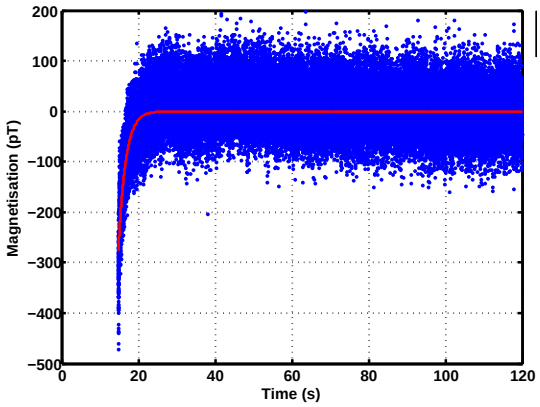

Figure 4.7: Plot (blue) and curve fit (red) showing the magnetisation decay recorded on the channel that detected the maximum change in magnetisation, after polarising a chicken bone.

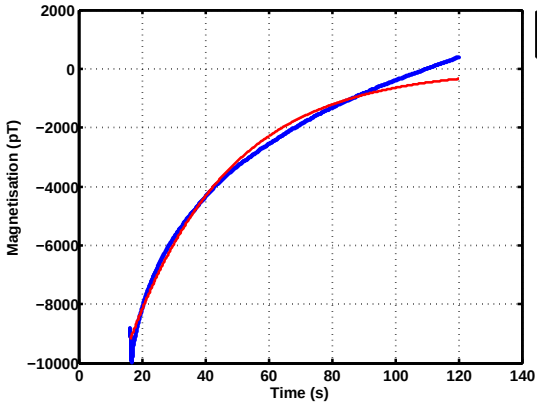

Figure 4.8: Plot (blue) and curve fit (red) showing the magnetisation decay recorded on the channel that detected the maximum change in magnetisation, after polarising chicken meat.

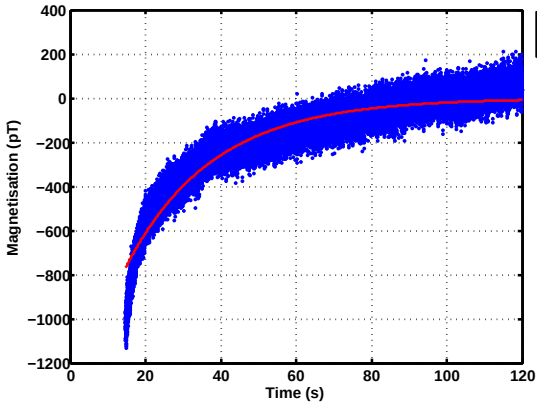

Figure 4.9: Plot (blue) and curve fit (red) showing the magnetisation decay recorded on the channel that detected the maximum change in magnetisation, after polarising powdered milk.

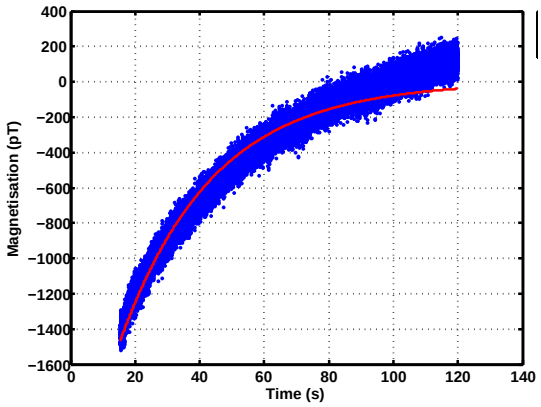

Figure 4.10: Plot (blue) and curve fit (red) showing the magnetisation decay recorded on the channel that detected the maximum change in magnetisation, after polarising powdered protein.

Sample	relaxation time (s)
chicken wing	33 ± 1
chicken meat	32 ± 0.06
powdered milk	23 ± 0.09
powdered protein	29 ± 0.07

Table 4.1: Relaxation time values for different samples.

4.4.2 Magnetic Relaxometry in the Human Wrist

In this experiment, we magnetised the wrist for 1 min, and immediately transferred it to the sample holder inside the MEG. The scan time was 180 s and the wrist was inserted in the scanner at 20 s from the start of the recording. The transit time was typically 5 s.

Figure 4.11 shows the magnetic field map obtained immediately after inserting a magnetised wrist inside the MEG scanner, and Figure 4.12 shows the MNE-reconstructed image generated from measurements of the magnetic field shift obtained after inserting the magnetised wrist inside the MEG scanner.

We thresholded all the following MNE-reconstructed images at the maximum intensity returned from the MNE calculation, and the minimum threshold at 15% of the maximum intensity. The white areas indicate the voxels whose intensity falls below the minimum threshold. The black areas fall outside the mask. The

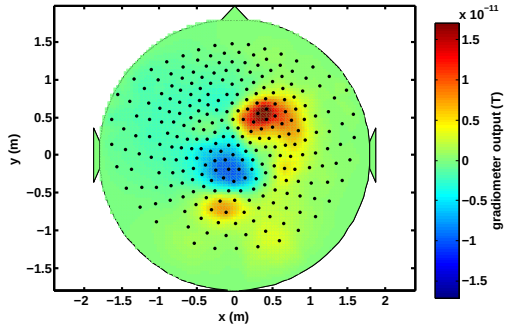

Figure 4.11: Magnetic field map showing the gradiometer output measured by the MEG SQUIDs after inserting a magnetised wrist in the MEG scanner.

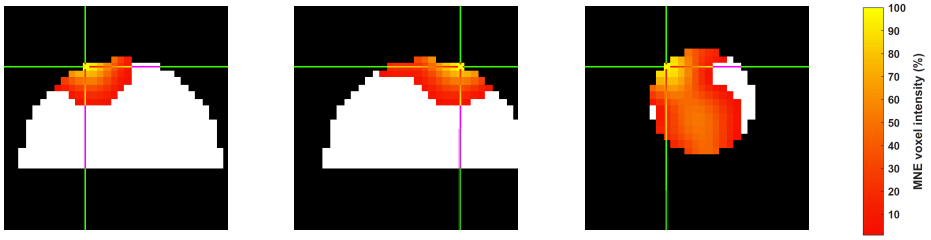

Figure 4.12: Plots showing the MNE-reconstructed image of the magnetic field shift measured immediately after inserting a magnetised wrist, overlaid onto coronal (left), sagittal (centre), and axial (right) slices of the mask used in creating the inverse image.

chosen slices are at the location of the voxel with the maximum intensity. The cross-hairs indicate the position of the two other slices.

As can be seen in Figure 4.12, the voxels whose intensity falls within 15% and 100% of the maximum intensity returned from the MNE calculation, correspond with the location of the wrist in the helmet. Thus, the MNE algorithm managed to locate the wrist.

We also looked at the change in remanent magnetisation over 160 s following magnetisation. Figure 4.13 shows the magnetic field map of the change in magnetisation over 160 s from magnetisation, and Figure 4.14 shows the corresponding MNE-reconstructed image.

We then proceeded to look at the field patterns and MNE-reconstructed images obtained from magnetic field shifts measured over 3 hours from magnetisation,

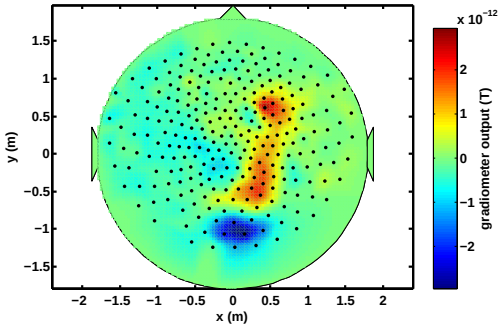

Figure 4.13: Magnetic field map showing the change in gradiometer output measured by the MEG SQUIDs in 160 s from magnetising the wrist in the MEG scanner.

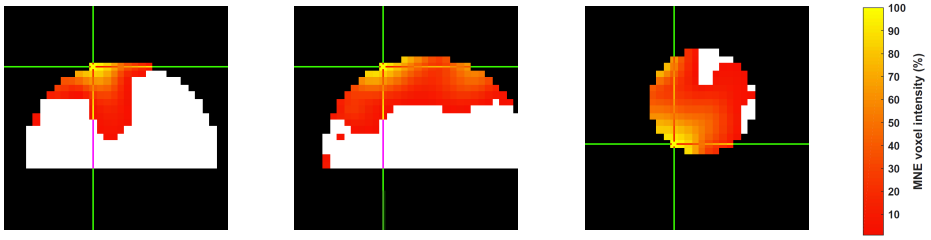

Figure 4.14: Plots showing the MNE-reconstructed image of change in remanent magnetisation over 160 s from magnetisation, overlaid onto coronal (left), sagittal (centre), and axial (right) slices of the mask used in creating the inverse image of the wrist.

at 1 hour intervals.

Figure 4.15 shows the magnetic field map obtained from the same subject's wrist at 1 h after magnetisation. The field has now decreased by half, to approximately 8 pT. Figure 4.16 shows the MNE-reconstructed image generated from this magnetic field. This image is similar to the images obtained immediately after magnetising the wrist.

At 2 h from magnetisation (Figure 4.17), the measured magnetic field was similar to that at 1 h from magnetisation, albeit slightly larger. The increase in the measured field could be attributed to small differences in the position of the wrist with respect to the MNE sensors. The MNE-reconstructed image (Figure 4.18) was almost identical to that obtained at 1 h from polarisation.

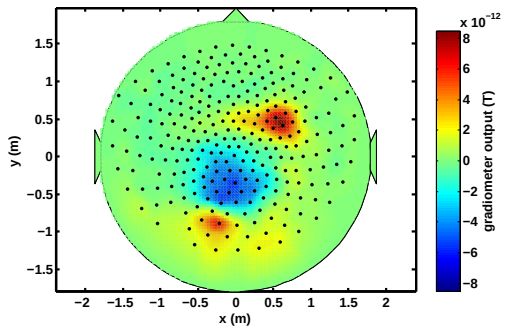

Figure 4.15: Magnetic field map showing the gradiometer output measured by the MEG SQUIDs at 1 h after magnetising the wrist.

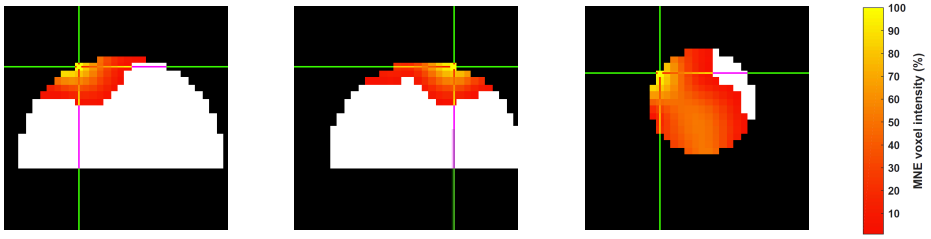

Figure 4.16: Plots showing the MNE-reconstructed image, overlaid onto coronal (left), sagittal (centre), and axial (right) slices of the mask used in creating the inverse image of a wrist, using the magnetic field shift measured at 1 h after polarisation.

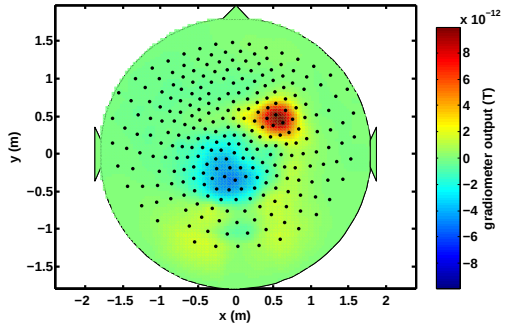

Figure 4.17: Magnetic field map showing the gradiometer output measured by the MEG SQUIDs at 2 h after magnetising the wrist.

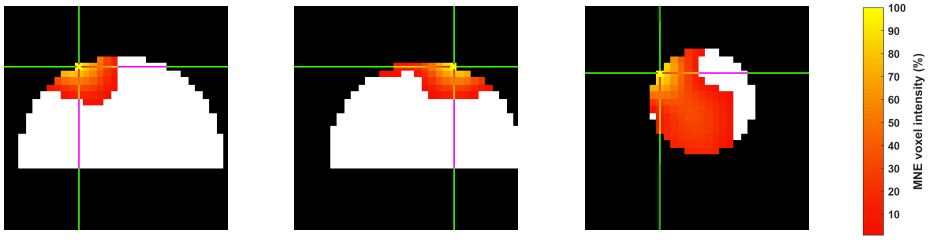

Figure 4.18: Plots showing the MNE-reconstructed image, overlaid onto coronal (left), sagittal (centre), and axial (right) slices of the mask used in creating the inverse image of a wrist, using the magnetic field shift measured at 2 h after polarisation.

The magnetic field map (Figure 4.19) obtained at 3 h after magnetising the wrist shows magnetic fields of a similar order to those obtained at 1 h from magnetisation.

The MNE image (Figure 4.20) obtained at 3 h after magnetisation is also very similar to that obtained at 1 h after magnetisation. This suggests that the statistical distribution of the likelihood of the MNE source localisation does not vary much in the human wrist between 1 h and 3 h from magnetisation. These MNE-reconstructed images do not indicate how much the magnetisation in the wrist is decaying, since the MNE images we generated are statistical, and do not show the absolute values of the reconstructed dipole source.

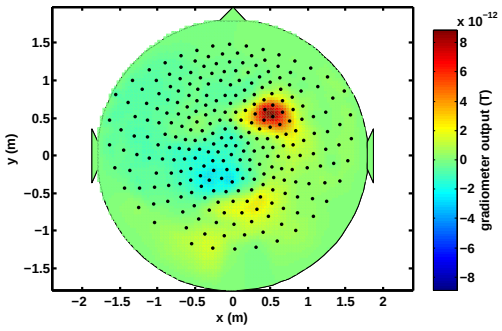

Figure 4.19: Magnetic field map showing the gradiometer output measured by the MEG SQUIDs at 3 h after magnetising the wrist.

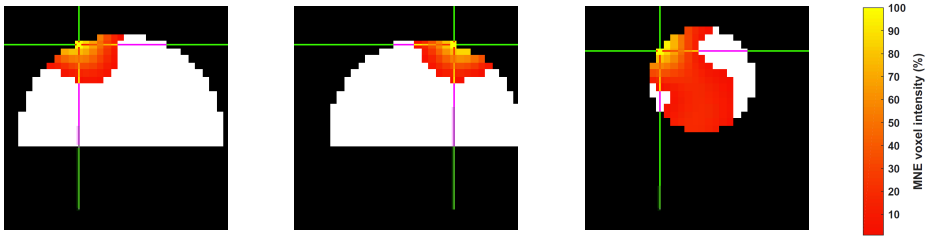

Figure 4.20: Plots showing the MNE-reconstructed image, overlaid onto coronal (left), sagittal (centre), and axial (right) slices of the mask used in creating the inverse image of a wrist, using the magnetic field shift measured at 3 h after polarisation.

Figure 4.21 shows how the magnitude of the MNE-reconstructed dipole changed over 1 h from polarisation. A decrease in the MNE-reconstructed dipole magnitude can be seen, with the largest decrease occurring within the first 5 min from magnetisation.

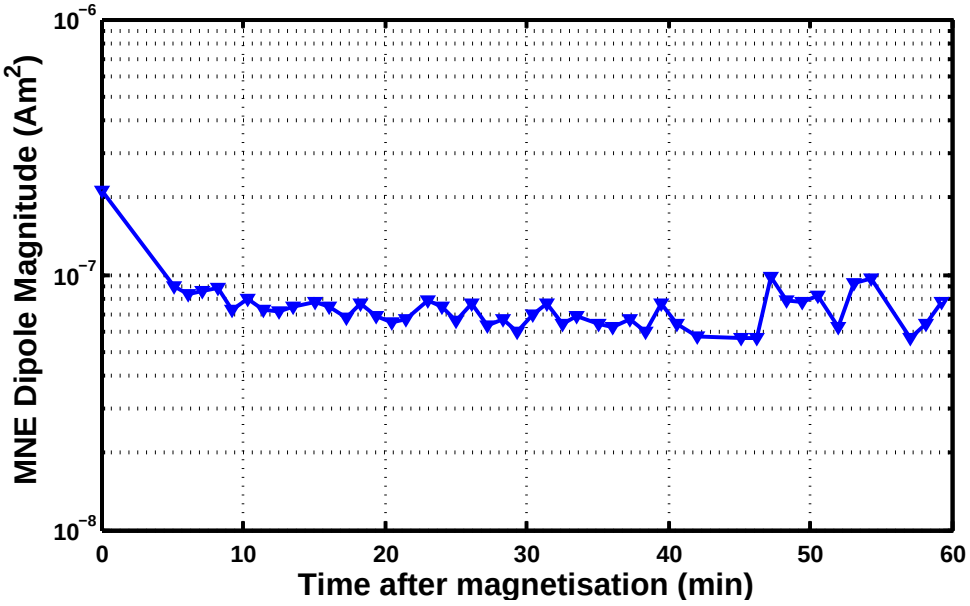

Figure 4.21: Plot showing magnitude of MNE-reconstructed dipole after magnetising wrist.

Figure 4.22 shows how the largest measured magnetic field varies over 3 h from magnetisation, for all subjects, including the repeated experiments on some of the subject. It can be seen that the initial largest measured magnetisation is approximately 100 times larger than the smallest one, but the final largest measured

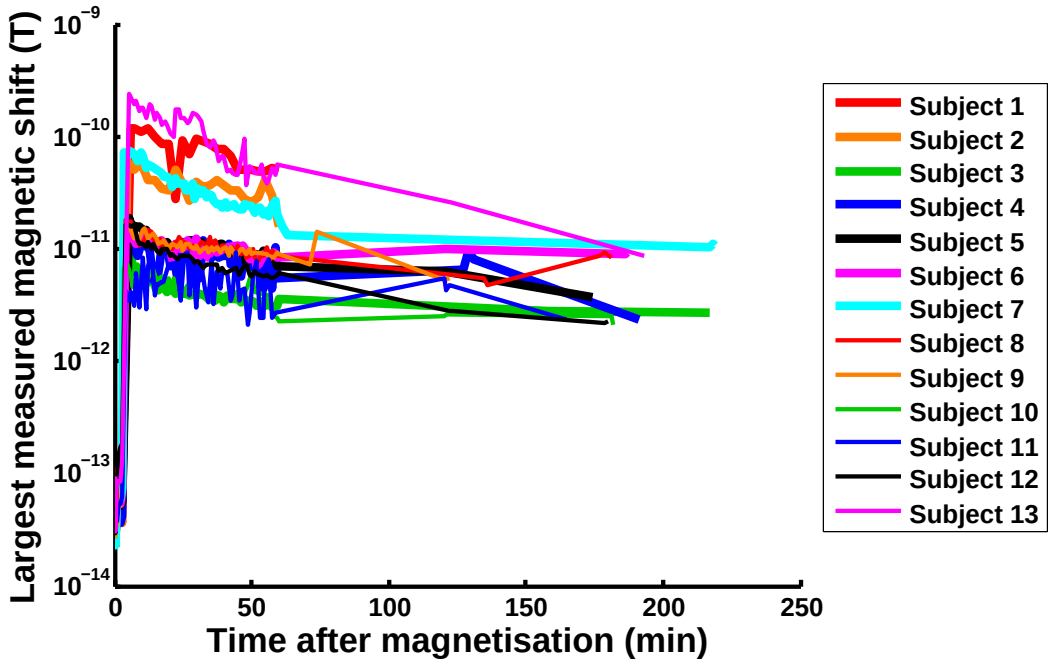

Figure 4.22: Plot showing the time evolution of the measured magnetisation shift recorded by the MEG SQUIDs over 3 h from magnetising the wrists, for all subjects.

magnetisation is only 10 times larger than the smallest one. Figure 4.23 zooms in on the first 180 s after magnetisation.

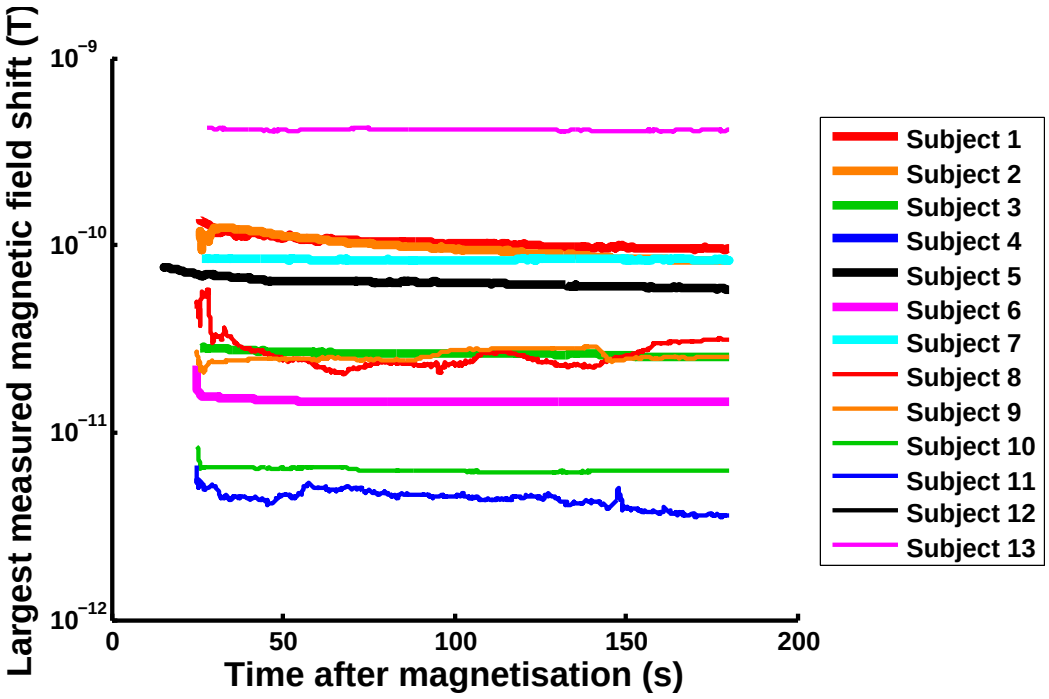

Figure 4.23: Plot showing the time evolution of the measured magnetisation shift recorded by the MEG SQUIDs over 3 min from magnetising the wrists, for all subjects.

4.4.3 Magnetic Relaxometry in the Human Hand

In this experiment, we exposed a participant's hand to an applied magnetic field for 1 min, and immediately transferred it to the sample holder inside the MEG. The scan time was 180 s and the hand was inserted in the scanner at 20 s from the start of the recording. The transit time was typically 5 s.

Figure 4.24 shows the magnetic field map obtained immediately after inserting the magnetised hand inside the MEG scanner, and Figure 4.25 shows the MNE-reconstructed image generated from measurements of the magnetic field shift obtained after inserting the magnetised hand inside the MEG scanner.

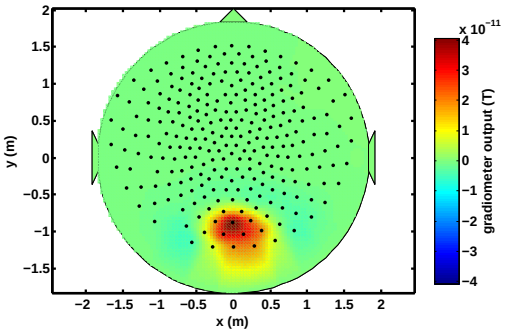

Figure 4.24: Magnetic field map showing the gradiometer output measured by the MEG SQUIDs after inserting a magnetised hand in the MEG scanner.

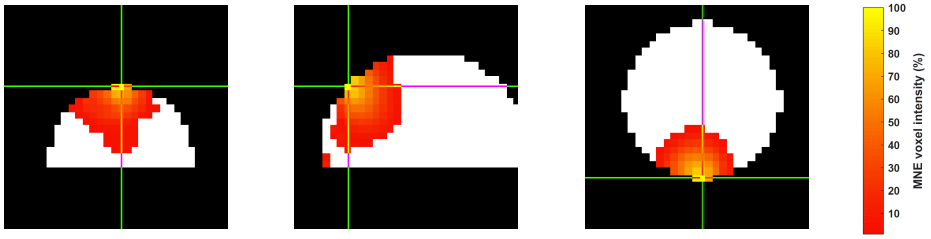

Figure 4.25: Plots showing the MNE-reconstructed image of the magnetic field shift measured immediately after inserting a magnetised hand, overlaid onto coronal (left), sagittal (centre), and axial (right) slices of the mask used in creating the inverse image.

We also looked at the magnetic decay that occured over 160 s from magnetising the wrist, in the measured magnetic fields. The magnetic field map in Figure 4.26 shows the change in the measured magnetic fields from immediately after magnetising the hand to 160 s later. It can be seen that the magnetic field decay is of the order of 2 pT. Comparing this to Figure 4.13, the decay in the hand is much less than the decay in the wrist, over 160 s from magnetisation.

Figure 4.27 shows an MNE-reconstructed image generated from the fields shown in Figure 4.26. Albeit the highest intensity voxels of the MNE-reconstructed image are located at a similar location in both Figures 4.25 and 4.27, the image obtained using the change in magnetisation is less focussed than the image obtained using the measured magnetic field shift.

We then monitored the magnetisation decay over 3 hours, and we looked at how accurately and precisely the MNE algorithm located the hand at different time intervals. After 1 h from magnetisation, the magnitude of the largest measured

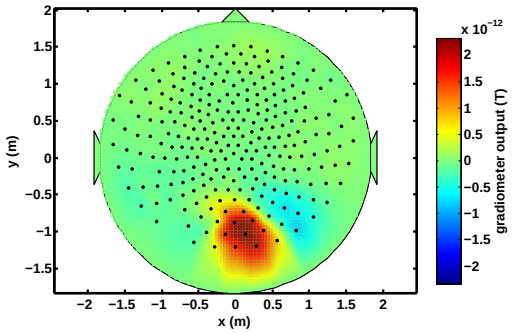

Figure 4.26: Magnetic field map showing the change in gradiometer output measured by the MEG SQUIDs in 160 s from magnetising the hand in the MEG scanner.

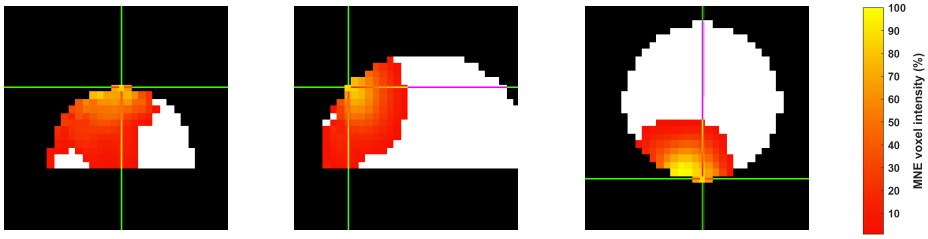

Figure 4.27: Plots showing the MNE-reconstructed image of the change in magnetisation measured over 160 sfrom magnetising the hand, overlaid onto coronal (left), sagittal (centre), and axial (right) slices of the mask used in creating the inverse image.

magnetic field (Figure 4.28) was half that measured immediately after magnetisation.

The MNE-reconstructed image (Figure 4.29) generated from measurements of the magnetic field shift at 1 h after magnetisation is similar to that obtained immediately after magnetisation. In both images, the highest intensity voxel was located at the same position.

At 2 h after magnetisation, the magnitude of the largest measured magnetic field (Figure 4.30) was further decreased to about 20 pT. The MNE-reconstructed image (Figure 4.31) generated from measurements of the magnetic field shift at 2 h after magnetisation is also similar to that obtained immediately after magnetisation, and at 1 h after magnetisation. In all three images, the highest intensity voxel was located at the same position.

As expected, at 3 h after magnetisation, the magnitude of the largest measured

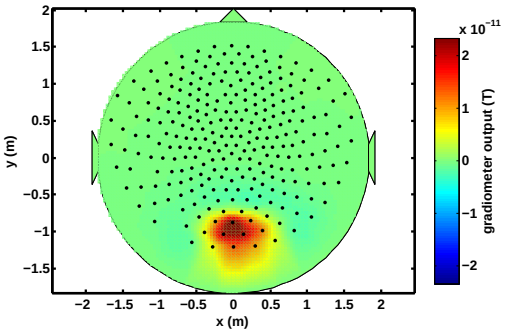

Figure 4.28: Magnetic field map showing the gradiometer output measured by the MEG SQUIDs at 1 h after inserting a magnetised hand in the MEG scanner.

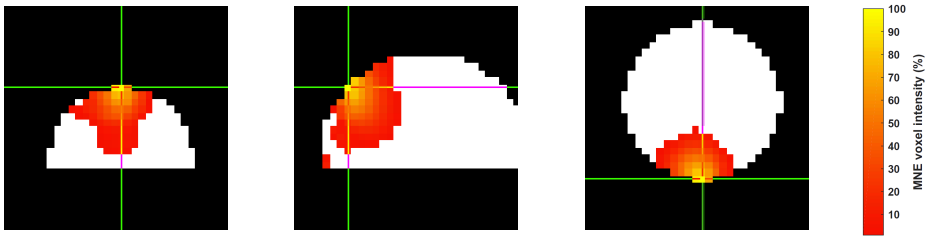

Figure 4.29: Plots showing the MNE-reconstructed image of the magnetic field shift measured at 1 h after inserting a magnetised hand, overlaid onto coronal (left), sagittal (centre), and axial (right) slices of the mask used in creating the inverse image.

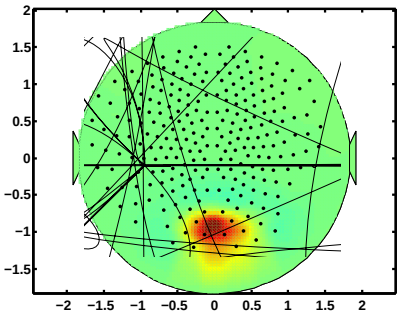

Figure 4.30: Magnetic field map showing the gradiometer output measured by the MEG SQUIDs at 2 h after inserting a magnetised hand in the MEG scanner.

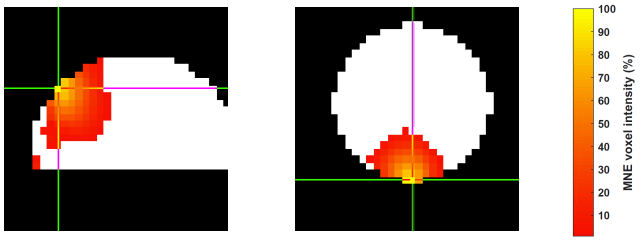

Figure 4.31: Plots showing the MNE-reconstructed image of the magnetic field shift measured at 2 h after inserting a magnetised hand, overlaid onto coronal (left), sagittal (centre), and axial (right) slices of the mask used in creating the inverse image.

magnetic field (Figure 4.32) was even further decreased. The MNE-reconstructed image (Figure 4.33) generated from measurements of the magnetic field shift at 3 h after magnetisation is also similar to the three other MNE images, obtained immediately after magnetisation, at 1 h after magnetisation, and at 2 h after magnetisation. The highest intensity voxel was still located at the exact position as for the three other images.

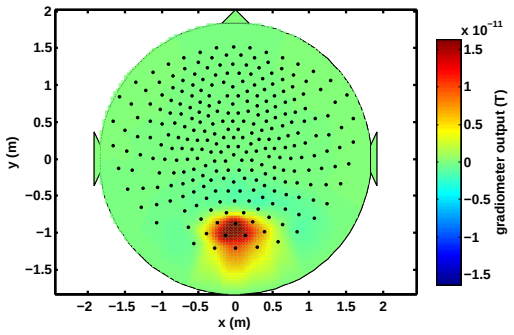

Figure 4.32: Magnetic field map showing the gradiometer output measured by the MEG SQUIDs at 3 h after inserting a magnetised hand in the MEG scanner.

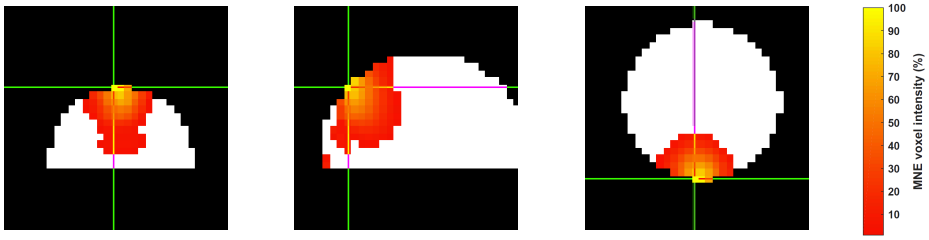

Figure 4.33: Plots showing the MNE-reconstructed image of the magnetic field shift measured at 3 h after inserting a magnetised hand, overlaid onto coronal (left), sagittal (centre), and axial (right) slices of the mask used in creating the inverse image.

Figure 4.34 shows the time evolution of the magnitude of the MNE-reconstructed dipole in 3 h from magnetisation. A decrease in the MNE-reconstructed dipole magnitude can be seen, as expected.

Figure 4.35 shows how the largest measured magnetic field varies over 3 h from magnetisation, for different subjects. The initial largest measured magnetisation is approximately 20 times larger than the smallest one, but the final largest measured magnetisation is almost 100 times larger than the smallest one. Figure 4.36 zooms in on the first 180 s after magnetisation.

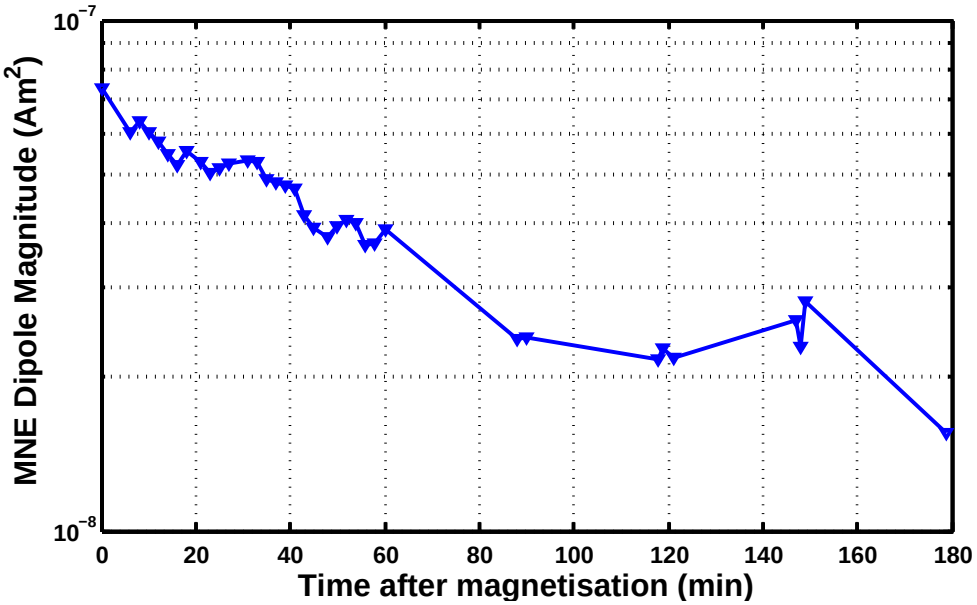

Figure 4.34: Plot showing time evolution of the magnitude of the MNE-reconstructed dipole after magnetising the hand.

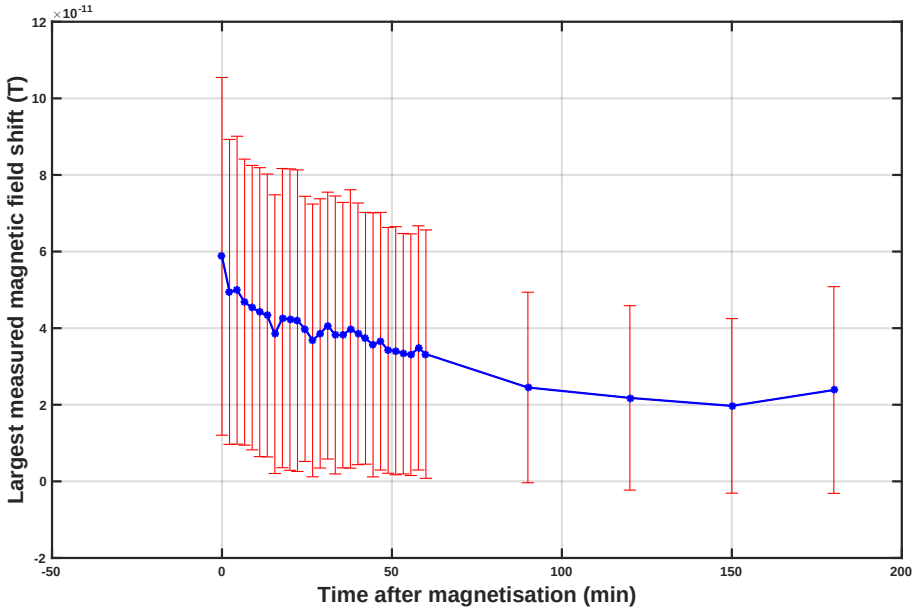

Figure 4.35: Plot showing the mean time evolution of the measured magnetisation shift recorded by the MEG SQUIDs over 3 h from magnetising the hands, for all subjects. The error bars indicate the standard deviation of the results.

Figure 4.37 shows a superposition of the MNE-reconstructed dipole magnitudes of all subjects: before magnetisation, immediately after magnetisation, at 180 s after magnetisation, at 1 h after magnetisation, at 2 h after magnetisation, and at 3 h after magnetisation. The data used to obtain these MNE-reconstructed dipole

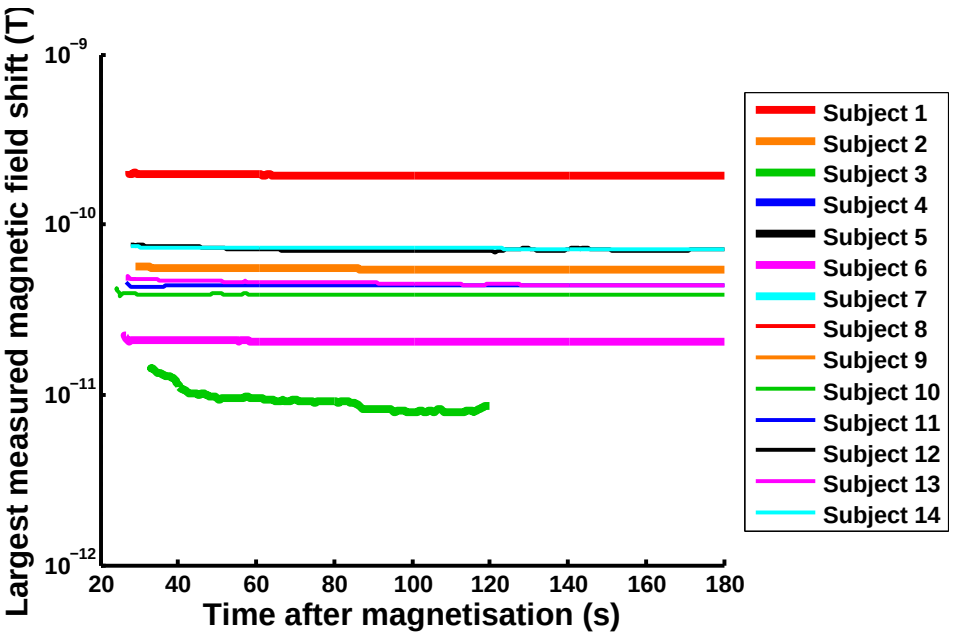

Figure 4.36: Plot showing the time evolution of the measured magnetisation shift recorded by the MEG SQUIDs over 3 min from magnetising the hands, for all subjects.

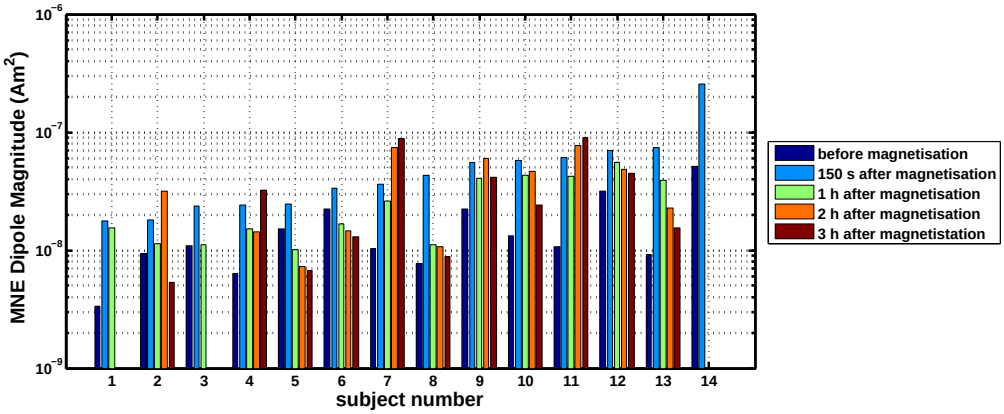

Figure 4.37: Plot showing the MNE-reconstructed dipole magnitudes for all subjects: before magnetisation, immediately after magnetisation, at 180 s after magnetisation, at 1 h after magnetisation, at 2 h after magnetisation, and at 3 h after magnetisation. The subjects are sorted in ascending order of the difference in magnetisation recorded by the SQUIDs before and immediately after inserting a magnetised hand in the MEG scanner.

magnitudes is the magnetisation change recorded after inserting the hand in the MEG scanner.

As expected, the largest magnitudes are obtained using the data acquired immediately after magnetising the hand, followed by the data acquired at 1 h, 2 h, 3 h after magnetising the hand, and lastly by the data acquired prior to magnetising

the hand.

4.4.4 Variation of Magnetisation Orientation with Orientation of Polarising Magnet relative to Sample, and Orientation of Sample in the MEG Helmet

We obtained the field map in Figure 4.38 after magnetising the hand, palm-down, and then positioning it palm-down in the MEG scanner. When we repeated this

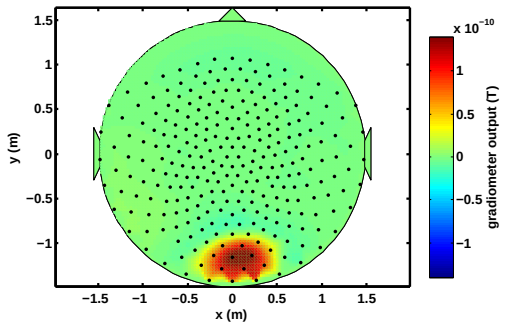

Figure 4.38: Magnetic field map showing the gradiometer output measured by the MEG SQUIDs for a hand that was magnetised palm-down on the positive pole of a magnet, and then positioned palm-down in the MEG scanner.

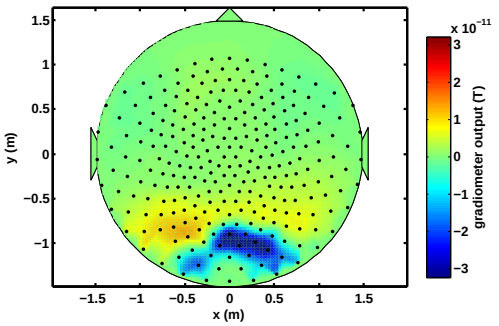

Figure 4.39: Magnetic field map showing the gradiometer output measured by the MEG SQUIDs for a hand that was magnetised palm-up on the positive pole of a magnet, and then positioned palm-down in the MEG scanner.

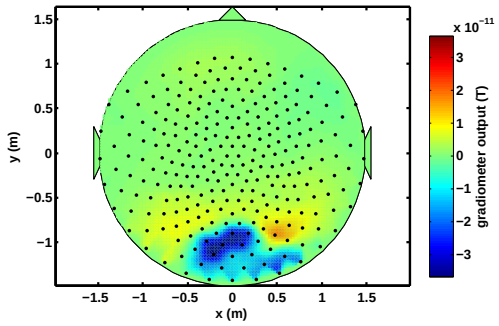

Figure 4.40: Magnetic field map showing the gradiometer output measured by the MEG SQUIDs for a hand that was magnetised palm-down on the positive pole of a magnet, and then positioned palm-up in the MEG scanner.

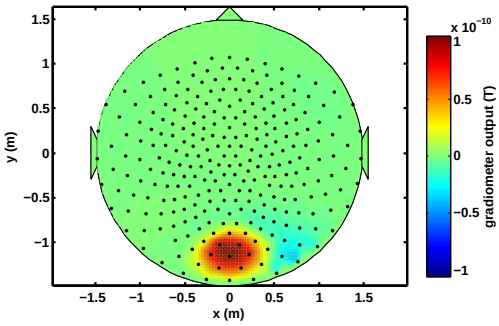

Figure 4.41: Magnetic field map showing the gradiometer output measured by the MEG SQUIDs for a hand that was magnetised palm-up on the positive pole of a magnet, and then positioned palm-up in the MEG scanner.

but magnetised the hand palm-up on the magnet, the magnetic field was reversed (Figure 4.39). The field map was also reversed when we changed the orientation of the hand in the MEG scanner (Figure 4.40). When we magnetised the hand palm-up and inserted it palm-up in the scanner, the field was once again in its original orientation.

These field maps show that the orientation of the magnetisation follows the orientation of the sample in the MEG helmet, and also depends on the orientation of the polarising magnet relative to the sample.

4.4.5 Magnetic Relaxometry in the Human Foot

In order to test whether the large magnetic field shift detected when inserting a hand in the MEG scanner is attributed to the fact that the hand could be exposed to fragments of magnetic materials, we ran the experiment on the human foot. The feet are less exposed to the environment than the hands are, and thus we expected to record a smaller magnetic field shift upon inserting the foot in the MEG scanner if the effects measured in the hand are due to environmental contamination.

We magnetised the foot for 1 min, and immediately transferred it to the helmet inside the MEG. The scan time was 180 s and the foot was inserted in the scanner at 20 s from the start of the recording. The transit time was 10 s.

Figure 4.42 shows the magnetic field map obtained immediately after inserting the magnetised foot inside the MEG scanner. The magnitude of the largest magnetic field shift measured is comparable to that measured for the wrist, and the hand.

We proceeded to look at how the magnetisation decayed over 2 h from magnetising the foot. At 1 h after magnetisation, the largest measured field was of the order of 30 pT, as seen in the field map in Figure 4.43.

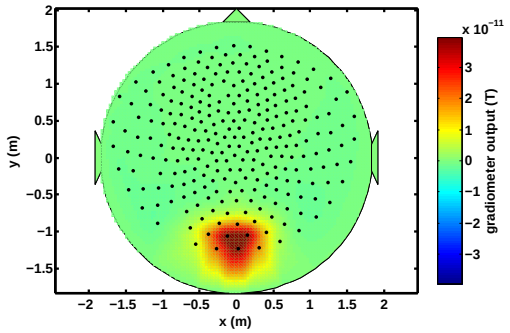

Figure 4.42: Magnetic field map showing the gradiometer output measured by the MEG SQUIDs after inserting a magnetised foot in the MEG scanner.

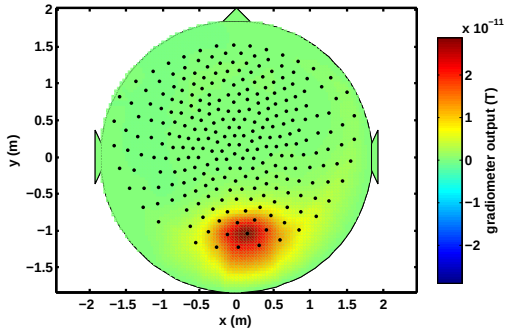

Figure 4.43: Magnetic field map showing the gradiometer output measured by the MEG SQUIDs at 1 h after inserting a magnetised foot in the MEG scanner.

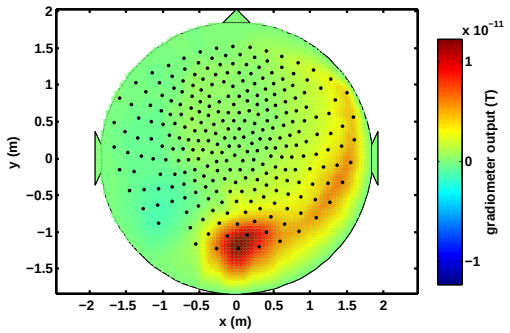

Figure 4.44: Magnetic field map showing the gradiometer output measured by the MEG SQUIDs at 2 h after inserting a magnetised foot in the MEG scanner.

At 2 h after magnetisation, the largest measured magnetic field shift is of the order of 10 pT.

Figure 4.45 shows the time evolution of the magnitude of the MNE-reconstructed dipole in 2 h from magnetisation. It can be seen that the magnitude of the MNE-

reconstructed dipole decreases with time, but it increases at 30 min and at 2 h after magnetisation. These increases are counter-intuitive, and could be attributed to something the participant's foot might have touched before scanning it at the times of the increases.

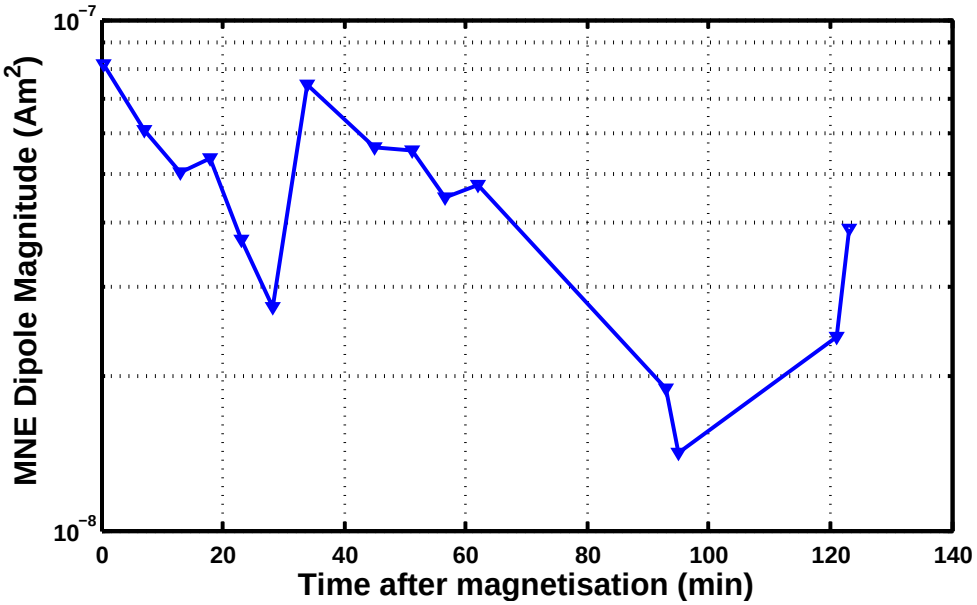

Figure 4.45: Plot showing time evolution of the magnitude of the MNE-reconstructed dipole after magnetising the foot.

4.5 Conclusions

The results of scanning different inanimate samples and analysing the decay of the magnetic fields that they produce, indicate that there is a long-lived magnetisation in many biological samples that have been exposed to a strong magnetic field. This was also observed when scanning magnetised human wrists and hands.

The origin of the long-lived magnetisation which we detect is as yet undetermined. For powdered milk, the magnetisation takes long to decay probably because of small iron traces. In the human body, the materials present include:

- Diamagnetic tissue,

- Haemoglobin-bound iron in the blood, which exhibits nearly paramagnetic behaviour,
- Antiferromagnetic ferrihydrite cores of ferritin, which is the iron-storage protein and is one of the major proteins of iron metabolism [81], and
- Ferrimagnetic magnetite [74].

Of these, only the last two could potentially yield long-lived magnetisation. It is important to determine whether or not the magnetisation of the ferrihydrite cores in ferritin may be contributing to the overall magnetisation of the tissue samples. Studies of human ferritin have determined that because of its very small grain size ($\approx 8\,\text{nm}$ diameter) and consequently very short relaxation times, the ferrihydrite core is superparamagnetic above 50 K [74], and thus since we conducted our experiments at room temperature, these particles behave as paramagnets and do not contribute to the measured remanent magnetisation. This leaves only magnetite as the likely source of the long-lived magnetisation. This is in agreement with the literature about remanent magnetisation linked to magnetite in post-mortem tissue [69], mentioned in the introductory section of this chapter.

Some of the field maps that we generated for the magnetised wrist show two peaks, rather than one. We deduced that the second peak is due to some magnetisation from the hand.

When we applied the MNE algorithm to the wrist and hand experiment, it managed to locate well the body part using the data from the magnetic field shift after magnetising the samples, or the data from the magnetisation relaxation. The localisation remained accurate till the end of our experiment (3 hours after magnetisation). Since the slightest change in the wrist/ hand's location changes the measured magnetic field distribution, it is recommended not to use the difference in the magnetic field distribution over time, when generating the MNE-reconstructed images of the wrist/hand.

The strengths of the MNE-reconstructed dipoles for the hand/wrist of different subjects are of a similar order, and the difference in saturation remanence suggests the presence of a range of particle sizes [72].

Electromyography (EMG) signals from nerves did not significantly affect our data since EMG occurs at frequencies ranging from 5 Hz to 450 Hz [82], and is not persistant over a long period of time.

When we ran the same experiment on the human foot, we saw that it takes longer for the participants to position their foot, rather than their wrist/ hand, in the scanner. However, since the strength of the magnetisation on the magnetised foot is much larger than the rest of the target volume in the MEG helmet, the foot could still be well located, even after 2 h from magnetisation.

The ability to gain and lose remanent magnetisation in our experiments is a characteristic of ferromagnetic or ferrimagnetic materials [70]. The presence of magnetite in human tissues has potential implications for at least two biomedical issues: human exposure to the strong static fields used in MRI, and the 50 Hz fields produced by the electric power system [70].

The work on long-lived magnetisation has been approved by the University of Nottinghams Faculty of Medical and Health Sciences Research Ethics Committee (reference K14072015).

Chapter 5

Theoretical Evaluation of the Use of Dipole Sources to Shimming at Ultra High Field

5.1 Introduction

As explained in previous chapters, it is difficult for Ultra Low Field (ULF) MRI to compete with high field MRI, since the higher the field is, the larger is the SNR. However, higher fields bring technical challenges. The use of higher static magnetic field strengths in MRI increases the effects of intrinsic magnetic susceptibility differences [83]. Susceptibility differences lead to field inhomogeneities which cause geometric distortion and signal loss, also known as *susceptibility artefacts* [84, 85]. In MRI, in order to mitigate these effects of inhomogeneity in the B_0 field, high quality uniform field magnets are normally supplied with a set of shim coils for fine tuning of field homogeneity [86, 87].

Magnetic homogeneity is measured in parts per million (ppm) and refers to the relative uniformity of the main magnetic field. One definition of magnetic ho-

mogeneity in ppm is the difference between the maximum and minimum field strength in a region divided by the average field, multiplied by 1 million [88]. Typically, magnetic field homogeneity over the target volume inside the bore of a magnet is 50-100ppm [89]. However, imaging requires approximately 1ppm homogeneity for good geometric sharpness and efficient spectral fat saturation [90].

The external magnetic field, B_0, is perturbed when an object with a finite magnetic susceptibility is placed inside the magnet. The Larmor frequencies will then depend on the object's spatial location. Such perturbations scale linearly with B_0 field strength, and as well as distorting the spectral lineshapes, they can also degrade the signal-to-noise (SNR) ratio.

Magnetic field inhomogeneity can be quantified by plotting field maps or measuring the linewidth as in Equation 5.1

$$\Delta\omega = \frac{2}{T_2^*} \tag{5.1}$$

where $\Delta\omega$ is the experimental linewidth and T_2^* depends on T_2 and magnetic inhomogeneity as in Equation 5.2.

$$\frac{1}{T_2^*} = \frac{1}{T_2} + \gamma\Delta B_0 \tag{5.2}$$

where ΔB_0 is the field inhomogeneity.

Since T_2^* is always smaller than T_2, a decrease in homogeneity will broaden the line width, and thus, a decrease in static magnetic field inhomogeneity is also referred to as *line broadening*.

A spin-echo (SE) sequence can refocus the contribution of field inhomogeneities

so that T_2 can be measured without being influenced by the non-uniformity of B_0. However, not all techniques can use SE procedures [91].

In this chapter, we discuss other ways of improving the field homogeneity for MRI at Ultra High Field (UHF).

5.2 Theory

The hypothesis behind this project was that we simulate the generation of magnetic fields using magnetic dipoles. We can then replace the dipoles by electromagnetic coils, or pieces of material with a large magnetic susceptibility, such as pyrolytic graphite, in a magnetic field. Knowing the magnetic dipole moment strengths required, we can calculate the number of turns and current that needs to be passed through the small electromagnetic coils, or what volume of pyrolytic graphite is required, in order to represent each dipole.

We can use this method to generate different magnetic field patterns, such as gradient fields and shimming fields. We can also generate magnetic fields that can be superimposed on an inhomogeneous field, such that the overall target field will be homogeneous.

In the following sections, we explain how magnetic fields can be generated.

5.2.1 Magnetic Fields

As explained in Section 2.2.7, the magnetic field from a magnetic dipole located at point $\mathbf{r}'$ is given by

$$\mathbf{B} = \frac{\mu_0}{4\pi} \frac{3\hat{\mathbf{n}}(\hat{\mathbf{n}}.\mathbf{m}) - \mathbf{m}}{|\mathbf{r} - \mathbf{r}'|^3}, \tag{5.3}$$

where $\mathbf{m}$ is the magnetic moment of the dipole, $|\mathbf{r} - \mathbf{r}'|$ is the linear distance between the location of the dipole and the detection point, and $\hat{\mathbf{n}}$ is the unit vector in the direction of $(\mathbf{r} - \mathbf{r}')$, as shown in Figure 2.15.

The magnetic dipole moment, $\mathbf{m}$, can be generated using electromagnetic coils, or pieces of pyrolytic graphite in a magnetic field.

Using small electromagnetic coils,

$$\mathbf{m} = NIA, \tag{5.4}$$

where N is the number of turns in the coil, I is the current passing through the coil, and A is the cross-sectional area of the coil.

As explained in Section 3.2.4, the magnetic moment, m, can also be produced by exposing a material of non-zero magnetic susceptibility, such as pyrolytic graphite, to a magnetic field.

$$\mathbf{m} = \chi \frac{B_0}{\mu_0} v, \tag{5.5}$$

where χ is the susceptibility of the material, v is the volume of the sample, and B_0 is the magnetic field to which it is exposed.

Pyrolytic Graphite

Since graphite is present in different forms, with varying amounts of impurities, it has a large range of magnetic susceptibilities, listed in Table 5.1.

Highly Oriented Pyrolytic Graphite (HOPG) refers to particular oriented car-

Type of graphite	χ/ppm
Polycrystalline	-14
	-160
	-204
Highly ordered pyrolytic[a]	-450
Highly ordered pyrolytic[b]	-85

Table 5.1: Magnetic volume susceptibility (χ) for different forms of graphite [92].
[a] Perpendicular to graphite basal plane.
[b] Parallel to graphite basal plane.

bon. It is typically manufactured by heating a hydrocarbon to decomposition temperature without oxygen. It has a high degree of preferred crystallographic orientation, thus leading to a highly anisotropic magnetic susceptibility. The diamagnetic susceptibility of HOPG, perpendicular to the graphite basal plane is the highest known [93]. The anisotropy of HOPG means that when placed in a magnetic field, its magnetic moment is not necessarily aligned with the applied field.

5.2.2 Magnetic Field Mapping

Field maps are a means of measuring B_0 inhomogeneity. A B_0 field map is an image in which pixel intensity is proportional to the strength of the local magnetic field. Quadrature detection of the MR signal gives information about the angular phase (ϕ) of measured transverse magnetisation according to

$$\phi = \phi_0 - \gamma \Delta B \; TE \tag{5.6}$$

where ϕ_0 is the initial phase of the magnetisation, ΔB is the field offset, and TE is the echo-time. Multiple images collected for incremental values of TE provide a B_0 field map. Phase differences that fall outside of the range $[-\pi, \pi]$ must be unwrapped. Unwrapping techniques can be spatial or temporal.

B_0 maps can be obtained using echo planar or spiral imaging. These techniques are useful for estimating in-vivo inhomogeneity. The accuracy depends on the largest τ value and the precision on the number of τ values, where τ is the change in echo time. For shimming the whole brain at 3 T, two to four τ values can be used and the maximum τ value can be $4 - 6ms$ [94].

5.2.3 Spherical Harmonics

In the absence of current sources and magnetic materials, any Cartesian component of the magnetic field, H, follows Laplace's equation,

$$\nabla^2 H = 0 \tag{5.7}$$

Equation 5.7 can be solved by decomposition into spherical harmonic functions, such that

$$T_{nm} = r^n P_{nm}(cos\theta) \begin{pmatrix} S_{nm} \sin m\phi \\ C_{nm} \cos m\phi \end{pmatrix} \tag{5.8}$$

where S_{nm} and C_{nm} are constants, P_{nm} are Ferrer's associated Legendre polynomials, r is the spherical radius, θ is the angle of declination and ϕ is the azimuthal angle.

Spherical harmonics are eigenfunctions of the Laplacian. In $\mathbf{R}^3$, $\{(x, y, z) : x, y, z \ \in \mathbf{R}\}$, the Laplacian is given in Equation 5.9.

$$\Delta^2 = \frac{\partial^2}{\partial x^2} + \frac{\partial^2}{\partial y^2} + \frac{\partial^2}{\partial z^2} \tag{5.9}$$

In spherical coordinates, $\{(r, \theta, \phi) : r \in \mathbf{R}_+, \theta \in [0, 2\pi), \phi \in [0, \pi]\}$ and $(x = r\cos\theta\sin\phi, y =$

$r \sin\theta \sin\phi, z = r \cos\phi$).

Table 5.2 gives the notation and Cartesian form of spherical harmonics up to $n = 3$ and $m = 1$. Spherical harmonics with $m = 0$ are called zonal and are generated by circular loops of wire or magnetic material, symmetrically distributed around the z-axis. Terms generated with $m \neq 0$ are tesseral and are generated by saddle coil arrangements that are not axially symmetric [89].

n	m	Notation	Cartesian Form	Interaction Type
0	0	Z0	1	0
1	0	Z1	z	1
1	1	X	x	0
		Y	y	0
2	0	Z2	$2z^2 - x^2 - y^2$	1
2	1	XZ	xz	2
		YZ	yz	2
2	2	XY	xy	1
		X2-Y2	$x^2 - y^2$	2
3	0	Z3	$2z^3 - 3z(x^2 + y^2)$	2
3	1	XZ2	$x(4z^2 - x^2 - y^2)$	2
		YZ2	$y(4z^2 - x^2 - y^2)$	2

Table 5.2: Spherical harmonics in cartesian form [95].

5.2.4 Basics of Shimming

Shimming of the B_0 field refers to the process of adjusting the applied fields to optimise the magnetic field homogeneity over a voxel [88, 91].

In the past, the field homogeneity of the magnet was improved by aligning the magnet pole faces to be more parallel by turning large bolts that held the pole faces. If the bolts ran out of range, thin pieces of brass, called *shim stock*, were placed between the magnet yoke and pole pieces. The process of placing and removing shim stock became known as *shimming* [89].

An electronic shimming process was later developed. A series of small electro-

magnets that produce very specific magnet field contours are placed around the sample. Each small electromagnet can be used to adjust the field. The process of adjusting the current passing through each electromagnet to modify the magnetic field homogeneity retained the name *shimming* [95].

Shim hardware allows the compensation of macroscopic susceptibility, i.e. large scale susceptibility variations. There are three main types of shimming:

- passive shimming,
- active shimming, and
- superconducting shimming.

In order to minimise the subject-independent B_0 field inhomogeneity, magnets are shimmed by a trained service engineer when installed on-site, using either passive shimming, whereby ferromagnetic discs/plates are used, or active shimming whereby additional superconducting shim coils are generally employed [96].

5.2.5 Passive Shimming

In passive shimming, also known as ferroshimming, the position of the iron or steel pieces around the bore of the magnet is adjusted until optimum field homogeneity is achieved. This is generally carried out at the time of installation and compensates for inhomogeneity attributed to the physical location of the magnet [97].

Passive shimming can also be subject-specific. Magnetic materials are positioned around a sample to cancel unwanted inhomogeneity. The passive shim field B_{PS} is combined with the active shim field to satisfy the shimming condition in Equation 5.11. Paramagnetic, diamagnetic and ferromagnetic materials can be used for passive shimming.

Passive shimming has also been used to reduce the inhomogeneity in the human head. The human head exhibits large inhomogeneities because of the difference in magnetic susceptibilies of air in the sinus and auditory cavities, and in the surrounding tissues [91, 98]. Placement of a small amount of highly diamagnetic material in the subject's mouth is both effective and safe to passively shim the brain [92].

Wilson et al used four 3 mm thick plates of HOPG, shaped to easily fit in the roof of the mouth, as in Figure 5.1. The plates were oriented perpendicular to B_0 and their total volume was 6.1 cm^3. The shim was fully enclosed within a customised and disposable mouth mould of the subject made from polymorph plastic.

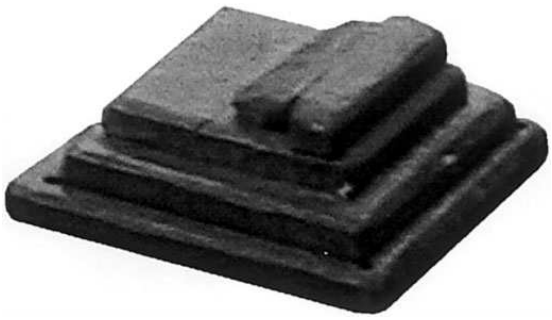

Figure 5.1: Photograph of the mouth shim, comprising four plates of pyrolytic graphite. Image taken from [92].

The amount of distortion in the B_0 field outside a sphere of radius a, made of a paramagnetic material, and placed inside a constant static magnetic field B_z is

$$\Delta B_z(r,\theta) = \frac{\chi}{3}\left(\frac{a}{r}\right)^3 (3\cos^2\theta - 1)B_z \tag{5.10}$$

where θ is the polar angle. In the human head, the paramagnetic sphere corresponds to the sphenoid / ethmoid air space. If a second material is placed near the first, then the field distortion from both will add linearly to first order if $\chi << 1$ for both materials. Wilson et al introduced the diamagnetic material near, but inferior to the paramagnetic sphere.

5.2.6 Active Shimming / RT Shimming

Active shimming, also known as Room Temperature (RT) shimming, is widely used in high field in-vivo MR applications. It refers to the use of sets of dedicated electromagnetic coils that can be tuned to shim the system for each subject and each sequence within a protocol, irrespective of patient size.

In order to generate a pure B_0 field, the condition in Equation 5.11 must be satisfied.

$$B_s(\mathbf{r}) + \delta B_0(\mathbf{r}) = -(B_{RTS}(\mathbf{r}) + B_{PS}(\mathbf{r})) \tag{5.11}$$

where B_s is the sample-induced field, δB_0 represents the imperfections in the field, B_{RTS} is the room temperature shim field and B_{PS} is the passive shim field.

Theoretically, any inhomogeneity can be shimmed with the correct B_{RTS}. However, in practice, the utility of an RT shim system depends on how many of the spherical harmonic terms are physically realisable. In in-vivo systems, this number is truncated at about second order.

Shim coils used to address the B_0 inhomogeneity have been constrained to non-spherical geometries since a spherical coil does not provide sufficient access to NMR samples. In in-vivo applications, shim coils are usually constructed on cylindrical formers located concentrically between the imaging gradient former and magnet heat shields. Helmholtz and Golay saddle can produce first and second order terms over extended regions in the centre of the coil. Typical shim coil designs can be seen in Figure 5.2.

Higher order shim coils can be produced by combining elements from lower order shim coils.

Standard RT shims are constrained by the Biot-Savart law and available bore

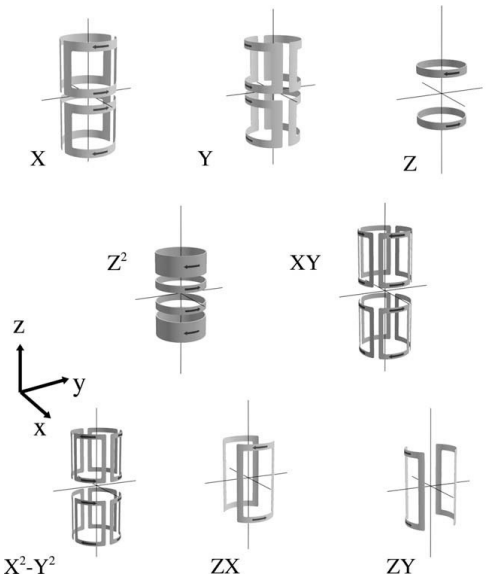

Figure 5.2: Shim coil designs for first and second order coils [99].

space. The Biot-Savart law states that the magnetic field generated by a small current element, rises linearly with the current amplitude and falls off quadratically with distance from the current element. The construction of higher order coils is more complicated for in-vivo systems because of the large sample volume. More current, or more turns in the coils are required for in-vivo systems. Thus, more bore space in the form of coil turns and coolant plumbing is needed.

Resistance and inductance depend on the shim former diameter and number of coil turns. The inductance of the current loop rises linearly with the coil radius and quadratically with the number of turns. A target field boundary element method optimises the target field errors, inductance and resistance. Along with the reduced former radius, these shim coils can be more efficient while using reduced inductances and resistances.

High efficiency and low resistance are paramount design factors in RT shim coils.

Local Active Shimming

Local electromagnetic shim coils can be placed in the human oral cavity. An array of three independently adjustable coils can be adjusted to make any angle with the z-axis. Shim fields produced by localised current loops can be optimised independently to shape a net local-shim on a subject-specific basis.

Juchem et al [98] use a small array of external local electrical coils to provide a local and high amplitude shim field in the pre frontal cortex. The zero to second order spherical harmonic terms are included in this shimming method to rectify potential smooth, large-scale field alterations over the rest of the brain. The method is inexpensive and requires only a limited number of external coils.

5.2.7 Dynamic Shim Updating (DSU)

The above methods work sufficiently with small shim volumes. The field maps in Figure 5.3 illustrate the effects of whole-brain least squares optimisation of B_0 field homogeneity in the human brain at 3 T. Second order shimming significantly improved the homogeneity. On the other hand, hardly any improvement can be

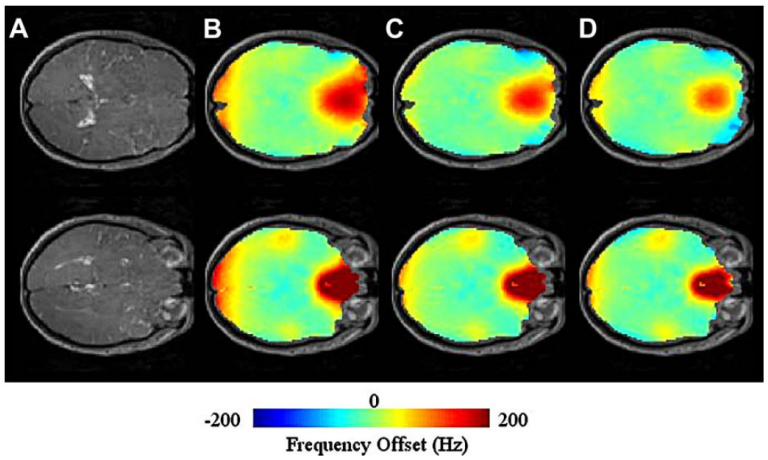

Figure 5.3: (A) MRI of two axial slices, Residual inhomogeneity after (B) first order shimming, (C) inclusion of second order shimming, (D) inclusion of third order shimming. Image taken from [91].

noted from the second order to the third order shimming in Figure 5.3.

Dynamic shimming is a technique whereby shims are updated in real time during MR acquisitions. This technique breaks down larger volumes into smaller voxels or single slices, and uses different shim settings for the different slices/voxels [100]. Volume specific shim settings are fast to adjust and thus, it is possible to optimise the magnetic field homogeneity over the whole brain by improving for the smaller volumes.

A set of generic, circular coils can be converted to a powerful magnetic field modelling system where each of the electrical coils is driven individually [101].

The principle of DSU for multi-slice GE MRI is shown in Figure 5.4. Whilst spins in the individual slices are excited to acquire a signal, the static shim setting remains unchanged, but the settings in the dynamic shim amplifiers are updated during each slice excitation. Static shim settings are usually sufficient for voxels in the centre of the brain, but voxels that are located close to the sinus or auditory cavities need locally optimised shim settings.

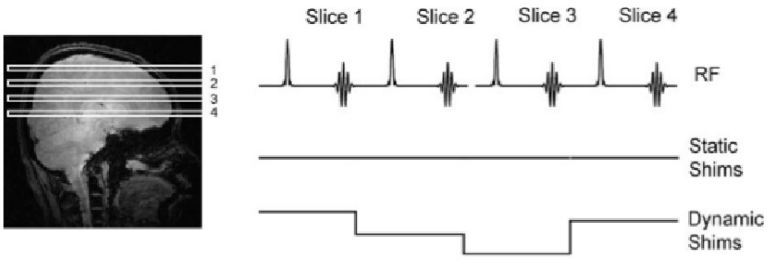

Figure 5.4: The principle of DSU in multi-volume acquisitions. Image taken from [91].

Fast updates in the shim amplifiers are critical for DSU. Currently, it is common that shim systems upload settings to the shim control hardware via serial communication before run-time. However, when used in DSU applications, two problems arise. Firstly, serial communication is slow and secondly, host computers cannot be relied on to send data at a specific time. The aforementioned problems can be mitigated by modifying shim control hardware to store locally the slice data

ahead of time.

Temporal DSU reduces in real-time B_0 fluctuations induced from small movements such as from subject respiration or/and movement [91].

Volume parcellation for improved DSU can be yet more efficient than DSU at improving the magnetic field homogeneity, since it can yield approximately the same results as slice-based dynamic shimming that uses up to third order shim terms. Sequential performance of shimming and image data acquisition over cuboidal sub-volumes, as opposed to planes, further improves the magnetic field inhomogeneity [102].

Passive shimming can offer more global homogeneity than DSU optimised over whole slices. However, DSU can be used following passive shimming to clean up the remaining inhomogeneity.

5.2.8 Coil Design

In designing shim coils, ideally each coil produces a given orthogonal harmonic field variation. To generate the desired field homogeneity correction within the limits imposed by the finite supply current available, coils should have:

- High current efficiency,
- Short switching time,
- Low power consumption, and
- Minimal interaction with other equipment [86].

Therefore, ways to improve the quality of the coils include:

- Use of distributed-winding coils,
- Stream functions for current density,

- Cylindrical harmonic expansion of magnetic field variation,
- Minimisation methods for power dissipation and inductance,
- Improved fabrication techniques, and
- High-current gradient drivers [86].

The most fundamental equation used in coil design is the Biot-Savart law (Equation 5.3). This equation is used to calculate fields produced by discrete-wire coils [103]. Where conductors of large cross-section are used, it is not appropriate, unless the current distribution within the conductor is known.

The measure of coil performance depends on the application for which it is used. For MRI, a figure of merit, β, suggested by Turner [104] is

$$\beta = \frac{\eta^2/L}{\sqrt{\frac{1}{V}\int d^3\mathbf{r}\left(\frac{B(\mathbf{r},\phi,\mathbf{z})}{B_0(\mathbf{r},\phi,\mathbf{z})}-1\right)^2}} \tag{5.12}$$

where η is the coil efficiency, L is the inductance, V is the volume of interest, B is the desired field, and B_0 is the achieved field.

Coil design methods are classified into coils with discrete windings, and the stream function method [86].

The simplest discrete coil is the Helmholtz pair, which is made up of two equal coaxial circular coils, at a spacing of their radius. Magnetic field patterns can be generated by varying the current and/or the number of turns in the coil, but also by keeping the current and coil turns fixed and changing the current element position [105].

The stream function, $I(\mathbf{z},\phi)$, when differentiated with respect to $\mathbf{z}$ or ϕ, gives the current density in the azimuthal or axial direction, respectively. $I(\mathbf{z},\phi)$ is the integral of the current density.

5.2.9 The Target Field Method

A powerful method of designing coils is the target field method [106]. Ampere's law is inverted to calculate the currents required directly from the specified desired field. The target field method uses the Fourier Transform. It assumes that the source of the magnetic field is a current density, **J**, on a shell of simple geometry (e.g. cylinder, plane, sphere). Target field methods include minimum inductance designs [107], which are preferred for minimising coil risetime, and minimum power designs [108], which are preferred when space is limited.

5.2.10 Equivalent Magnetisation Current (EMC) Method

The Equivalent Magnetisation Current method is based on the known equivalence between current and magnetisation. This coil design method is independent of the current-carrying surface. The surface can be of any arbitrary shape, and it does not need to be connected. It is discretised in small elements in which magnetisation is directed parallel to the direction of the normal to the surface.

By applying the EMC method, the equivalent magnetic energy, delivered power, force and torque can be obtained [109].

5.3 Method

The hypothesis of this study was that we can use a small array of external electromagnetic coils or pieces of pyrolytic graphite, to generate a target field that is specified at discrete target locations.

We simulated the generation of a particular magnetic field distribution over a specified volume, using magnetic dipoles. We used `MATLAB` to run these simulations. The magnetic fields that we tried to generate were:

- a z-gradient of strength $1\,\mathrm{mT\,m^{-1}}$,
- an x-gradient of strength $1\,\mathrm{mT\,m^{-1}}$,
- the spherical harmonic XY, with a peak of 0.1 mT over the target volume,
- the spherical harmonic $Z3$, with a peak of 0.1 mT over the target volume, and
- the inverse of a brain field map.

We laid 48 dipoles on the surface of a cylinder. The cylinder had a cross-sectional diameter of 27 cm, and a height of 35 cm. The 48 dipoles were arranged in 6 rings, equally distributed along the length of the cylinder. The 8 dipoles in each ring were equidistantly spaced around the cross-sectional circumference.

The target points were arranged in a cubic array of resolution 1 cm, within a spherical volume of diameter 19 cm. The centres of the cylinder and sphere coincide. Figure 5.5 shows the arrangement of the dipoles, and the target volume.

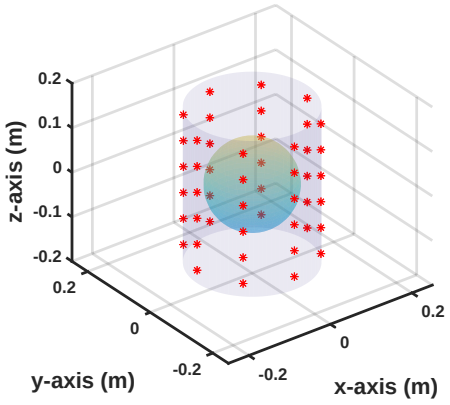

Figure 5.5: Diagram showing the dipole positions on a cylindrical surface and the spherical target volume.

We ran simulations with dipoles whose moments are aligned normal, or parallel, to the cylinder surface as shown in Figures 5.6 and 5.7. Dipoles whose moments are aligned parallel to the field can be implemented using an isotropic magnetic material, while an anisotropic material, such as HOPG, is needed to produce dipoles that are not oriented parallel to the field. Electromagnetic coils can also

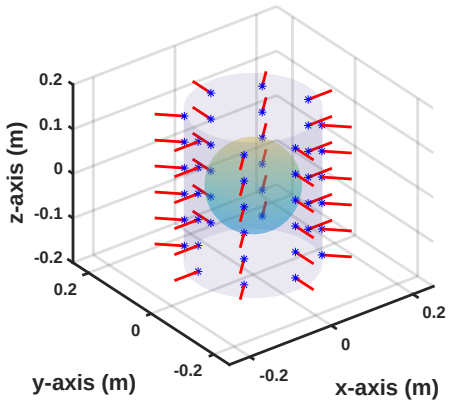

Figure 5.6: Diagram showing dipoles normal to cylinder surface.

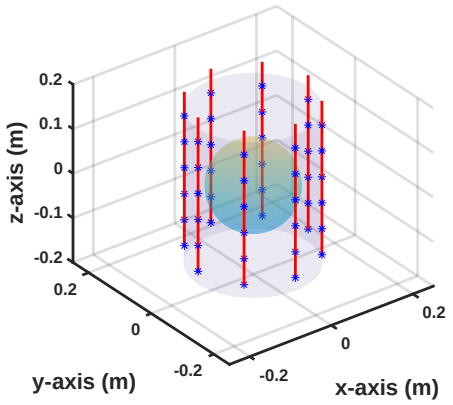

Figure 5.7: Diagram showing dipoles parallel to cylinder surface.

be used to implement dipoles whose moment is aligned parallel to the field, as well as in any other direction.

We used the Biot-Savart law to calculate the dipole strengths required to generate the target field. In order to reduce the total "power" of the dipoles, which could be used to minimise the power dissipation in an array of electromagnetic coils, or the total amount of material in an array of passive shims, we then applied a constraint on the dipole strength. We used the regularised least squares method to minimise

$$\frac{1}{M}\sum_{m=1}^{M}\left(B_{m\_target}-B_m\right)^2+\lambda_P\frac{1}{N}\sum_{n=1}^{N}k_n^2 \tag{5.13}$$

where M is the number of target points at which the desired magnetic field is specified, B_{m_target} is the target magnetic field at the m^{th} spatial position, B_m is the magnetic field generated with the optimised dipole strengths at the same position, λ_P is an adjustable constant used to weigh the regularisation term which minimises the total power of the dipoles, N is the total number of dipoles, and k_n is the n^{th} dipole magnitude. The starting values of k in the minimisation algorithm were set to the dipole strengths required to generate the target field without constraints. In order to solve this problem, we employed the function `fmincon` provided in the `MATLAB` optimisation toolbox.

The value of λ_P was chosen such that the maximum difference between the target field and the generated field did not exceed 10 µT. In the cases when the maximum peak difference between the target field and the generated field was larger than 10 µT for any λ_P, we set λ_P at the value that gave the least maximum field difference.

We then allowed the dipole moments to align in an optimal orientation, and looked at the improvement in the magnetic field generation, and power requirements.

We also applied our algorithm to a shim for the brain. The hypothesis was that if we generate a field that is opposite to the field map of the brain, we can superimpose it on the field map of the brain such that the resultant field is zero.

Prior to shimming for the brain, we acquired a B_0 field map of the brain at 7 T, using a TE of 9 ms and TR of 31 ms. The image was 112 x 112 x 25 voxels, and the voxel size was 2 mm.

Using the modulus data, we generated a mask that removed all data that was higher than 15 % of the maximum value. We applied this mask to the phase data. The remaining target field had a maximum value of 5.6×10^{-7} T, and RMS 1.7×10^{-7} T. We then used the dipole arrangement to generate a field that is opposite to the phase data. The dipoles were allowed to align themselves at an

optimal angle. The target points had a resolution of 2 mm, rather than 1 cm because rapid target field variations require a higher resolution of target points [109].

In selecting a suitable value for λ_P in this case, we set λ_P as the smallest value possible that yields dipole strengths smaller than the unconstrained dipole strengths.

5.4 Results

5.4.1 Creating a Z-Gradient using Magnetic Dipoles

Dipoles Oriented Normal to the Cylinder Surface, with No Constraints on their Strength

Figure 5.8 shows the dipole strengths that are required to generate a target gradient field in the z-direction, with a strength of $1\,\mathrm{mT\,m^{-1}}$, using dipoles whose moments are aligned normal to the cylinder surface, when no constraints are applied on their strength.

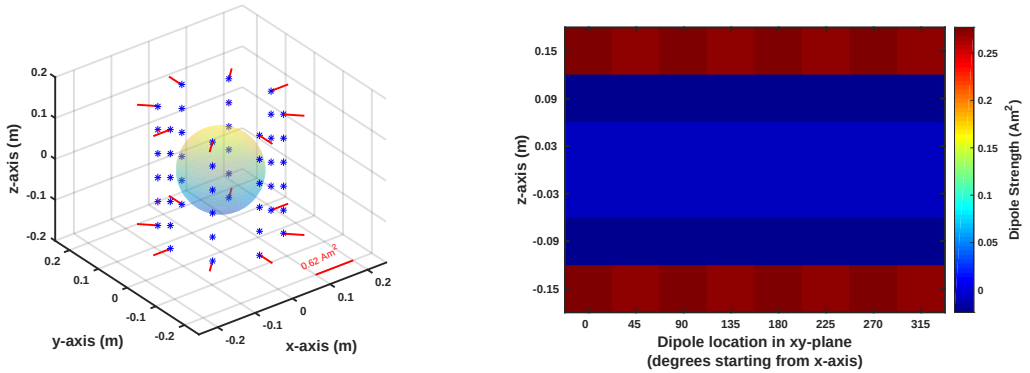

Figure 5.8: Diagram showing the dipole strengths required to generate a z-gradient field of $1\,\mathrm{mT\,m^{-1}}$, if dipole moments are oriented normal to the cylinder surface, and their strength is not constrained.

The actual fields generated at points within the target volume, from these dipoles are shown in Figure 5.9. In this figure and all similar subsequent figures, the

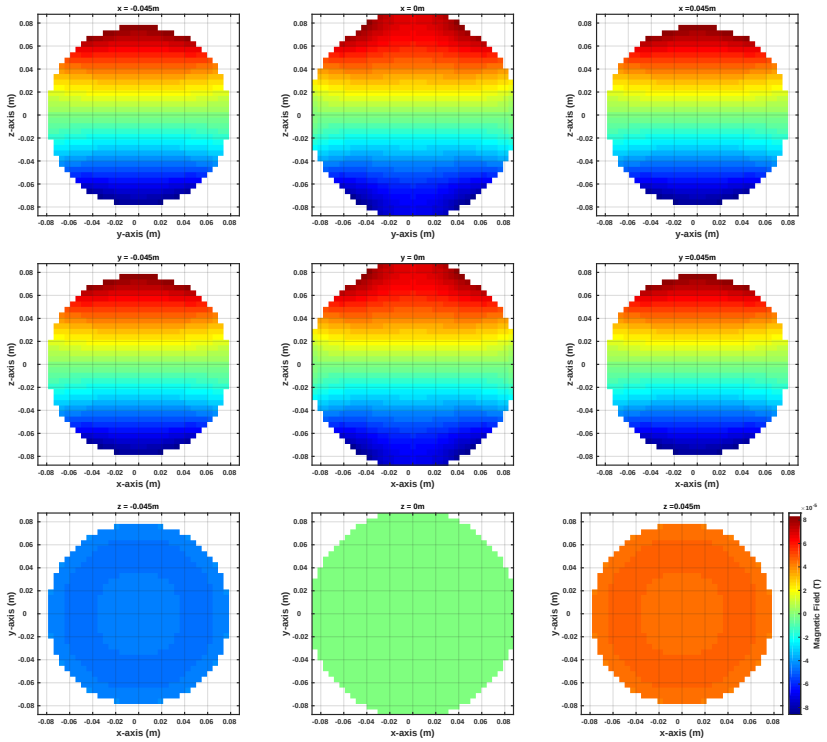

Figure 5.9: The magnetic field generated for a target field which corresponds to a z-gradient of $1\,\mathrm{mT\,m^{-1}}$, using dipoles whose magnetisation vectors are oriented normal to the cylinder surface, and whose strengths are unconstrained.

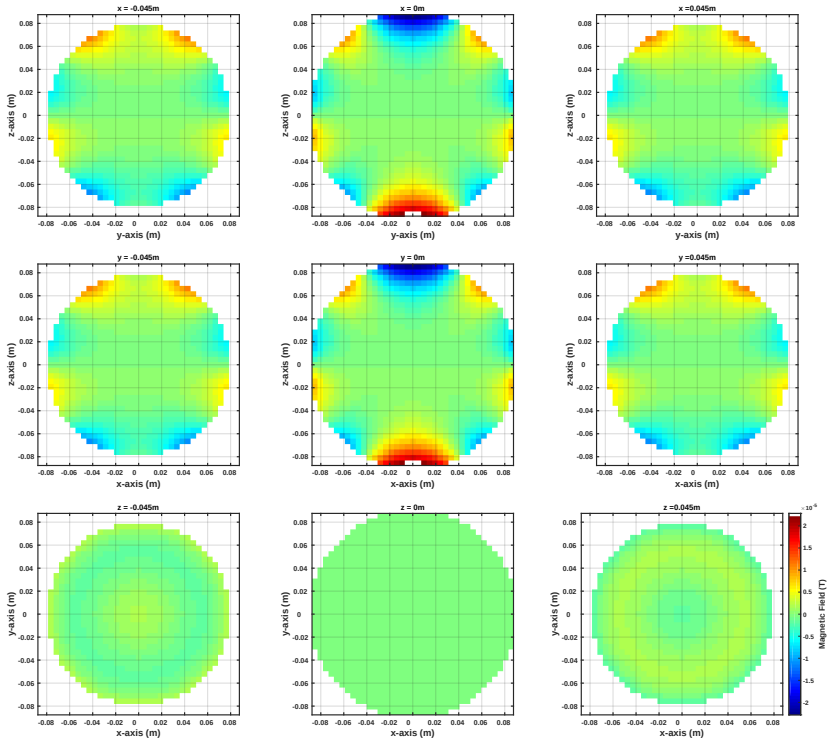

Figure 5.10: The difference between the magnetic field generated, and the target field which corresponds to a z-gradient of $1\,\mathrm{mT\,m^{-1}}$, using dipoles whose magnetisation vectors are oriented normal to the cylinder surface, and whose strengths are unconstrained.

first row shows three slices in the y-z plane, the second row shows three slices in the x-z plane, and the third row shows three slices in the x-y plane.

Figure 5.10 shows the difference between the magnetic field generated, and the target gradient field of $1\,\mathrm{mT\,m^{-1}}$ in the z-direction, using dipoles whose magnetisation vectors are oriented normal to the cylinder surface, and whose strengths are unconstrained.

Dipoles Oriented Normal to the Cylinder Surface, with Constrained Total Power Consumption

We then constrained the total dipole power, as in Equation 5.13. We looked at how the magnetic field deviation between the target field and the generated field, varied with different constraints on the power.

Figures 5.11 - 5.14 show the magnetic field generated with the optimised dipole strengths for different values of λ_P, and Figure 5.15 shows how the peak and RMS dipole strength, and the peak and RMS field deviation between the target field and the generated field vary for different values of λ_P.

It can be seen in Figure 5.15 that with a higher λ_P, the dipole strengths are kept to smaller values and the difference between the target field and the generated field is larger. With a smaller λ_P, the dipole strengths are allowed to take larger values, and the difference between the target field and the generated field is less.

We also saw that reducing λ_P, does not reduce the difference between the target field and the generated field indefinitely. There is a value for λ_P below which, the difference between the target field and the generated field does not change much. Thus, the generated magnetic field in Figure 5.14 for $\lambda_P = 0.001$ is not significantly closer to the target field than the magnetic field in Figure 5.13 for $\lambda_P = 0.01$.

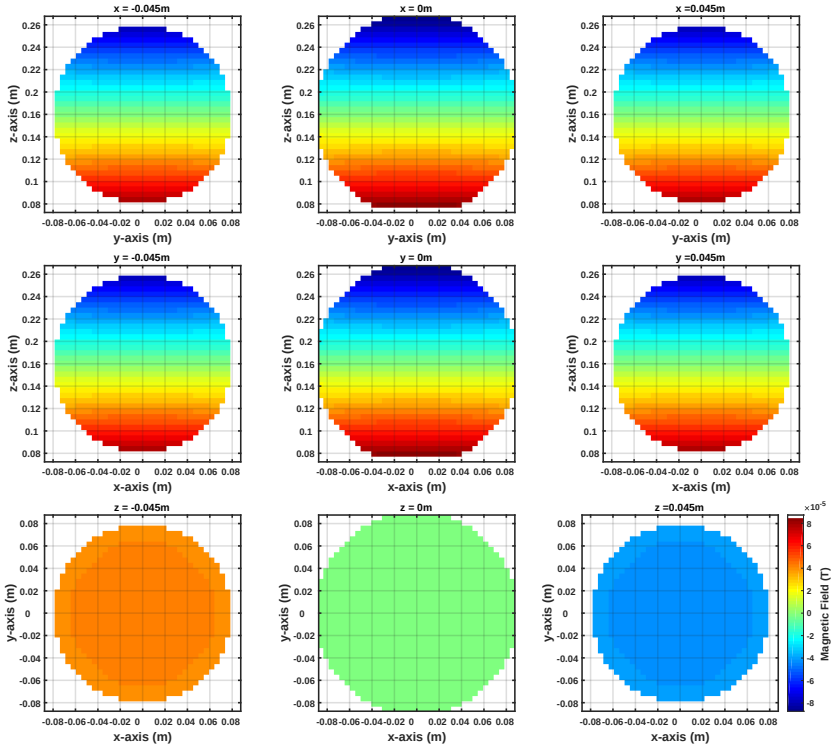

Figure 5.11: The difference between the magnetic field generated, and the target field which corresponds to a z-gradient of $1\,\mathrm{mT\,m^{-1}}$, using dipoles whose magnetisation vectors are oriented normal to the cylinder surface, and optimised to reduce the total power with a regularisation constant $\lambda_P = 10$.

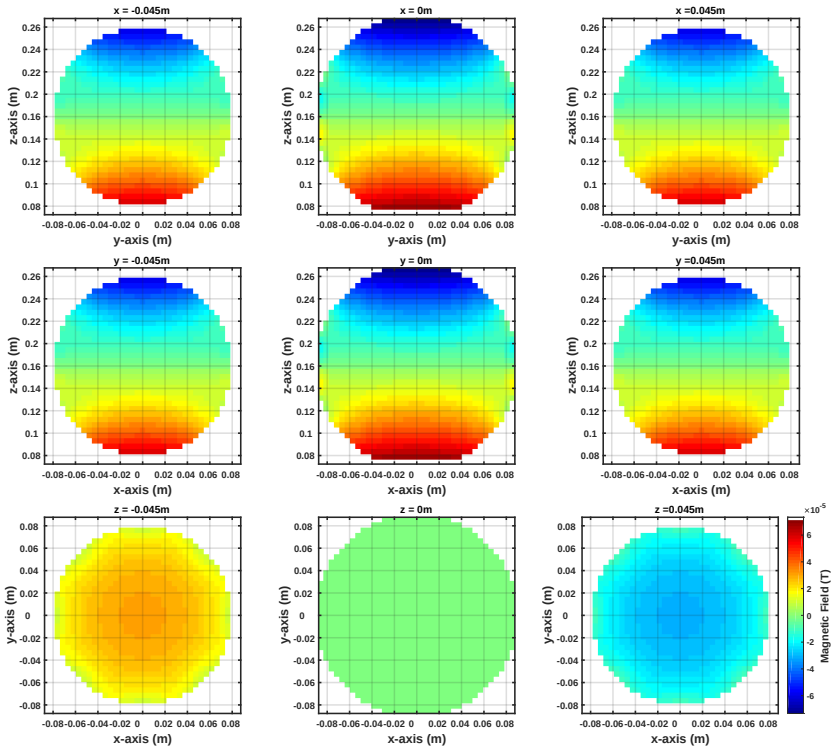

Figure 5.12: The difference between the magnetic field generated, and the target field which corresponds to a z-gradient of $1\,\mathrm{mT\,m^{-1}}$, using dipoles whose magnetisation vectors are oriented normal to the cylinder surface, and optimised to reduce the total power with a regularisation constant $\lambda_P = 1$.

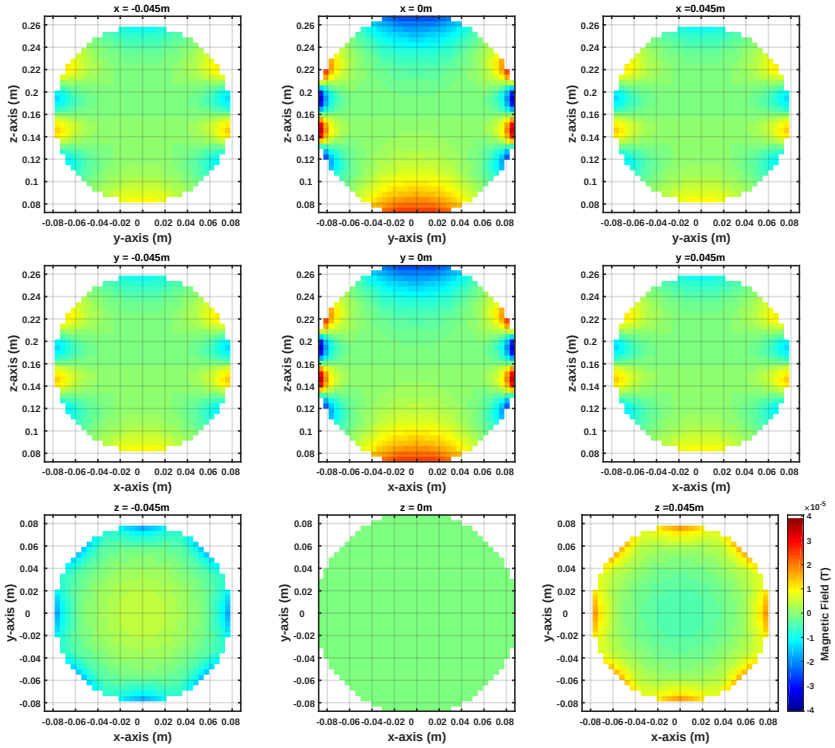

Figure 5.13: The difference between the magnetic field generated, and the target field which corresponds to a z-gradient of $1\,\mathrm{mT\,m^{-1}}$, using dipoles whose magnetisation vectors are oriented normal to the cylinder surface, and optimised to reduce the total power with a regularisation constant $\lambda_P = 0.01$.

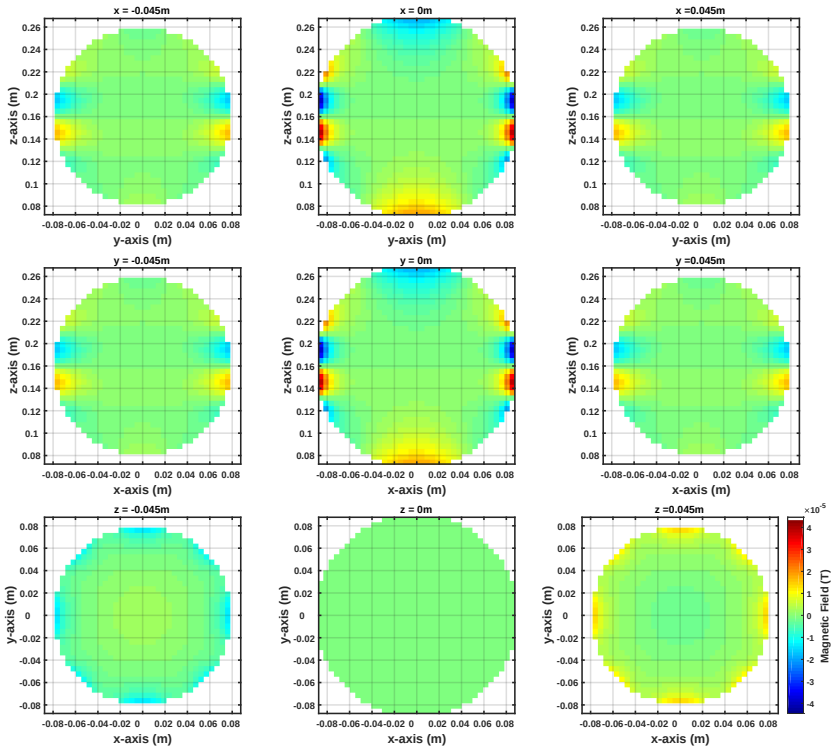

Figure 5.14: The difference between the magnetic field generated, and the target field which corresponds to a z-gradient of $1\,\mathrm{mT\,m^{-1}}$, using dipoles whose magnetisation vectors are oriented normal to the cylinder surface, and optimised to reduce the total power with a regularisation constant $\lambda_P = 0.001$.

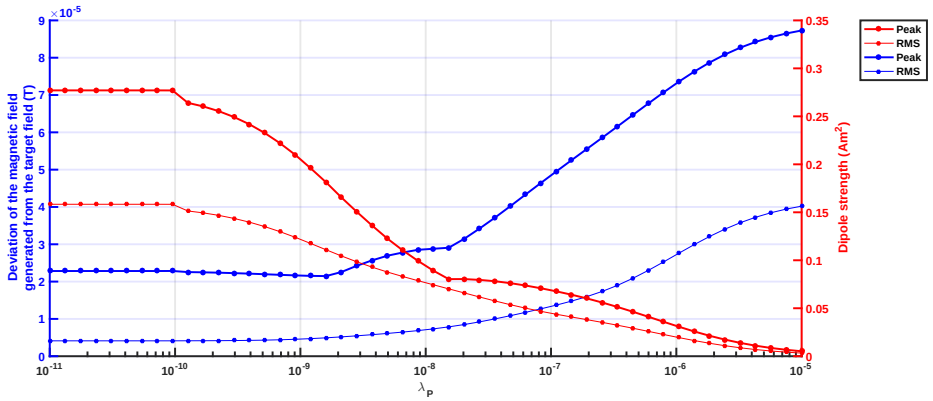

Figure 5.15: A plot of peak and RMS dipole strengths, and peak and RMS field deviations of the magnetic field generated from the target field which corresponds to a z-gradient of $1\,\mathrm{mT\,m^{-1}}$, using dipoles whose magnetisation vectors are oriented normal to the cylinder surface, against different values of the regularisation constant, λ_P.

In all the following simulations that constrain the total dipole power, the highest λ_P was chosen such that the peak field deviation did not exceed $10\,\mu\mathrm{T}$ when possible, and otherwise we set λ_P at the value that gave the least maximum field difference.

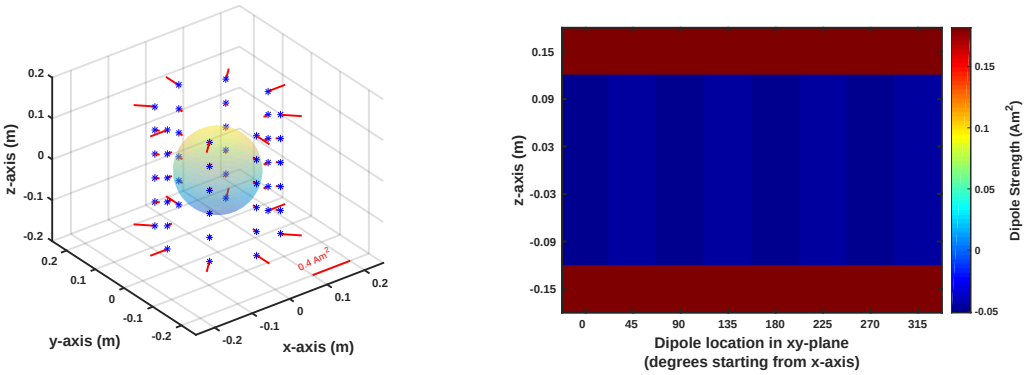

Figure 5.16: Diagram showing the dipole strengths required to generate a target field which corresponds to a z-gradient field of $1\,\mathrm{mT\,m^{-1}}$, if dipole moments are oriented normal to the cylinder surface, and optimised to reduce the total power with a regularisation term $\lambda_P = 1.56 \times 10^{-9}$.

Figure 5.16 shows the optimised dipole strengths required to generate a z-gradient field of $1\,\mathrm{mT\,m^{-1}}$, with moments oriented normal to the cylinder surface, and with a power regularisation term $\lambda_P = 1.56 \times 10^{-9}$. Figure 5.17 shows the magnetic field generated with these optimised dipole strengths, and Figure 5.18 shows the difference between the magnetic field generated, and the target field.

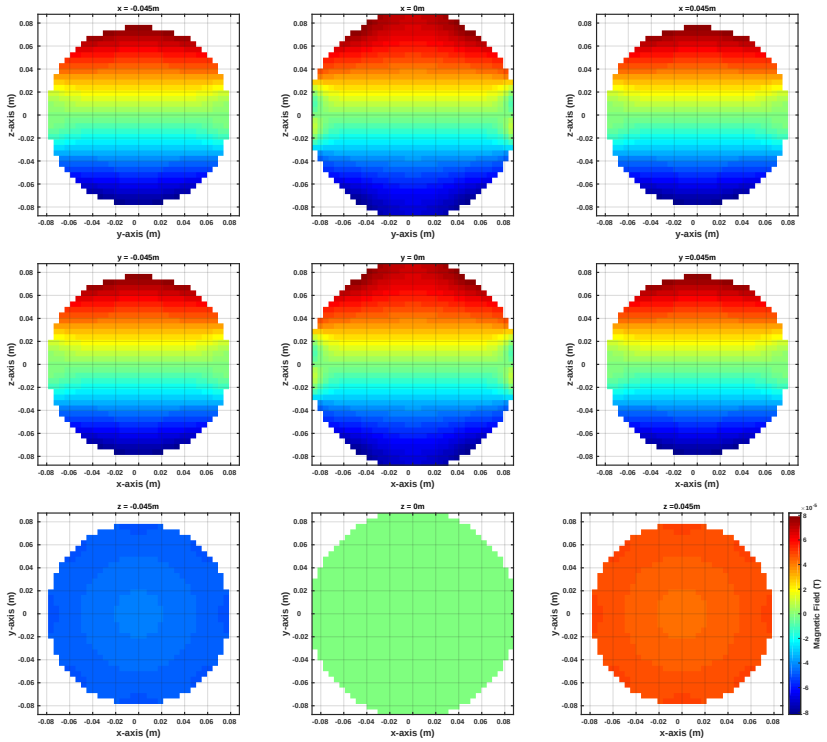

Figure 5.17: The magnetic field generated for a target field which corresponds to a z-gradient of $1\,\mathrm{mT\,m^{-1}}$, using dipoles whose magnetisation vectors are oriented normal to the cylinder surface, and optimised to reduce the total power with a regularisation term $\lambda_P = 1.56 \times 10^{-9}$.

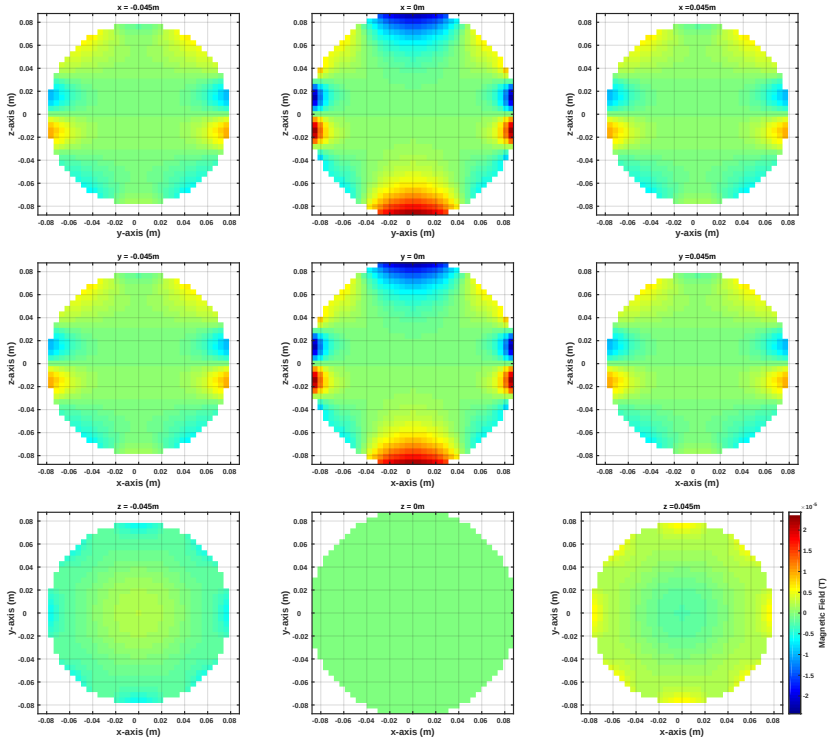

Figure 5.18: The difference between the magnetic field generated, and the target field which corresponds to a z-gradient of $1\,\mathrm{mT\,m^{-1}}$, using dipoles whose magnetisation vectors are oriented normal to the cylinder surface, and optimised to reduce the total power with a regularisation constant $\lambda_P = 1.56 \times 10^{-9}$.

Dipoles Oriented Parallel to the Cylinder Surface, with No Constraints on their Strength

We then used dipoles that are oriented parallel, rather than normal, to the cylinder surface, and used them to generate the $1\,\mathrm{mT\,m^{-1}}$ gradient field in the z-direction. Figure 5.19 shows the dipole strengths that are required if no constraints are applied on their strength.

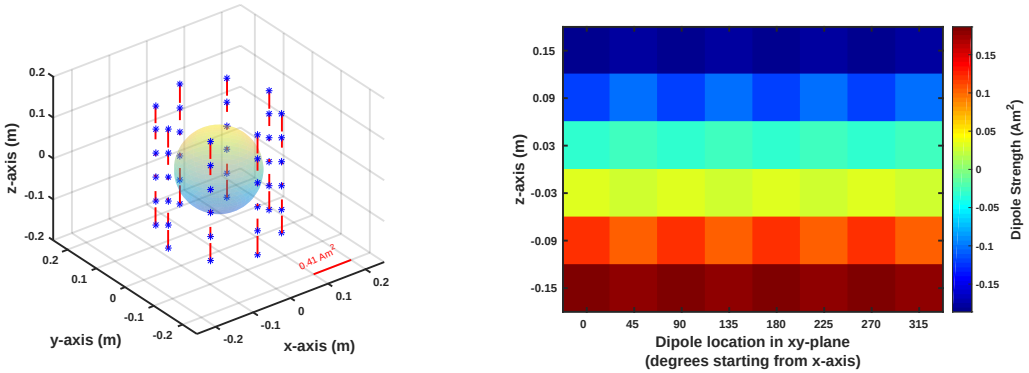

Figure 5.19: Diagram showing the dipole strengths required to generate a z-gradient field of $1\,\mathrm{mT\,m^{-1}}$, if dipole moments are oriented parallel to the cylinder surface, and their strength is not constrained.

The actual fields generated at points within the target volume, from these dipoles are shown in Figure 5.20. Figure 5.21 shows the difference between the magnetic field generated, and the target field.

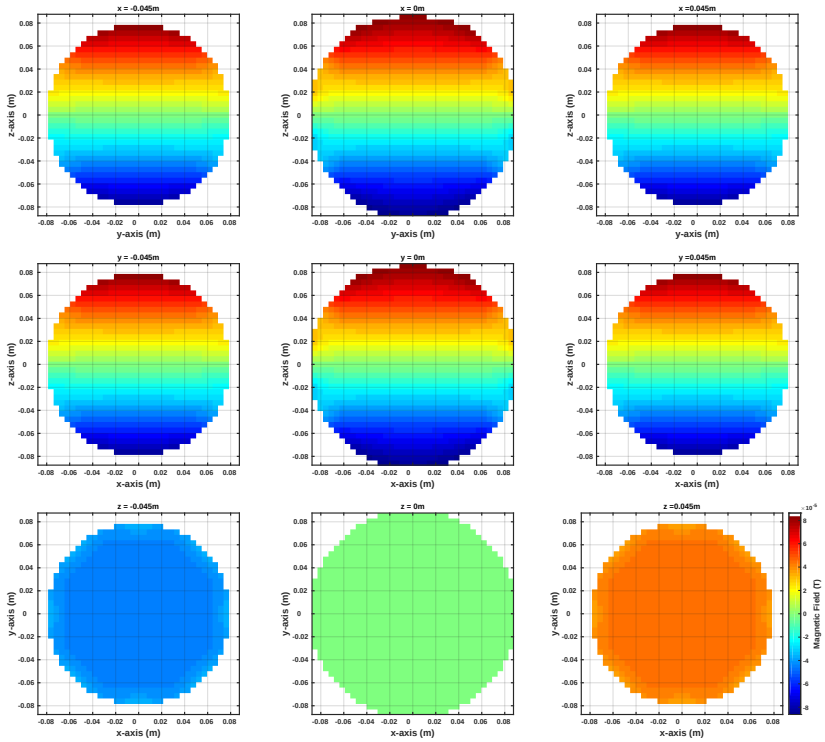

Figure 5.20: The magnetic field generated for a target field which corresponds to a z-gradient of $1\,\mathrm{mT\,m^{-1}}$, using dipoles whose magnetisation vectors are oriented parallel to the cylinder surface, and whose strengths are unconstrained.

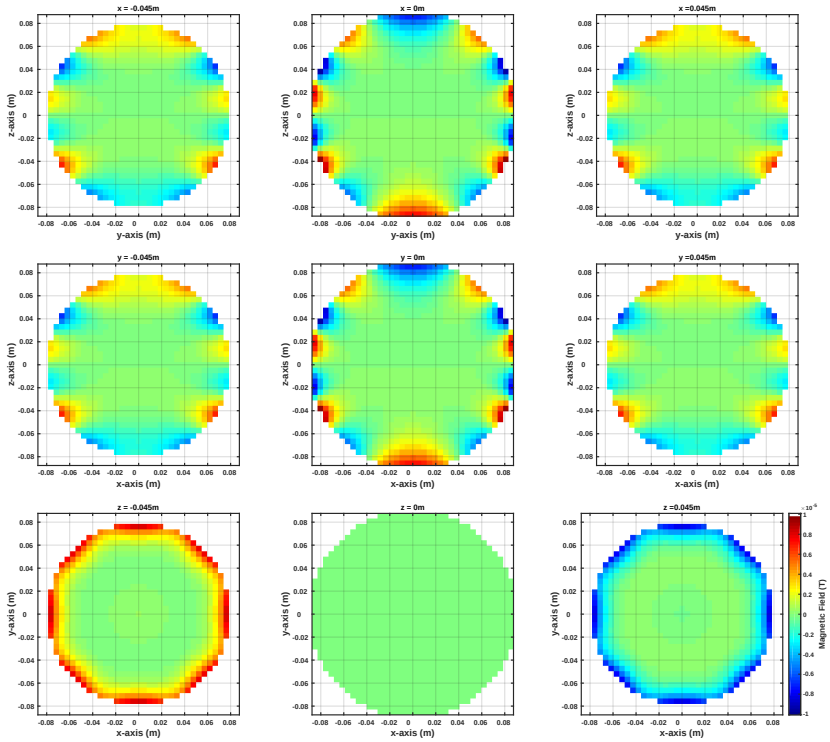

Figure 5.21: The difference between the magnetic field generated, and the target field which corresponds to a z-gradient of $1\,\mathrm{mT\,m^{-1}}$, using dipoles whose magnetisation vectors are oriented parallel to the cylinder surface, and whose strengths are unconstrained.

Dipoles Oriented Parallel to the Cylinder Surface, with Constrained Total Power Consumption

We then optimised the dipole strengths in order to reduce the total power. Figure 5.22 shows how the peak and RMS dipole strength, and the peak and RMS field deviation between the target field and the generated field vary for different values of λ_P. In order to minimise the total power consumption, while keeping the peak field deviation to less than 10 µT, we set $\lambda_P = 4.37 \times 10^{-10}$.

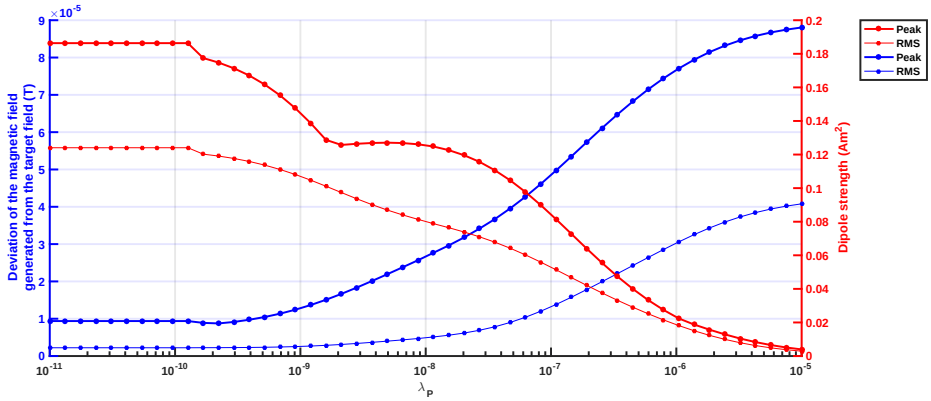

Figure 5.22: A plot of peak and RMS dipole strengths, and peak and RMS field deviations of the magnetic field generated from the target field which corresponds to a z-gradient of 1 mT m^{-1}, using dipoles whose magnetisation vectors are oriented parallel to the cylinder surface, against different values of the regularisation constant, λ_P.

Figure 5.23 shows the optimised dipole strengths required to generate a z-gradient field of 1 mT m^{-1}, with moments oriented parallel to the cylinder surface, and with a power regularisation term $\lambda_P = 4.37 \times 10^{-10}$. Figure 5.24 shows the magnetic field generated with these optimised dipole strengths, and Figure 5.25 shows the difference between the magnetic field generated, and the target field.

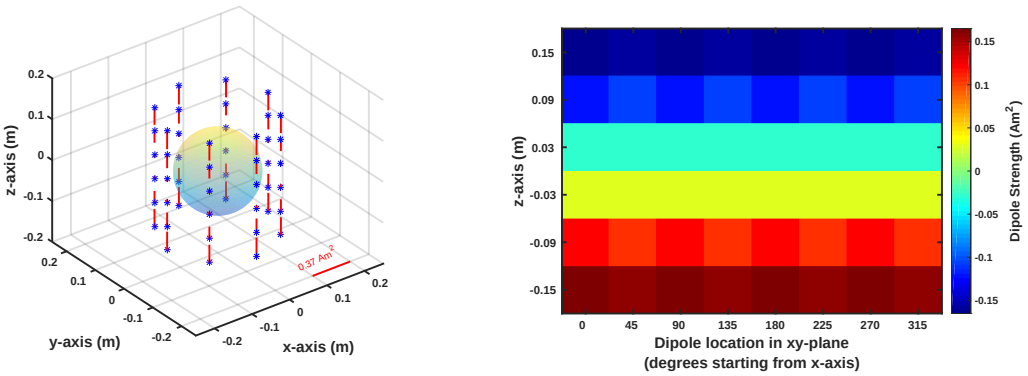

Figure 5.23: Diagram showing the dipole strengths required to generate a z-gradient field of $1\,\mathrm{mT\,m^{-1}}$, if dipole moments are oriented parallel to the cylinder surface, and optimised to reduce the total power with a regularisation term $\lambda_P = 4.37 \times 10^{-10}$.

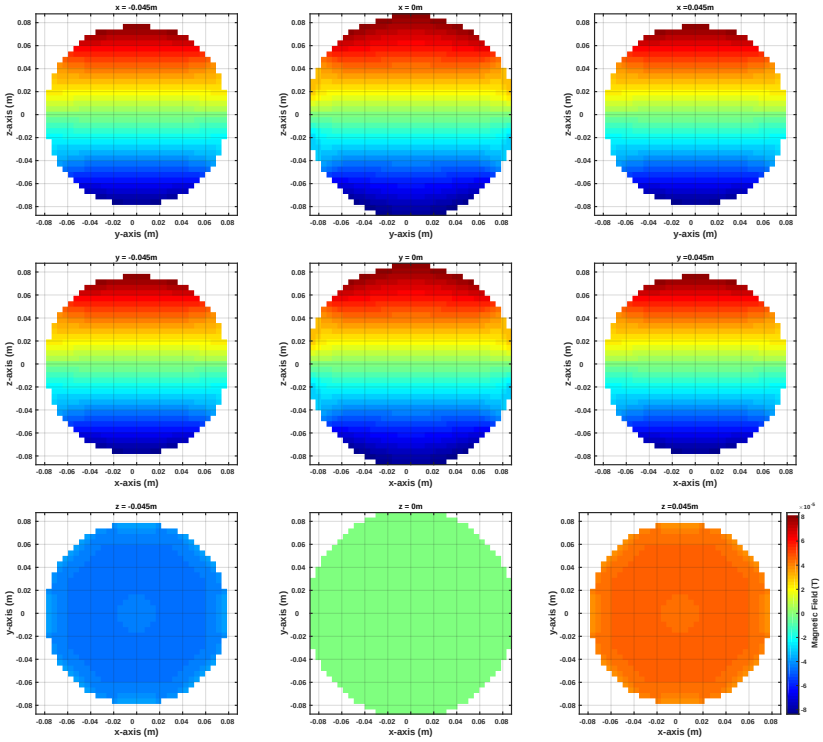

Figure 5.24: The magnetic field generated for a target field which corresponds to a z-gradient of $1\,\mathrm{mT\,m^{-1}}$, using dipoles whose magnetisation vectors are oriented parallel to the cylinder surface, and optimised to reduce the total power with a regularisation term $\lambda_P = 4.37 \times 10^{-10}$.

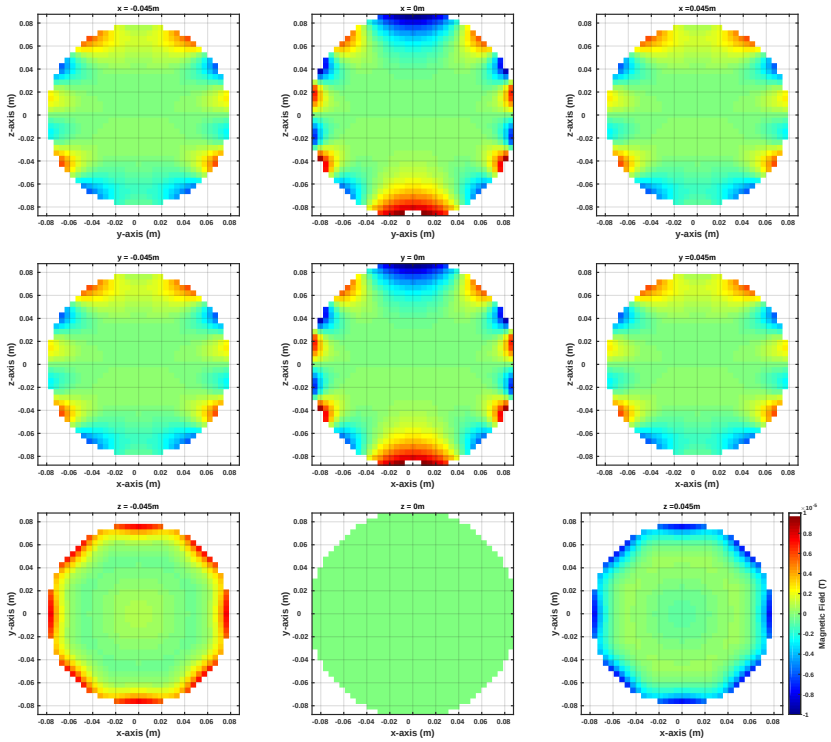

Figure 5.25: The difference between the magnetic field generated, and the target field which corresponds to a z-gradient of $1\,\mathrm{mT\,m^{-1}}$, using dipoles whose magnetisation vectors are oriented parallel to the cylinder surface, and optimised to reduce the total power with a regularisation constant $\lambda_P = 4.37 \times 10^{-10}$.

Dipoles Oriented at an Optimum Angle, with No Constraints on their Strength

In this section, we allow each dipole to align itself at an optimal angle that should allow a better power cost, and less magnetic field deviation than that obtained with strictly normal and parallel orientations.

Figure 5.26 shows the dipole strengths that are required to generate a target gradient field in the z-direction, with a strength of $1\,\mathrm{mT\,m^{-1}}$, when the dipoles are allowed to align in any direction, and if no constraints are applied on their strength.

The actual fields generated at points within the target volume, from these dipoles are shown in Figure 5.27.

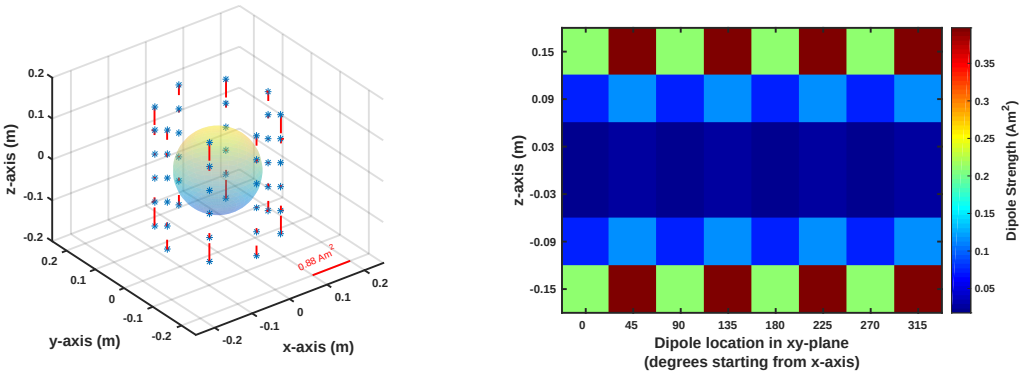

Figure 5.26: Diagram showing the dipole strengths required to generate a z-gradient field of $1\,\mathrm{mT\,m^{-1}}$, if dipole moments are allowed to align in any orientation, and their strength is not constrained.

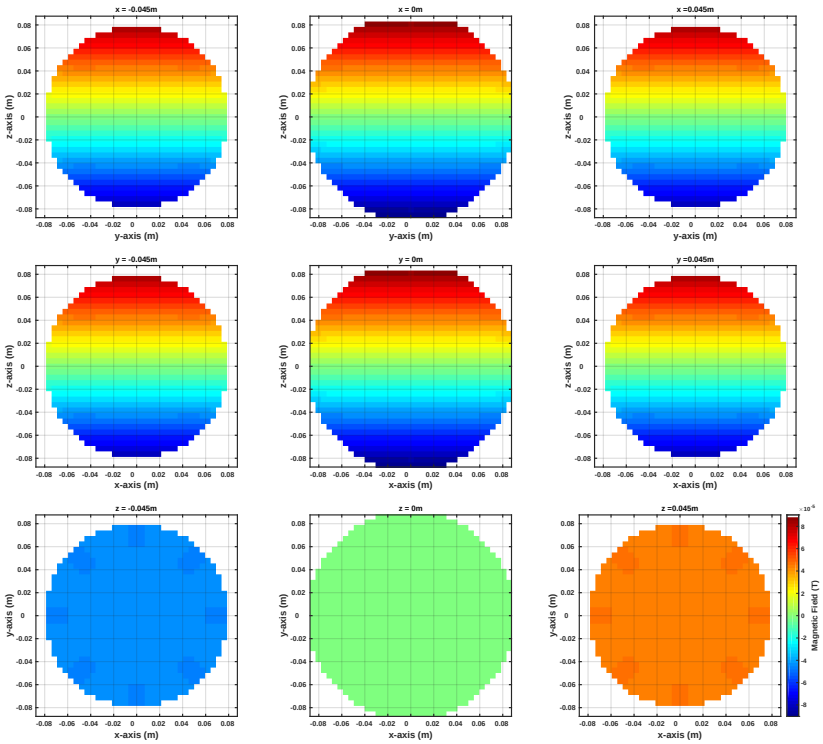

Figure 5.27: The magnetic field generated for a target field which corresponds to a z-gradient of $1\,\mathrm{mT\,m^{-1}}$, using dipoles whose magnetisation vectors are allowed to align in any orientation, and whose strengths are unconstrained.

Figure 5.28 shows the difference between the magnetic field generated, and the target gradient field of $1\,\mathrm{mT\,m^{-1}}$ in the z-direction, using dipoles whose magnetisation vectors are allowed to align in any orientation, and whose strengths are unconstrained.

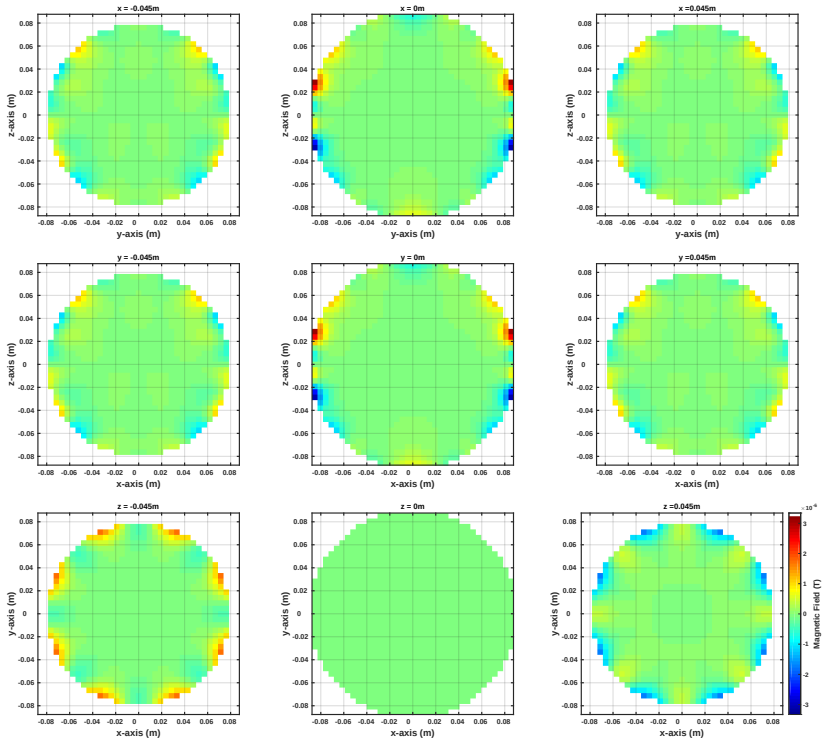

Figure 5.28: The difference between the magnetic field generated, and the target field which corresponds to a z-gradient of $1\,\mathrm{mT\,m^{-1}}$, using dipoles whose magnetisation vectors are allowed to align in any orientation, and whose strengths are unconstrained.

Dipoles Oriented at an Optimum Angle, with Constrained Total Power Consumption

We then optimised the dipole strengths in order to reduce the total power. Figure 5.29 shows how the peak and RMS dipole strength, and the peak and RMS field deviation between the target field and the generated field vary for different values of λ_P. In order to minimise the total power consumption, while keeping the peak field deviation to less than $10\,\mu\mathrm{T}$, we set $\lambda_P = 1.97 \times 10^{-9}$.

Figure 5.30 shows the optimised dipole strengths required to generate a z-gradient field of $1\,\mathrm{mT\,m^{-1}}$, with moments allowed to align in any orientation, and with a power regularisation term $\lambda_P = 1.97 \times 10^{-9}$. Figure 5.31 shows the magnetic field generated with these optimised dipole strengths, and Figure 5.32 shows the difference between the magnetic field generated, and the target gradient field of $1\,\mathrm{mT\,m^{-1}}$ in the z-direction.

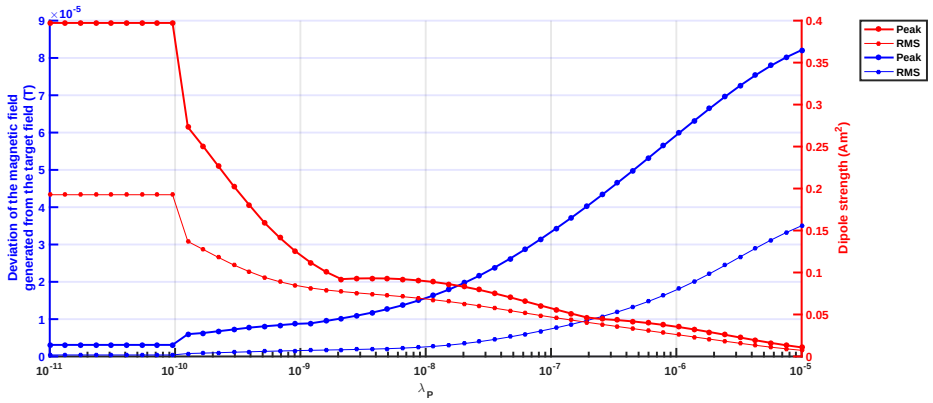

Figure 5.29: A plot of peak and RMS dipole strengths, and peak and RMS field deviations of the magnetic field generated from the target field which corresponds to a z-gradient of $1\,\mathrm{mT\,m^{-1}}$, using dipoles whose magnetisation vectors are allowed to align in any orientation, against different values of the regularisation constant, λ_P.

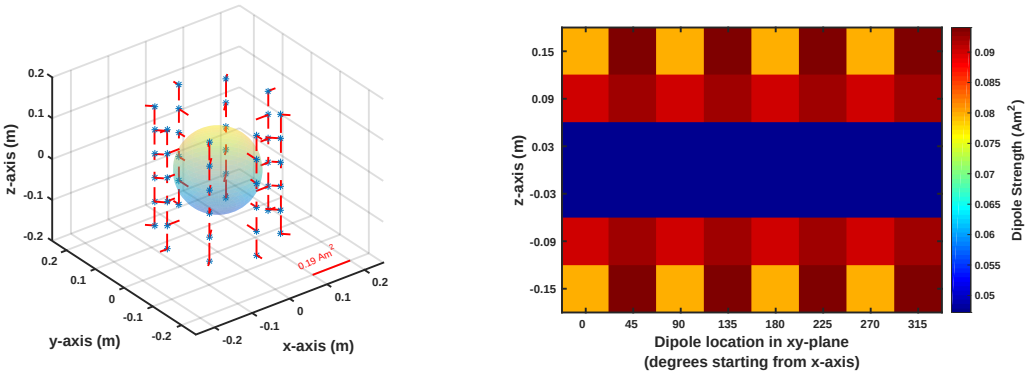

Figure 5.30: Diagram showing the dipole strengths required to generate a z-gradient field of $1\,\mathrm{mT\,m^{-1}}$, if dipole moments are allowed to align in any orientation, with a regularisation term $\lambda_P = 1.97 \times 10^{-9}$.

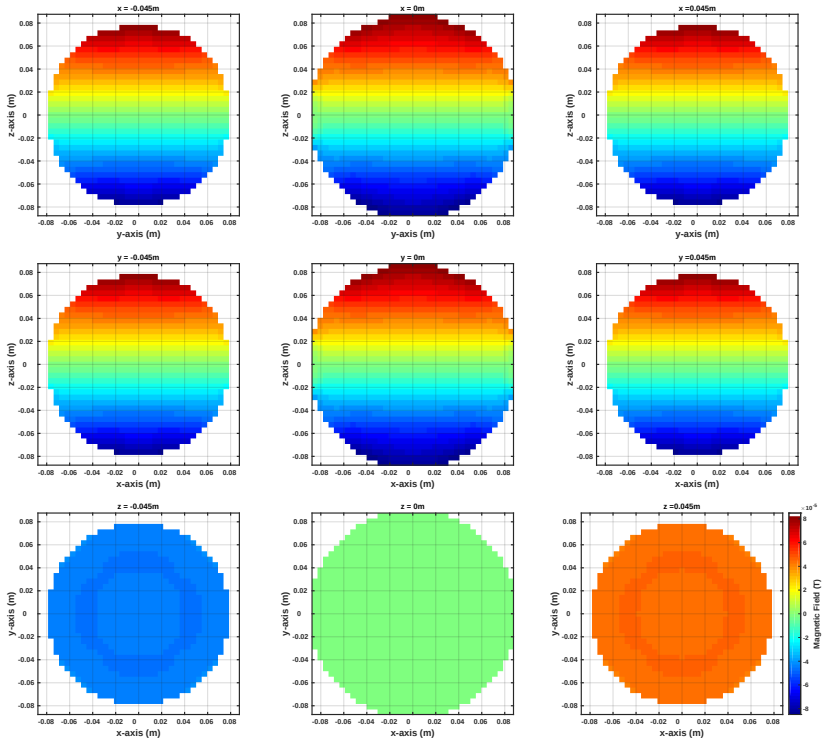

Figure 5.31: The magnetic field generated for a target field which corresponds to a z-gradient of $1\,\mathrm{mT\,m^{-1}}$, using dipoles whose magnetisation vectors are allowed to align in any orientation, and optimised to reduce the total power with a regularisation term $\lambda_P = 1.97 \times 10^{-9}$.

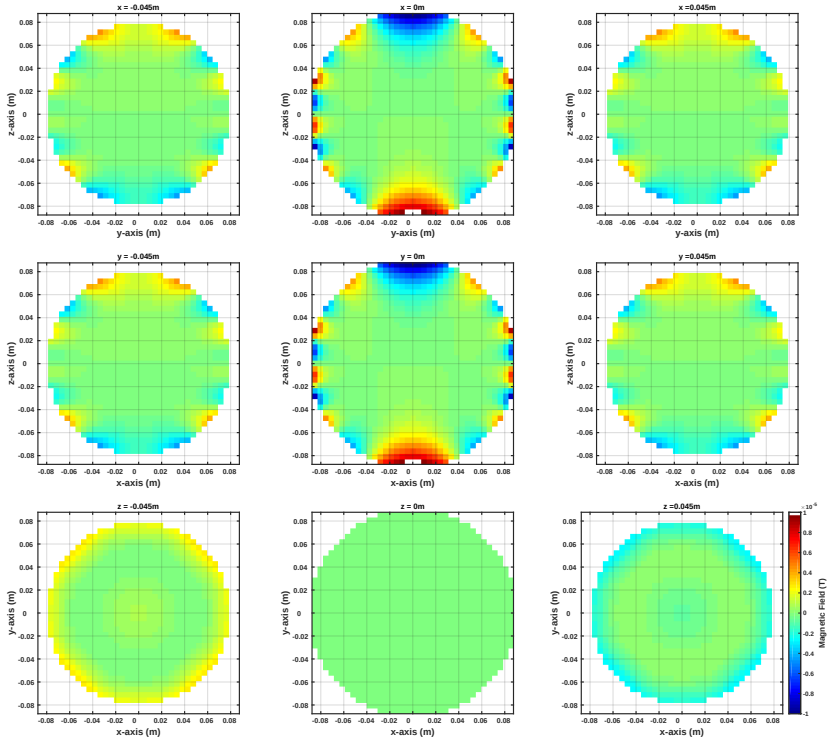

Figure 5.32: The difference between the magnetic field generated, and the target field which corresponds to a z-gradient of $1\,\mathrm{mT\,m^{-1}}$, using dipoles whose magnetisation vectors are allowed to align in any orientation, and optimised to reduce the total power with a regularisation constant $\lambda_P = 1.97 \times 10^{-9}$.

Alignment	Maximum dipole strength, ($\mathrm{A\,m^2}$)	RMS dipole strength, ($\mathrm{A\,m^2}$)	Maximum field deviation (T)	RMS field deviation (T)
normal	0.182	0.111	2.43×10^{-5}	4.43×10^{-6}
parallel	0.165	0.115	1×10^{-5}	2.08×10^{-6}
optimum	0.094	0.078	1×10^{-5}	1.62×10^{-6}

Table 5.3: Comparison of dipole strengths and magnetic field deviation from a target field which corresponds to a z-gradient of $1\,\mathrm{mT\,m^{-1}}$, using three different dipole orientation configurations, and optimised to reduce the peak and RMS dipole strengths required, while keeping the peak field deviation to less than $10\,\mu\mathrm{T}$.

We saw that when no constraints were applied to the dipole strengths, both the maximum dipole strength and the rms of the dipoles required when the dipoles were allowed to align at an optimum orientation, were approximately twice those required when dipoles were aligned normal or parallel to the dipole surface.

This is counterintuitive since we expected that dipoles aligned at an optimum orientation need less strength. However, the deviation between the target field and the generated fields is approximately tenfold smaller when the dipoles were allowed to align at an optimum direction, than when they were strictly normal or parallel to the cylinder surface.

Table 5.3 lists the dipole strengths and magnetic field deviations from a target field which corresponds to a z-gradient of $1\,\mathrm{mT\,m^{-1}}$, using the three different dipole orientation configurations, and dipole strengths optimised to reduce the total power while keeping the peak field deviation to less than $10\,\mu\mathrm{T}$..

When dipole strengths were constrained to the smallest strength whilst keeping the peak field deviation to less than $10\,\mu\mathrm{T}$, the total dipole power for the optimum-aligned dipoles was approximately a third less than that required when dipoles are normal, or parallel, to the cylinder surface.

These results suggest that allowing the dipoles to align at an optimum orientation is favourable to achieve a smaller field deviation and to reduce the required dipole

strengths.

5.4.2 Creating an X- (or Y-) Gradient using Magnetic Dipoles

Dipoles Oriented Normal to the Cylinder Surface, with No Constraints on their Strength

Figure 5.33 shows the dipole strengths that are required to generate a target gradient field in the x-direction, with a strength of $1\,\mathrm{mT\,m^{-1}}$, using dipoles whose moments are aligned normal to the cylinder surface, and if no constraints are applied on their strength.

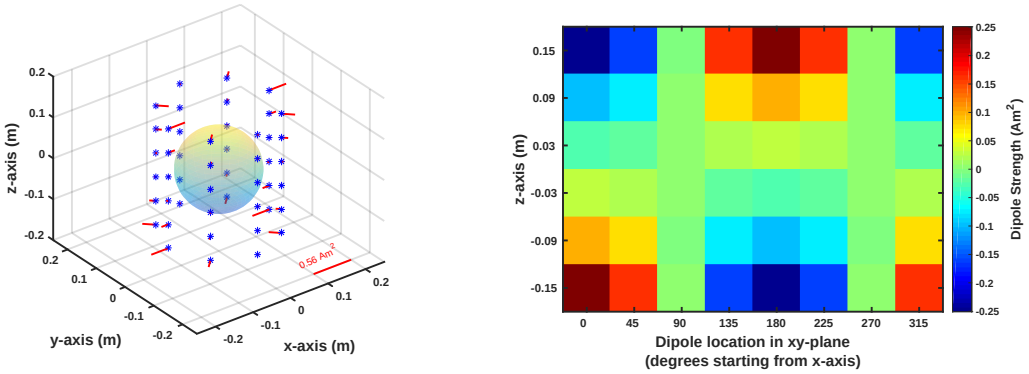

Figure 5.33: Diagram showing the dipole strengths required to generate an x-gradient field of $1\,\mathrm{mT\,m^{-1}}$, if dipole moments are oriented normal to the cylinder surface, and their strength is not constrained.

The actual fields generated at points within the target volume, from these dipoles are shown in Figure 5.34. Figure 5.35 shows the difference between the magnetic field generated, and the target field.

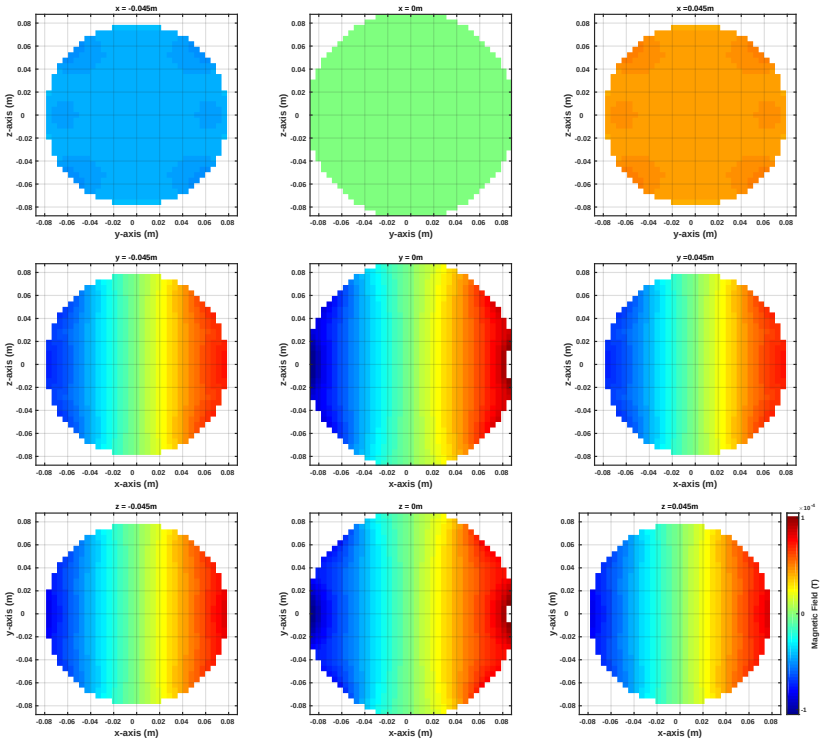

Figure 5.34: The magnetic field generated for a target field which corresponds to an x-gradient of $1\,\mathrm{mT\,m^{-1}}$, using dipoles whose magnetisation vectors are oriented normal to the cylinder surface, and whose strengths are unconstrained.

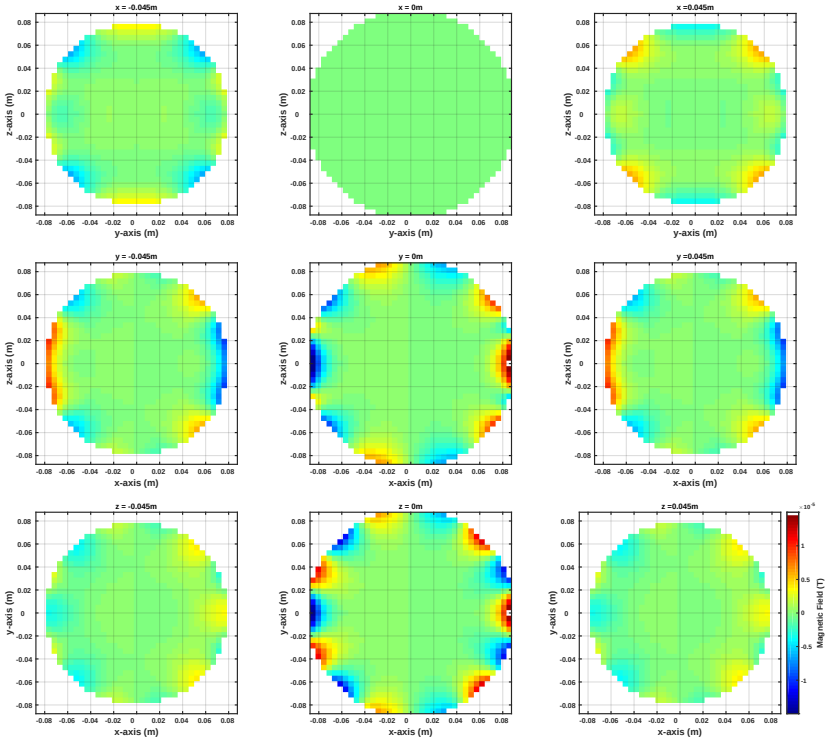

Figure 5.35: The difference between the magnetic field generated, and the target field which corresponds to an x-gradient of $1\,\mathrm{mT\,m^{-1}}$, using dipoles whose magnetisation vectors are oriented normal to the cylinder surface, and whose strengths are unconstrained.

Dipoles Oriented Normal to the Cylinder Surface, with Constrained Total Power Consumption

We then applied a constraint on the total power of the dipoles. Figure 5.36 shows how the peak dipole strength, RMS dipole strength, and the RMS field deviation between the target field and the generated field vary for different values of λ_P. In order to minimise the total power consumption, while keeping the peak field deviation to less than 10 µT, we set $\lambda_P = 5.18 \times 10^{-8}$.

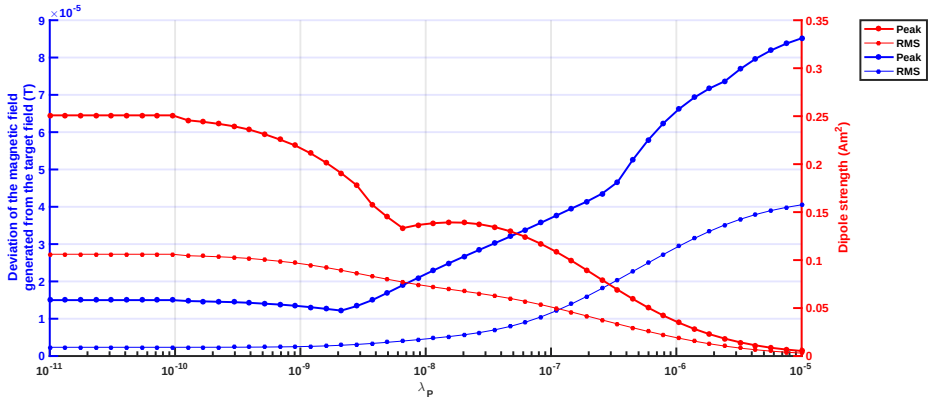

Figure 5.36: A plot of peak and RMS dipole strengths, and peak and RMS field deviations of the magnetic field generated from the target field which corresponds to an x-gradient of $1\,\mathrm{mT\,m^{-1}}$, using dipoles whose magnetisation vectors are oriented normal to the cylinder surface, against different values of the regularisation constant, λ_P.

Figure 5.37 shows the optimised dipole strengths required to generate an x-gradient field of $1\,\mathrm{mT\,m^{-1}}$, with moments oriented normal to the cylinder surface, and with a power regularisation term $\lambda_P = 2.11 \times 10^{-9}$. Figure 5.38 shows the magnetic field generated with these optimised dipole strengths, and Figure 5.39 shows the difference between the magnetic field generated, and the target field.

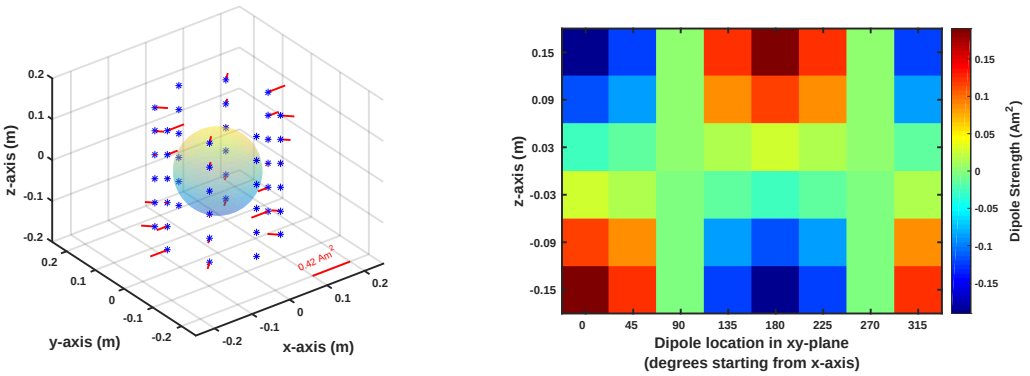

Figure 5.37: Diagram showing the dipole strengths required to generate a z-gradient field of $1\,\mathrm{mT\,m^{-1}}$, if dipole moments are oriented parallel to the cylinder surface, and and optimised to reduce the total power with a regularisation term $\lambda_P = 2.11 \times 10^{-9}$.

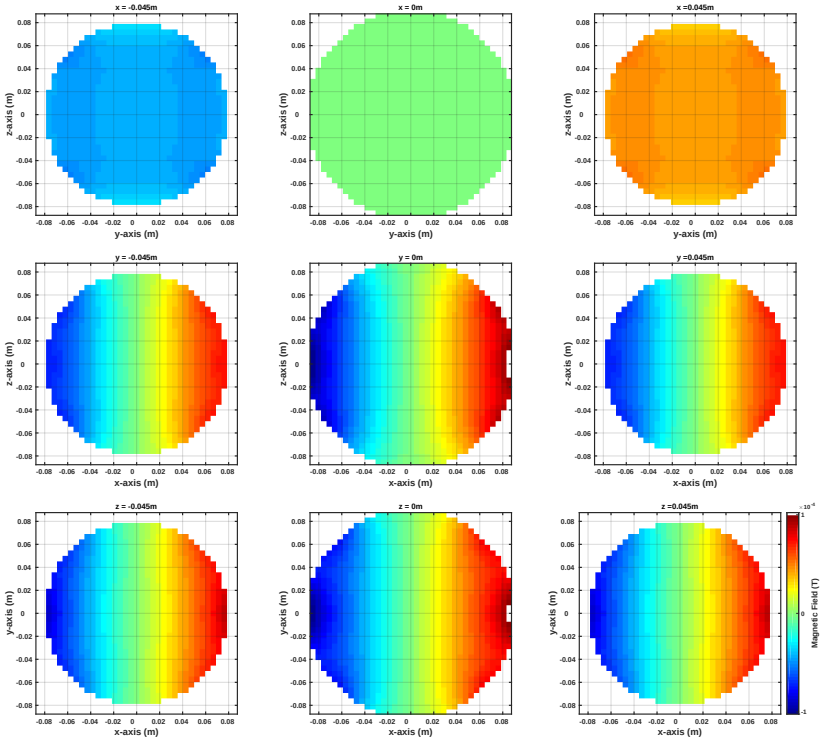

Figure 5.38: The magnetic field generated for a target field which corresponds to an x-gradient of $1\,\mathrm{mT\,m^{-1}}$, using dipoles whose magnetisation vectors are oriented normal to the cylinder surface, and optimised to reduce the total power with a regularisation term $\lambda_P = 2.11 \times 10^{-9}$.

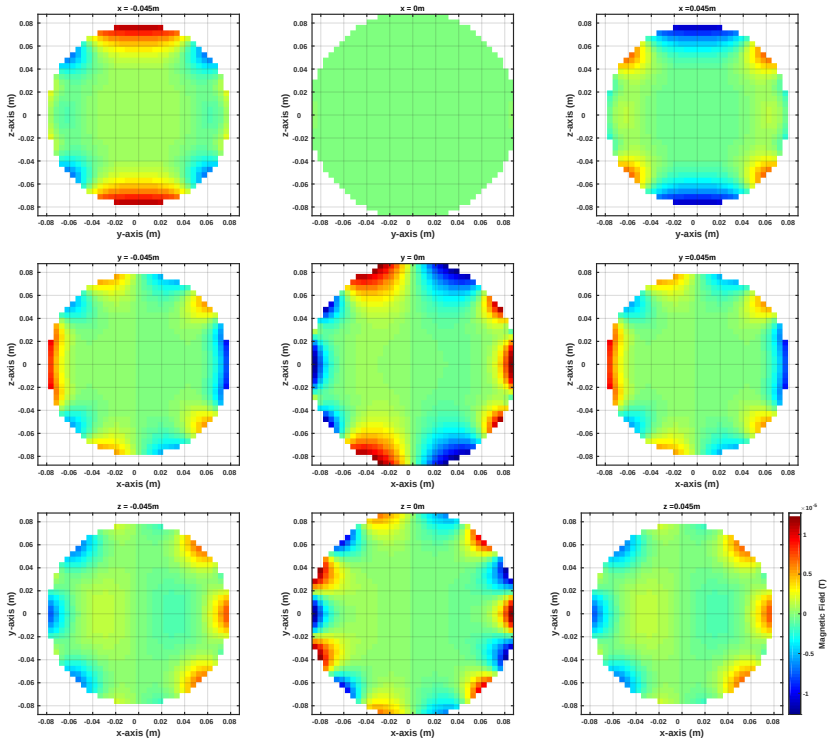

Figure 5.39: The difference between the magnetic field generated, and the target field which corresponds to an x-gradient of $1\,\mathrm{mT\,m^{-1}}$, using dipoles whose magnetisation vectors are oriented normal to the cylinder surface, and optimised to reduce the total power with a regularisation constant $\lambda_P = 2.11 \times 10^{-9}$.

Dipoles Oriented Parallel to the Cylinder Surface, with No Constraints on their Strength

We then used dipoles that are oriented parallel, rather than normal, to the cylinder surface, and used them to generate the $1\,\mathrm{mT\,m^{-1}}$ gradient field in the x-direction. Figure 5.40 shows the dipole strengths that are required if no constraints are applied on their strength.

The actual fields generated at points within the target volume, from these dipoles are shown in Figure 5.41. Figure 5.42 shows the difference between the magnetic field generated, and the target field.

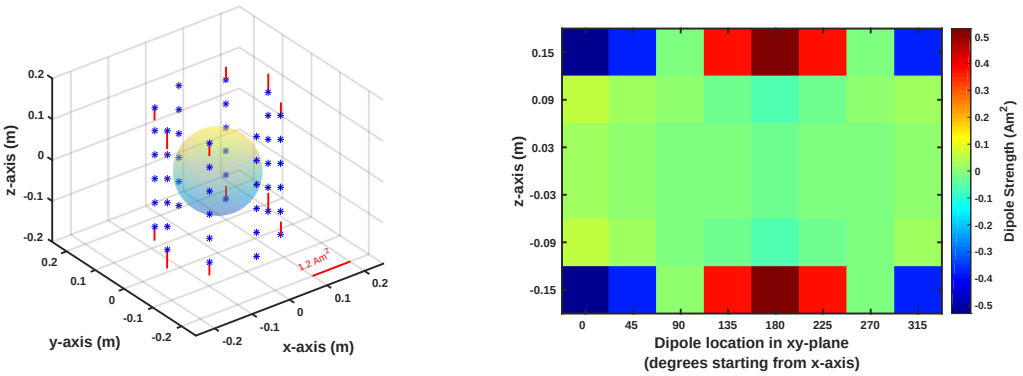

Figure 5.40: Diagram showing the dipole strengths required to generate an x-gradient field of $1\,\mathrm{mT\,m^{-1}}$, if dipole moments are oriented parallel to the cylinder surface, and their strength is not constrained.

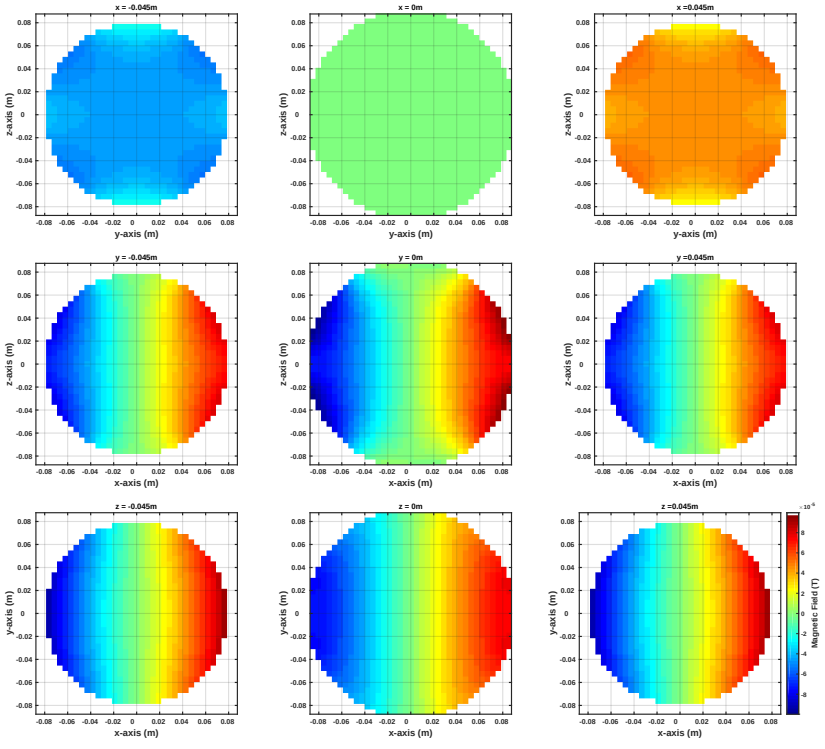

Figure 5.41: The magnetic field generated for a target field which corresponds to an x-gradient of $1\,\mathrm{mT\,m^{-1}}$, using dipoles whose magnetisation vectors are oriented parallel to the cylinder surface, and whose strengths are unconstrained.

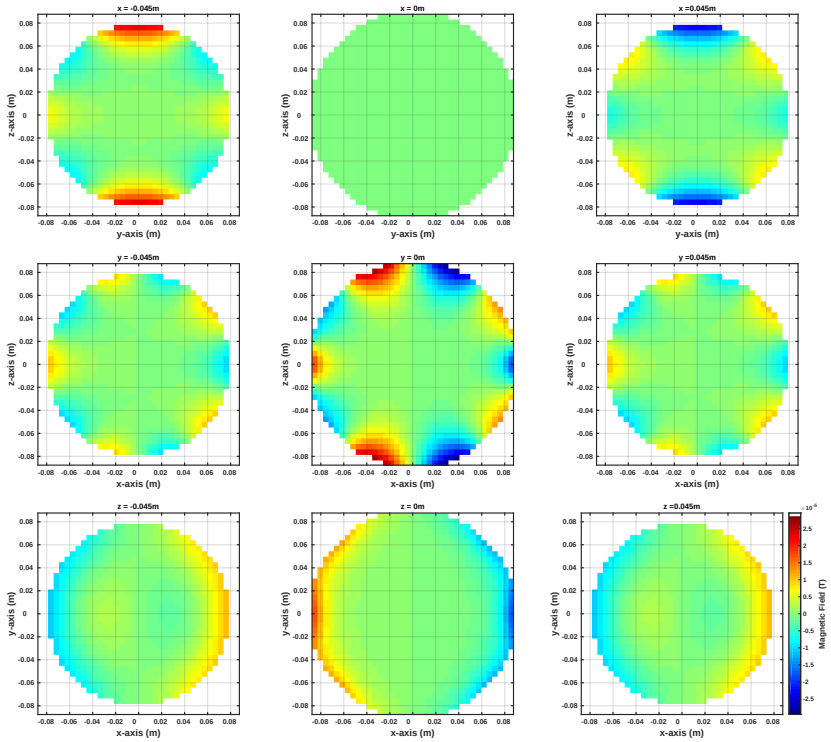

Figure 5.42: The difference between the magnetic field generated, and the target field which corresponds to an x-gradient of $1\,\mathrm{mT\,m^{-1}}$, using dipoles whose magnetisation vectors are oriented parallel to the cylinder surface, and whose strengths are unconstrained.

Dipoles Oriented Parallel to the Cylinder Surface, with Constrained Total Power Consumption

We then optimised the dipole strengths in order to reduce the total power. Figure 5.43 shows how the peak dipole strength, RMS dipole strength, and the RMS field deviation between the target field and the generated field vary for different values of λ_P. In order to minimise the total power consumption, while keeping the peak field deviation to less than $10\,\mu\mathrm{T}$, we set $\lambda_P = 3.75 \times 10^{-10}$.

Figure 5.44 shows the optimised dipole strengths required to generate an x-gradient field of $1\,\mathrm{mT\,m^{-1}}$, with moments oriented parallel to the cylinder surface, and with a power regularisation term $\lambda_P = 3.75 \times 10^{-10}$. Figure 5.45 shows the magnetic field generated with these optimised dipole strengths, and Figure 5.46 shows the difference between the magnetic field generated, and the target field.

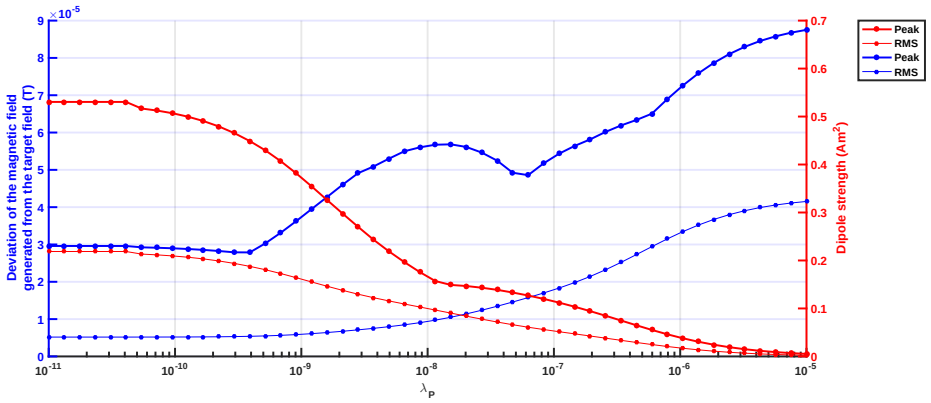

Figure 5.43: A plot of peak and RMS dipole strengths, and peak and RMS field deviations of the magnetic field generated from the target field which corresponds to an x-gradient of $1\,\mathrm{mT\,m^{-1}}$, using dipoles whose magnetisation vectors are oriented parallel to the cylinder surface, against different values of the regularisation constant, λ_P.

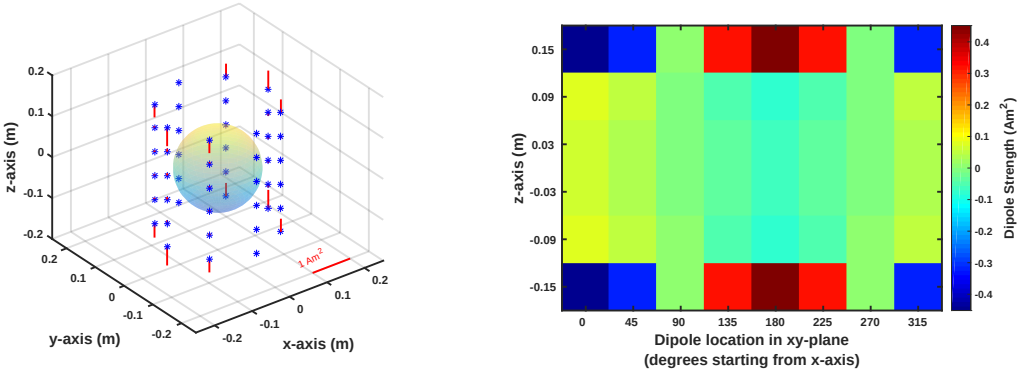

Figure 5.44: Diagram showing the dipole strengths required to generate an x-gradient field of $1\,\mathrm{mT\,m^{-1}}$, if dipole moments are oriented parallel to the cylinder surface, and and optimised to reduce the total power with a regularisation term $\lambda_P = 3.75 \times 10^{-10}$.

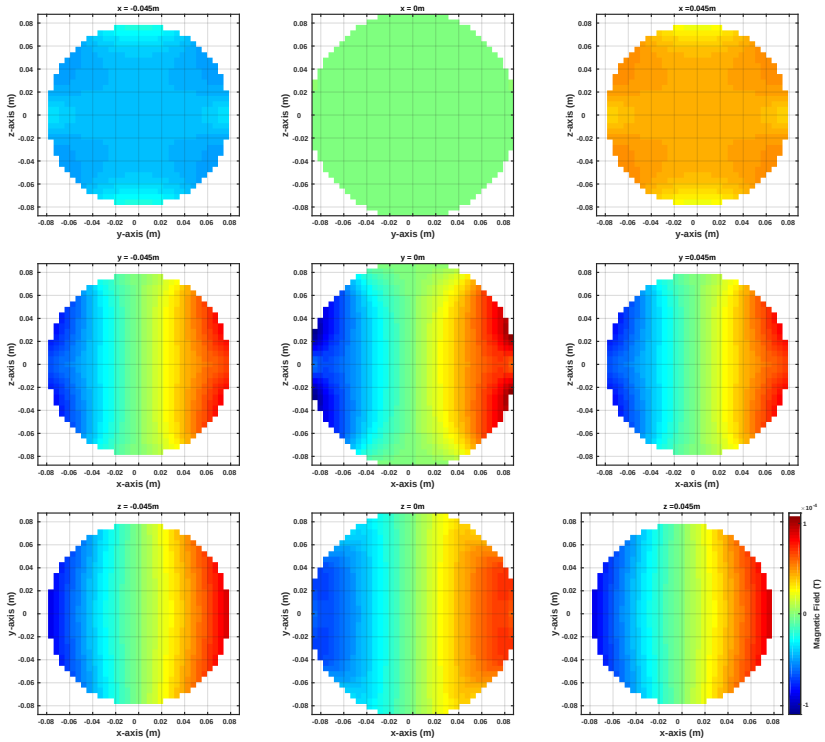

Figure 5.45: The magnetic field generated for a target field which corresponds to an x-gradient of $1\,\mathrm{mT\,m^{-1}}$, using dipoles whose magnetisation vectors are oriented parallel to the cylinder surface, and optimised to reduce the total power with a regularisation term $\lambda_P = 3.75 \times 10^{-10}$.

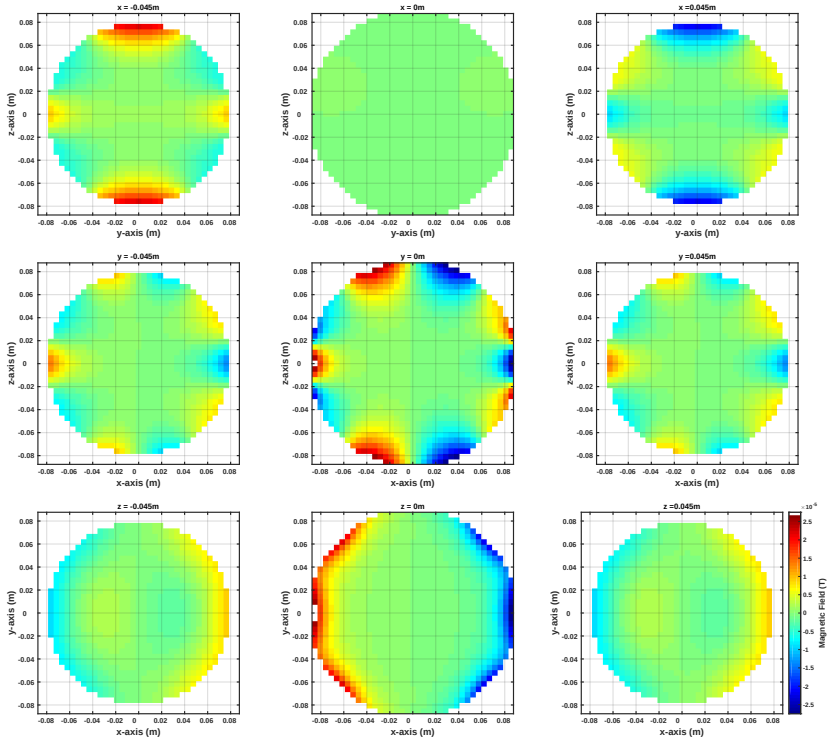

Figure 5.46: The difference between the magnetic field generated, and the target field which corresponds to an x-gradient of $1\,\mathrm{mT\,m^{-1}}$, using dipoles whose magnetisation vectors are oriented parallel to the cylinder surface, and optimised to reduce the total power with a regularisation constant $\lambda_P = 3.75 \times 10^{-10}$.

Dipoles Oriented at an Optimum Angle, with No Constraints on their Strength

Figure 5.47 shows the dipole strengths that are required to generate a target gradient field in the x-direction, with a strength of $1\,\mathrm{mT\,m^{-1}}$, when the dipoles are allowed to align in any direction, and if no constraints are applied on their strength.

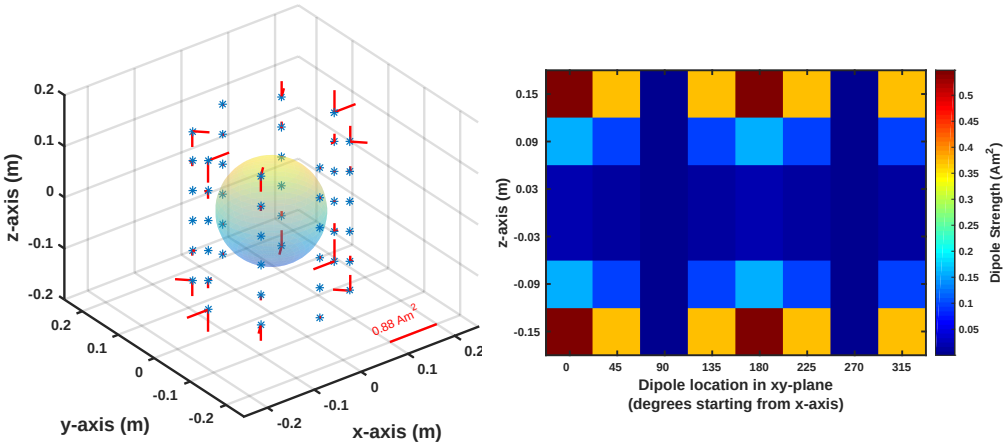

Figure 5.47: Diagram showing the dipole strengths required to generate an x-gradient field of $1\,\mathrm{mT\,m^{-1}}$, if dipole moments are allowed to align in any orientation, and their strength is not constrained.

The actual fields generated at points within the target volume, from these dipoles are shown in Figure 5.48. Figure 5.49 shows the difference between the magnetic field generated, and the target field.

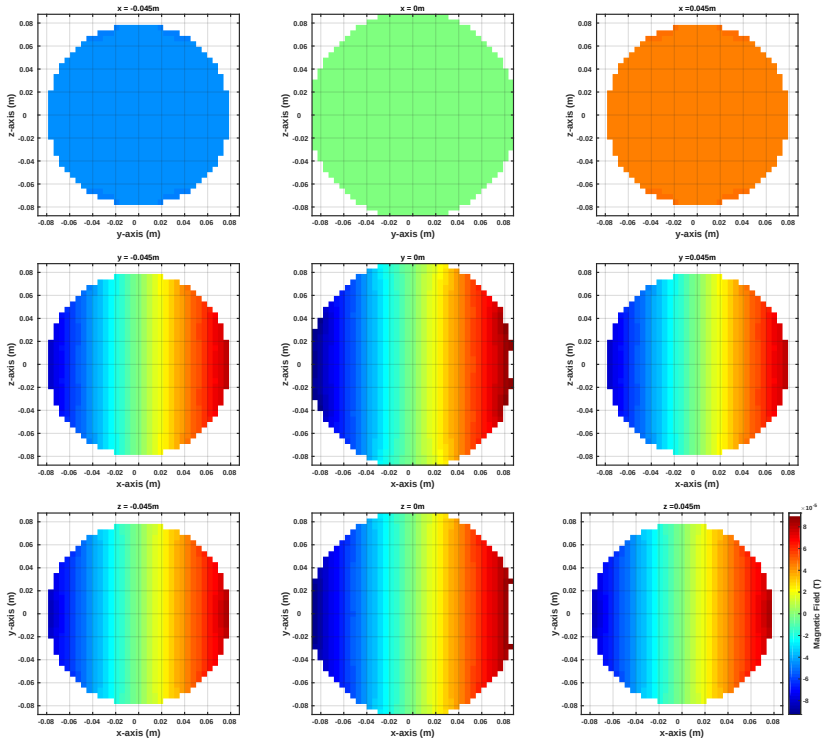

Figure 5.48: The magnetic field generated for a target field which corresponds to an x-gradient of $1\,\mathrm{mT\,m^{-1}}$, using dipoles whose magnetisation vectors are allowed to align in any orientation, and whose strengths are unconstrained.

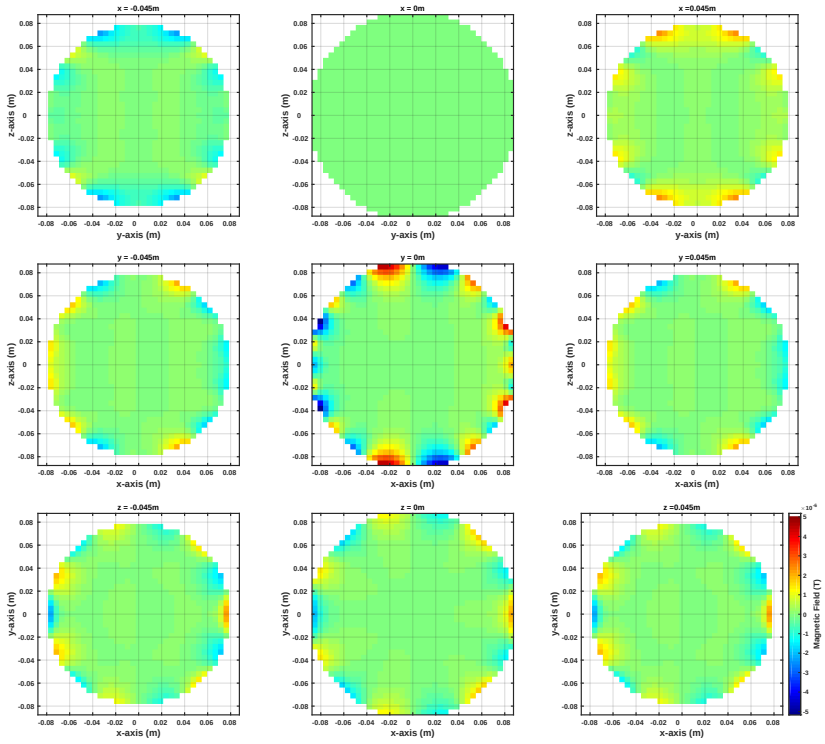

Figure 5.49: The difference between the magnetic field generated, and the target field which corresponds to an x-gradient of $1\,\mathrm{mT\,m^{-1}}$, using dipoles whose magnetisation vectors are allowed to align in any orientation, and whose strengths are unconstrained.

Dipoles Oriented at an Optimum Angle, with Constrained Total Power Consumption

We then optimised the dipole strengths in order to reduce the total power. Figure 5.50 shows how the peak dipole strength, RMS dipole strength, and the RMS field deviation between the target field and the generated field vary for different values of λ_P. In order to minimise the total power consumption, while keeping the peak field deviation to less than 10 µT, we set $\lambda_P = 3.79 \times 10^{-10}$.

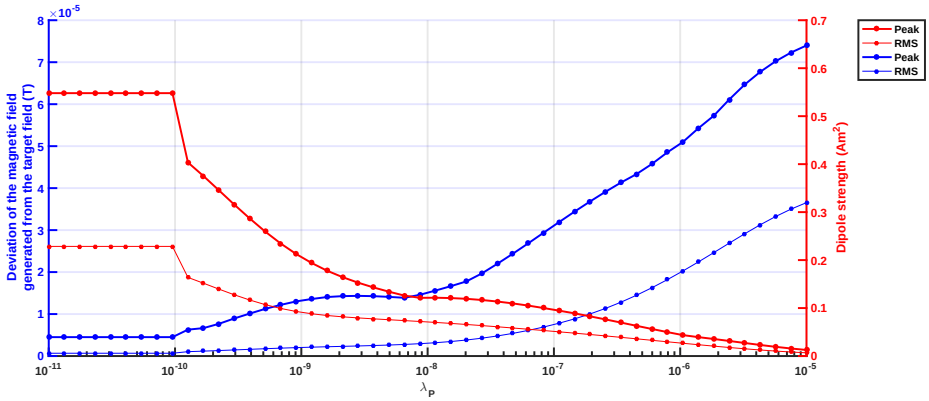

Figure 5.50: A plot of peak and RMS dipole strengths, and peak and RMS field deviations of the magnetic field generated from the target field which corresponds to an x-gradient of $1\,\mathrm{mT\,m^{-1}}$, using dipoles whose magnetisation vectors are allowed to align at an optimum angle, against different values of the regularisation constant, λ_P.

Figure 5.51 shows the optimised dipole strengths required to generate an x-gradient field of $1\,\mathrm{mT\,m^{-1}}$, with moments allowed to align in any orientation, and with a power regularisation term $\lambda_P = 3.79 \times 10^{-10}$. Figure 5.52 shows the magnetic field generated with these optimised dipole strengths, and Figure 5.53 shows the difference between the magnetic field generated, and the target field.

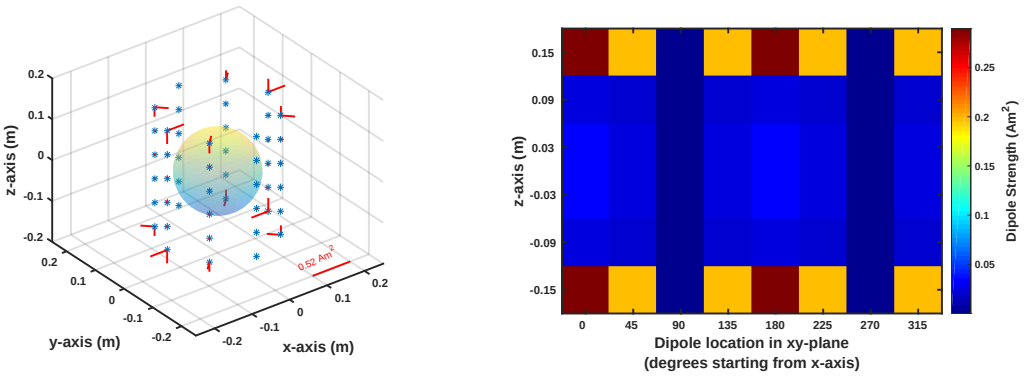

Figure 5.51: Diagram showing the dipole strengths required to generate an x-gradient field of $1\,\mathrm{mT\,m^{-1}}$, if dipole moments are allowed to align in any orientation, and optimised to reduce the total power with a regularisation term $\lambda_P = 3.79 \times 10^{-10}$.

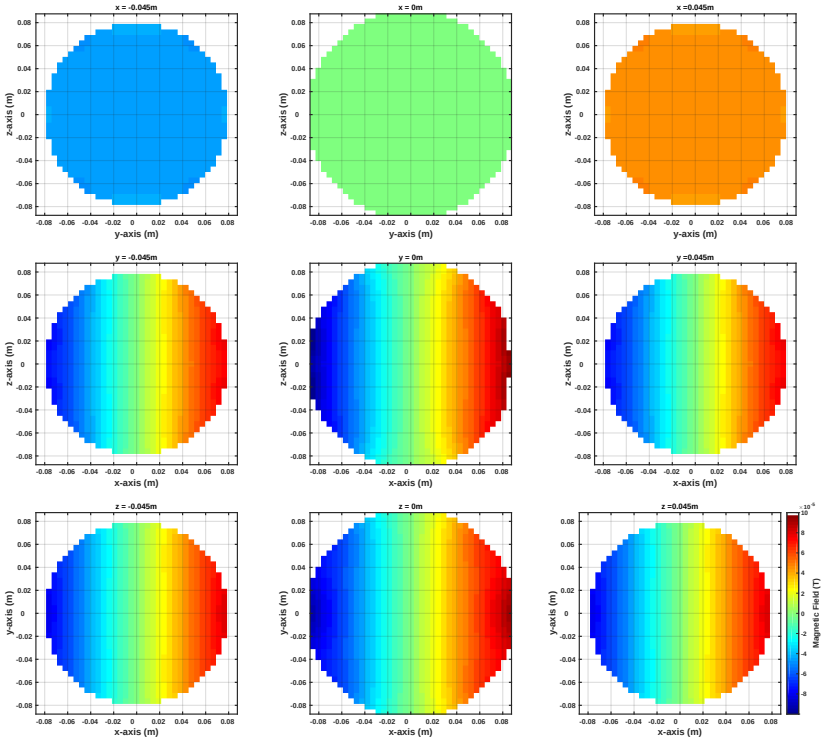

Figure 5.52: The magnetic field generated for a target field which corresponds to an x-gradient of $1\,\mathrm{mT\,m^{-1}}$, using dipoles whose magnetisation vectors are allowed to align in any orientation, and optimised to reduce the total power with a regularisation term $\lambda_P = 3.79 \times 10^{-10}$.

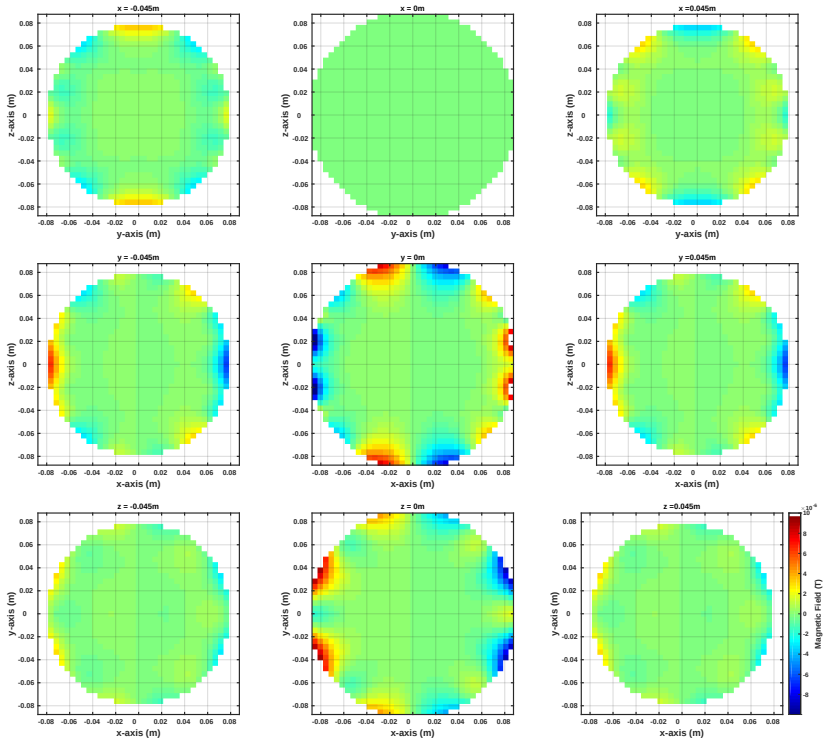

Figure 5.53: The difference between the magnetic field generated, and the target field which corresponds to an x-gradient of $1\,\mathrm{mT\,m^{-1}}$, using dipoles whose magnetisation vectors are allowed to align in any orientation, and optimised to reduce the total power with a regularisation constant $\lambda_P = 3.79 \times 10^{-10}$.

We saw that when no constraints were applied to the dipole strengths, both the peak and RMS strengths of the dipoles required when the dipoles were allowed to align at an optimum orientation, were larger than those required when dipoles were aligned normal or parallel to the dipole surface. This is counterintuitive since we expected that dipoles aligned at an optimum orientation need less strength. However, the deviation between the target field and the generated fields is smaller when the dipoles were allowed to align at an optimum direction, than when they were strictly normal or parallel to the cylinder surface.

Table 5.4 lists the dipole strengths and magnetic field deviations from a target field which corresponds to an x-gradient of $1\,\mathrm{mT\,m^{-1}}$, using the three different dipole orientation configurations, and dipole strengths optimised to reduce the total power while keeping the peak field deviation to less than $10\,\mu\mathrm{T}$.

When dipole strengths were constrained to the smallest strength whilst keep-

Alignment	Maximum dipole strength, ($\mathrm{A\,m^2}$)	RMS dipole strength, ($\mathrm{A\,m^2}$)	Maximum field deviation (T)	RMS field deviation (T)
normal	0.191	0.089	1.216×10^{-5}	2.886×10^{-6}
parallel	0.452	0.189	2.754×10^{-5}	5.378×10^{-6}
optimum	0.290	0.118	1×10^{-5}	1.59×10^{-6}

Table 5.4: Comparison of dipole strengths and magnetic field deviation from a target field which corresponds to an x-gradient of $1\,\mathrm{mT\,m^{-1}}$, using three different dipole orientation configurations, and optimised to reduce the peak and RMS dipole strengths required, while keeping the peak field deviation to less than $10\,\mu\mathrm{T}$.

ing the peak field deviation to less than $10\,\mu\mathrm{T}$, the strengths required for the optimum-aligned dipoles were less than those required for dipoles that are aligned parallel to the cylinder surface. Also, the deviation of the target field from the field generated with optimum-aligned dipoles was less than the deviation of the target field from the field generated with dipoles that are aligned parallel, or normal, to the cylinder surface. These results suggest that allowing the dipoles to align at an optimum orientation is favourable to achieve a smaller field deviation and to reduce the required dipole strengths.

Moreover, in generating this x-gradient target field, we saw that without dipole strength constraints, the peak field deviation obtained with dipoles that were normal to the cylinder surface was approximately half the deviation obtained with dipoles that were aligned parallel to the cylinder. On the contrary, in generating the z-gradient, we saw that without dipole strength constraints, the peak field deviation obtained with dipoles that were parallel to the cylinder surface was approximately half the deviation obtained with dipoles that were aligned normal to the cylinder.

5.4.3 Creating an XY Shimming Field

We simulated the generation of an XY shimming field of peak amplitude 0.1 mT, using magnetic dipoles and allowing them to align at an optimum orientation.

Dipoles Oriented at an Optimum Angle, with No Constraints on their Strength

Figure 5.54 shows the dipole strengths that are required to generate an XY shimming field, when the dipoles are allowed to align in any direction, and if no constraints are applied on their strength. It can be seen that the dipole moment component that is parallel to the cylinder surface is much larger than the component that is normal to the cylinder surface.

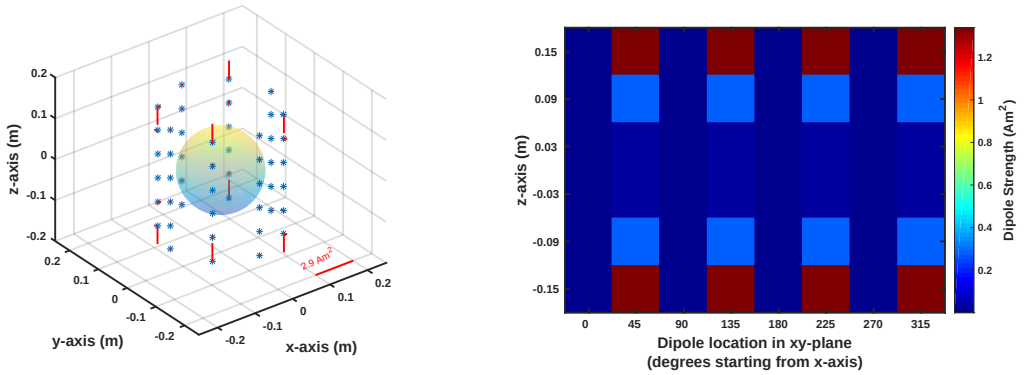

Figure 5.54: Diagram showing the dipole strengths required to generate an XY shimming field, if dipole moments are allowed to align in any orientation, and their strength is not constrained.

The actual fields generated at points within the target volume, from these dipoles are shown in Figure 5.55. Figure 5.56 shows the difference between the magnetic field generated, and the target field.

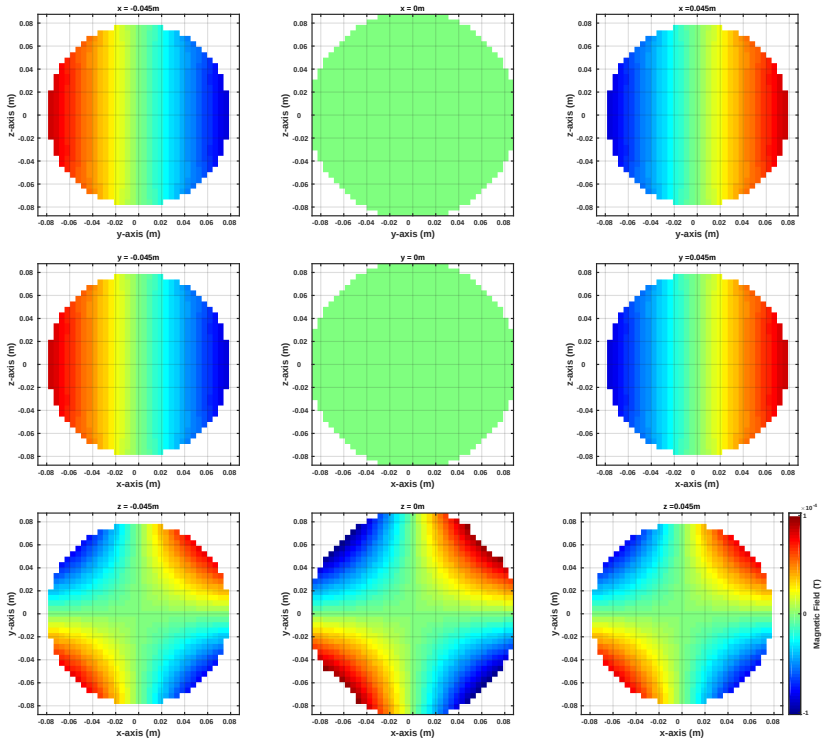

Figure 5.55: The magnetic field generated for a target field which corresponds to an XY shimming field of amplitude 0.1 mT, using dipoles whose magnetisation vectors are allowed to align in any orientation, and whose strengths are unconstrained.

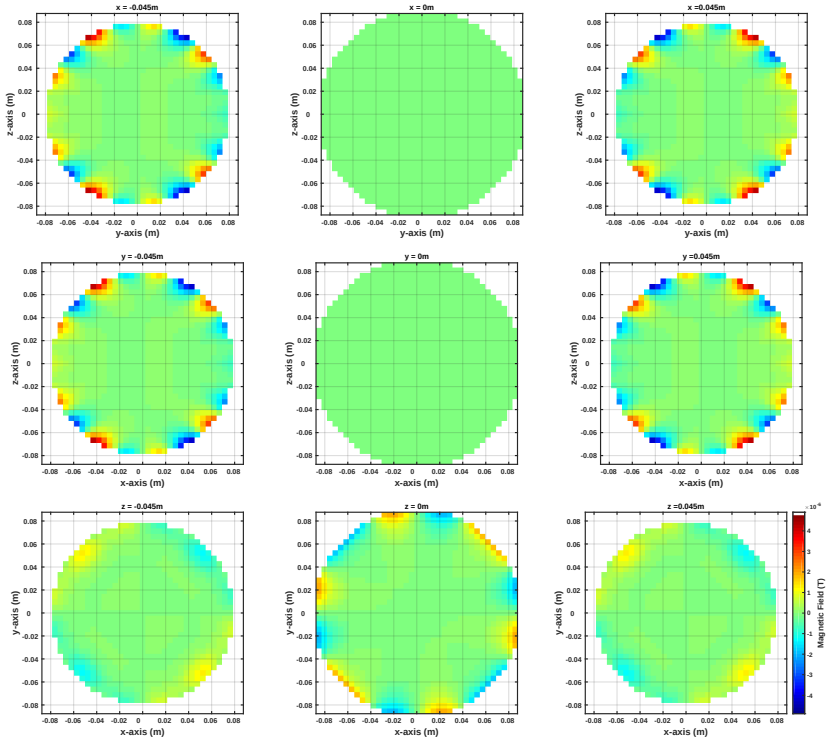

Figure 5.56: The difference between the magnetic field generated, and the target field which corresponds to an XY shimming field of amplitude 0.1 mT, using dipoles whose magnetisation vectors are allowed to align in any orientation, and whose strengths are unconstrained.

Dipoles Oriented at an Optimum Angle, with Constrained Total Power Consumption

We then optimised the dipole strengths in order to reduce the total power. Figure 5.57 shows how the peak dipole strength, RMS dipole strength, and the RMS field deviation between the target field and the generated field vary for different values of λ_P. In order to minimise the total power consumption, while keeping the peak field deviation to less than 10 µT, we set $\lambda_P = 2.68 \times 10^{-8}$.

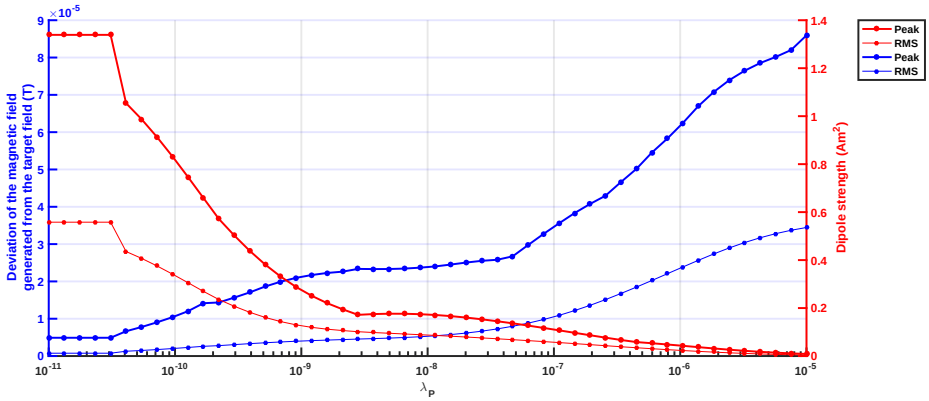

Figure 5.57: A plot of peak and RMS dipole strengths, and peak and RMS field deviations of the magnetic field generated from the target field which corresponds to an XY shimming field of maximum amplitude 0.1 mT, using dipoles whose magnetisation vectors are allowed to align at an optimum angle, against different values of the regularisation constant, λ_P.

Figure 5.58 shows the optimised dipole strengths required to generate an XY shimming field of maximum amplitude 0.1 mT, with moments allowed to align in any orientation, and with a power regularisation term $\lambda_P = 8.75 \times 10^{-11}$. Figure 5.59 shows the magnetic field generated with these optimised dipole strengths, and Figure 5.60 shows the difference between the magnetic field generated, and the target field.

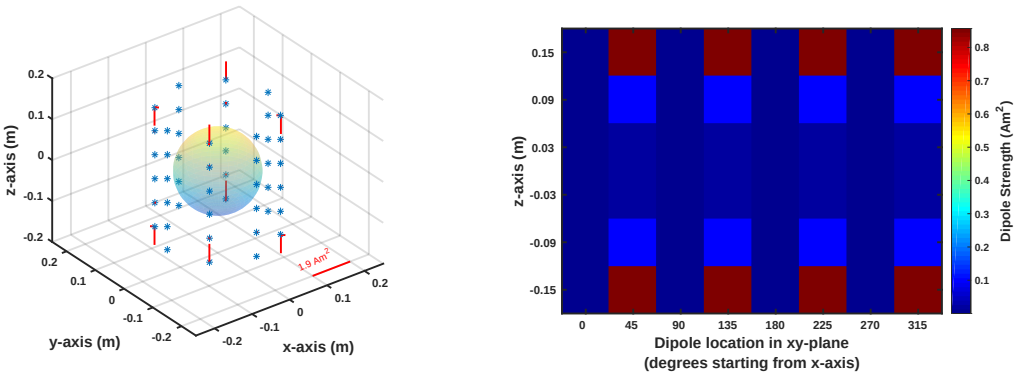

Figure 5.58: Diagram showing the dipole strengths required to generate an XY shimming field, if dipole moments are allowed to align in any orientation, and optimised to reduce the total power with a regularisation term $\lambda_P = 8.75 \times 10^{-11}$.

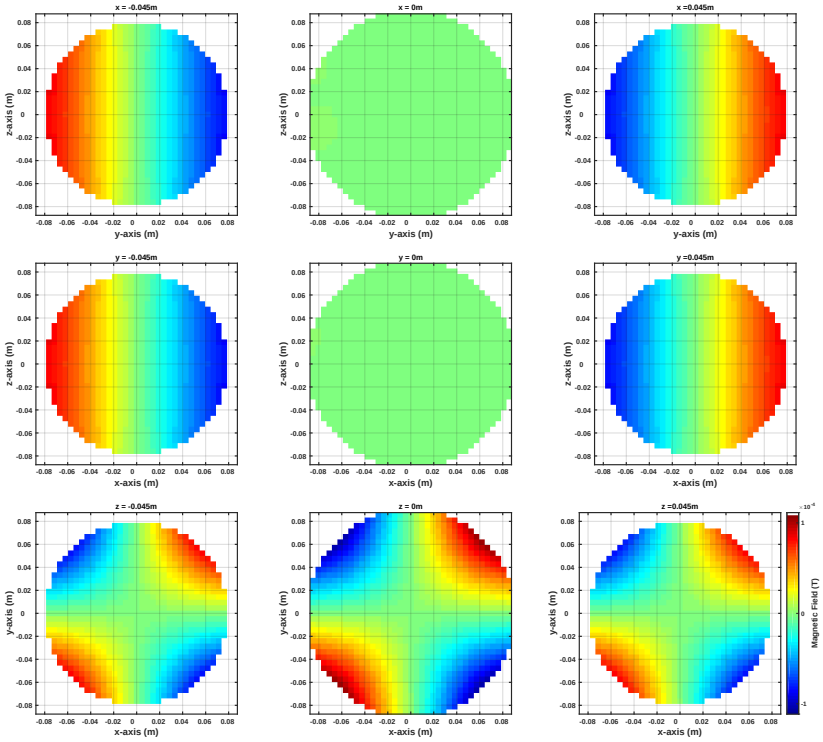

Figure 5.59: The magnetic field generated for a target field which corresponds to an XY shimming field of amplitude 0.1 mT, using dipoles whose magnetisation vectors are allowed to align in any orientation, and optimised to reduce the total power with a regularisation term $\lambda_P = 8.75 \times 10^{-11}$.

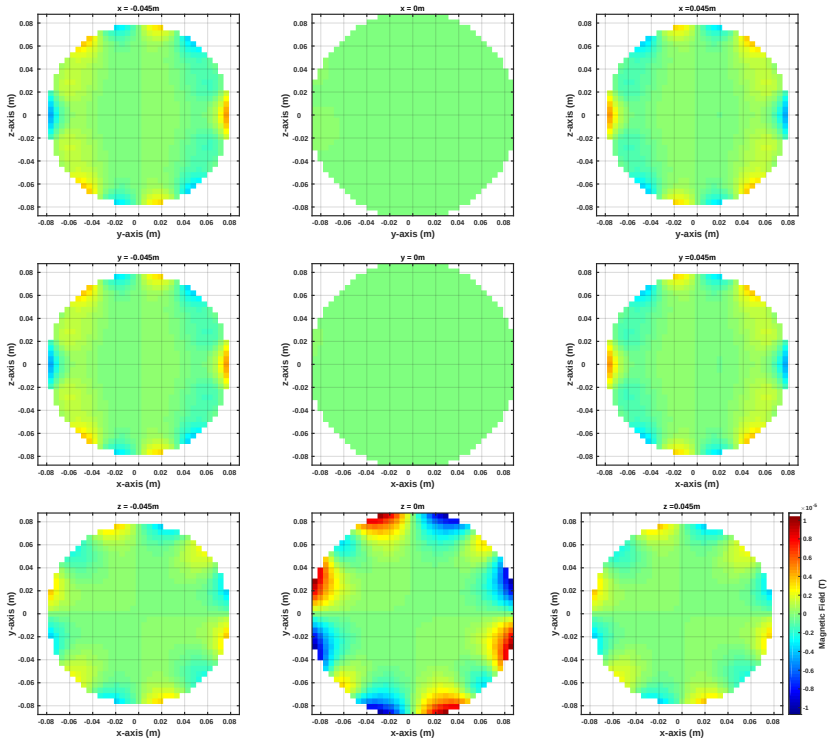

Figure 5.60: The difference between the magnetic field generated, and the target field which corresponds to an XY shimming field of amplitude 0.1 mT, using dipoles whose magnetisation vectors are allowed to align in any orientation, and optimised to reduce the total power with a regularisation constant $\lambda_P = 8.75 \times 10^{-11}$.

5.4.4 Creating a $Z3$ Shimming Field

We simulated the generation of a $Z3$ shimming field of peak amplitude 0.1 mT, using magnetic dipoles and allowing them to align at an optimum orientation.

Dipoles Oriented at an Optimum Angle, with No Constraints on their Strength

Figure 5.61 shows the dipole strengths that are required to generate a $Z3$ shimming field, when the dipoles are allowed to align in any direction, and if no constraints are applied on their strength.

The actual fields generated at points within the target volume, from these dipoles are shown in Figure 5.62. Figure 5.63 shows the difference between the magnetic field generated, and the target field.

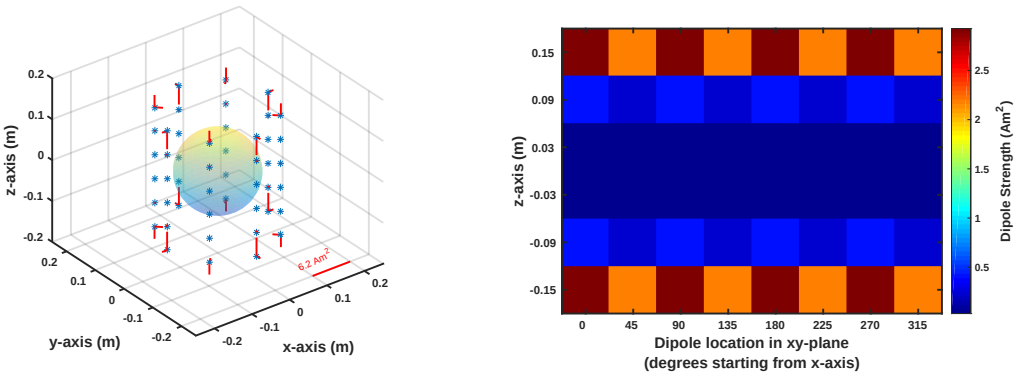

Figure 5.61: Diagram showing the dipole strengths required to generate a $Z3$ shimming field, if dipole moments are allowed to align in any orientation, and their strength is not constrained.

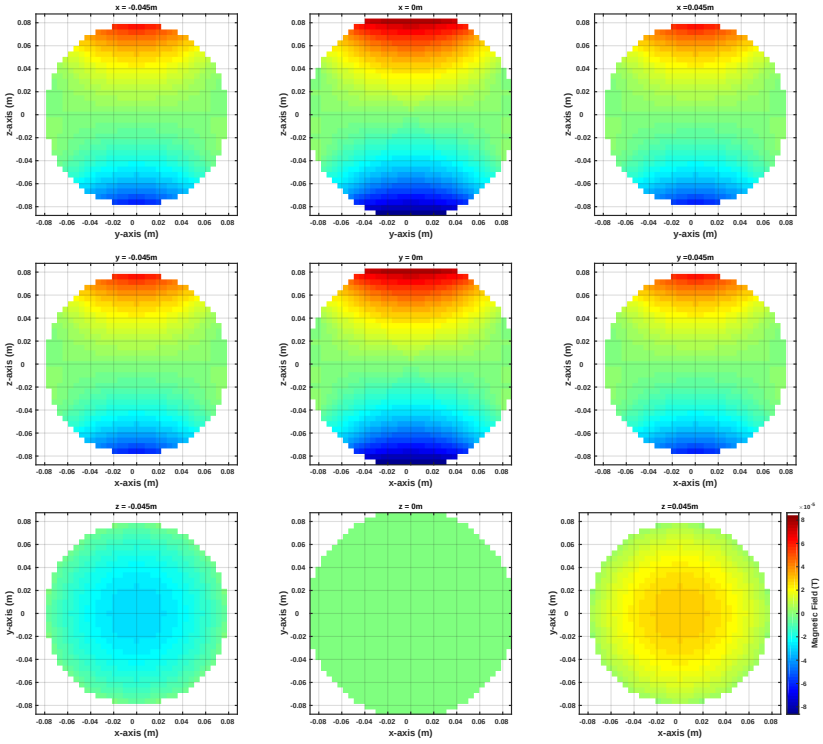

Figure 5.62: The magnetic field generated for a target field which corresponds to a $Z3$ shimming field of amplitude 0.1 mT, using dipoles whose magnetisation vectors are allowed to align in any orientation, and whose strengths are unconstrained.

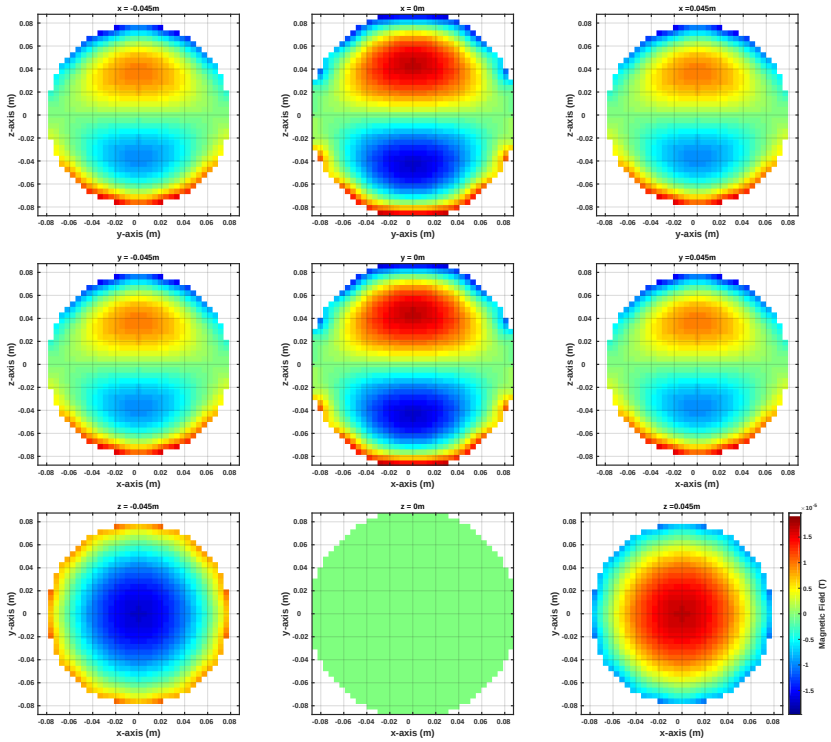

Figure 5.63: The difference between the magnetic field generated, and the target field which corresponds to a $Z3$ shimming field of amplitude 0.1 mT, using dipoles whose magnetisation vectors are allowed to align in any orientation, and whose strengths are unconstrained.

Dipoles Oriented at an Optimum Angle, with Constrained Total Power Consumption

We then optimised the dipole strengths in order to reduce the total power. Figure 5.64 shows how the peak dipole strength, RMS dipole strength, and the RMS field deviation between the target field and the generated field vary for different values of λ_P. In order to minimise the total power consumption, while keeping the peak field deviation to less than 10 µT, we set $\lambda_P = 2.68 \times 10^{-8}$.

Figure 5.65 shows the optimised dipole strengths required to generate a $Z3$ shimming field, of maximum amplitude 0.1 mT, with moments allowed to align in any orientation, and with a power regularisation term $\lambda_P = 8.38 \times 10^{-11}$. Figure 5.66 shows the magnetic field generated with these optimised dipole strengths, and Figure 5.67 shows the difference between the magnetic field generated, and the target field.

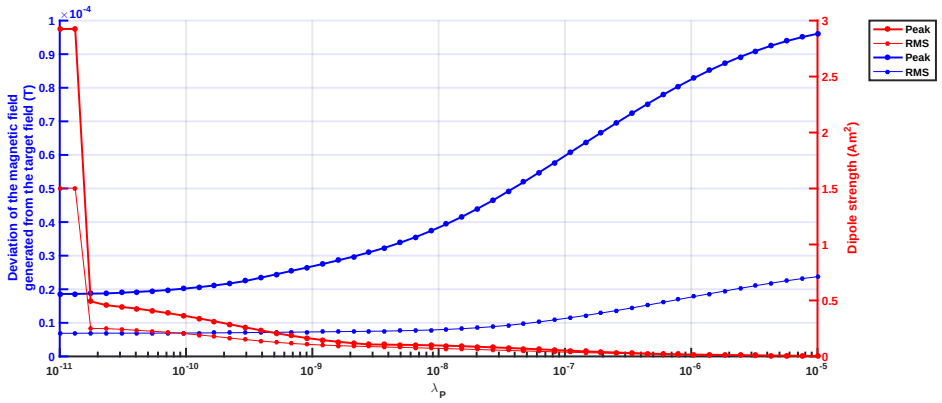

Figure 5.64: A plot of peak and RMS dipole strengths, and peak and RMS field deviations of the magnetic field generated from the target field which corresponds to a $Z3$ shimming field of maximum amplitude 0.1 mT, using dipoles whose magnetisation vectors are allowed to align at an optimum angle, against different values of the regularisation constant, λ_P.

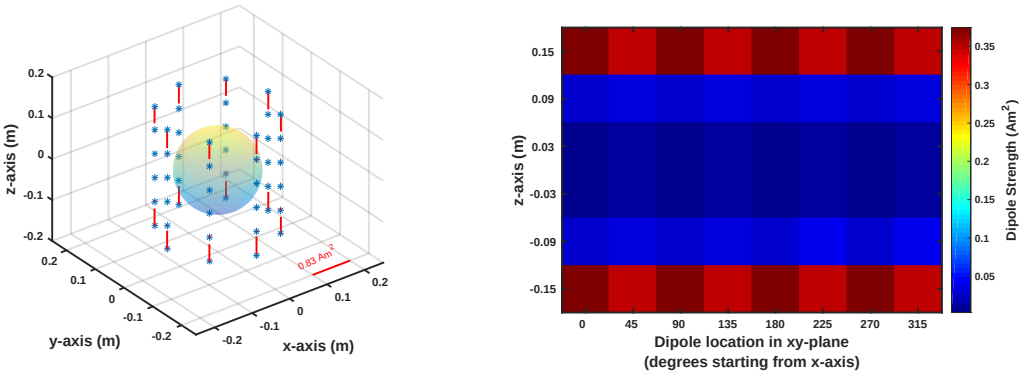

Figure 5.65: Diagram showing the dipole strengths required to generate a $Z3$ shimming field, if dipole moments are allowed to align in any orientation, and optimised to reduce the total power with a regularisation term $\lambda_P = 2.68 \times 10^{-8}$.

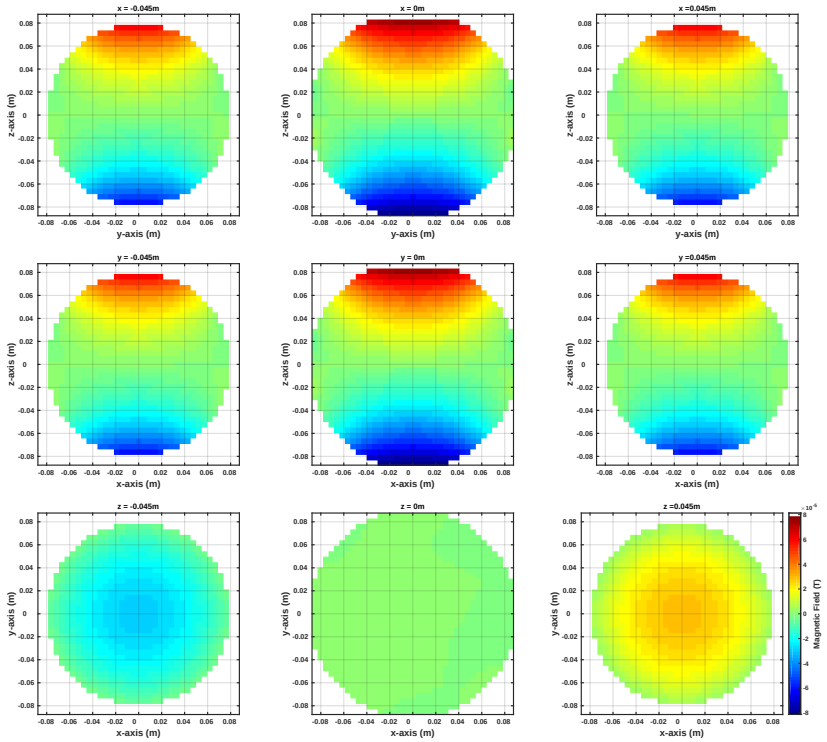

Figure 5.66: The magnetic field generated for a target field which corresponds to a $Z3$ shimming field of amplitude 0.1 mT, using dipoles whose magnetisation vectors are allowed to align in any orientation, and optimised to reduce the total power with a regularisation term $\lambda_P = 8.38 \times 10^{-11}$.

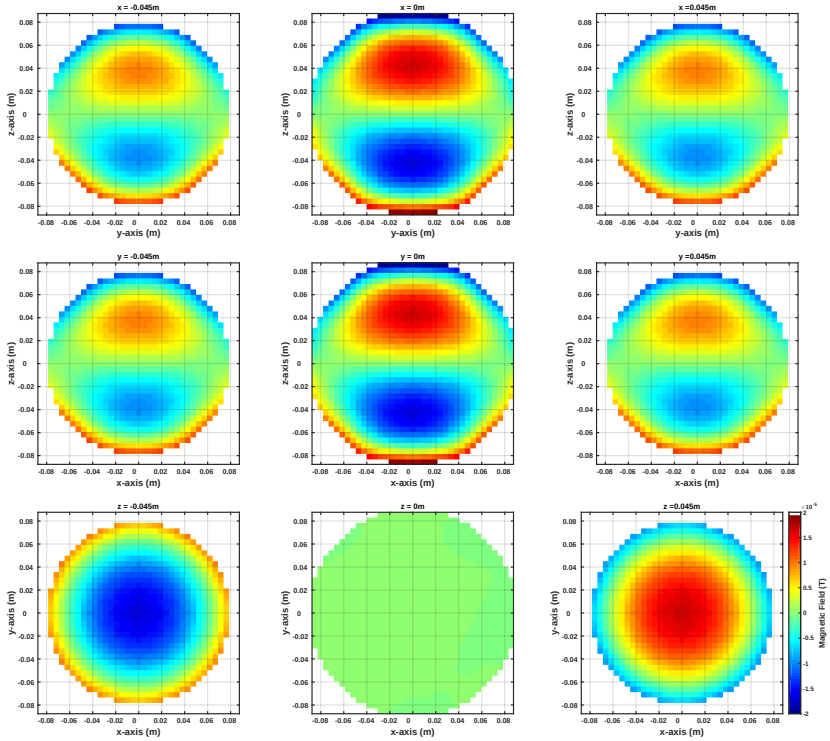

Figure 5.67: The difference between the magnetic field generated, and the target field which corresponds to a $Z3$ shimming field of amplitude 0.1 mT, using dipoles whose magnetisation vectors are allowed to align in any orientation, and optimised to reduce the total power with a regularisation constant $\lambda_P = 8.38 \times 10^{-11}$.

5.4.5 Shimming for a Brain Field Map

Dipoles Oriented at an Optimum Angle, with No Constraints on their Strength

Figure 5.68 shows the dipole strengths that are required to generate a target field which is opposite to the brain field map, when the dipoles are allowed to align in any direction, and if no constraints are applied on their strength.

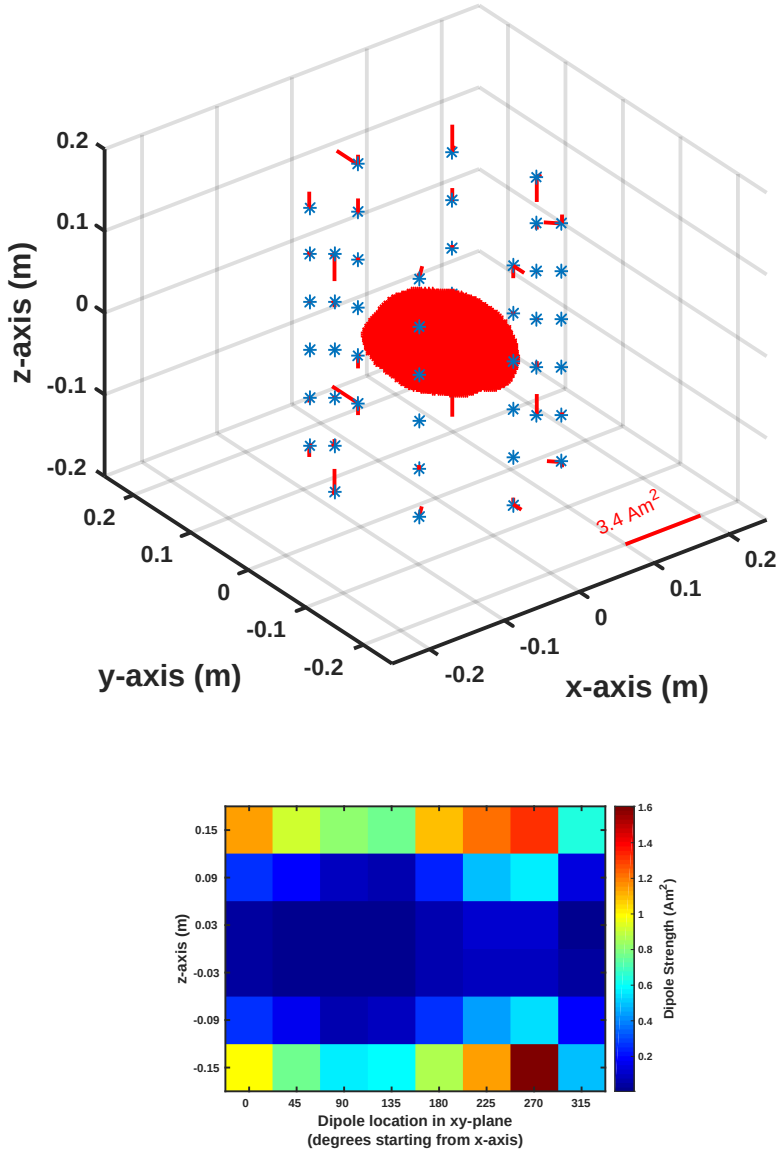

Figure 5.68: Diagram showing the dipole strengths required to generate a target field which is opposite to the brain field map, with dipole moments allowed to align in any orientation, and their strength is not constrained.

Figure 5.69 shows several slices of the field map of the brain (left), the actual fields generated for a target field which is opposite the brain's field map, using these dipoles (centre), and the two fields superimposed (right).

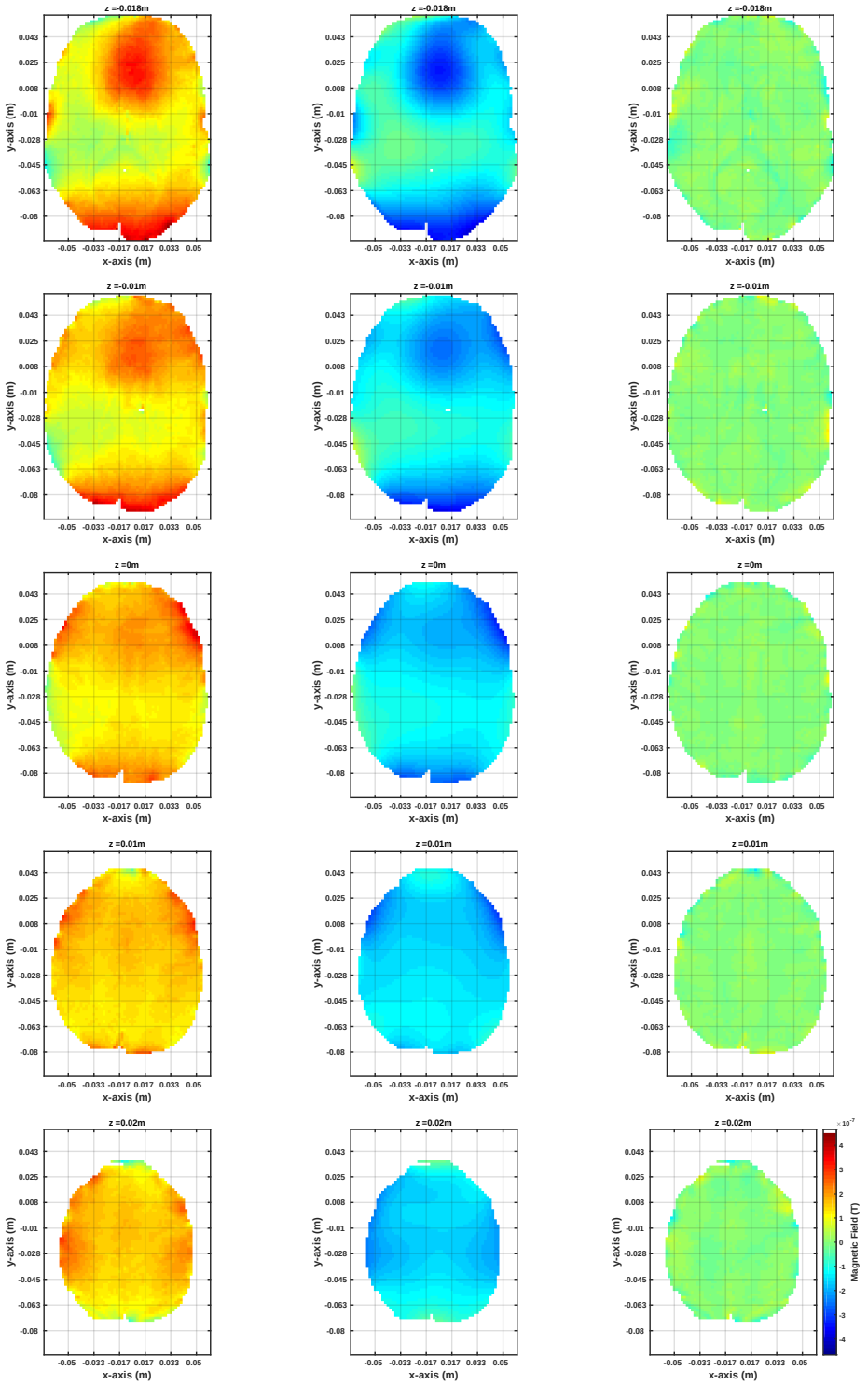

Figure 5.69: The field map of the brain (left), the magnetic field generated for a target field which is opposite to the brain field map using dipoles whose magnetisation vectors are allowed to align in any orientation, and whose strengths are unconstrained (centre), and the two fields superimposed (right).

Dipoles Oriented at an Optimum Angle, with Constrained Total Power Consumption

We then optimised the dipole strengths in order to reduce the total power. Since the target field has a lot of spatial variations, we looked at how the field will improve if we allow the dipoles to align themselves, using three orthogonal directions, rather than just two. We found that using three orthogonal directions, rather than two, does not result in a significant decrease in the dipole strengths required, nor in the difference between the generated field and target field. Thus, we kept using two orthogonal directions, and in order to minimise the total power consumption, we set $\lambda_P = 3.14 \times 10^{-11}$.

Figure 5.70 shows the optimised dipole strengths required to generate a target field which is opposite to the brain field map, with moments allowed to align in any orientation, and with a power regularisation term $\lambda_P = 3.14 \times 10^{-11}$. Figure 5.71 shows several slices of the field map of the brain (left), the actual fields generated for a target field which is opposite the brain's field map, using the optimised dipole strengths (centre), and the two fields superimposed (right).

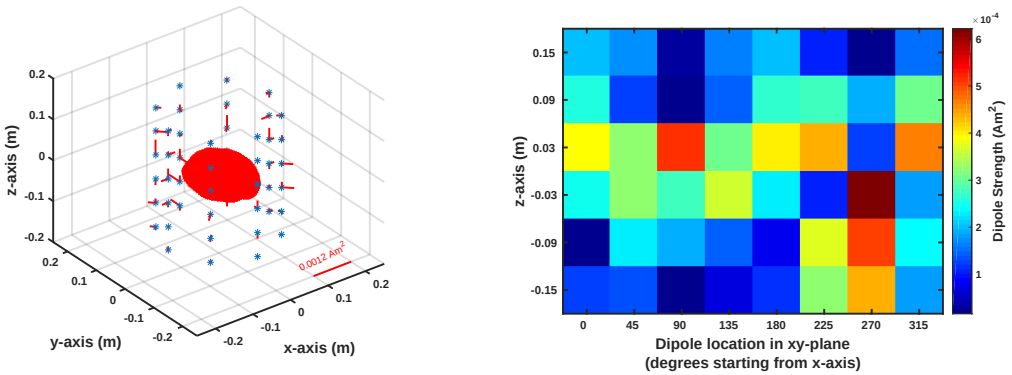

Figure 5.70: Diagram showing the dipole strengths required to generate a target field which is opposite to the brain field map, with dipole moments allowed to align in any orientation, and optimised to reduce the total power with a regularisation term $\lambda_P = 3.14 \times 10^{-11}$.

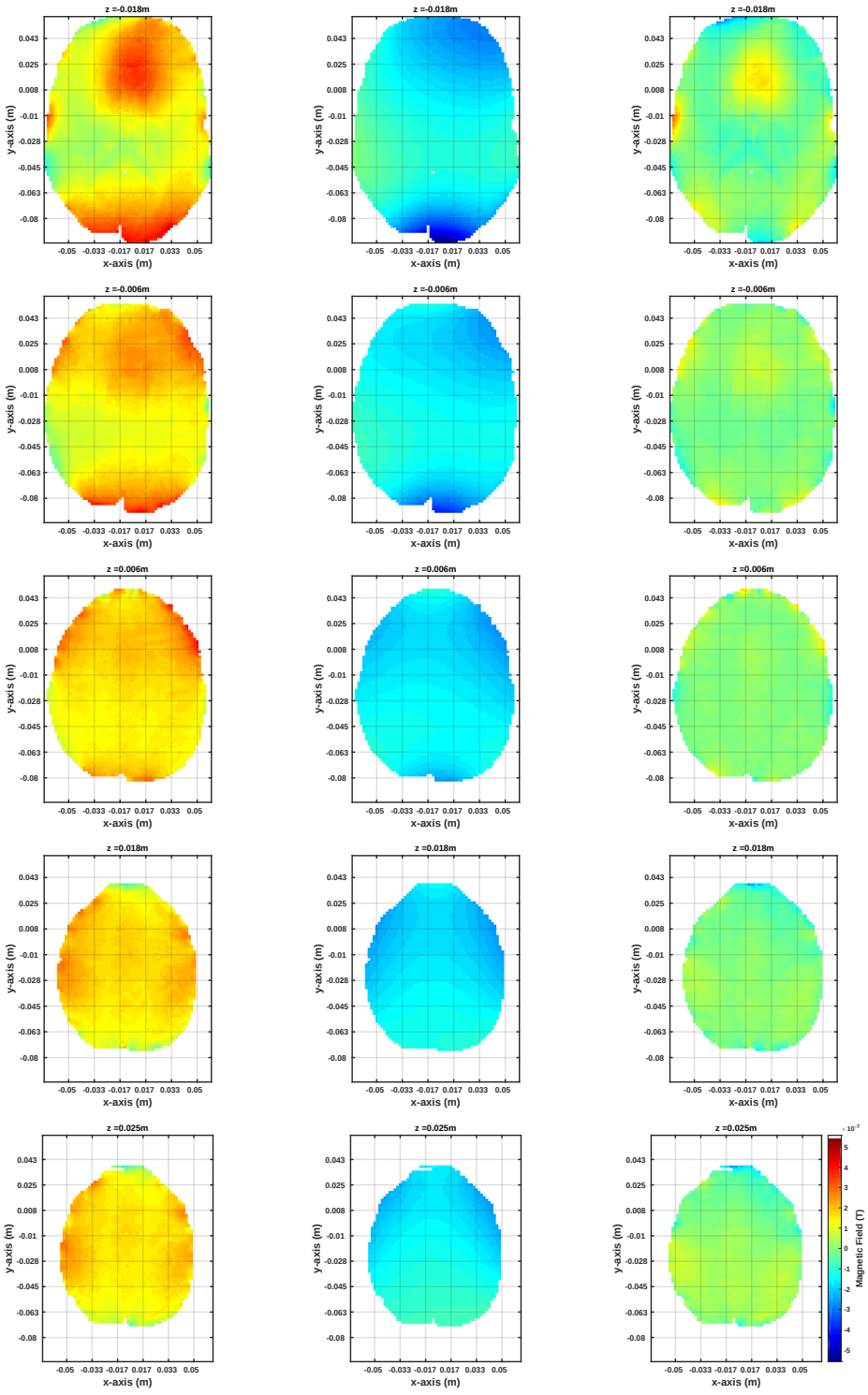

Figure 5.71: The field map of the brain (left), the magnetic field generated for a target field which is opposite to the brain field map using dipoles whose magnetisation vectors are allowed to align in any orientation, and optimised to reduce the total power with a regularisation term $\lambda_P = 3.14 \times 10^{-11}$. (centre), and the two fields superimposed (right).

Table 5.5 lists the dipole strengths and magnetic field deviations from a target field which corresponds to the inverse of the brain's field map, using dipoles aligned at an optimum orientation.

Dipoles strength constraints	Maximum dipole strength, ($\mathrm{A\,m^2}$)	RMS dipole strength, ($\mathrm{A\,m^2}$)	Maximum field deviation (T)	RMS field deviation (T)
unconstrained	1.60	5.9×10^{-1}	2×10^{-7}	1.5×10^{-8}
constrained	2.7×10^{-7}	3.2×10^{-8}	6.2×10^{-4}	2.7×10^{-4}

Table 5.5: Comparison of dipole strengths and magnetic field deviation from a target field which corresponds to the inverse of a brain's field map, using dipoles aligned at an optimum orientation. In the first case, the dipoles' strengths were unconstrained, and in the second case they were optimised to reduce the peak and RMS dipole strengths required.

The table shows that the unconstrained dipoles managed to generate a field which when superimposed onto the brain's field map, has a peak amplitude that is approximately 40 % of the peak value of the brain's field map, and an RMS that is approximately 9 % of the RMS of the brain's field map.

When dipole strengths are optimised to reduce the total power with a regularisation term $\lambda_P = 3.14 \times 10^{-11}$, the peak amplitude of the superimposed target and generated fields, is approximately 60 % of the peak of the brain's field map. The RMS of the superimposed field is approximately 20 % of the RMS of the brain's field map.

5.4.6 Dipole Field Implementation using Small Electromagnetic Coils

In the previous sections, we calculated the magnetic dipole strengths required to generate different magnetic target fields. In this section, we use the calculated dipole strengths to calculate the parameter values of electromagnetic coils that represent these dipoles.

We looked at the implementation of the z-gradient field, from dipoles that were allowed to align themselves at an optimum orientation, but with constrained strengths. Figure 5.30 showed that the different dipole strengths required were $0.094\,\mathrm{A\,m^2}$, $0.092\,\mathrm{A\,m^2}$, $0.090\,\mathrm{A\,m^2}$, and $0.047\,\mathrm{A\,m^2}$.

These strengths can be produced using small electromagnetic coils, since

$$k = N\ I\ A \tag{5.14}$$

where k is the magnetic dipole moment required, N is the number of turns in the coil, I is the current passing through the coil, and A is the area of the coil.

Table 5.6 lists possible parameters that can be used to implement the four different dipole strengths needed, and the power that will be dissipated by each coil if 0.5 mm thick wires are used. The coil radius was set at 1 cm for the coil to resemble a dipole.

Dipole moment	Coil Radius, A	Coil Turns, N	Coil Current, I	Coil Power, P
$0.094\,\mathrm{A\,m^2}$	0.01 m	20	14.96 A	0.047 W
$0.092\,\mathrm{A\,m^2}$	0.01 m	20	14.64 A	0.045 W
$0.090\,\mathrm{A\,m^2}$	0.01 m	20	9.87 A	0.021 W
$0.047\,\mathrm{A\,m^2}$	0.01 m	20	7.48 A	0.012 W

Table 5.6: Coil parameters to implement dipole field.

5.4.7 Dipole Field Implementation using Pyrolytic Graphite

Pyrolytic graphite can also be used to generate the target magnetic field. Knowing the dipole strength required to generate a particular field (e.g. to shim for a brain field map), we can calculate the volume of pyrolytic graphite using Equation 3.14. For pyrolytic graphite of magnetic susceptibility 204ppm, in a magnetic field of 7 T, the volume of pyrolytic graphite needed to represent the dipoles required is calculated using

$$m = \chi \frac{B_0}{\mu_0} v \tag{5.15}$$

Using Equation 5.15, the largest dipole required, $6.22 \times 10^{-4}\,\mathrm{A\,m^2}$, can be represented using $0.55\,\mathrm{cm^3}$ of pyrolytic graphite.

5.5 Conclusions

Our simulations showed that in generating a z-gradient field, dipoles whose magnetic moments are oriented parallel to the cylinder surface can generate a field that is closer to the target field, than dipoles oriented normal. On the other hand, in generating an x-gradient field, dipoles oriented normal to the cylinder can generate a field that is closer to the target field, than dipoles oriented parallel.

We also saw that when the dipole moments' orientations were allowed to vary, a similar level of magnetic field homogeneity could be achieved with lower peak and RMS dipole strengths.

In creating the XY and $Z3$ shimming fields, even though both target fields had the same maximum peak of 0.1 mT, less power was needed to generate the XY shimming field than to generate the $Z3$ field. Moreover, the RMS and maximum

deviation between the target field and the generated field was also smaller for the XY shimming field.

In shimming for the brain, we saw that superimposing a target field that is the inverse of the brain field map, onto the brain field map, flattens the magnetic field. The algorithm performed best for slices that lay towards the centre of the target volume. The largest field deviation was found in the first slice, both when dipoles were unconstrained, and when they were constrained. Also, the more rapid the target field variation, the more target points should be specified.

The use of pyrolytic graphite in generating the target fields allows for the simulation of dipoles oriented at any orientation. This can be easily achieved by rotating the pyrolytic graphite. There is however a limitation to the use of pyrolytic graphite in dipole simulation. Since it is diamagnetic, it cannot be used to generate negative magnetisation along the field direction. Negative fields can be generated using paramagnetic materials, such as Tungsten ($\chi = 6.8 \times 10^{-5}$) and Aluminium ($\chi = 2.2 \times 10^{-5}$).

A possible improvement for the work in this chapter is to allow for dipoles to optimally align themselves in three degrees of freedom, not just two. Such a setup could be implemented by freely rotating the coil axis, or using three orthogonal coils at each dipole location, or by rotating the pieces of the pyrolytic graphite. We tried to use three orthogonal directions when we generated a magnetic field for a target field that was equivalent to the inverse of a brain field map. Using three orthogonal directions, we did not see any significant decrease in the required dipole strength, or the difference between the generated field and the target field. Thus, we stuck to two orthognal directions - normal and parallel to the cylinder surface.

Another improvement could be to allow dipoles to optimally position themselves on the predefined surface, and to extend the method as a shape optimisation

approach.

The method could also be developed to design a hybrid system where electromagnetic coils and magnetised pyrolytic graphite may co-exist. The algorithm could produce a magnetisation volume, and current map, and a designer may choose which regions will be filled with current, or with pyrolytic graphite.

Chapter 6

Conclusion

In the first part of this thesis, we ran simulations that showed that magnetic field measurements from a typical MEG gradiometer detector array can be used to localise and quantify magnetisation. In MEG, the sources are typically described in terms of current dipoles whereas in our studies, the sources are described in terms of magnetic moments.

Because of the high sensitivity of the SQUID sensors for detecting extremely small magnetic fields, we could measure the decaying longitudinal nuclear magnetisation for the first time using a standard MEG system, from samples that have been pre-polarised in a magnetic field. We also mapped magnetic susceptibility effects, and we used the field from each sensor position to derive the source locations and magnitudes.

While looking at the NMR signals in the experiments above, we identified a long-lived magnetisation in biological samples, whose magnetisation orientation is fixed by the sample orientation. We deduced this magnetisation must be coming from remanent ferrimagnetism and/or ferromagnetism of a tissue constituent that is most likely magnetite. We then ran experiments on samples including human tissue (the hand, wrist, and foot) for the first time using MEG, and we

characterised the magnetisation behaviour. We could locate well the body part using the data from the magnetic field shift after magnetising the samples, or the data from the magnetisation relaxation. The localisation remained accurate until at least 3 h after magnetisation.

In the second part of this thesis, we saw that we can generate different magnetic target fields using magnetic dipoles, and we can then implement these dipoles using either small electromagnetic coils or pieces of a strongly diamagnetic material such as pyrolytic graphite. These methods should offer means of generating magnetic fields that can be used in shimming to generate homogeneous magnetic fields which are paramount at UHF. In our simulations, we generated different gradient and shimming fields with a maximum field deviation of 10 µT where possible, and otherwise a maximum of 28 µT. In shimming for a brain field map, we managed to reduce the maximum field in the original field map by approximately 40 %, and the RMS by 80 %.

Bibliography

[1] M. Hamalainen, R. Hari, R. J. Ilmoniemi, J. Knuutila, and O. V. Lounasmaa. Magnetoencephalography - Theory, Instrumentation, and Applications to Non-invasive Studies of the Working Human Brain. *Reviews of Modern Physics*, 65(2):413–497, April 1993.

[2] W. A. Edelstein, G. H. Glover, C. J. Hardy, and R. W. Redington. The intrinsic signal-to-noise ratio in NMR imaging. *Magnetic Resonance in Medicine*, 3(4):604–618, August 1986.

[3] F. Schick. Whole-body MRI at high field: technical limits and clinical potential. *European Radiology*, 15(5):946–959, May 2005.

[4] A. C. Papanicolaou, E. M. Castillo, R. BillingsleyMarshall, E. Pataraia, and P. G. Simos. A Review of Clinical Applications of Magnetoencephalography. volume 68 of *Magnetoencephalography*, pages 223–247. Academic Press, 2005.

[5] C. D. Gratta, V. Pizzella, F. Tecchio, and G. L. Romani. Magnetoencephalography - a noninvasive brain imaging method with 1 ms time resolution. *Reports on Progress in Physics*, 64(12):1759, 2001.

[6] D. J. Sheltraw and E. A. Coutsias. Invertibility of current density from near-field electromagnetic data. *ResearchGate*, 94(8):5307–5315, November 2003.

[7] J. Clarke, A. Pines, R. McDermott, and A. Trabesinger. SQUID Detected NMR and MRI at Ultralow Fields, March 2008.

[8] J. Clarke and A. I. Braginski. *The SQUID Handbook: Applications of SQUIDs and SQUID Systems*. John Wiley & Sons, December 2006. Google-Books-ID: yRUl4iUDt2gC.

[9] H. Rogalla and P. H. Kes. *100 Years of Superconductivity*. Taylor & Francis, November 2011. Google-Books-ID: fnbRBQAAQBAJ.

[10] J. Wilkswo. SQUIDs remain best tools for measuring brain's magnetic field. *Phys Today*, 57(2):15, 2004.

[11] S. Nagarajan and K. Sekihara. Magnetoencephalographic Imaging. In S. Supek and C. J. Aine, editors, *Magnetoencephalography: From Signals to Dynamic Cortical Networks*, page 169. Springer Berlin Heidelberg, Berlin, Heidelberg, 2014.

[12] E. Somersalo. The Inverse Problem of Magnetoencephalography: Source Localization and the Shape of a Ball. *SIAM News*, 40(2), March 2007.

[13] Y. S. Greenberg. Application of superconducting quantum interference devices to nuclear magnetic resonance. *Reviews of Modern Physics*, 70(1):175–222, January 1998.

[14] A. M. Coffey, M. Truong, and E. Y. Chekmenev. Low-field MRI can be more sensitive than high-field MRI. *Journal of magnetic resonance (San Diego, Calif. : 1997)*, 237:169–174, 2013.

[15] V. Kelha, J. Pukki, R. Peltonen, A. Penttinen, R. Ilmoniemi, and J. Heino. Design, construction, and performance of a large-volume magnetic shield. *IEEE Transactions on Magnetics*, 18(1):260–270, 1982.

[16] H. Nowak. Biomagnetism. In *Magnetism in Medicine*, pages 85–135. Wiley, 1998.

[17] S. Baillet. Why a magnetically-shielded room?, 2010.

[18] S. P. Singh. Magnetoencephalography: Basic principles. *Annals of Indian Academy of Neurology*, 17(Suppl 1):S107–S112, March 2014.

[19] J. Bardeen, L. N. Cooper, and J. R. Schrieffer. Theory of Superconductivity. *Physical Review*, 108(5):1175–1204, December 1957.

[20] M. Brookes. Magnetoencephalography (MEG) - From Signal Detection to Inverse Solution. January 2015.

[21] B. D. Josephson. Possible new effects in superconductive tunnelling. *Physics Letters*, 1(7):251–253, July 1962.

[22] A. M. v. d. Brink, A. A. Odintsov, P. A. Bobbert, and G. Schn. Coherent Cooper pair tunneling in systems of Josephson junctions: Effects of quasiparticle tunneling and of the electromagnetic environment. *Zeitschrift fr Physik B Condensed Matter*, 85(3):459–467, October 1991.

[23] Y.-H. Lee and K. Kim. Instrumentation for Measuring MEG Signals. In *Magnetoencephalography: From Signals to Dynamic Cortical Networks*, page 29. Springer, Berlin, 2014.

[24] A. N. Matlashov, L. J. Schultz, M. A. Espy, R. H. Kraus, I. M. Savukov, P. L. Volegov, and C. J. Wurden. SQUIDs vs. Induction Coils for Ultra-Low Field Nuclear Magnetic Resonance: Experimental and Simulation Comparison. *IEEE transactions on applied superconductivity : a publication of the IEEE Superconductivity Committee*, 21(3):465–468, 2011.

[25] S. Supek and C. J. Aine, editors. *Magnetoencephalography: From Signals to Dynamic Cortical Networks*. Springer Berlin Heidelberg, Berlin, Heidelberg, 2014.

[26] R. Cantor. DC SQUIDs: Design, Optimization and Practical Applications. In *SQUID Sensors: Fundamentals, Fabrication and Applications*, page 203. Springer Science+Business Media Dordrecht, 1995.

[27] D. Cohen. Magnetoencephalography: Detection of the Brain's Electrical Activity with a Superconducting Magnetometer. *Science (New York, N.Y.)*, 175(4022):664–666, February 1972.

[28] J. C. Mosher, R. M. Leahy, and P. S. Lewis. EEG and MEG: forward solutions for inverse methods. *IEEE transactions on bio-medical engineering*, 46(3):245–259, March 1999.

[29] J. Sarvas. Basic Mathematical and Electromagnetic Concepts of the Biomagnetic Inverse Problem. *Physics in Medicine and Biology*, 32(1):11, January 1987.

[30] J. D. Jackson. Maxwell Equations, Macroscopic Electromagnetism, Conservation Laws. In *Classical Electrodynamics*. Wiley, 3rd edition, 1999.

[31] J. D. Jackson. Magnetostatics, Faraday's Laws, Quasi-Static Fields. In *Classical Electrodynamics*. Wiley, 3rd edition, 1999.

[32] R. V. Uitert, D. Weinstein, and C. Johnson. Volume Currents in Forward and Inverse Magnetoencephalographic Simulations Using Realistic Head Models. *Annals of Biomedical Engineering*, 31(1):21–31, January 2003.

[33] J. Hauiesen and T. Knosche. Forward Modeling and Tissue Conductivities. In *Magnetoencephalography: From Signals to Cortical Networks*. Springer Berlin Heidelberg, Berlin, Heidelberg, 2014.

[34] R. Ramrez. Source localization. *Scholarpedia*, 3(11):1733, 2008.

[35] J. Vrba and S. E. Robinson. Signal processing in magnetoencephalography. *Methods (San Diego, Calif.)*, 25(2):249–271, October 2001.

[36] M. S. Hmlinen and R. J. Ilmoniemi. Interpreting magnetic fields of the brain: minimum norm estimates. *Medical & Biological Engineering & Computing*, 32(1):35–42, 1984.

[37] J. C. A. Barata and M. S. Hussein. The Moore-Penrose Pseudoinverse. A Tutorial Review of the Theory, 2011.

[38] A. Tikhonov. Solution of Incorrectly Formulated Problems and the Regularization Method. *Soviet Math. Dokl.*, 5:1035/1038, 1963.

[39] A. M. Dale, A. K. Liu, B. R. Fischl, R. L. Buckner, J. W. Belliveau, J. D. Lewine, and E. Halgren. Dynamic Statistical Parametric Mapping. *Neuron*, 26(1):55–67, April 2000.

[40] T. M. Inc. Interpolating Scattered Data - MATLAB & Simulink - MathWorks United Kingdom, 2015.

[41] J.-D. Boissonnat and F. Cazals. Smooth surface reconstruction via natural neighbour interpolation of distance functions. *Computational Geometry*, 22(1):185–203, May 2002.

[42] D. Haro, L. P, T. Karaulanov, E. C. Vreeland, B. Anderson, H. J. Hathaway, D. L. Huber, A. N. Matlashov, C. P. Nettles, A. D. Price, T. C. Monson, and E. R. Flynn. Magnetic relaxometry as applied to sensitive cancer detection and localization. *Biomedical Engineering / Biomedizinische Technik*, 0(0), June 2015.

[43] M. Espy, M. Flynn, J. Gomez, C. Hanson, R. Kraus, P. Magnelind, K. Maskaly, A. Matlashov, S. Newman, M. Peters, H. Sandin, I. Savukov, L. Schultz, A. Urbaitis, P. Volegov, and V. Zotev. Applications of Ultra-Low Field Magnetic Resonance for Imaging and Materials Studies. *IEEE Transactions on Applied Superconductivity*, 19(3):835–838, June 2009.

[44] B. Inglis, K. Buckenmaier, P. Sangiorgio, A. F. Pedersen, M. A. Nichols, and J. Clarke. MRI of the human brain at 130 microtesla. *Proceedings of the Na-*

tional Academy of Sciences of the United States of America, 110(48):19194–19201, November 2013.

[45] J. O. N. Panu T Vesanen. Hybrid ultra-low-field MRI and magnetoencephalography system based on a commercial whole-head neuromagnetometer. *Magnetic resonance in medicine : official journal of the Society of Magnetic Resonance in Medicine / Society of Magnetic Resonance in Medicine*, 69(6):spcone, 2013.

[46] I. M. Savukov, V. S. Zotev, P. L. Volegov, M. A. Espy, A. N. Matlashov, J. J. Gomez, and R. H. Kraus Jr. MRI with an atomic magnetometer suitable for practical imaging applications. *Journal of Magnetic Resonance*, 199(2):188–191, August 2009.

[47] V. S. Zotev, P. L. Volegov, A. N. Matlashov, I. M. Savukov, T. Owens, and M. A. Espy. SQUID-based microtesla MRI for in vivo relaxometry of the human brain. *IEEE Trans.Appl.Supercond.*, 19:823, 2009.

[48] V. S. Zotev, A. N. Matlashov, P. L. Volegov, I. M. Savukov, M. A. Espy, J. C. Mosher, J. J. Gomez, and R. H. Kraus Jr. Microtesla MRI of the human brain combined with MEG. *Journal of Magnetic Resonance*, 194(1):115–120, September 2008. arXiv: 0711.0222.

[49] D. J. Michalak, S. Xu, T. J. Lowery, C. W. Crawford, M. Ledbetter, L.-S. Bouchard, D. E. Wemmer, D. Budker, and A. Pines. Relaxivity of gadolinium complexes detected by atomic magnetometry. *Magnetic Resonance in Medicine*, 66(2):605–608, August 2011.

[50] R. K. Jr, M. Espy, P. Magnelind, and P. Volegov. *Ultra-Low Field Nuclear Magnetic Resonance: A New MRI Regime*. OUP USA, February 2014.

[51] S. Lee, M. Mossle, W. Myer, N. Kelso, A. Trabesinger, A. Pines, and J. Clarke. SQUID-detected MRI at 132 uT with T1-weighted contrast

established at 10 uT-300 mT. *Magnetic Resonance in Medicine*, (53):9–14, 2005.

[52] M. Genetti, F. Grouiller, S. Vulliemoz, L. Spinelli, M. Seeck, C. M. Michel, and K. Schaller. Noninvasive language mapping in patients with epilepsy or brain tumors. *Neurosurgery*, 72(4):555–565; discussion 565, April 2013.

[53] S. Ogawa, T. M. Lee, A. R. Kay, and D. W. Tank. Brain magnetic resonance imaging with contrast dependent on blood oxygenation. *Proceedings of the National Academy of Sciences of the United States of America*, 87(24):9868–9872, December 1990.

[54] M. H. Lev and P. Ellen Grant. MEG versus BOLD MR Imaging: Functional Imaging, the Next Generation? *American Journal of Neuroradiology*, 21:1369–1370, 2000.

[55] M. Brookes. An Introduction to MEG and EEG, June 2014.

[56] J. Clarke, M. Hatridge, and M. Mssle. SQUID-detected magnetic resonance imaging in microtesla fields. *Annual Review of Biomedical Engineering*, 9:389–413, 2007.

[57] I. Vella, M. Ali, J. Medica, M. Brookes, and R. Bowtell. Nuclear Magnetisation Detection using a MEG System. MEG UK, January 2015. Conference Poster.

[58] R. M. Brown. Nuclear Magnetic Resonance in Weak Fields. *Physical Review*, 78(5):530–532, June 1950.

[59] M. H. Levitt. *Spin Dynamics: Basics of Nuclear Magnetic Resonance*. Wiley, 2nd edition, March 2008.

[60] R. Feynman. *The Feynman Lectures on Physics*, volume 3. Basic Books, the new millennium edition, 2010.

[61] C. Guy and D. ffytche. Magnetic Resonance Imaging. In *An introduction to The Principles of Medical Imaging*. Imperial College Press, revised edition, 2005.

[62] N. Bloembergen, E. M. Purcell, and R. V. Pound. Relaxation Effects in Nuclear Magnetic Resonance Absorption. *Physical Review*, 73(7):679–712, April 1948.

[63] M. Goldman. Formal Theory of SpinLattice Relaxation. *Journal of magnetic resonance (San Diego, Calif. : 1997)*, 149(2):160–87, 2001.

[64] R. Bowtell, M. Ali, J. Medica, I. Vella, and M. Brookes. Mapping Magnetisation using a Magnetoencephalography System. *ISMRM 23rd Annual Meeting and Exhibition*, June 2015.

[65] M. Hmlinen. Anatomical correlates for magnetoencephalography: integration with magnetic resonance images. *Clinical Physics and Physiological Measurement: An Official Journal of the Hospital Physicists' Association, Deutsche Gesellschaft Fur Medizinische Physik and the European Federation of Organisations for Medical Physics*, 12 Suppl A:29–32, 1991.

[66] P. Adjamian, G. R. Barnes, A. Hillebrand, I. E. Holliday, K. D. Singh, P. L. Furlong, E. Harrington, C. W. Barclay, and P. J. G. Route. Co-registration of magnetoencephalography with magnetic resonance imaging using bite-bar-based fiducials and surface-matching. *Clinical Neurophysiology: Official Journal of the International Federation of Clinical Neurophysiology*, 115(3):691–698, March 2004.

[67] C. U. B. R. I. Centre. Co-registration of MRI and MEG data, 2014. Available at http://sites.cardiff.ac.uk/cubric/cubric-users/user-documentation/meg-resources/co-registration-of-mri-and-meg-data/.

[68] M. I. S. Limited. Software, 2013.

[69] J. L. Kirschvink, A. Kobayashi-Kirschvink, and B. J. Woodford. Magnetite biomineralization in the human brain. *Proceedings of the National Academy of Sciences*, 89(16):7683–7687, August 1992.

[70] J. L. Kirschvink, A. Kobayashi-Kirschvink, J. C. Diaz-Ricci, and S. J. Kirschvink. Magnetite in human tissues: a mechanism for the biological effects of weak ELF magnetic fields. *Bioelectromagnetics*, Suppl 1:101–113, 1992.

[71] H. A. Lowenstam and S. Weiner. *On Biomineralization*. Oxford University Press, April 1989.

[72] P. P. Schultheiss-Grassi and J. Dobson. Magnetic analysis of human brain tissue. *Biometals*, 12(1):67–72, March 1999.

[73] H. Coetzee. Biomagnetism and Bio-Electromagnetism: The Foundation of Life, 2015.

[74] F. Brem, A. M. Hirt, M. Winklhofer, K. Frei, Y. Yonekawa, H.-G. Wieser, and J. Dobson. Magnetic iron compounds in the human brain: a comparison of tumour and hippocampal tissue. *Journal of the Royal Society Interface*, 3(11):833–841, December 2006.

[75] R. Kotitz, W. Weitschies, L. Trahms, and W. Semmler. Investigation of Brownian and Neel relaxation in magnetic fluids. *Journal of Magnetism and Magnetic Materials*, 201:102–104, 1999.

[76] V. Singh, V. Banerjee, and M. Sharma. Dynamics of magnetic nanoparticle suspensions. August 2012.

[77] S. Dattagupta. *Relaxation Phenomena in condensed Matter Physics*. Elsevier, December 2012.

[78] W. Coffey, Y. P. Kalmykov, and J. T. Waldron. *The Langevin Equation: With Applications in Physics, Chemistry, and Electrical Engineering*. World Scientific, 1996.

[79] P. C. Fannin and S. W. Charles. The study of a ferrofluid exhibiting both Brownian and Neel relaxation. *Journal of Physics D: Applied Physics*, 22(1):187, 1989.

[80] S. D. Muthukumaraswamy. High-frequency brain activity and muscle artifacts in MEG/EEG: a review and recommendations. *Frontiers in Human Neuroscience*, 7, April 2013.

[81] R. Casiday and R. Frey. Iron in Biology: Study of Iron Content in Ferritin, The Iron-Storage Protein., November 2000.

[82] C. J. De Luca. The use of surface electromyography in biomechanics. *Journal of applied biomechanics*, 1997.

[83] K. Hammond, J. Lupo, D. Kelley, and S. Nelson. Comparison of the B0 Field and Shimming in the Human Brain at 3t and 7t. *Proc. Intl. Soc. Mag. Reson. Med.*, (14), 2006.

[84] K. Krupa and M. Bekiesiska-Figatowska. Artifacts in Magnetic Resonance Imaging. *Polish Journal of Radiology*, 80:93–106, February 2015.

[85] F. Gaillard and U. Bashir. Magnetic susceptibility artifact | Radiology Reference Article | Radiopaedia.org, 2013.

[86] R. Turner. Gradient coil design: A review of methods. *Magnetic Resonance Imaging*, 11(7):903–920, January 1993.

[87] P. Glover and A. Howes. MPAGS MR2 MR Hardware, 2013. Lecture Notes.

[88] D. Mc Robbie, E. Moore, M. Graves, and M. Prince. *MRI From Picture to Proton*. Cambridge University Press, 2007.

[89] P. Glover. MPAGS Module MR2: NMR Hardware, 2012.

[90] C. Westbrook, C. Kaut Roth, and J. Talbot. *MRI In Practice*. Blackwell Publishing, third edition, 2005.

[91] K. Koch, D. Rothman, and R. de Graaf. Optimization of static magnetic field homogeneity in the human and animal brain in vivo. *Progress in Nuclear Magnetic Resonance Spectroscopy*, 54:69–96, 2009.

[92] J. L. Wilson, M. Jenkinson, and P. Jezzard. Optimization of static field homogeneity in human brain using diamagnetic passive shims. *Magnetic Resonance in Medicine*, 48(5):906–914, November 2002.

[93] D. B. Fischbach. Diamagnetic Susceptibility of Pyrolytic Graphite. *Physical Review*, 123(5):1613–1614, September 1961.

[94] A. M. Blamire, D. L. Rothman, and T. Nixon. Dynamic shim updating: a new approach towards optimized whole brain shimming. *Magnetic Resonance in Medicine*, 36(1):159–165, July 1996.

[95] V. W. Miner and W. W. Conover. The shimming of high resolution NMR magnets, 1997.

[96] J. Hornak. Imaging Hardware, 1996.

[97] R. Cusack, B. Russell, S. Cox, C. De Panfilis, C. Schwarzbauer, and R. Ansorge. An evaluation of the use of passive shimming to improve frontal sensitivity in fMRI. *NeuroImage*, 24:82–91, 2005.

[98] C. Juchem, T. Nixon, S. McIntyre, D. Rothman, and R. de Graaf. Magnetic field homogenization of the human prefrontal cortex with a set of localized electrical coils. *Magnetic Resonance in Medicine*, 63:171–180, 2010.

[99] M. Poole. *Improved equipment and techniques for dynamic shimming in high field MRI.* PhD thesis, The University of Nottingham, 2007.

[100] B. Keating and T. Ernst. Real-time dynamic frequency and shim correction for single-voxel magnetic resonance spectroscopy. *Magnetic Resonance in Medicine*, 68(5):1339–1345, 2012.

[101] C. Juchem, T. Nixon, S. McIntyre, V. Boer, and D. Rothman. Dynamic multi-coil shimming of the human brain at 7t. *Journal of Magnetic Resonance*, 212:280–288, 2011.

[102] M. Poole and R. Bowtell. Volume parcellation for improved dynamic shimming. *Magn Reson Mater Phy*, 21:31–40, 2008.

[103] B. A. Chronik, A. Alejski, and B. K. Rutt. Design and fabrication of a three-axis edge ROU head and neck gradient coil. *Magnetic Resonance in Medicine*, 44(6):955–963, December 2000.

[104] R. Turner. Minimum inductance coils. *Journal of Physics E: Scientific Instruments*, 21(10):948, 1988.

[105] E. C. Wong, A. Jesmanowicz, and J. S. Hyde. Coil optimization for MRI by conjugate gradient descent. *Magnetic Resonance in Medicine*, 21(1):39–48, September 1991.

[106] R. Turner. A target field approach to optimal coil design. *Journal of Physics D: Applied Physics*, 19(8):L147, 1986.

[107] M. A. Martens, L. S. Petropoulos, R. W. Brown, J. H. Andrews, M. A. Morich, and J. L. Patrick. Insertable biplanar gradient coils for magnetic resonance imaging. *Review of Scientific Instruments*, 62(11):2639–2645, November 1991.

[108] R. Bowtell and P. Mansfield. Minimum power flat gradient pairs for NMR microscopy. *Book of abstracts: Eighth Annual Meeting of the Society of Magnetic Resonance in Medicine*, page 977, 1989.

[109] H. S. Lopez, F. Liu, M. Poole, and S. Crozier. Equivalent Magnetization Current Method Applied to the Design of Gradient Coils for Magnetic Resonance Imaging. *IEEE Transactions on Magnetics*, 45(2):767–775, February 2009.

Appendices

Appendix A

Magnetic Dipole Source Localisation for Magnetic Dipoles Oriented at Different Orientations

Figures A.1 - A.8 show the MNE-reconstructed FWHM magnetic dipole source localisation for magnetic dipoles located at (-0.085, 0, 0.06)m and oriented at varying angles in the y-z plane. These figures show no correlation between the MNE-reconstruction accuracy and the true orientation of the test dipole.

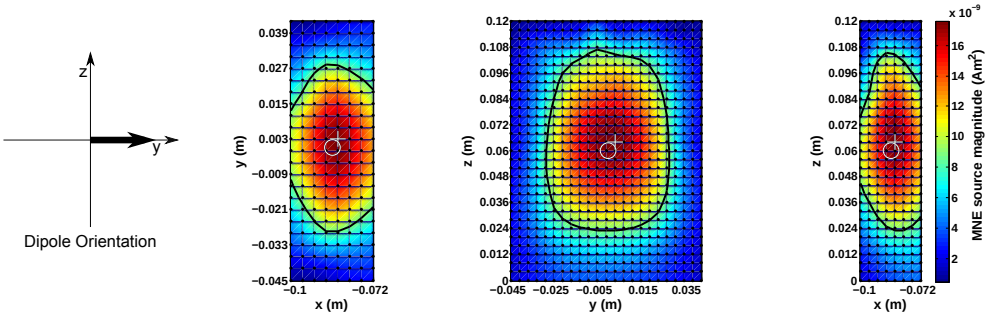

Figure A.1: Plots showing MNE-reconstructed FWHM magnetic dipole source localisation in the x-y plane at $z = 0.064\,\mathrm{m}$ (left), y-z plane at $x = -0.084\,\mathrm{m}$ (centre) and x-z plane at $y = 0.003\,\mathrm{m}$ (right) for a magnetic dipole with moment magnitude $10\,\mathrm{nA\,m^2}$ located at (-0.085, 0, 0.06)m and oriented at (0,1,0).

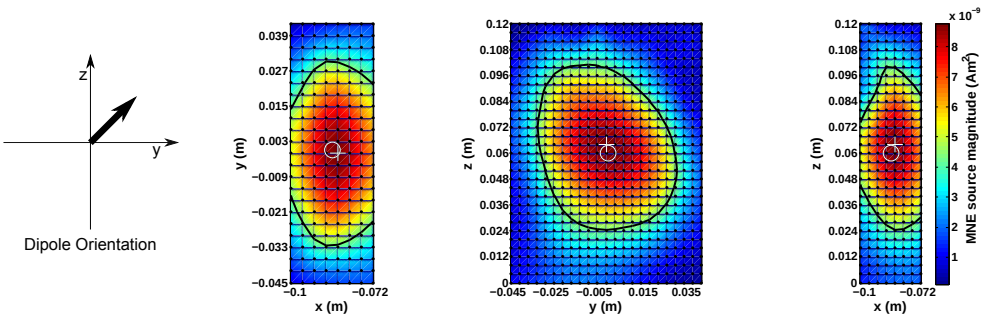

Figure A.2: Plots showing MNE-reconstructed FWHM magnetic dipole source localisation in the x-y plane at $z = 0.064\,\mathrm{m}$ (left), y-z plane at $x = -0.084\,\mathrm{m}$ (centre) and x-z plane at $y = -0.001\,\mathrm{m}$ (right) for a magnetic dipole with moment magnitude $10\,\mathrm{nA\,m^2}$ located at (-0.085, 0, 0.06)m and oriented at (0,1,1).

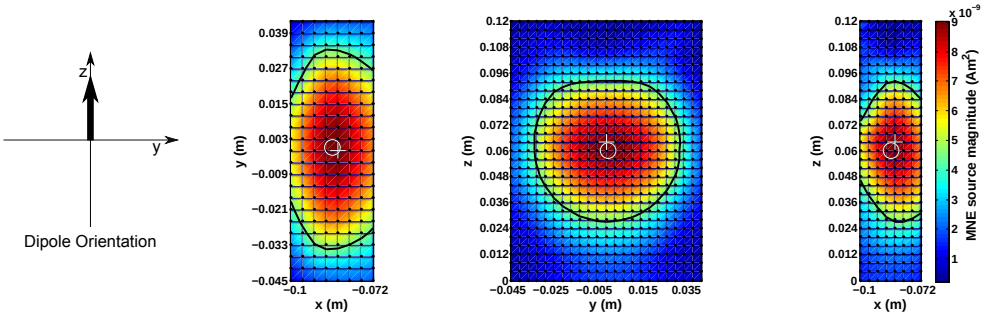

Figure A.3: Plots showing MNE-reconstructed FWHM magnetic dipole source localisation in the x-y plane at $z = 0.064\,\mathrm{m}$ (left), y-z plane at $x = -0.084\,\mathrm{m}$ (centre) and x-z plane at $y = -0.001\,\mathrm{m}$ (right) for a magnetic dipole with moment magnitude $10\,\mathrm{nA\,m^2}$ located at (-0.085, 0, 0.06)m and oriented at (0,0,1).

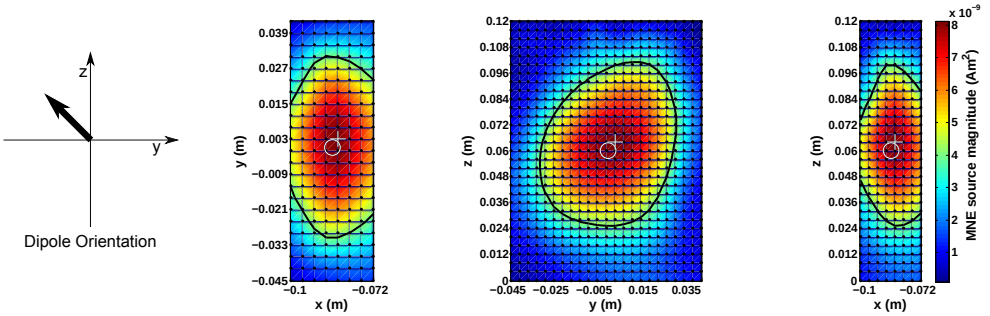

Figure A.4: Plots showing MNE-reconstructed FWHM magnetic dipole source localisation in the x-y plane at $z = 0.064\,\mathrm{m}$ (left), y-z plane at $x = -0.084\,\mathrm{m}$ (centre) and x-z plane at $y = 0.003\,\mathrm{m}$ (right) for a magnetic dipole with moment magnitude $10\,\mathrm{nA\,m^2}$ located at (-0.085, 0, 0.06)m and oriented at (0,-1,1).

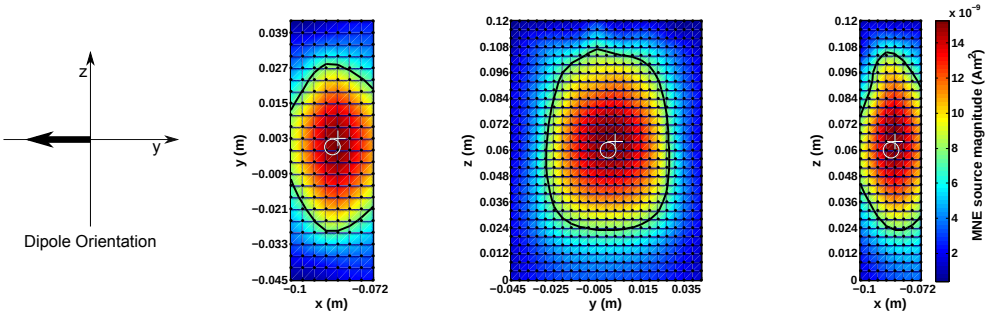

Figure A.5: Plots showing MNE-reconstructed FWHM magnetic dipole source localisation in the x-y plane at $z = 0.064\,\mathrm{m}$ (left), y-z plane at $x = -0.084\,\mathrm{m}$ (centre) and x-z plane at $y = 0.003\,\mathrm{m}$ (right) for a magnetic dipole with moment magnitude $10\,\mathrm{nA\,m^2}$ located at (-0.085, 0, 0.06)m and oriented at (0,-1,0).

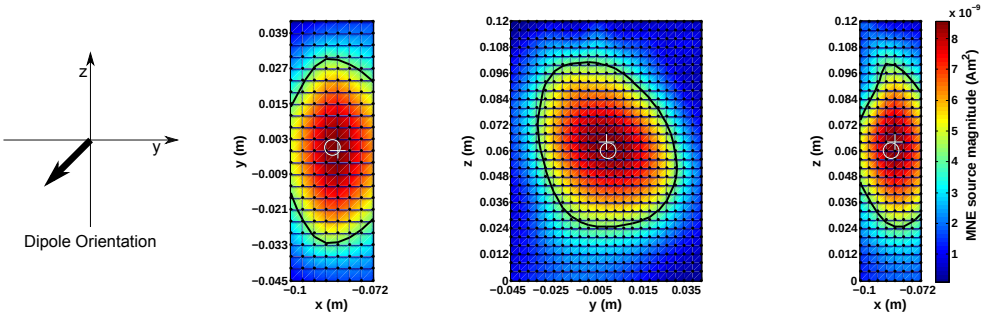

Figure A.6: Plots showing MNE-reconstructed FWHM magnetic dipole source localisation in the x-y plane at $z = 0.064\,\mathrm{m}$ (left), y-z plane at $x = -0.084\,\mathrm{m}$ (centre) and x-z plane at $y = -0.001\,\mathrm{m}$ (right) for a magnetic dipole with moment magnitude $10\,\mathrm{nA\,m^2}$ located at (-0.085, 0, 0.06)m and oriented at (0,-1,-1).

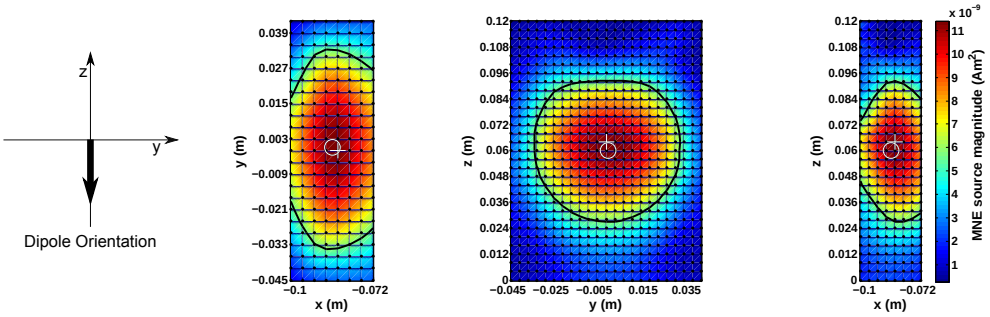

Figure A.7: Plots showing MNE-reconstructed FWHM magnetic dipole source localisation in the x-y plane at $z = 0.064\,\mathrm{m}$ (left), y-z plane at $x = -0.084\,\mathrm{m}$ (centre) and x-z plane at $y = -0.001\,\mathrm{m}$ (right) for a magnetic dipole with moment magnitude $10\,\mathrm{nA\,m^2}$ located at (-0.085, 0, 0.06)m and oriented at (0,0,-1).

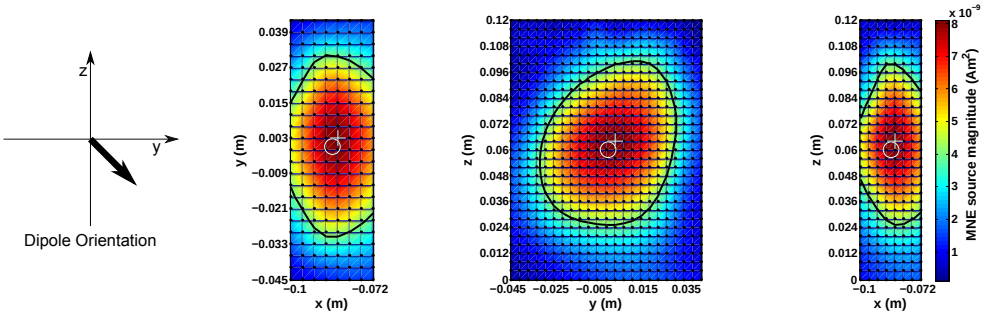

Figure A.8: Plots showing MNE-reconstructed FWHM magnetic dipole source localisation in the x-y plane at $z = 0.064\,\mathrm{m}$ (left), y-z plane at $x = -0.084\,\mathrm{m}$ (centre) and x-z plane at $y = 0.003\,\mathrm{m}$ (right) for a magnetic dipole with moment magnitude $10\,\mathrm{nA\,m^2}$ located at (-0.085, 0, 0.06)m and oriented at (0,1,-1).

Figures A.9 - A.16 show the MNE-reconstructed FWHM magnetic dipole source localisation for magnetic dipoles located at (-0.085, 0, 0.06)m and oriented at varying angles in the x-z plane. These figures show no correlation between the MNE-reconstruction accuracy and the true orientation of the test dipole.

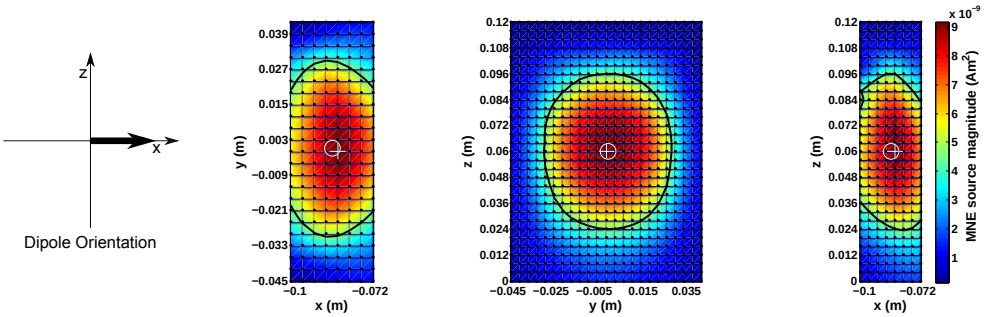

Figure A.9: Plots showing MNE-reconstructed FWHM magnetic dipole source localisation in the x-y plane at $z = 0.06\,\mathrm{m}$ (left), y-z plane at $x = -0.084\,\mathrm{m}$ (centre) and x-z plane at $y = -0.001\,\mathrm{m}$ (right) for a magnetic dipole with moment magnitude $10\,\mathrm{nA\,m^2}$ located at (-0.085, 0, 0.06)m and oriented at (1,0,0).

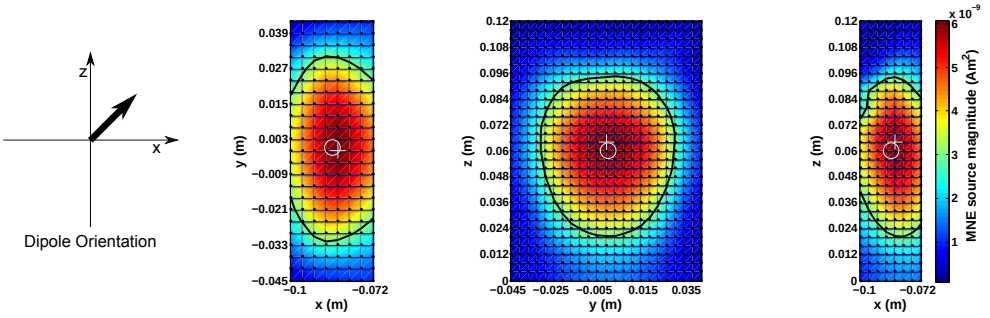

Figure A.10: Plots showing MNE-reconstructed FWHM magnetic dipole source localisation in the x-y plane at $z = 0.064\,\mathrm{m}$ (left), y-z plane at $x = -0.084\,\mathrm{m}$ (centre) and x-z plane at $y = -0.001\,\mathrm{m}$ (right) for a magnetic dipole with moment magnitude $10\,\mathrm{nA\,m^2}$ located at (-0.085, 0, 0.06)m and oriented at (1,0,1).

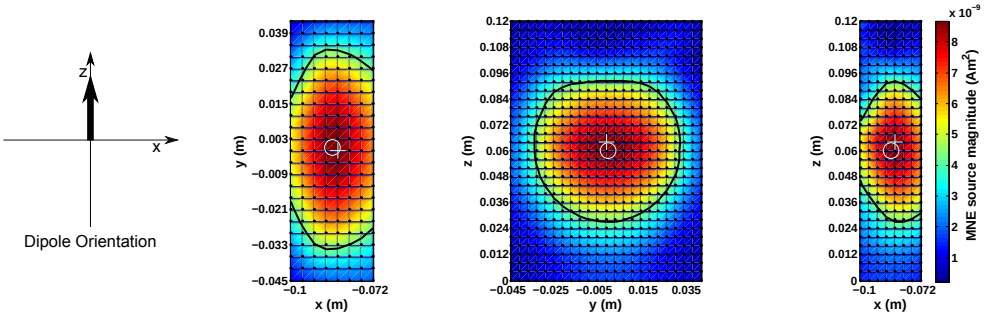

Figure A.11: Plots showing MNE-reconstructed FWHM magnetic dipole source localisation in the x-y plane at $z = 0.064\,\mathrm{m}$ (left), y-z plane at $x = -0.084\,\mathrm{m}$ (centre) and x-z plane at $y = -0.001\,\mathrm{m}$ (right) for a magnetic dipole with moment magnitude $10\,\mathrm{nA\,m^2}$ located at (-0.085, 0, 0.06)m and oriented at (0,0,1).

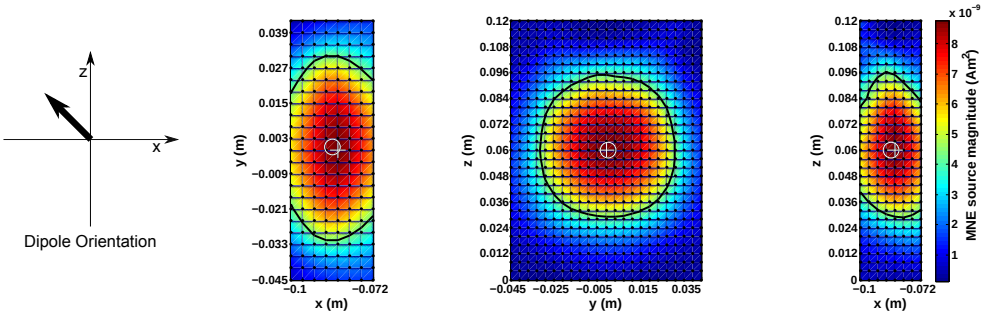

Figure A.12: Plots showing MNE-reconstructed FWHM magnetic dipole source localisation in the x-y plane at $z = 0.06\,\mathrm{m}$ (left), y-z plane at $x = -0.084\,\mathrm{m}$ (centre) and x-z plane at $y = -0.001\,\mathrm{m}$ (right) for a magnetic dipole with moment magnitude $10\,\mathrm{nA\,m^2}$ located at (-0.085, 0, 0.06)m and oriented at (-1,0,1).

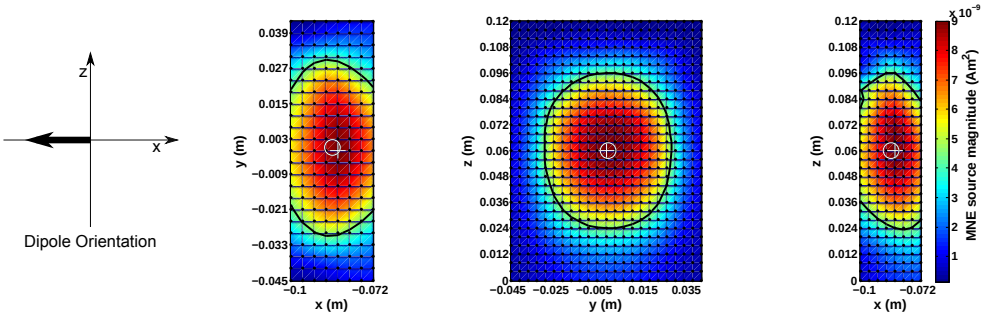

Figure A.13: Plots showing MNE-reconstructed FWHM magnetic dipole source localisation in the x-y plane at $z = 0.06\,\mathrm{m}$ (left), y-z plane at $x = -0.084\,\mathrm{m}$ (centre) and x-z plane at $y = -0.001\,\mathrm{m}$ (right) for a magnetic dipole with moment magnitude $10\,\mathrm{nA\,m^2}$ located at (-0.085, 0, 0.06)m and oriented at (-1,0,0).

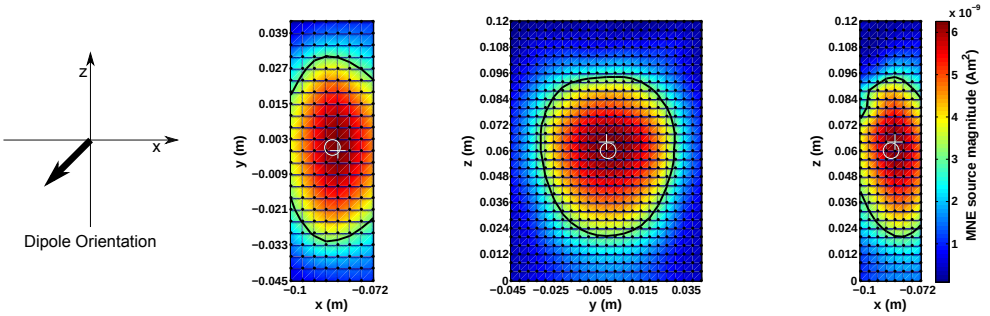

Figure A.14: Plots showing MNE-reconstructed FWHM magnetic dipole source localisation in the x-y plane at $z = 0.064\,\mathrm{m}$ (left), y-z plane at $x = -0.084\,\mathrm{m}$ (centre) and x-z plane at $y = -0.001\,\mathrm{m}$ (right) for a magnetic dipole with moment magnitude $10\,\mathrm{nA\,m^2}$ located at (-0.085, 0, 0.06)m and oriented at (-1,0,-1).

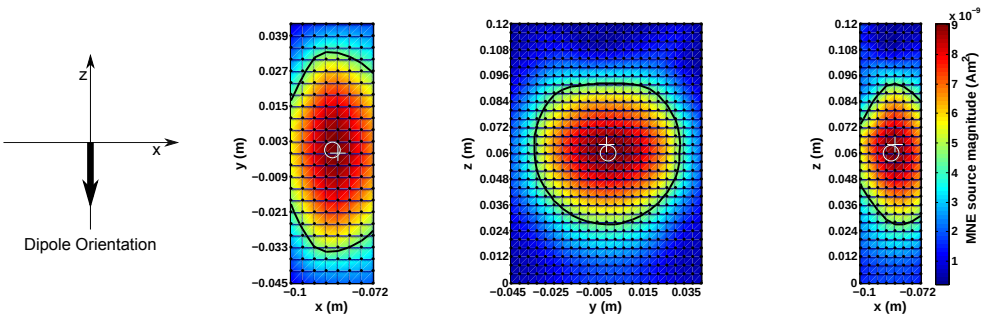

Figure A.15: Plots showing MNE-reconstructed FWHM magnetic dipole source localisation in the x-y plane at $z = 0.064\,\mathrm{m}$ (left), y-z plane at $x = -0.084\,\mathrm{m}$ (centre) and x-z plane at $y = -0.001\,\mathrm{m}$ (right) for a magnetic dipole with moment magnitude $10\,\mathrm{nA\,m^2}$ located at (-0.085, 0, 0.06)m and oriented at (0,0,-1).

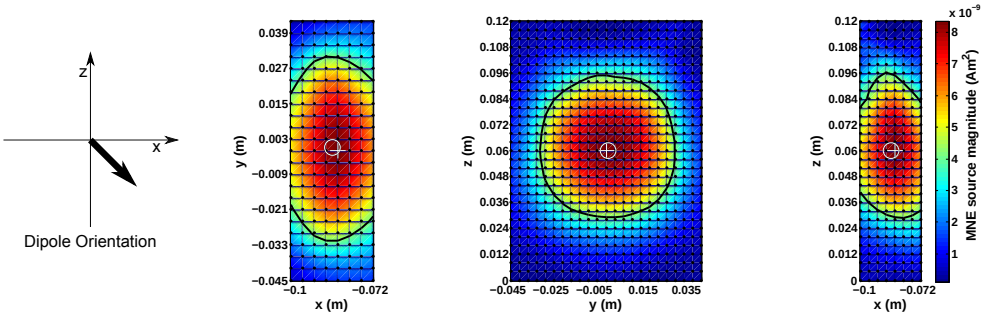

Figure A.16: Plots showing MNE-reconstructed FWHM magnetic dipole source localisation in the x-y plane at $z = 0.06\,\mathrm{m}$ (left), y-z plane at $x = -0.084\,\mathrm{m}$ (centre) and x-z plane at $y = -0.001\,\mathrm{m}$ (right) for a magnetic dipole with moment magnitude $10\,\mathrm{nA\,m^2}$ located at (-0.085, 0, 0.06)m and oriented at (1,0,-1).